

UNIVERSITÀ DEGLI STUDI DI NAPOLI FEDERICO II



Dottorato in Ingegneria Aerospaziale - XXVI ciclo

Spectral Analysis and Classification of Hyper- and Multispectral Data of Planetary Surfaces

Dott.ssa Francesca ZAMBON

Responsabile del corso di Dottorato: Prof. Ing. Luigi DE LUCA

Relatori:

Dott.ssa Maria Cristina DE SANCTIS, INAF-IAPS Roma

Prof. Pasquale PALUMBO, Università Parthenope (NA)

Ai miei genitori
To my parents

Acknowledgements

I wish to thank all the people with whom I have been in touch during the last three years spent for my PhD:

- My family, and the people who have supported my PhD: my external advisors Maria Cristina De Sanctis and Fabrizio Capaccioni.
- My friend and colleague Federico Tosi for his help and for his useful advices.
- My roommate Alessandro Frigeri, who taught me many useful tools that were crucial to achieve the expertise needed to complete this project.
- Cristian Carli for his patience and kindness.
- A special thank goes to my friend Francesca Scipioni, with whom I shared many things in these last few years and who will miss me a lot.
- Gianrico Filacchione, who has always been very helpful with me.
- All the people of the VIR and the Dawn teams.
- Andrea Longobardo, always nice and willingness.
- Giuliano for his cheerfulness and availability.
- The other PhD student and post-doc fellows of the IAPS Institute: Mauro Ciarniello, Andrea Raponi and Fabrizio Oliva for the pleasant moments spent together.
- Eliana and Roberto for their helpfulness.
- Chris, who revised the English of this thesis.
- All the IAPS people who have been nice to me.
- All my friends and in particular Leo, Daniel, Marco and Mirella.
- All the girls with whom I shared my home.
- Finally, a special acknowledgement to Roberto who tolerated me every day trying to be unsuccessfully patient.

Contents

Introduzione	26
Introduction	30
1 Reflectance spectroscopy	35
1.1 Remote sensing	35
1.2 Reflectance	41
1.2.1 Reflectance quantities	41
1.2.2 Bidirectional reflectance and other reflectances types .	43
1.2.3 Bidirectional reflectance distribution function	45
1.3 Reflectance spectroscopy and mineralogy	50
1.4 Scattering	50
1.5 Absorption	52
1.5.1 Molecular rotation	52
1.5.2 Electronic processes	52
1.5.3 Free carriers of charge	57
1.5.4 Vibrational processes	58
1.5.5 Band shape	60
1.6 Continuum	60
1.7 Main minerals in airless bodies	61
1.7.1 Pyroxenes	61
1.7.2 Olivine	70
1.7.3 Feldspar	72
1.8 Hydrate minerals	74
2 Data analysis methods	77
2.1 Planetary Data System (PDS)	78
2.2 Coordinate Systems	81
2.3 Projections	85
2.4 Projections and mosaics of VIR data	93
2.5 Classification methods	97

2.5.1	ISODATA	97
2.5.2	MINIMUM DISTANCE	100
2.6	Spectral unmixing	100
2.7	Linear unmixing	105
2.8	Estimation of the number of endmembers	105
2.9	Endmember extraction	107
2.9.1	Method used for the VIR data on board Dawn	109
3	Messenger and Dawn missions	111
3.1	The Dawn Mission	111
3.1.1	The Dawn spacecraft	114
3.1.2	Dawn Gamma Ray and Neutron Detector (GRaND)	115
3.1.3	Framing Camera (FC)	116
3.1.4	Visible and Infrared spectrometer (VIR)	119
3.2	VIR data	125
3.3	The Messenger mission	126
3.3.1	The spacecraft	127
3.3.2	Scientific instruments	129
3.3.3	MDIS (Mercury Dual Imaging System)	131
3.3.4	MASCS (Mercury Atmospheric and Surface Composition Spectrometer)	135
3.4	VIRS and MDIS data	139
4	Mercury and Vesta	145
4.1	Mercury	145
4.1.1	Mercury origin and structure	147
4.1.2	The magnetic field	149
4.1.3	The exosphere	151
4.2	Vesta	151
4.2.1	Vesta composition	151
4.2.2	Vesta's surface	155
4.2.3	Vesta mineralogy	159
4.2.4	Hydrate material on Vesta	165
4.2.5	Olivine on Vesta	166
5	Classification of VIRS and MDIS data	173
5.1	Reduction of VIRS-MASCS spectra	173
5.1.1	Classification of VIRS data	180
5.2	Reduction of MDIS-WAC images	185
5.2.1	Classification of MDIS-WAC data	186
5.3	Comparison between VIRS and MDIS-WAC results	191

6	Spectral analysis of the BM units on Vesta	193
6.1	Classification of the BM units	193
6.2	Dataset description	197
6.3	Description of the spectral parameters	200
6.3.1	Error estimation and temperature correction	201
6.4	Bright Material spectral analysis	202
6.4.1	Band centers	202
6.4.2	Band depth analysis	208
6.4.3	Band Area Ratio analysis	212
6.4.4	Molar content of Wo and Fs in the bright material	213
6.5	Peculiar cases of Bright Material units	216
6.5.1	Diagenitic Bright Material units	216
6.5.2	Low band depth Bright Material units	217
6.5.3	High albedo Bright Material units	217
7	Linear unmixing applied to VIR data	221
7.1	Description of the method	221
7.2	Linear unmixing applied to laboratory mixtures	222
7.3	Linear unmixing applied to the bright regions	227
7.3.1	Evaluation of the method	242
	Conclusioni	243
	Conclusions	255
A	Maps obtained by the VIR data	261
B	Maps and projection of retrieved data	273
B.1	Single cube projections	273
B.2	Global temperature maps	282
C	Tables	295

List of Figures

1.1	The electromagnetic spectrum (Richards, 2013).	35
1.2	Scanning modes https://www.e-education.psu.edu/geog480/node/494	38
1.3	Diagram of the remote sensing system (Richards, 2013).	39
1.4	Scheme of the concept of hyperspectral remote sensing and image spectroscopy. For each pixel of an image it is possible to extract a spectrum (Dor et al., 2012).	40
1.5	Scheme of incident and reflected beam (Nicodemus et al., 1977).	42
1.6	Scheme of different type of reflectance (Schaepman-Strub et al., 2006).	44
1.7	Geometry of the incident and reflected beam in the bidirectional reflectance case (Nicodemus et al., 1977).	47
1.8	Reflectance spectra of pyroxenes at different grain size. (Clark, 1999).	51
1.9	Summary of the absorption feature for some minerals with the corresponding processes that cause them (Clark, 1999).	53
1.10	Visible and Infrared spectra of olivines and pyroxenes. The absorption bands due to the transition of the Fe are visible in both the spectra. Here are shown two samples of olivine with different content FeO. Band shape and position vary with the composition. The same behavior can be observed for the two different pyroxenes on the bottom. (Clark, 1999).	55
1.11	In the plot are shown the reflectance spectra of the hematite (iron oxide) and goethite (hydroxide). The absorption bands at 0.9 and 0.86 μm are due to the conduction band transitions (Clark, 1999).	56
1.12	Effect of the conduction band in sulfure and cinnabar (Clark, 1999).	57
1.13	Examples of spectra of mineral that present the vibrational absorption band of H_2O , OH and CO_3^{-2} (Clark, 1999).	59

1.14	Top. Continuum for a montmorillonite spectrum. Middle. Continuum for mixtures of montmorillonite plus carbon black (0.5 wt % carbon black). Bottom. Continuum for mixtures of montmorillonite plus carbon black (0.5 wt % carbon black) (Clark and Roush, 1984).	61
1.15	Types of octahedral in pyroxenes.	63
1.16	Clinopyroxenes symmetrical structure.	64
1.17	Orthopyroxenes symmetrical structure.	64
1.18	Ternary diagram of pyroxenes.	65
1.19	A. Orthoferrosilite RELAB spectra with a grain size $<45\mu\text{m}$. B. Orthopyroxene RELAB spectra. Plot represents the same hypersthene sample at different grain sizes. The column on the left indicates the spectrum name with the relative grain sizes. C. Enstatitic pyroxene in red and diopsidic pyroxene in blue are represented. Spectrum name is indicated in the left column.	67
1.20	Howardite, diogenite and eucrite RELAB spectra with a grain size interval between 0 and $25\mu\text{m}$. Howardites are plotted in different shades of green, diogenite in blue and eucrite in red. .	69
1.21	Olivine symmetrical structure.	70
1.22	Olivine spectra selected by RELAB data base. Left column indicates the spectrum name. In green is represented the fosterite (Mg_2SiO_4) and in magenta the fayalite (Fe_2SiO_4) with a grain size range between 25 and $45\mu\text{m}$. The other two spectra are relative to two olivine sample with a grain size interval between 0 and $25\mu\text{m}$ called "green olivine" and "Jackson city" .	72
1.23	Feldspar diagram.	73
1.24	Plagioclase spectra selected by RELAB data base. Left column indicates the spectrum name.	74
2.1	PDS data levels (JPL, 2009).	79
2.2	Example of PDS label file.	80
2.3	Planetocentric and planetographic coordinates (http://planetarynames.wr.usgs.gov/Page/Website).	82
2.4	IAU-accepted coordinate systems for planets and satellites (http://planetarynames.wr.usgs.gov/TargetCoordinates). .	84
2.5	Representation of the latitude (ϕ) and longitude (λ) (http://kartoweb.itc.nl/geometrics/coordinate%20systems/coordsys.html).	86
2.6	Representation of the geoid and the ellipsoid (http://therucksack.tripod.com/MiBSAR/LandNav/Datums/MapDatums.htm). . . .	87

2.7	Representation of the surfaces of projection in the three different orientations.	88
2.8	Representation of three principal point of view (http://www.geografia-applicata.it/wordpress/wp-content/uploads/2011/04/03_Proiezioni_Cartografiche.pdf).	88
2.9	Examples of different types of projection (http://www.geografia-applicata.it/wordpress/wp-content/uploads/2011/04/03_Proiezioni_Cartografiche.pdf).	89
2.10	Top. Ellipses of distortion in the oblique stereographic projection. Bottom. Ellipses of distortion in the equatorial orthographic projection (C. A. Furuti - www.progonos.com/furuti)	91
2.11	Top. Ellipses of distortion in the equatorial cylindrical equidistant projection. Bottom. Ellipses of distortion in the Mercator projection (C. A. Furuti - www.progonos.com/furuti)	92
2.12	Exemple of VIR cube at $1.4\mu\text{m}$	93
2.13	Example of a map file produced by mosrange	94
2.14	Cylindrical projection of the VIR image shown in Fig. 2.12.	95
2.15	Mosaic of the Bellicia and Arruntia region in cylindric projection (Ammannito et al., 2013b).	96
2.16	Scheme of the ISODATA algorithm (Akamatsu et al., 1996).	99
2.17	Linear unmixing concept. The radiance of each pixel is the linear combination of the different endmember (m) each one with the correspondent abundance (α) (Bioucas-Dias et al., 2012).	101
2.18	Nonlinear mixing scheme. Right. Intimate mixture scheme. Left. Multilayered scene (Bioucas-Dias et al., 2012).	102
2.19	Scheme of the hyperspectral unmixing process (Bioucas-Dias et al., 2012).	103
2.20	Simplex representation (Bioucas-Dias et al., 2012).	103
2.21	Example of simplex in the real case (Plaza, 2013).	104
3.1	Vesta phases of the mission divided for the spacecraft altitude (Russell and Raymond, 2011).	112
3.2	Details of phases of the mission for Vesta (Russell and Raymond, 2011).	113
3.3	Global view of the Dawn spacecraft http://dawn.jpl.nasa.gov/technology/spacecraft.asp	114
3.4	Representation of GRaND (Prettyman et al., 2011).	115
3.5	Dawn framing camera (Sierks et al., 2011).	116
3.6	Dawn framing camera characteristics (Sierks et al., 2011).	117

3.7	Scheme of the Framing Camera optical system (Sierks et al., 2011).	117
3.8	Framing camera filter specification (Sierks et al., 2011).	118
3.9	VIR (De Sanctis et al., 2011).	119
3.10	VIR principal characteristics (De Sanctis et al., 2011).	121
3.11	Right. Scheme of the Shafer configuration in VIR telescope. Left. VIR optical layout (De Sanctis et al., 2011).	122
3.12	Scheme of the Offner configuration for VIR (De Sanctis et al., 2011).	122
3.13	Scheme of a beam inside VIR telescope (De Sanctis et al., 2011).	123
3.14	VIR grating (De Sanctis et al., 2011).	123
3.15	Scheme of a VIR cube (De Sanctis et al., 2011).	125
3.16	Journey stages of Messenger (http://messenger.jhuapl.edu).	126
3.17	Representation of the Messenger spacecraft (http://messenger.jhuapl.edu/spacecraft/overview.html).	128
3.18	Messenger Payload (http://messenger.jhuapl.edu).	130
3.19	Representation of MDIS camera (Mick et al., 2013).	131
3.20	Wide angle camera filters Mick et al. (2013).	132
3.21	Characteristics of the WAC and NAC cameras (Mick et al., 2013).	133
3.22	WAC and NAC optical layout (Mick et al., 2013).	134
3.23	Technical characteristics of UVVS and VIRS (Espiritu and Malaret, 2012).	136
3.24	MASCS overview (Espiritu and Malaret, 2012).	137
3.25	VIRS scheme (Espiritu and Malaret, 2012).	137
3.26	Optical scheme of UVVS and VIRS (Espiritu and Malaret, 2012).	138
3.27	MDIS data processing levels (Mick et al., 2013).	142
4.1	Mercury internal structure compared with the Earth (Solomon et al., 2007).	147
4.2	Representation of Mercury's magnetosphere (Solomon et al., 2007).	150
4.3	Representation of Vesta's internal structure (Zuber et al., 2011).	152
4.4	Base model of the internal structure of Vesta (Thomas et al., 1997a,b; Zuber et al., 2011).	152
4.5	Vesta parameters (Zuber et al., 2011).	153
4.6	Vesta map with the names of the principal features. The coordinate system used for this map is claudia double prime (Section 2.2) http://planetarynames.wr.usgs.gov/images/vesta.pdf .	154

4.7	RGB images of Vesta observed by Hubble highlight Vesta mineralogical diversity (Li et al., 2010).	155
4.8	Cylindrical projections of Vesta color mosaics relative to the approach phase (~ 480 m/ pixel), derive from the Framing Camera images. A. Photometrically corrected 0.75-mm filter global mosaic showing east- west and north-south dichotomies in reflectance. B. Clementine color ratios mosaic ($CR = R(0.75)/R(0.45)$, $CG = R(0.75)/R(0.92)$, and $CB = R(0.45)/R(0.75)$). C. Rainbow-color coded map of $R(0.75)/R(0.92)$ ratio. C. Rainbow-color coded map of $R(0.98)/R(0.92)$ ratio (Euclite-Diogenite) showing diogenite-rich regions as red and euclite-rich regions as blue (Reddy et al., 2012a).	157
4.9	Vesta digital terrain model in Mollweide projection (Jaumann et al., 2012).	158
4.10	Vesta albedo map. Top. Albedo map in false color. Bottom. Albedo map in grayscale (Schröder et al., 2013).	158
4.11	Band II center vs. band I center scatter plot relative to the Survey phase of the mission. The colored circles delimit the diogenite (violet), howardite (green) and euclite (yellow) regions (De Sanctis et al., 2012a).	160
4.12	Band center and band depth maps of Vesta relative to the Survey phase of the mission (De Sanctis et al., 2012a).	161
4.13	Band I center maps of Vesta relative to the HAMO and HAMO2 phase of the mission (Ammannito et al., 2013a).	162
4.14	Band II center maps of Vesta relative to the HAMO and HAMO2 phase of the mission (Ammannito et al., 2013a).	163
4.15	Lithologies present on Vesta's surface (Ammannito et al., 2013a).	164
4.16	Map of the $2.8\mu\text{m}$ band on Vesta (De Sanctis et al., 2012b).	166
4.17	A. Olivine rich area on Vesta compared with Vesta average spectrum. B. Olivine-rich area compared with laboratory mixture with different amount of olivine. C. Band II center vs band I center of the HED, olivine and pyroxenes mixture and the olivine-rich area on Vesta (Ammannito et al., 2013b).	169
5.1	Portion of a region covered by VIRS data in the first flyby.	175
5.2	Comparison between the radiance ($\text{W}/\text{m}^2 \text{ sr}^{-1} \text{ nm}$) of the MDIS-NAC image and that of the VIRS spectra does not show any correlation.	175
5.3	Portions of two regions of the flyby II covered by VIRS.	176

5.4	Comparison between the radiance ($\text{W/m}^2 \text{ sr}^{-1} \text{ nm}$) of the MDIS-NAC image and that of the VIRS spectra shows a good correlation.	177
5.5	Dark spectrum.	178
5.6	Example of VIRS reflectance spectrum.	179
5.7	Radiance spectrum of the two merged channels (VIS+NIR). The noisy bands of the visible channel have been removed. . .	179
5.8	Spectral modes of the obtained classes for reflective data VIS+NIR relative to flyby II.	181
5.9	Projection of the classes on Mercury's surface.	182
5.10	Projection of the classes on Mercury's surface.	183
5.11	Projection of the classes on Mercury's surface.	184
5.12	Image of the WAC Rudaki area at 433nm.	185
5.13	Result of the ISODATA classification method.	187
5.14	Mean classes obtain by ISODATA classification.	188
5.15	Result of the MINIMUM DISTANCE classification method. . .	189
5.16	Mean classes obtain by MINIMUM DISTANCE classification method.	190
6.1	Equiangular projection of the Framing Camera clear filter images relative to the bright material units of Types 1 and 2. Violet arrows represent the CWM, green arrows the SM, and the blue arrows the RM. <i>Imagescredit:NASA/JPL-Caltech/UCLA/MPS/DLR/IDA</i>	195
6.2	Location of the BM on Vesta global albedo map. As in Fig. 6.1, we represent in violet the CWM, in green the SM, and in blue the RM. BM names are indicated with the first three letters of the crater name in which they are found. BM in unnamed craters are indicated with the letters "BU" followed by a progressive number. We employ the Claudia coordinates system.	196
6.3	Spectra for the Arruntia, Bellicia, and BU5 BM locations. CWM are plotted in violet, SM are green, RM are in blue, the surrounding region (SR) are in red. Left column: Reflectance spectra normalized at $0.55\mu\text{m}$. Right column: Continuum-removed spectra. Arruntia and Bellicia are olivine-bearing locations, while BU5 is a more typical example of BM. The gap at $1.1 \mu\text{m}$ is the connection between the VIR visible and infrared channels.	198

- 6.4 The mean spectra of Tuccia, Aelia and BU15 BM units. Tuccia and BU15 are the brightest BM units in our study set. BU15 contains a very bright streak (region bounded by the black circle in Fig. 6.11) that has band depths shallower than the surroundings, unlike the other bright units. The magenta spectra in BU15 plot are an example of spectra of the very bright streak. In Aelia, the reduction of the bands in the RM is due to the presence of admixed dark material. The colors of the spectra are indicative of the BM types, as described in Fig. 6.3. Left column: Reflectance spectra normalized at $0.55\mu\text{m}$. Right column: Continuum-removed spectra. The gap at $1.1\mu\text{m}$ is the connection between the VIR visible and infrared channels. 199
- 6.5 Plot of Band I vs. Band II centers of the BM. Symbols and colors designate the BM types. The colored circles delimit the HED regions. 204
- 6.6 Summary diagram of the bright material composition. Each color represents the percentage of diogenitic, howarditic and eucritic BM units. 205
- 6.7 (A): The plot of normal visual albedo vs. band II center does not show a relationship between albedo and band centers. (B): Plot of normal visual albedo vs. band II depth. Solid line represents the best fit. 207
- 6.8 (A): Band I vs. Band II depth for the BM units. The corresponding best fit line is shown. (B): Band depths of the BM regions compared with those of the HED RELAB samples at different grain size. 210
- 6.9 Plot of Band I center vs. BAR for the different types of BM units along with those for the HED RELAB samples of grain size $<25\mu\text{m}$ 213
- 6.10 Pyroxene diagram for Vesta's BM units and the surrounding regions. Tuccia and Eumachia, the most eucritic BM units exhibit high amounts of Wo and Fs, while BU8, BU5 and Aelia are those with the lowest content of Wo and Fs. Bellicia's position in the plot is not representative of its pyroxenes because of the presence of large amounts of olivine. We include it in the diagram, only to show the strong contrast between Bellicia and the other BM. 215

6.11	VIR LAMO image of BU15 at 0.55 μm (VIR cube 385962328) overlapped with the corresponding Framing Camera image (FC21B0015548_11361091538F1D). The images are represented in stereographic projection. The black circle indicates the very bright streak inside the BU15-SM.	219
7.1	Mixtures of two pyroxenes, enstatite and diopside. In this case the linear approach gives good results with small differences between the laboratory data and the retrieved coefficients. . .	224
7.2	Mixtures of pyroxenes and olivine. For high olivine content the mixed spectrum (red) does not match the laboratory spectrum (blue) perfectly; in particular the second band totally disappears in the mixed spectrum for very high olivine content. Despite a high χ^2 value, the amount of olivine is correctly estimated within 4%, in the mixture with the highest content of olivine.	225
7.3	Mixtures of pyroxenes and plagioclase. For high content of plagioclase the linear approach is unsuited to describe the mixture. The amount of plagioclase is underestimated by 19% respect to the real value, and the fit curve (red) does not match the laboratory mixture (blue) in the continuum range between the first and the second band.	226
7.4	Amounts of eucrite, diogenite and olivine of the retrieved by linear spectral mixing.	228
7.5	Amounts of the different eucrite and diogenite types in the bright units on Vesta.	229
7.6	Locations of the bright units containing cumulate eucrite. . . .	230
7.7	VIR spectra of different BM units compared with the best mixed spectra. In each plot we indicate the endmember with the relative amounts and the χ^2 value. The green spectrum represents the mixed spectrum, while the blue spectrum is the average spectrum of the correspondent BU provided by VIR. .	234
7.8	VIR spectra of different BM units compared with the best mixed spectra. In each plot we indicate the endmember with the relative amounts, and the χ^2 value. The green spectrum represents the mixed spectrum, while the blue spectrum is the average spectrum of the correspondent BU provided by VIR. .	235

- 7.9 VIR spectra of different BM units compared with the best mixed spectra. In each plot we indicate the endmember with the relative amounts, and the χ^2 value. The green spectrum represents the mixed spectrum, while the blue spectrum is the average spectrum of the correspondent BU provided by VIR. . 236
- 7.10 VIR spectra of different BM units compared with the best mixed spectra. In each plot we indicate the endmember with the relative amounts, and the χ^2 value. The green spectrum represents the mixed spectrum, while the blue spectrum is the average spectrum of the correspondent BU provided by VIR. . 237
- 7.11 VIR spectra of different BM units compared with the best mixed spectra. In each plot we indicate the endmember with the relative amounts, and the χ^2 value. The green spectrum represents the mixed spectrum, while the blue spectrum is the average spectrum of the correspondent BU provided by VIR. . 238
- 7.12 VIR spectra of different BM units compared with the best mixed spectra. In each plot we indicate the endmember with the relative amounts, and the χ^2 value. The green spectrum represents the mixed spectrum, while the blue spectrum is the average spectrum of the correspondent BU provided by VIR. . 239
- 7.13 VIR spectra of different BM units compared with the best mixed spectra. In each plot we indicate the endmember with the relative amounts, and the χ^2 value. The green spectrum represents the mixed spectrum, while the blue spectrum is the average spectrum of the correspondent BU provided by VIR. . 240
- 7.14 VIR spectra of different BM units compared with the best mixed spectra. In each plot we indicate the endmember with the relative amounts, and the χ^2 value. The green spectrum represents the mixed spectrum, while the blue spectrum is the average spectrum of the correspondent BU provided by VIR. . 241
- 7.15 Top: Diogenite abundances vs band II center. The linear relation between band II center and abundance of diogenite indicates that diogenite abundance decreases as the band II center decreases, according with the pyroxenes mineralogy. Bottom: Eucrite abundances vs band II center. Eucrite abundance increases with increasing band II center, as expected. When the two endmembers are both eucrite the total amount of eucrite is 1 which correspond to an amount of diogenite equal to zero. 244

7.16	Top: Band II center vs. band I center of the bright units compared with those of the eucrite and diogenite sample. Bottom: Band II depth vs. band I depth of the bright units compared with those of the eucrite and diogenite samples. Endmembers identified by linear unmixing are in bold characters.	245
7.17	Top: Spectra of the whole diogenite sample. Colored spectra are those selected as endmembers. Bottom: Spectra of the whole diogenite sample with continuum removed.	246
7.18	Top: Spectra of the whole eucrite sample. Colored spectra are those selected as endmembers. Bottom: Spectra of the whole eucrite sample with continuum removed.	247
7.19	Top: Spectra of the selected olivine. Bottom: Spectra of selected olivines with continuum removed.	248
7.20	Abundances estimated for the ten lowest χ^2 values for BU12-SM. In this case the fit is not optimal and for small χ^2 variations, different endmembers may be found.	249
7.21	Abundances estimated for the ten lowest χ^2 values for BU12-SM. In this case the fit is not optimal and for small χ^2 variations, different endmembers may be found.	250
7.22	Abundances estimated for the ten lowest χ^2 values for the BU1-RM. In this case χ^2 is low, and the fit is good. For small χ^2 variations, the endmembers remain the same.	251
7.23	Abundances estimated for the ten lowest χ^2 values for the BU1-RM. In this case χ^2 is low, and the fit is good. For small χ^2 variations, the endmembers remain the same.	252
A.1	RGB (red: reflectance at $1.9\mu\text{m}$, green: reflectance at $1.5\mu\text{m}$, blue: reflectance at $1.2\mu\text{m}$) images of Tarpeia crater mosaics in Vesta south pole derived by the VIR data relative to the LAMO phase mission in polar stereographic projection (http://dawn.jpl.nasa.gov/multimedia/tarpeia\$_\$crater.asp).	262
A.2	RGB image of the Oppia region derived by the VIR data relative to the Survey phase mission in simple cylindrical projection (De Sanctis et al., 2012a) (http://dawn.jpl.nasa.gov/multimedia/tarpeia\$_\$temperature.asp).	263
A.3	Vesta global mosaic derived by the VIR data relative to the HAMO phase mission at $0.55\mu\text{m}$ in orthographic projection (http://dawn.jpl.nasa.gov/multimedia/imageoftheday/image.asp?date=20120208). The image has been selected for the Dawn Events Calendar (http://dawn.jpl.nasa.gov/multimedia/calendar.asp).	264

A.4	Vesta global mosaic derived by the VIR data relative to the HAMO2 phase mission at $0.55\mu\text{m}$ in simple cylindrical projection.	265
A.5	Vesta mosaic of the north pole derived by the VIR data of the HAMO2 phase mission at $0.55\mu\text{m}$ in polar stereographic projection.	266
A.6	Vesta mosaic of the south pole derived by the VIR data relative to the HAMO2 phase mission at $0.55\mu\text{m}$ in polar stereographic projection.	267
A.7	Vesta global mosaic derived by the VIR data relative to the HAMO and HAMO2 phase mission at $0.55\mu\text{m}$ in orthographic projection.	268
A.8	Vesta global mosaic derived by the VIR data relative to the LAMO phase mission at $0.55\mu\text{m}$ in orthographic projection.	269
A.9	Mosaic of Bellicia and Arruntia region relative to the HAMO2 phase mission in simple cylindrical projection (Ammannito et al., 2013b) (http://dawn.jpl.nasa.gov/multimedia/Two\$_\$Craters\$_\$Olivine.asp).	270
A.10	Mosaic of Bellicia region relative to the HAMO2 phase mission in simple cylindrical projection (Ammannito et al., 2013b) (http://dawn.jpl.nasa.gov/multimedia/Contrast\$_\$enhanced\$_\$Bellicia\$_\$Crater.asp).	271
B.1	Temperature mosaic of the Tarpeia region in Vesta south pole derived by the VIR data relative to the LAMO phase mission in polar stereographic projection (http://dawn.jpl.nasa.gov/multimedia/tarpeia\$_\$temperature.asp).	274
B.2	Marcia images relative to the Survey phase mission in equirectangular projection. In this figure are represented temperature, reflectance at $1.4\mu\text{m}$ no photometrically corrected and photometrically corrected by Akimov and incidence angle (Tosi et al., 2014a).	275
B.3	Very dark material near Marcia Crater relative to the HAMO2 phase mission in equirectangular projection. In the after left panel is represented a LAMO camera clear filter image of the same region in equirectangular projection. In this figure are the reflectance at $1.4\mu\text{m}$ no photometrically corrected and photometrically corrected by Akimov with the relative temperature (Tosi et al., 2014a).	276

B.4	Very dark unit in the Numisia crater region relative to the Survey phase mission in equirectangular projection. In the after left panel is represented a HAMO camera clear filter image of the same region in equirectangular projection. In this figure are the reflectance at $1.4\mu\text{m}$ no photometrically corrected and photometrically corrected by Akimov with the relative temperature (Tosi et al., 2014a).	277
B.5	Very bright unit Tuccia images relative to the HAMO phase mission in equirectangular projection. In the after left panel is represented a HAMO camera clear filter image of the same region in equirectangular projection. In this figure are the reflectance at $1.4\mu\text{m}$ no photometrically corrected and photometrically corrected by Akimov with the relative temperature (Tosi et al., 2014a).	278
B.6	Very bright Unit 3 (BU3) images relative to the HAMO phase mission in equirectangular projection. In the after left panel is represented a LAMO camera clear filter image of the same region in equirectangular projection. In this figure are the reflectance at $1.4\mu\text{m}$ no photometrically corrected and photometrically corrected by Akimov with the relative temperature (Tosi et al., 2014a).	279
B.7	Bright material in Pinaria crater images relative to the HAMO phase mission in equirectangular projection. In the after left panel is represented a HAMO camera clear filter image of the same region in equirectangular projection. In this figure are the reflectance at $1.4\mu\text{m}$ no photometrically corrected and photometrically corrected by Akimov with the relative temperature (Tosi et al., 2014a).	280
B.8	Crater Myia in Matronalia Rupes images relative to the HAMO phase mission in equirectangular projection. In the after left panel is represented a LAMO camera clear filter image of the same region in equirectangular projection. In this figure are the reflectance at $1.4\mu\text{m}$ no photometrically corrected and photometrically corrected by Akimov with the relative temperature (Tosi et al., 2014a).	281
B.9	Temperature global mosaic of Vesta derived by the VIR data relative to the Survey phase mission in equirectangular projection (Tosi et al., 2014b).	283
B.10	Temperature global mosaic of Vesta derived by the VIR data relative to the Survey phase mission in equirectangular projection (Tosi et al., 2014b).	284

B.11 Temperature global mosaic of Vesta derived by the VIR data relative to the Survey phase mission filtered by local solar time between 8 and 10 h in equirectangular projection (Tosi et al., 2014b).	285
B.12 Temperature global mosaic of Vesta derived by the VIR data relative to the Survey phase mission filtered by local solar time between 10 and 12 h in equirectangular projection (Tosi et al., 2014b).	286
B.13 Temperature global mosaic of Vesta derived by the VIR data relative to the Survey phase mission filtered by local solar time between 12 and 14 h in equirectangular projection (Tosi et al., 2014b).	287
B.14 Temperature global mosaic of Vesta derived by the VIR data relative to the Survey phase mission filtered by local solar time between 14 and 16 h in equirectangular projection (Tosi et al., 2014b).	288
B.15 Temperature global mosaic of Vesta derived by the VIR data relative to the HAMO phase mission in equirectangular projection (Tosi et al., 2014b).	289
B.16 Temperature global mosaic of Vesta derived by the VIR data relative to the HAMO phase mission filtered by local solar time between 10 and 12 h in equirectangular projection (Tosi et al., 2014b).	290
B.17 Temperature global mosaic of Vesta derived by the VIR data relative to the HAMO phase mission filtered by local solar time between 10 and 12 h in equirectangular projection (Tosi et al., 2014b).	291
B.18 Temperature global mosaic of Vesta derived by the VIR data relative to the LAMO phase mission in ortographic projection (Tosi et al., 2014b).	292
B.19 Temperature global mosaic of Vesta derived by the VIR data relative to the LAMO phase mission in equirectangular projection (Tosi et al., 2014b).	293

List of Tables

1.1	Distribution function of the types of reflectances shown in Fig. 1.6 (Nicodemus et al., 1977).	48
1.2	Summary of the reflectance quantities used.	49
1.3	Nomenclature and composition of pyroxenes (Morimoto et al., 1988).	66
1.4	Nomenclature and composition of olivines.	71
3.1	Table showing the main information related to the EDR of the first flyby for the two data sets VIS and NIR.	140
3.2	Table showing the main information related to the EDR of the first flyby for the two data sets VIS and NIR.	141
4.1	Mercury physical and orbital parameters	146
5.1	Characteristics of the file of the first two of Mercury flybys carried out by Messenger.	174
5.2	Characteristics of the geometries file.	174
5.3	Classes obtained from the ISODATA classification of the VIRS data.	180
6.1	Classification of the BM according to the normal visual albedo. The bright regions are classified in five categories. The first column indicates how much BM units are bright, with respect to Vesta geometric albedo.	196

7.1	Results obtained for mixtures of enstatite and diopside, olivine and pyroxene, and plagioclase and pyroxenes. The first column reports the amount of each endmember in the laboratory mixtures. The second and third columns show the value of the coefficients obtained by linear mixing relative to each endmember. The fourth column reports the difference between the amount of coefficients for laboratory mixtures and those obtained by the mixing. In fifth column, χ^2 values indicative of the fit accuracy are reported.	223
7.2	A list of the endmembers considered. We select 26 eucrites, 10 diogenites and 2 olivines samples, with a grain size up to $25\mu\text{m}$, typical of Vesta bright regions. In the first column we report the name of the sample while in the second column the type. The third column indicates how many time each sample has been identified as endmember. The fourth column reports the percentage of the presence of the single sample relating to the type. For example, Bereba appears 11 times as endmember, and corresponds to 13% of all the eucrite sample.	231
7.3	Classifications of the eucrite and diogenite. For definitions please refer to the "Meteoritical society bulletin" (http://www.lpi.usra.edu/meteor/about.php).	232
7.4	Results of the linear unmixing applied to the bright material VIR data. In the third and fifth columns letter E indicates eucrite, D diogenite, Ol olivine.	233
C.1	Band center positions for Crater Wall Material.	295
C.2	Band center positions for Slope Material.	296
C.3	Band center positions for Radial Material.	297
C.4	Molar content of wollastonite and ferrosilite for Crater Wall Material.	298
C.5	Molar content of wollastonite and ferrosilite for Slope Material.	299
C.6	Molar content of wollastonite and ferrosilite for Radial Material.	300

C.7	Overview of CWM characteristics. In the table are reported the values of the latitude and longitude of the crater wall material (second and third columns). The fourth column contains the normal visual albedo and the fifth one the how the crater wall material albedo exceed the mean albedo of Vesta. Band I and II depth, while Band area ratio (BAR) are reported in sixth, seventh and eighth columns. In the three columns there are the phase, incidence and emission angles. All the values reported are the average of bright areas. Values of latitude and longitude refer to the Claudia coordinates system.	301
C.8	Overview of SM characteristics. In the table are reported the values of the latitude and longitude of the slope material (second and third columns). The fourth column contains the normal visual albedo and the fifth one the how the slope material albedo exceed the mean albedo of Vesta. Band I and II depth and (Band Area Ratio) BAR are reported in sixth, seventh and eighth columns. In the three columns there are the phase, incidence and emission angles. All the values reported are the average of bright areas. Values of latitude and longitude refer to the Claudia coordinates system.	302
C.9	Overview of RM characteristics. In the table are reported the values of the latitude and longitude of the radial material (second and third columns). The fourth column contains the normal visual albedo and the fifth one the how the radial material albedo exceed the mean albedo of Vesta. Band depth I, II and (Band Area Ratio) BAR are reported in sixth, seventh and eighth columns. In the three columns there are the phase, incidence and emission angles. All the values reported are the average of bright areas. Values of latitude and longitude refer to the Claudia coordinates system.	303
C.10	Band centers and band depths values of the very bright steak in BU15-SM (black circle in Fig. 6.11) and of its surroundings.	304
C.11	Band depths values of RELAB samples of HEDs with different grain size.	305
C.12	Band center I and BAR values of RELAB samples of HEDs with grain size between 0 and $25\mu\text{m}$	306

Introduzione

Lo scopo di questa tesi è quello di preparare e analizzare dati hyperspettrali e multispettrali di superfici planetarie di corpi senza atmosfera. Nel primo capitolo, illustriamo il concetto e l'importanza del telerilevamento e i principi della spettroscopia di riflettanza. Il secondo descrive i metodi utilizzati per ridurre e analizzare i dati, mentre nel terzo capitolo diamo una visione globale delle missioni Dawn e Messenger, dedicate rispettivamente allo studio di Vesta e Mercurio, e in particolare descriveremo gli strumenti di cui abbiamo analizzato i dati. Il quarto capitolo descrive brevemente Mercurio e Vesta, sottolineando i principali risultati ottenuti da queste missioni. Nel quinto capitolo mostriamo i risultati ottenuti dell'analisi dei dati di Messenger, mentre nel sesto illustriamo l'analisi spettrale dettagliata delle regioni chiare di Vesta. Alla fine, nel settimo capitolo, deriviamo la composizione delle unità chiare di Vesta utilizzando il "linear spectral unmixing". Infine, nelle conclusioni riassumiamo il lavoro fatto e i principali risultati ottenuti. In appendice abbiamo riportato tutte le mappe prodotte e pubblicate durante la tesi.

Il telerilevamento di immagini multispettrali e iperspettrali trova molte applicazioni nelle missioni spaziali sia per lo studio e il monitoraggio della Terra che per quello di altri corpi del Sistema Solare (Capitolo 1). Gli strumenti in grado di produrre dati multispettrali e iperspettrali sono: spettrometri a immagine, spettrometri puntuali, e camere multicanale. Gli spettrometri a immagine forniscono allo stesso tempo l'informazione spaziale e spettrale. Un'immagine iperspettrale è costituita da una matrice, chiamata cubo, composta da S (Samples) \times L (Lines) \times B (Bands). I samples e le lines (pixels) forniscono l'informazione spaziale della scena acquisita, e ad ogni pixel viene associato un certo numero di bande, quindi uno spettro. Le dimensioni del cubo variano in base alle caratteristiche dello strumento. La risoluzione del pixel dipende dalle proprietà dello spettrometro e dall'altitudine dello spacecraft. La risoluzione spettrale dipende dal numero di bande. Una buona risoluzione spaziale e spettrale, e un adeguato intervallo spettrale, permettono di determinare la composizione dell'oggetto

considerato.

Gli spettrometri puntuali non producono immagini iperspettrali, ma acquisiscono un pixel per volta a cui viene associato lo spettro, quindi è necessario un tempo maggiore per mappare l'intero corpo, e i dati devono essere trattati diversamente. Le camere a bordo di satelliti sono spesso provviste di una decina di canali, producendo così immagini multispettrali utili per rivelare differenze in composizione di una data area.

In ogni caso, i dati devono essere georeferenziati e proiettati. A differenza dei dati prodotti da spettrometri a immagine, i dati prodotti da spettrometri puntuali devono essere proiettati su un'immagine per associare l'informazione spettrale a quella spaziale.

Generalmente, i dati forniti dagli spettrometri sono prodotti in 2 o più canali distinti, ciascuno contenente centinaia di bande, questi canali devono essere uniti per avere l'intero spettro. Ogni canale corrisponde a un intervallo spettrale, ad esempio visibile o infrarosso. Le camere contengono un filtro per ogni lunghezza d'onda. Le immagini che sono prodotte separatamente, devono essere precedentemente coregistrate e unite in ordine di lunghezza d'onda in un unico file.

In questo lavoro mostriamo come preparare e estrarre informazioni scientifiche da questi dati (Capitoli 2, 5, 6, 7). In particolare i dati che abbiamo analizzato provengono da tre strumenti: Mercury Atmospheric and Surface Composition Spectrometer (MASCS), Mercury Dual Imaging System (MDIS) a bordo di Messenger, and Visible and InfraRed (VIR) spectrometer a bordo di Dawn.

Messenger appartiene al programma discovery della NASA, ed è stata la prima missione ad entrare in orbita attorno a Mercurio. Mercurio è il pianeta più vicino al Sole, ma allo stesso tempo il meno esplorato, a causa delle sue condizioni estreme dovute alla vicinanza con Sole. Nel 1974 Mariner 10, è stata la prima missione ad esplorare Mercurio, durante i tre flyby del pianeta ha mappato $\sim 45\%$ della sua superficie (Solomon et al., 2007), lasciando molte questioni irrisolte. Dopo Mariner 10 Mercurio è rimasto inesplorato per circa 30 anni. Nel 2004 è stata lanciata la sonda Messenger, e nel marzo del 2011 è entrata in orbita intorno a Mercurio, permettendo di rispondere a molti quesiti rimasti senza risposta.

Qui abbiamo analizzato i dati forniti da MASCS e MDIS relativi ai primi due flyby di Mercurio. MASCS, lo spettrometro di Messenger, ha acquisito più di 1.6 milioni di spettri ed è composto da due unità: l'Ultraviolet and Visible Spectrometer (UVVS), per lo studio dell'atmosfera, e il the Visible and Infrared Spectrograph (VIRS), dedicato alla composizione della superficie e che ha fornito i dati che abbiamo analizzato. VIRS ha acquisito spettri pixel per pixel, in un intervallo di lunghezze d'onda tra 215 and 1400 nm

(<http://starbrite.jpl.nasa.gov>). MDIS è composto da due unità: una camera ad alta risoluzione Narrow Angle Camera (NAC), e una Wide Angle Camera (WAC) contenente 12 filtri (Mick et al., 2013).

Dato che gli spettri di Mercurio non mostrano evidenti segnature spettrali, abbiamo utilizzato due differenti metodi di classificazione (Capitoli 5). I metodi di classificazione sono algoritmi di clustering, che si basano sul raggruppare in classi pixel con caratteristiche simili (Adams and Gillespie, 2006). Questi metodi sono divisi in due categorie: unsupervised and supervised. Nei metodi unsupervised è l'algoritmo che decide le classi di riferimento (endmembers), mentre in quelli supervised è l'utente a scegliere gli endmembers. Questi metodi sono molto utili quando non si hanno informazioni *a priori* sui dati (Adams and Gillespie, 2006). Qui, abbiamo applicato il metodo di classificazione ISODATA (Ball and Hall, 1965; Memarsadeghi et al., 2007) ai dati di VIRS, e abbiamo associato le classi trovate alle immagini della regione corrispondente. Abbiamo inoltre applicato ISODATA alle immagini di MDIS-WAC per determinare le classi di riferimento da utilizzare nel metodo di classificazione supervised della DISTANZA MINIMA (Wacker and Landgrebe, 1972). In questo modo siamo stati in grado di separare le classi rappresentative dei differenti tipi di terreni da quelle affette da condizioni di illuminazione non favorevoli. Abbiamo infine confrontato i risultati della classificazione dei dati di MDIS-WAC con quella dei dati di VIRS, trovando una relazione tra l'informazione spettrale e la corrispondente immagine.

Anche Dawn è una missione di tipo discovery della NASA, volta allo studio dei due principali asteroidi della fascia principale: Vesta e Ceres (Russell et al., 2007, 2012, 2013). Dawn è stata lanciata nel settembre del 2007 ed è entrata in orbita attorno a Vesta nel luglio del 2011. La missione a Vesta si è conclusa nel settembre 2012, dopodiché Dawn ha intrapreso il suo viaggio verso Cerere (Russell and Raymond, 2011) (Capitolo 3).

Vesta è stata oggetto di numerosi studi, osservazioni e lavori teorici. L'interesse per Vesta è cresciuto quando Feierberg and Drake (1980) hanno proposto una possibile connessione tra questo asteroide e le meteoriti di howardite, eucrite e diogenite (in seguito ci riferiremo ad esse come HED). Vesta è il secondo oggetto più massivo della fascia principale di asteroidi, con un diametro di 525 km (Thomas et al., 1997a; Zuber et al., 2011), e gli spettri in riflettanza della sua superficie sono caratterizzati dalle bande di assorbimento dei pirosseni (McCord et al., 1970; Gaffey, 1997; Zuber et al., 2011; Pieters et al., 2011; De Sanctis et al., 2012a, De Sanctis et al., 2013). Dawn è dotato di uno spettrometro a immagine visibile e vicino infrarosso (VIR), progettato per mappare la mineralogia degli asteroidi Vesta e Cerere in un intervallo di lunghezze d'onda tra 0.25 e 5.0 μm (De Sanctis et al., 2011; Russell and Raymond, 2011). Tutti gli spettri di VIR relativi alla superficie

di Vesta mostrano entrambe le bande di assorbimento a 0.9- (banda I) and 1.9- μm (banda II), confermando la presenza di pirosseni a basso contenuto di calcio (De Sanctis et al., 2012a).

Qui presentiamo il primo studio dettagliato delle proprietà spettrali delle unità chiare di Vesta (Bright Material (BM) units). Queste unità chiare sono caratterizzate da un'alta albedo, fino al 40% maggiore rispetto a quella media di Vesta (Li et al., 2010, 2013; Schröder et al., 2013). Le unità chiare non sono uniformemente distribuite e non sono spazialmente correlate con quelle più scure (dark material), suggerendo un'origine differente (McCord et al., 2012).

I parametri spettrali più indicati per la caratterizzazione mineralogica di Vesta sono i centri delle bande I e II (Gaffey, 1997; De Sanctis et al., 2012a; McSween et al., 2013b). Le profondità delle bande danno informazione sull'abbondanza dei minerali presenti, sulla dimensione dei grani, mentre il Band Area Ratio (BAR) è utile per valutare la presenza di olivina in miscela olivina-pirosseno (Cloutis et al., 1986). Questi parametri permettono la derivazione dell'abbondanza di wollastonite (Wo) and ferrosilite (Fs) nei pirosseni. Burbine et al. (2007, 2009) e Gaffey et al. (2002) hanno ricavato le formule per il calcolo dei contenuti molari di Wo e Fs, in due modi diversi sempre utilizzando le posizioni dei centri delle bande di assorbimento. Noi abbiamo applicato gli stessi metodi ai dati di VIR per ricavare il contenuto di wollastonite e ferrosilite delle BM units (vedi Capitoli 6).

Per completare la nostra analisi abbiamo applicato il linear spectral unmixing agli spettri delle unità chiare di Vesta. I metodi di unmixing lineare sono basati sul supporre che uno spettro misurato sia dato dalla combinazione lineare di n spettri noti scelti come endmembers. I coefficienti della combinazione lineare rappresentano le abbondanze di ciascun endmember (Bioucas-Dias et al., 2012; Plaza, 2013). Esistono molti algoritmi per determinare il numero di endmember e quali sono quelli rappresentativi della scena osservata (Bioucas-Dias et al., 2012; Plaza, 2013). Nel nostro caso sappiamo *a priori*, dall'analisi spettrale che le unità chiare di Vesta, considerando la scala spaziale dei dati, sono composte da eucrite, diogenite and olivina. Nel Capitolo 7 riportiamo i risultati ottenuti.

Introduction

The aim of this thesis is to prepare and analyze hyperspectral and multispectral data of the surfaces of airless bodies. In the first chapter, we illustrate the concept and the importance of remote sensing, and the principles of reflectance spectroscopy. The second chapter describes the methods used to reduce and analyze the data, while in the third chapter we give an overview of the Dawn and Messenger missions, dedicated to the study of Vesta and Mercury respectively, and in particular on the instruments that provided the data analyzed. The fourth chapter describes briefly Mercury and Vesta, underlying the principal results obtained by these missions. In the fifth chapter we show the results obtained by the analysis of Messenger data, while in the sixth chapter we illustrate the detailed spectral analysis that we performed on the bright regions on Vesta. At the end, in the seventh chapter, we derive the composition of Vesta bright units by linear spectral unmixing. Finally, in the conclusion we summarize the work done and the main findings. In the appendix we collect all the maps produced and published during the thesis.

Multispectral and hyperspectral remote sensing finds many applications in space missions both for the study and monitoring of the Earth and for other Solar System bodies (Chapter 1). Three main kinds of instruments are those able to produce multispectral and hyperspectral data: Imaging spectrometers, point spectrometers, and multichannel cameras. Imaging spectrometers are able to produce spatial information and spectral information at the same time. The hyperspectral images consist in a 3D matrix, called cube, of S (Samples) X L (Lines) X B (Bands). Samples and lines (pixels) retain the spatial information of the acquired scene, and to each pixel are associated a certain number of bands (wavelengths), and thus a spectrum. The cube dimension varies according to the instrument characteristics. Pixel resolution depends upon the characteristics of the spectrometer and on the spacecraft altitude. The spectral resolution depends on the number of bands. A good spatial and spectral resolution, and an adequate spectral range, allow determining the composition of the selected target.

Point spectrometers do not produce hyperspectral images, but acquire one

pixel at a time to which is associated a spectrum. Therefore time is needed to cover a whole body, and the data must be treated differently. Cameras on board satellites are often provided for a dozen channels, producing multispectral data useful to reveal differences in composition of a given area. In any case, the data must be georeferenced and projected. Unlike the data produced by the imaging spectrometer, data produced by the point spectrometer must be projected on a camera image to associate the spectral information to the spatial locations.

Generally data provided by spectrometers are produced in two or more distinct channels, each one containing hundreds bands, that must be merged to have the whole spectrum. Each channel corresponds to a spectral range, e.g. visible or infrared. Cameras contain a filter for each wavelength of interest. The images are produced separately in order to obtain a multispectral cube, and must be previously coregistered, and merged in a unique file in order of wavelength.

Here we show how to prepare and extract scientific information from these data (Chapters 2, 5, 6, 7). In particular the data analyzed are provided by three instruments: Mercury Atmospheric and Surface Composition Spectrometer (MASCS), Mercury Dual Imaging System (MDIS) onboard Messenger, and Visible and InfraRed (VIR) spectrometer onboard Dawn.

Messenger belongs to the NASA discovery program, and is the first mission to enter in orbit around Mercury. Mercury is the closest planet to the Sun, and at the same time the less explored, because of its extreme environment due to its proximity to the Sun. In 1974 Mariner 10, the first mission to explore Mercury, during the three Hermean flybys mapped $\sim 45\%$ of its surface (Solomon et al., 2007), leaving many questions unanswered. Mercury remained unexplored for about 30 years. In 2004 Messenger was launched, and in March 2011 entered orbit around Mercury, enabling some answers to many unsolved questions.

Here we analyze the data provided by MASCS and MDIS relative to the first two flybys of Mercury. MASCS, the Messenger spectrometer, acquired more than 1.6 million spectra. It is composed of two units: the Ultraviolet and Visible Spectrometer (UVVS), for the study of the atmosphere, and the Visible and Infrared Spectrograph (VIRS), dedicated to the surface composition, which provides the data analyzed. VIRS acquired spectra, pixel by pixel, in a range of wavelength between 215 and 1400 nm (<http://starbrite.jpl.nasa.gov>). MDIS is composed of two units: a high resolution camera Narrow Angle Camera (NAC), and a Wide Angle Camera (WAC) containing 12 filters (Mick et al., 2013).

Due to the lack of clear spectral features in the Hermean spectra, we used two different classification methods (Chapter 5). Classification meth-

ods are clustering algorithms based on group pixels with similar characteristics in their classes (Adams and Gillespie, 2006). They are divided in two categories: unsupervised and supervised. In the unsupervised methods the algorithm decides the training classes (endmembers), while in the supervised methods the users choose the endmembers. These methods are very useful when no *a priori* information is available (Adams and Gillespie, 2006). Here, we apply the ISODATA unsupervised classification method (Ball and Hall, 1965; Memarsadeghi et al., 2007) to the VIRS data, and we associate the retrieved classes with the imaged scene. We also apply ISODATA to the MDIS-WAC images to derive the training classes to be used in the MINIMUM DISTANCE supervised classification method (Wacker and Landgrebe, 1972). In this way we have been able to separate classes representative of different terrains that are affected by the illumination conditions. The results of the classifications of MDIS-WAC with those of VIRS are compared finding a relation between the spectral information and the corresponding images.

Dawn is a NASA discovery mission too, devoted to the exploration of the two largest main belt asteroids: Vesta and Ceres (Russell et al., 2007, 2012, 2013). The Dawn spacecraft was launched in September 2007 and entered orbit around Vesta in July 2011. The mission at Vesta ended in September 2012. After that, Dawn started its journey to Ceres (Russell and Raymond, 2011) (Chapter 3).

Vesta has been the subject of numerous studies, observations and theoretical work. Interest in Vesta increased when McCord et al. (1970) proposed a link between this asteroid and howardites, eucrites and diogenites (hereafter referred to as the HEDs) meteorites.

Vesta is the second-most massive object in the main asteroid belt, with an average diameter of 525 km (Thomas et al., 1997a; Zuber et al., 2011), and the reflectance spectrum of its surface is characterized by pyroxene absorption bands (McCord et al., 1970; Gaffey, 1997; Zuber et al., 2011; Pieters et al., 2011; De Sanctis et al., 2012a, De Sanctis et al., 2013). Dawn carries a Visible and Infrared imaging spectrometer (VIR), designed to map the mineralogy of Vesta and Ceres by collecting hyperspectral images in the wavelength range 0.25 to 5.0 μm (De Sanctis et al., 2011; Russell and Raymond, 2011). All VIR spectra of Vesta surface's show both the 0.9- and 1.9- μm absorption bands, confirming the widespread occurrence of iron-bearing low-calcium pyroxenes (De Sanctis et al., 2012a).

Here we present the first detailed study of the spectral properties of the Bright Materials (BM) units on Vesta. Bright units are characterized by high albedo, up to 40% greater than the Vesta's average (Li et al., 2010, 2013; Schröder et al., 2013). Bright areas are non-uniformly distributed and are not spatially correlated with the dark material, suggesting a different

origin (McCord et al., 2012).

The most diagnostic spectral parameter for mineralogical characterization of the Vesta material are the centers of band I and band II (Gaffey, 1997; De Sanctis et al., 2012a; McSween et al., 2013b). Band depths give information on the abundance and grain size of the absorbing minerals, while the Band Area Ratio (BAR) is useful for evaluating the presence of olivine in an olivine-pyroxene mixture (Cloutis et al., 1986). These parameters allow for a computation of the abundance of the wollastonite (Wo) and ferrosilite (Fs) pyroxene endmembers. Burbine et al. (2007, 2009) and Gaffey et al. (2002) derived the formulas to retrieve the molar content of Wo and Fs, in two different ways by using their band center positions. Here, we apply the same methods to the VIR data to retrieve the wollastonite and ferrosilite contents for the BM units (see Chapter 6).

To complete our analysis we apply linear spectral unmixing to the bright material spectra. Linear unmixing methods suppose that a measured spectrum can be a linear combination of n known spectra chosen as endmembers. The coefficients of the linear combination represent the abundance of each endmember (Bioucas-Dias et al., 2012; Plaza, 2013). Many algorithms exist to determine the number and of endmembers and which ones are present (Bioucas-Dias et al., 2012; Plaza, 2013). In our case we know *a priori*, from the spectral analysis, that bright material units at the spatial scale of the data are composed of eucrite, diogenite and olivine. In Chapter 7 we report the results obtained.

Chapter 1

Reflectance spectroscopy

1.1 Remote sensing

Remote sensing enables taking measurements of a body from a distance without requiring direct contact with the object (Richards, 2013; Dor et al., 2012). This technique proved to be very useful for the study of the Earth, in order to supervise for instance the weather, the deforestation, the desertification, the expansion of the urban areas and so on. Remote sensing is also fundamental for the study of the other bodies of the Solar System. Through remote sensing measurements it has been possible to analyze the planetary atmospheres, the mineralogical composition of terrestrial planet, satellites and asteroids, allowing us to extend our knowledge of the Solar System.

Electromagnetic radiation revealed after the interaction between the radiation emitted by a source, (e.g. the Sun) and the body of interest allow us to obtain much information about the body. Typical bandwidths relevant for the study of the planetary surfaces is between the ultraviolet and the thermal infrared wavelengths (Fig. 1.1).

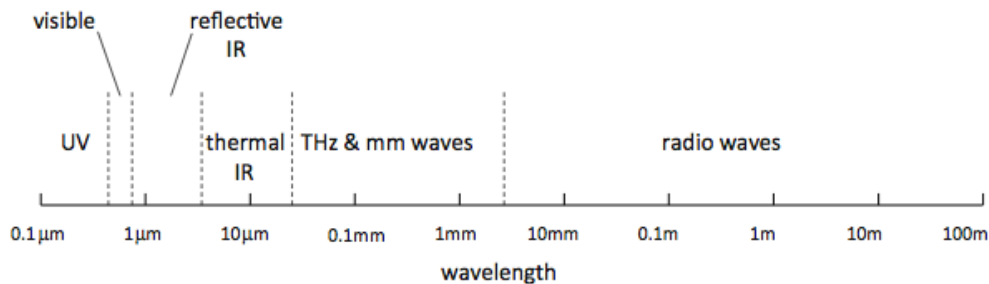


Figure 1.1: The electromagnetic spectrum (Richards, 2013).

The analysis of a surface during a remote sensing observation is limited by the atmosphere. In this work we study the mineralogy of airless bodies, such as Mercury and the asteroid Vesta; thus problems of an atmosphere will not be treated. Instruments devoted to the investigation of surface composition are cameras and spectrometers. The various typologies of instruments are characterized by different sensors. Fig. 1.2 summarizes the different types of sensors that defines the scanning mode and thus the typology of data produced.

Digital camera detectors have a matrix of a certain number of pixels (often 1024x1024) provided with a dozen filters, able to produce multispectral images. In contrast, a spectrometer for the study of the surface composition can contain hundreds channels. When airborne and spaceborne sensors are capable of acquiring images of many pixels simultaneously in hundreds of contiguous spectral bands, we can speak of hyperspectral remote sensing (HRS) and imaging spectroscopy (IS) (Goetz et al., 1985; Dor et al., 2012). Spectra can be acquired principally using two types of systems: pushbroom or whiskbroom.

A pushbroom scanner consists in a linear array, and is used in many spaceborne imaging systems (Fig. 1.2). Each line of imagery is captured at a unique moment in time, corresponding with an instantaneous position and attitude of the aircraft (<https://www.e-education.psu.edu/geog480/node/494>). The position and the orientation of the spacecraft are very important for a correct georeferenciation. Many spectrometers, e.g. VIR onboard Dawn, ITRES CASI, SASI, and TABI use this system, that is very useful to produce large quantity of spectra in a short time (<https://www.e-education.psu.edu/geog480/node/494>).

Whiskbroom systems consist in a single pixel array. Each pixel is captured at a unique moment in time. The instantaneous position of the scanning device must also be factored into the image rectification (<https://www.e-education.psu.edu/geog480/node/494>). An example of an instrument that use this system is MASCS on board Messenger.

As we show in the following Chapters, data produced by these two types of scanning modes must be treated differently.

HRS together with IS are two important technologies in remote sensing, that allow providing spatial and spectral information at the same time. The typical spectral resolution for the geology application is 10 nm, but for new issues, such as assessing vegetation fluorescence, it could be <1 nm (Guanter et al., 2006; Grace et al., 2007; Dor et al., 2012).

Radiation that interacts with a surface can be absorbed, scattered and reflected; in the following chapters, we describe these processes. The range of wavelength diagnostic of our scope is visible and near-infrared.

The radiation coming from a surface is processed by the instruments on board a spacecraft and transmitted to a ground receptor, from which will be derived the data to be analyzed (Fig. 1.3) (Richards, 2013). Spectrometers are the typical instrument used to derive the mineralogy of a surface. The accuracy of the measurements depend on the characteristics of the instruments. The principal properties of a spectrometer are: spectral range, spectral bandwidth, spectral sampling, signal/noise ratio (S/N) (Clark, 1999). Spectral range defines regions of the electromagnetic spectrum to consider and thus what we want to analyze for a body and which types of information we want to derive. Spectral bandwidth is the width of an individual spectral channel. Narrow width is indicative of a better accuracy (Clark, 1999). Spectral sampling is the distance in wavelength between the spectral bandpass profiles for each channel as a function of wavelength (Clark, 1999). This parameter represents the distance in terms of wavelength of two adjoining channels. Spectral sampling is related to the number of channels. High numbers of channels provide a spectrum more accurate for a given spectral range. S/N allows distinguishing the spectral features. The capability to recognize a feature depends on the strength of a feature and on the S/N ratio. The S/N ratio must be high enough to identify clearly the spectral features characteristic of the body of interest (Clark, 1999).

In this work we analyze data provided by VIR, the Visible and InfraRed spectrometer onboard Dawn, the mission to the asteroids Vesta and Ceres and those of the Messenger camera (MDIS) and spectrometer (MASCS) (See Chapter 3). In the next chapters, we describe how to reduce and use the hyperspectral data to derive the mineralogy and the spectral properties of Mercury's and Vesta's surfaces.

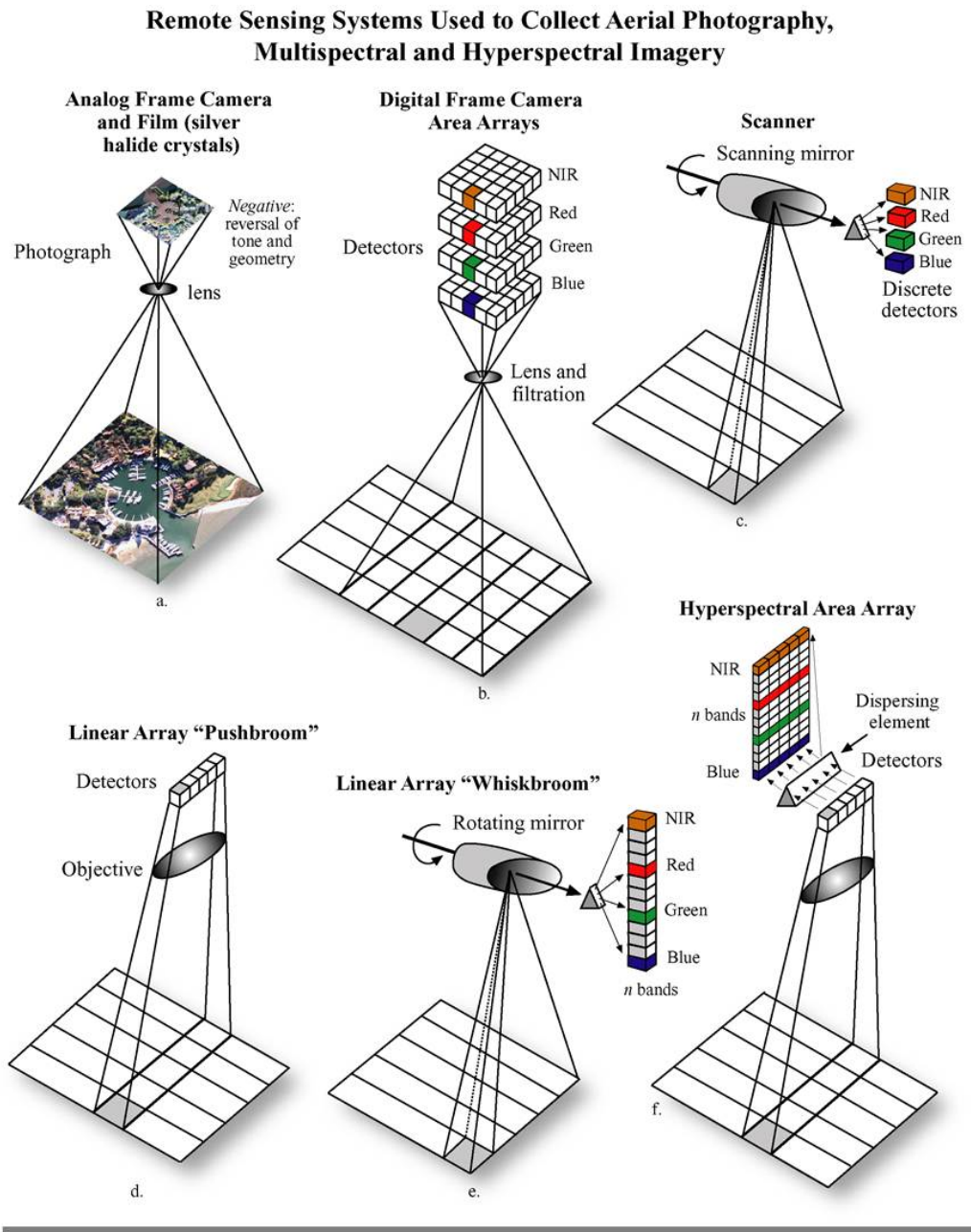


Figure 1.2: Scanning modes <https://www.e-education.psu.edu/geog480/node/494>.

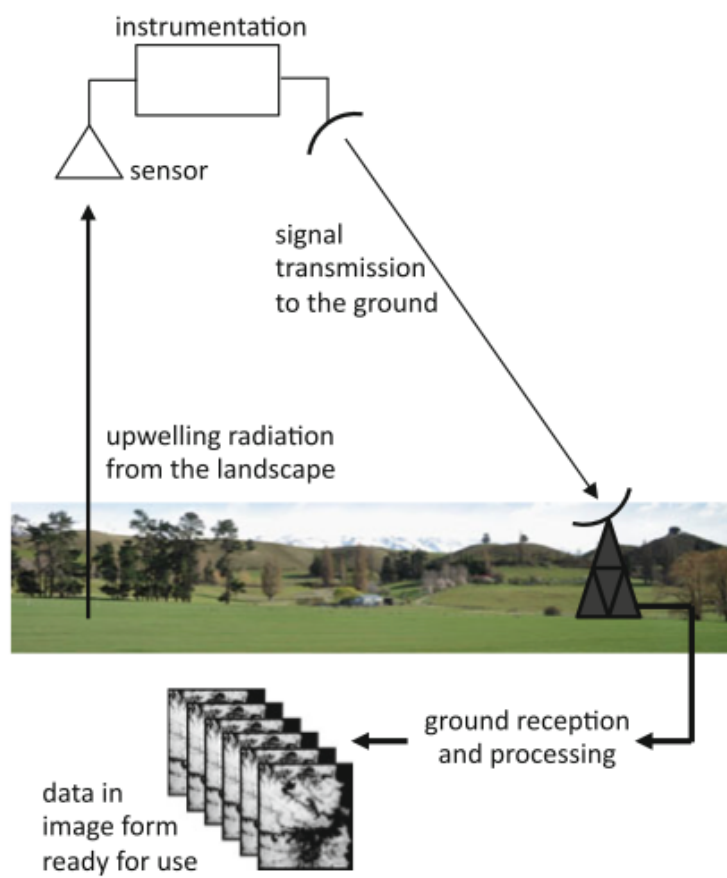


Figure 1.3: Diagram of the remote sensing system (Richards, 2013).

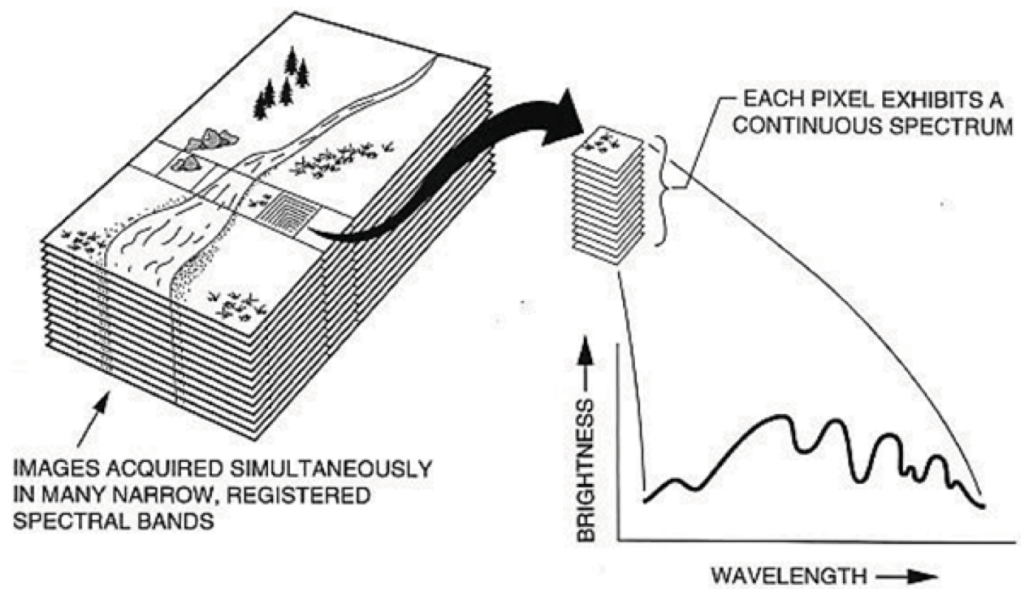


Figure 1.4: Scheme of the concept of hyperspectral remote sensing and image spectroscopy. For each pixel of an image it is possible to extract a spectrum (Dor et al., 2012).

1.2 Reflectance

In this section, we describe the principal quantities involved in reflectance spectroscopy, and the physical mechanisms that cause the absorption processes, useful to determine the mineralogy of a surface. Reflectance spectra are retrieved by remote sensing measurement, and are composed of a continuum and the features indicating the composition caused by the absorption processes. The band center position indicates the composition; the depth of a band depends on the absorption but is also influenced by the particle size of a surface and the presence of opaque minerals; while the shape depends on lattice properties and on the temperature.

1.2.1 Reflectance quantities

Nicodemus et al. (1977) proposed a nomenclature and an overview for reflectance quantities. Subsequently Martonchik et al. (2000) and Schaepman-Strub et al. (2006) integrated and improved this work. Here we describe the principal quantities used in reflectance spectroscopy. Table 1.2 summarizes all the quantities and parameters used.

- *Radiance* is the flux in a beam per units-area and solid angle (Nicodemus et al., 1977; Martonchik et al., 2000; Schaepman-Strub et al., 2006):

$$L(\theta, \phi) = \frac{d^2\Phi}{dAd\omega\cos\theta} \quad (1.1)$$

where Φ is the flux, ω the solid angle, and θ the zenith angle i.e. the angle between the beam and the Z axes. In Fig. 1.5 there is a schematic representation of the quantities mentioned above (Nicodemus et al., 1977).

- *Reflectance* is defined as the ratio between the *radiant exitance* (or exitent flux density) and *irradiance* (or incidence flux density) (see Table 1.2)

$$\rho(\theta_i, \phi_i, \omega_i, \theta_r, \phi_r, \omega_r, \lambda) = \frac{d\Phi_r}{d\Phi_i}. \quad (1.2)$$

where Φ_i and Φ_r are the incidence and radiant flux reflected respectively. Reflectance is a dimensionless quantity and ranges from 0 to 1, and it depends on the zenith and azimuth angles θ and ϕ (respectively) relative to the incoming (i) and reflected (r) radiances associated with solid angle ω (see Table 1.2 and Fig. 1.5), and the wavelength (Schaepman-Strub et al., 2006).

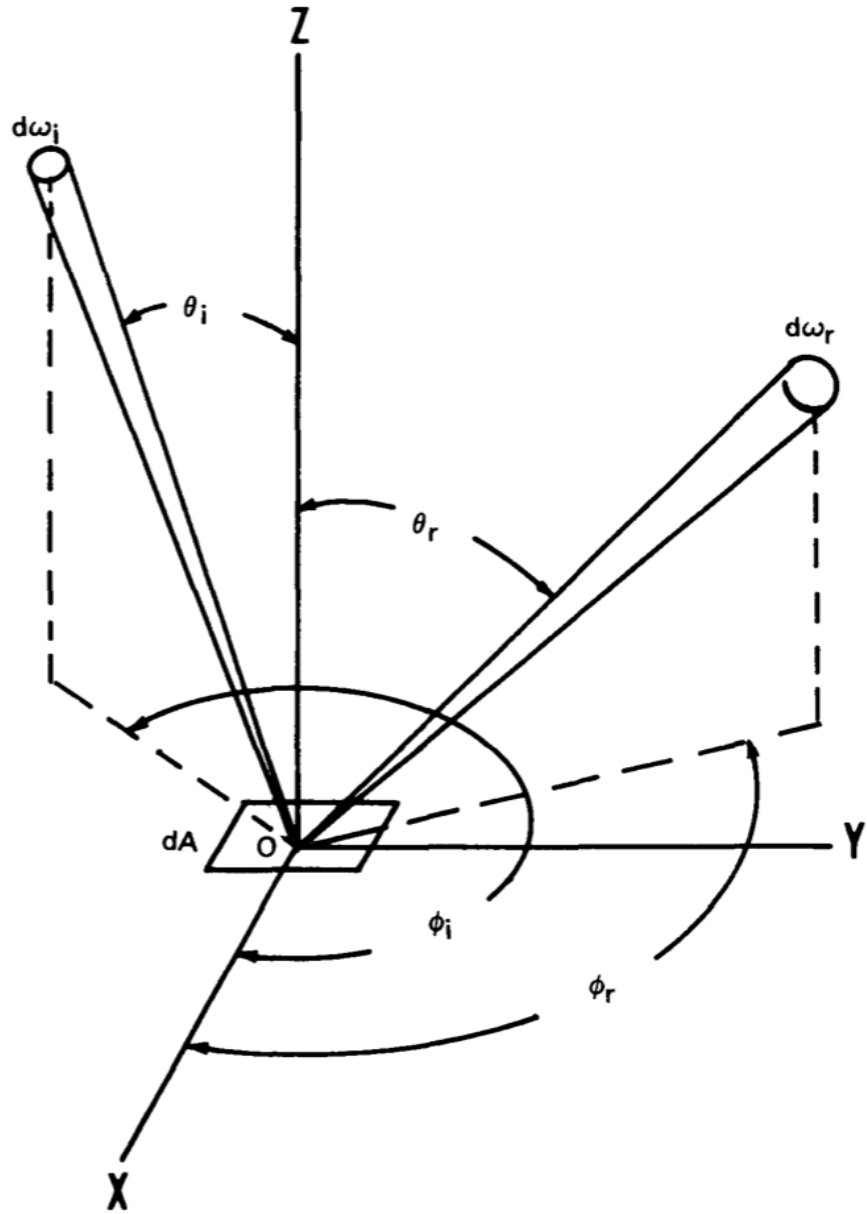


Figure 1.5: Scheme of incident and reflected beam (Nicodemus et al., 1977).

- *Reflectance factor* is defined as the ratio of the radiant flux reflected by a surface (Φ_r) to that reflected into the same reflected-beam geometry and wavelength range by an ideal (lossless) and diffuse (Lambertian) ($\Phi_{r,id}$) standard surface, irradiated under the same conditions (Schaepman-Strub et al., 2006)

$$R_f(\theta_i, \phi_i, \omega_i, \theta_r, \phi_r, \omega_r, \lambda) = \frac{d\Phi_r}{d\Phi_{r,id}} \quad (1.3)$$

This quantity is also dimensionless and in some cases (e.g. for strongly forward-reflecting surfaces such as snow) can be > 1 (Painter and Dozier, 2004; Schaepman-Strub et al., 2006).

1.2.2 Bidirectional reflectance and other reflectance types

It is possible to define different type of reflectance, based on the geometry of the incidence and emitted radiation. In general, reflectances are directional, conical and hemispherical, and these types can be combined each other; thus we can have bidirectional reflectance, directional-conical reflectance, directional-hemispherical reflectance and so on. Fig. 1.6 summarized the geometries that defines the different type of reflectances (Nicodemus, 1965; Nicodemus et al., 1977; Hapke, 1993; Schaepman-Strub et al., 2006). Reflectances commonly used in remote sensing are the bidirectional reflectance and the directional-hemispherical reflectance (Clark and Roush, 1984). In the next section we derive the bidirectional reflectance distribution function from which it is possible to derive the others. The distribution function of the reflectance types shown in Fig. 1.6 are also reported in Table 1.1.

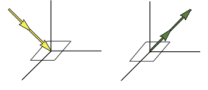
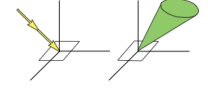

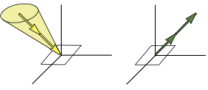
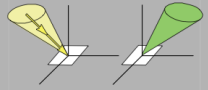
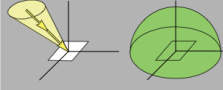
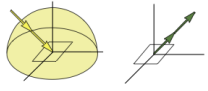
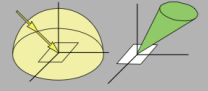
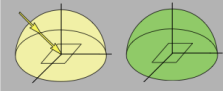
<i>Incoming/Reflected</i>	Directional	Conical	Hemispherical
<i>Directional</i>	Bidirectional CASE 1 	Directional-conical CASE 2 	Directional-hemispherical CASE 3 
<i>Conical</i>	Conical-directional CASE 4 	Biconical CASE 5 	Conical-hemispherical CASE 6 
<i>Hemispherical</i>	Hemispherical-directional CASE 7 	Hemispherical-conical CASE 8 	Bihemispherical CASE 9 

Figure 1.6: Scheme of different type of reflectance (Schaepman-Strub et al., 2006).

1.2.3 Bidirectional reflectance distribution function

The bidirectional reflectance distribution function has been introduced by Nicodemus (1965), and is defined by Hapke (1993) as "the radiance emerging in a given direction from a surface illuminated by a collimated irradiance per unit incidence irradiance" (Fig. 1.6) and by Clark and Roush (1984) as "the brightness of a surface relative to the brightness of a Lambert surface identically illuminated". Bidirectional reflectance describes the intrinsic reflectance properties of a surface and from it integrating over the corresponding solid angle it is possible to derive the other types of reflectances (Schaepman-Strub et al., 2006) (see Table 1.1). Here we derive the bidirectional reflectance distribution function.

In section 1.2.1 the radiance has been defined (formula 1.1). The reflected radiance can be written also as:

$$dL_r = \tilde{S}d\Phi_i$$

where Φ_i is the incoming flux and $\tilde{S} = \tilde{S}(\theta_i, \phi_i, x_i, y_i, \theta_r, \phi_r, x_r, y_r)$ is the bidirectional scattering-surface reflectance-distribution function (Nicodemus et al., 1977). \tilde{S} is a completely general, and represents the connection between the ingoing and outgoing flux. Moreover, consider that

$$L_i = L_i(\theta_i, \phi_i)$$

We can write the incidence flux as

$$d\Phi_i = L_i \cos\theta_i d\omega_i dA_i$$

remembering the definition of irradiance (Table 1.2), we have that

$$d\Phi_i = dE_i dA_i$$

where E_i is the incidence irradiance. If we integrate the reflected radiance over A_i we obtain

$$\begin{aligned} dL_r(\theta_i, \phi_i, \theta_r, \phi_r, x_r, y_r) &= \int_{A_i} \tilde{S}d\Phi_i = \\ &= dE_i \int_{A_i} \tilde{S}dA_i \end{aligned}$$

Assuming that the scattering processes are uniform and isotropic across the reference plane, thus \tilde{S} does not depend on the incident (x_i, y_i) and reflection point (x_r, y_r) , but from their distance r (Fig. 1.7). Hence, we can define

$$f_r(\theta_i, \phi_i, \theta_r, \phi_r) = \int_{A_i} \tilde{S}(\theta_i, \phi_i, \theta_r, \phi_r, r) dA_i$$

We can write the reflected irradiance as

$$dL_r = dE_i f_r(\theta_i, \phi_i, \theta_r, \phi_r)$$

The function f_r is the bidirectional reflectance-distribution function, and we can define it as

$$f_r(\theta_i, \phi_i, \theta_r, \phi_r) = \frac{dL_r}{dE_i} \quad (1.4)$$

Integrating over the appropriate solid angle, it is possible to obtain the reflectance of the cases shown in Fig. 1.6. In Table 1.1 we report the reflectances corresponding with the types in Fig. 1.6.

After introducing the bidirectional reflectance distribution function, we find an expression for this function and for the scattering function. Several authors have addressed the question (e.g. Hapke, 1981, Goguen, 1981, Lumme and Bowell, 1981). Here we report the reflectance function for a give wavelength proposed by Hapke (Hapke, 1981, 1993):

$$\rho(\bar{w}, \lambda, \mu_0, \mu, g) = \frac{\bar{w}}{4\pi} \frac{\mu_0}{\mu_0 + \mu} \{[1 + B(g)]P(g) + H(\mu_0)H(\mu) - 1\} \quad (1.5)$$

where \bar{w} is the average single-scattering albedo, g is the phase angle, $B(g)$ is the backscattering function, $P(g)$ is the average single scattering phase function, H is the Chandrasekhar function (Chandrasekhar, 1960; Hapke, 1981, 1993), μ_0 is the cosine of the angle of the incident light and μ is the cosine of the angle of the emitted light. This expression has many variables, that can be difficult to derive. The single-scattering albedo of a grain is

$$w = S_E + \frac{(1 + S_E)(1 + S_I)\{r_1 + \exp[-2(k(k + s))^{1/2}d/3]\}}{1 - r_1 S_I + (r_1 - S_I) \exp[-2(k(k + s))^{1/2}d/3]}$$

where S_E and S_I are respectively the external and internal scattering processes, s is the scattering coefficient, d is the particle diameter, k the absorption coefficient and $r_1 = \frac{1 - [kd/(kd + sd)]^{1/2}}{1 + [kd/(kd + sd)]^{1/2}}$ (Hapke, 1981, 1993; Clark and Roush, 1984; Clark, 1999).

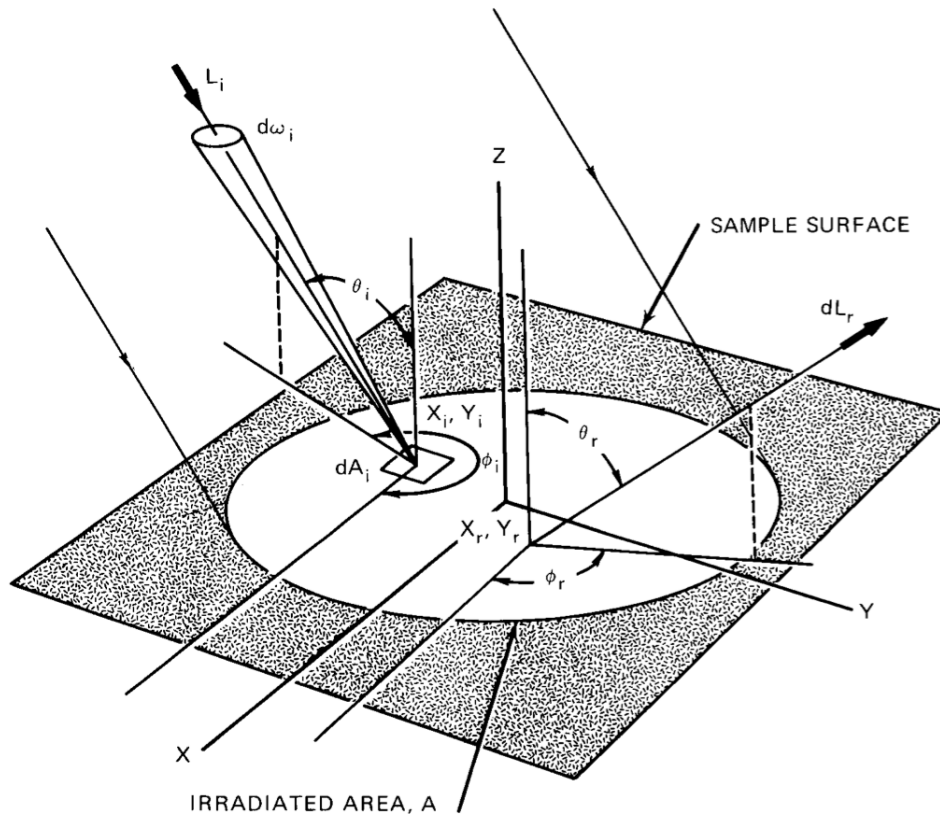


Figure 1.7: Geometry of the incident and reflected beam in the bidirectional reflectance case (Nicodemus et al., 1977).

Distribution Function of different types of reflectance	
Reflectance type	Distribution Function
Bidirectional	$d\rho(\theta_i, \phi_i, \theta_r, \phi_r) = f_r(\theta_i, \phi_i, \theta_r, \phi_r)d\Omega_r$
Directional-conical	$\rho(\theta_i, \phi_i, \omega_r) = \int_{\omega_r} f_r(\theta_i, \phi_i, \theta_r, \phi_r)d\Omega_r$
Directional-hemispherical	$\rho(\theta_i, \phi_i, 2\pi) = \int_{2\pi} f_r(\theta_i, \phi_i, \theta_r, \phi_r)d\Omega_r$
Conical-directional	$d\rho(\omega_i, \theta_r, \phi_r) = \frac{d\Omega_r}{d\Omega_i} \int_{\omega_i} f_r(\theta_i, \phi_i, \theta_r, \phi_r)d\Omega_i$
Biconical	$\rho(\omega_i, \omega_r) = \frac{1}{d\Omega_i} \int_{\omega_i} \int_{\omega_r} f_r(\theta_i, \phi_i, \theta_r, \phi_r)d\Omega_i d\Omega_r$
Conical-hemispherical	$\rho(\omega_i, 2\pi) = \frac{1}{d\Omega_i} \int_{\omega_i} \int_{2\pi} f_r(\theta_i, \phi_i, \theta_r, \phi_r)d\Omega_i d\Omega_r$
Hemispherical-directional	$d\rho(2\pi, \theta_r, \phi_r) = \frac{d\Omega_r}{\pi} \int_{2\pi} f_r(\theta_i, \phi_i, \theta_r, \phi_r)d\Omega_i$
Hemispherical-conical	$\rho(2\pi, \omega_r) = \frac{1}{\pi} \int_{2\pi} \int_{\omega_r} f_r(\theta_i, \phi_i, \theta_r, \phi_r)d\Omega_i d\Omega_r$
Bihemispherical	$\rho(2\pi, 2\pi) = \frac{1}{\pi} \int_{2\pi} \int_{2\pi} f_r(\theta_i, \phi_i, \theta_r, \phi_r)d\Omega_i d\Omega_r$

Table 1.1: Distribution function of the types of reflectances shown in Fig. 1.6 (Nicodemus et al., 1977).

Nomenclature of the reflectance quantities		
Symbol	Definition	Unit-Dimension
i	Incident	
r	Reflected	
id	Ideal (lossless) and diffuse (isotropic or lambertian)	
x_i, y_i	Coordinates of the incident beam	
x_r, y_r	Coordinates of the reflected beam	
ϕ_i	Azimuth angle of the incidence beam (Fig. 1.5). Angle between the incidence beam and the X axis.	[rad]
ϕ_r	Azimuth angle of the reflected beam (Fig. 1.5). Angle between the reflected beam and the X axis.	
θ_i	Zenith angle of the incidence beam (Fig. 1.5). Angle between the incidence beam and the Z axis.	[rad]
θ_r	Zenith angle of the reflected beam (Fig. 1.5). Angle between the reflected beam and the Z axis.	[rad]
ω	Solid angle $\equiv \int \int \sin \theta d\theta d\phi$ (Fig. 1.5)	[sr]
Ω	Projected solid angle $\equiv \int \cos \theta d\omega = \int \int \cos \theta \sin \theta d\theta d\phi$	[sr]
A	Area	[m ²]
E	Irradiance or incident flux density $\equiv d\Phi_i/dA$	[Wm ⁻²]
M	radiant exitance or exitent flux density $\equiv d\Phi_r/dA$	[Wm ⁻²]
Φ	Radiant flux	[W]
λ	Wavelength of radiation	[nm]
L	Radiance	[W m ⁻² sr ⁻¹]
ρ	Reflectance	[dimensionless]
R_f	Reflectance ratio	[dimensionless]
f_r	Bidirectional reflectance distribution function	[sr ⁻¹]
S	Bidirectional scattering-surface reflectance	[m ⁻² sr ⁻¹]

Table 1.2: Summary of the reflectance quantities used.

1.3 Reflectance spectroscopy and mineralogy

Reflectance spectroscopy is very useful to derive the properties of a surface. From spectral parameters position and the depth of an absorption band, the bandwidth, and the slope, it is possible to infer the mineralogy of a planetary surface. In the next sections we refer to the work of Clark and Roush (1984), Hapke (1993), Burns (1993) and Clark (1999).

Regoliths or soil on a surface of planets consist of an intimate mixture of different minerals, including igneous rocks and alteration products formed by chemical and mechanical weathering and impact events. Such assemblages are present in a range of particle sizes which absorb sunlight incident on them (Burns, 1993). When a beam of light encounters a surface, a part of this beam can be reflected and a part refracted. The complex refraction index is

$$m = n - iK$$

where n is the real part and K is the imaginary part called extinction coefficient. While the reflection is described by the Fresnel equation

$$R = \frac{(n - 1)^2 + K^2}{(n + 1)^2 + K^2}$$

The intensity of the absorbed light is given by the empirical Beer's law

$$I = I_0 e^{-kx} \quad (1.6)$$

where I_0 is the intensity of the incident light, $k = 4\pi K/\lambda$ is the absorption coefficient and x is the distance traveled through the medium (Clark, 1999).

1.4 Scattering

Scattering processes occur every time a photon interacts with a surface. The photon scatter many times with the grains of a surface, and in any interaction part of the energy carried by the photon is absorbed, according to the Beer's law (1.6), generating bands on a reflectance spectra centered in a particular wavelength. Photons can be completely absorbed or can be emitted at a different wavelength. Scattering processes are generally complex, and the path of the photon is a random walk (Clark and Roush, 1984). In presence of bright grain the photons are scattered hundred times before to be emitted, while in the case of dark grain the majority of photons will be absorbed in few interactions (Clark, 1999). Scattering processes are influenced by the size of the grains of a surface. Large-grain photons have a longer internal path,

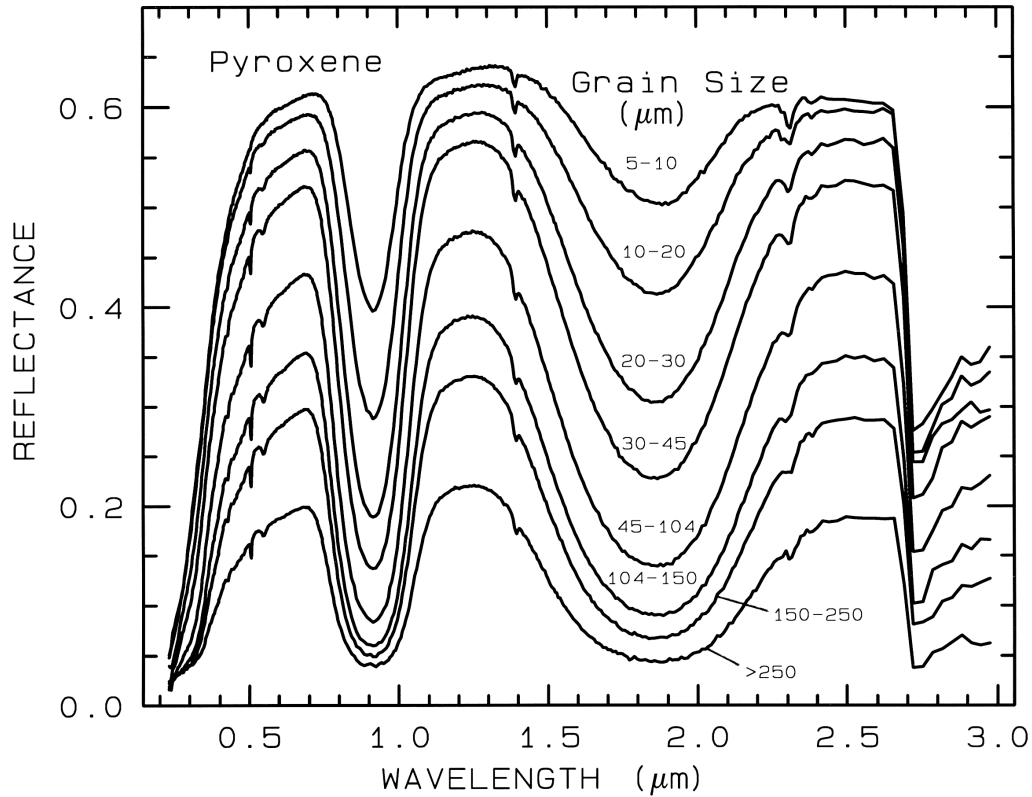


Figure 1.8: Reflectance spectra of pyroxenes at different grain size. (Clark, 1999).

so the photons are absorbed. For small-grain photons, higher surface reflection indicates a lower absorption (Clark, 1999). In the visible and infrared ranges multiple scattering dominates thus increasing grain size corresponds to increasing reflectance and the depth of the bands is a function of the grain size (Clark, 1999). Fig. 1.8 shows the variation of the band depth with the grain size. Band depth increases with increasing grain size, in agreement with the observation done before. Below a certain grain size ($100\mu\text{m}$), more complex processes occur and grain size decreases again (Fig. 1.8) (Clark, 1999). Thus the depth of a band does not depend only on the absorbing minerals but also on the grain size and the presence of opaque materials. These factors are closely linked and it is not easy to distinguish the single contributions. In the next section, we describe the processes that cause the absorption. Definition of the band depth is reported in Section 1.6.

1.5 Absorption

In this section we discuss the mechanisms that cause the absorption. The interaction processes between radiation and matter can be classified in four categories: rotational, vibrational, electron excitation and free carriers (Hapke, 1993). Below we describe these mechanisms. In Fig. 1.9 we show a summary of the absorption band present in some minerals and the processes that cause the absorption.

1.5.1 Molecular rotation

Molecular rotation is due to the presence of a permanent electric-dipole moment, that influences the complex dielectric constant. Thus, in the presence of an electric field, molecules change their orientation. Capability of a molecule to rotate depends on the state. The molecules in liquids and gases can rotate, and the permanent dipole moment can cause a large polarization. In solids (as in the case that we will consider), the capability of rotation depends on the shape of the molecule and on the strength of the interaction. A spherical molecule with a small dipole moment can easily rotate. In general, in a solid, a molecule cannot rotate easily. The time necessary to flip a molecule into another orientation is called *relaxation time* (Hapke, 1993). If the relaxation time is larger than the period of the applied magnetic field, the molecule does not have time to rotate and the dielectric constant is small. Molecular rotation depends also on the temperature. Thermal agitation randomizes the orientation of the molecules, and the part of the dielectric constant associated with the rotational transition decreases with decreasing temperature (Hapke, 1993).

1.5.2 Electronic processes

When an electron interacts with a photon of a specific wavelength, part of the energy carried by the photon is absorbed, the photon is emitted at a different wavelength and the electron jumps from a lower energy state to one of higher energy (Burns, 1993; Hapke, 1993; Clark, 1999). Electrons in isolated atoms or ions have discrete energy states that can be calculated using the Schrödinger equation. In a solid, the electrons interact and the wave function of the outer electrons perturbs those of the others. This causes a splitting of the energy level of the electron, so many atoms present a close energy level that causes several wide bands in which the electrons can exist, separated by gaps. Here we describe the absorption due to electronic processes.

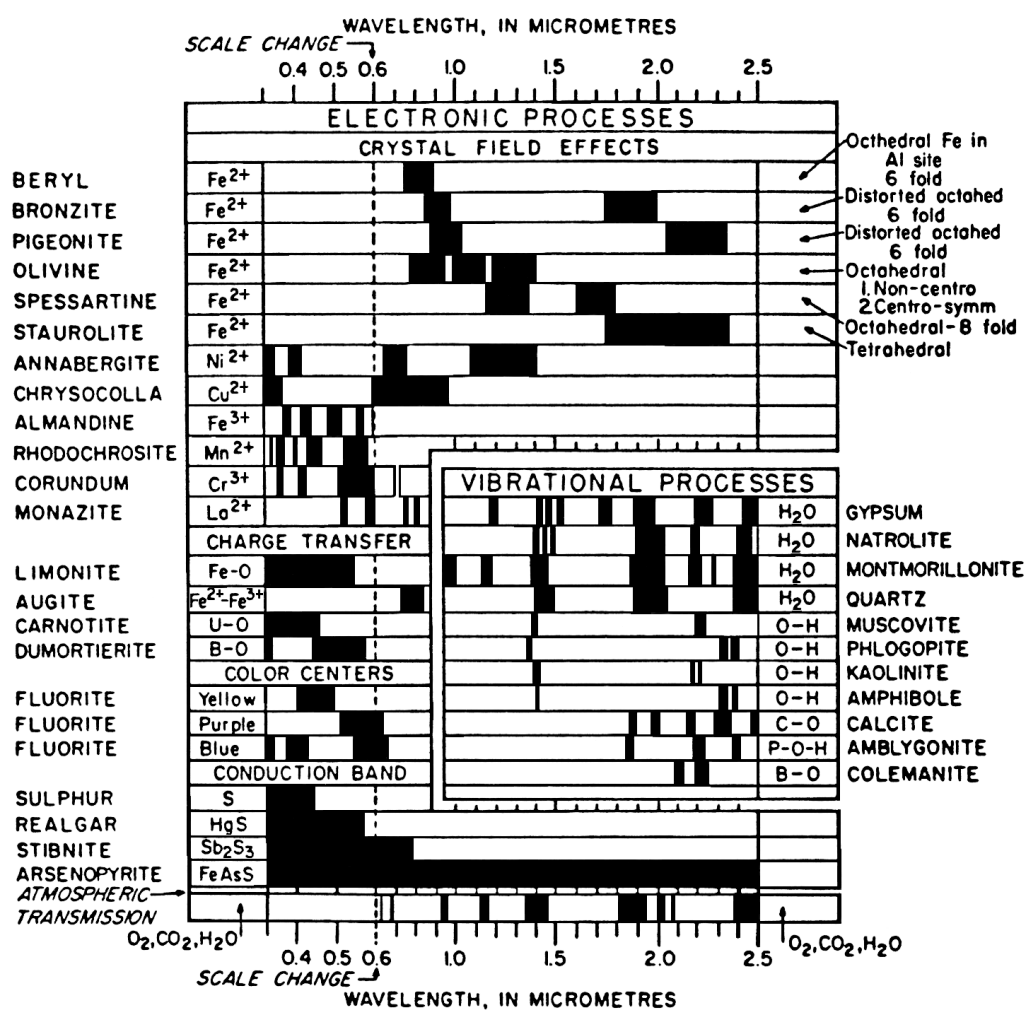


Figure 1.9: Summary of the absorption feature for some minerals with the corresponding processes that cause them (Clark, 1999).

- **Crystal field effects in transition elements.** *Crystal field absorption* is generated by light absorption that causes electron jumps from lower energy orbitals to higher energy orbitals (Burns, 1993; Hapke, 1993; Clark, 1999). In the transition elements (e.g. Ni, Cr, Fe) this process is associated with the orbitals *d* and *f* that are partially filled. This is responsible for the iron-bearing absorption band of the minerals (e.g. pyroxenes and olivines) present in planetary surfaces and asteroids, such as the Moon and Vesta. These orbitals are degenerate, for example there are five *d* orbitals with the same energy and thus five-fold degenerations. The degeneracies are removed when the ions are in a solid. The nonisotropic electric field of the ions remove the degeneracies, thus the orbitals have different energy levels. This process is called *crystal-field splitting*. The probability of transitions between two orbitals depend on the selection rules (Burns, 1993; Hapke, 1993; Clark, 1999). The crystal structure and the crystal-field splitting vary from mineral to mineral, thus the same ion can produce different absorption if associated with different crystal structure. In Fig. 1.10 are shown the Fe absorption feature for olivine and pyroxenes. These minerals that we will describe further on are very important for our analysis.
- **Charge transfer absorption.** Absorption due to charge transfer occurs when the absorption of a photon causes electrons to move from one ion to another or, within the same ion, between two different valence states, as occurs in metals. The strength of this transition is hundreds to thousands of times greater than those of the crystal field. The absorption band can be found from the ultraviolet to visible wavelengths and is diagnostic for minerals. These transitions are responsible of the red color of iron oxides and hydroxides. An example of an absorption band due to mechanism is shown in Fig. 1.11 (Hapke, 1993; Clark, 1999).
- **Interband and impurity transition.** Absorption due to the interband transition occurs when radiation excites electrons between the valence and the conduction band. This type of absorption is very strong and occurs in the far ultraviolet wavelength (Hapke, 1993).

In contrast, the impurity transition occurs when an electron is excited from the valence band and to an impurity level and vice versa (Hapke, 1993).
- **Conduction bands.** In some minerals an electron can reside in a high-energy-level *conduction band* or in a low-energy-level *valence band*. The

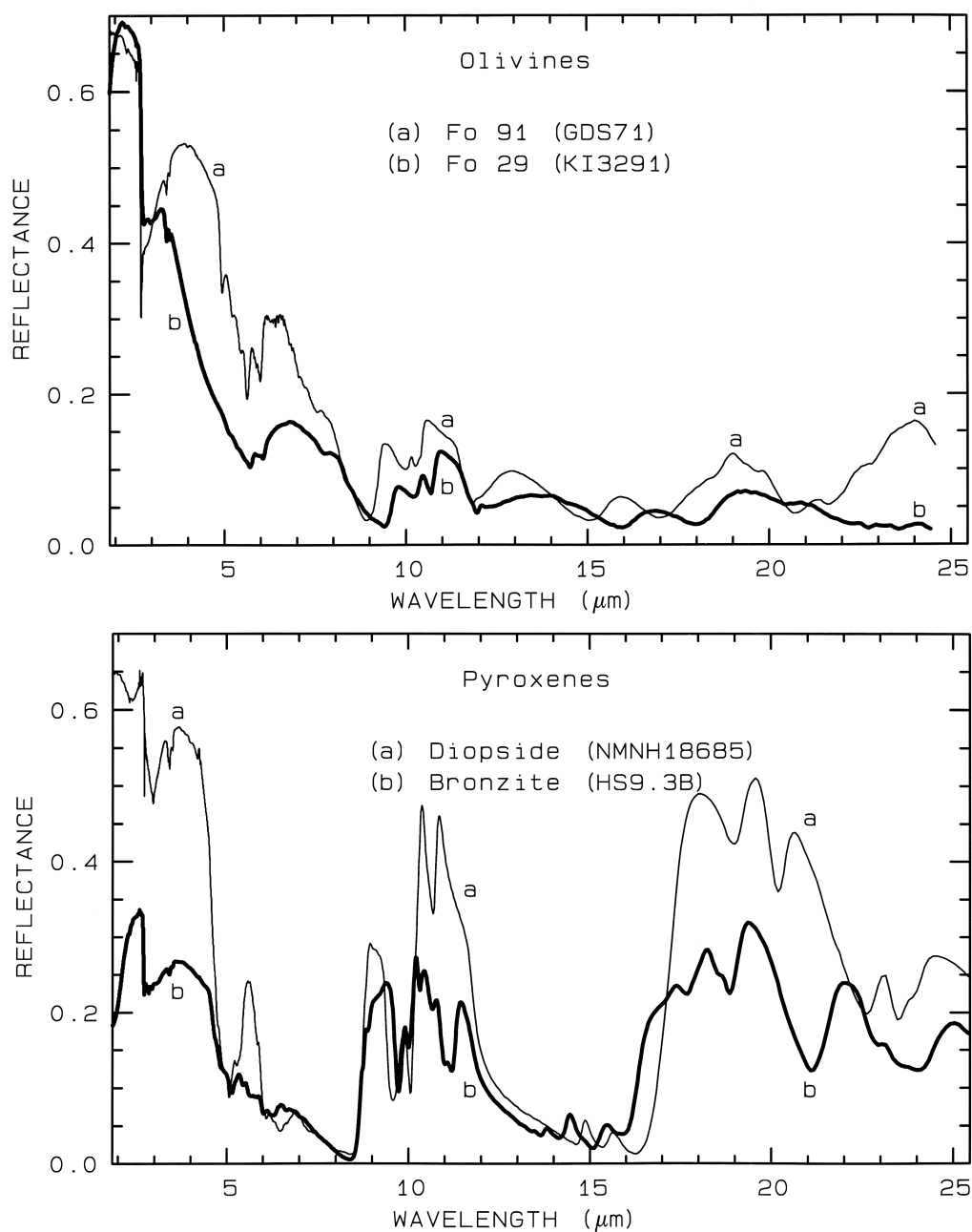


Figure 1.10: Visible and Infrared spectra of olivines and pyroxenes. The absorption bands due to the transition of the Fe are visible in both the spectra. Here are shown two samples of olivine with different content FeO. Band shape and position vary with the composition. The same behavior can be observed for the two different pyroxenes on the bottom. (Clark, 1999).

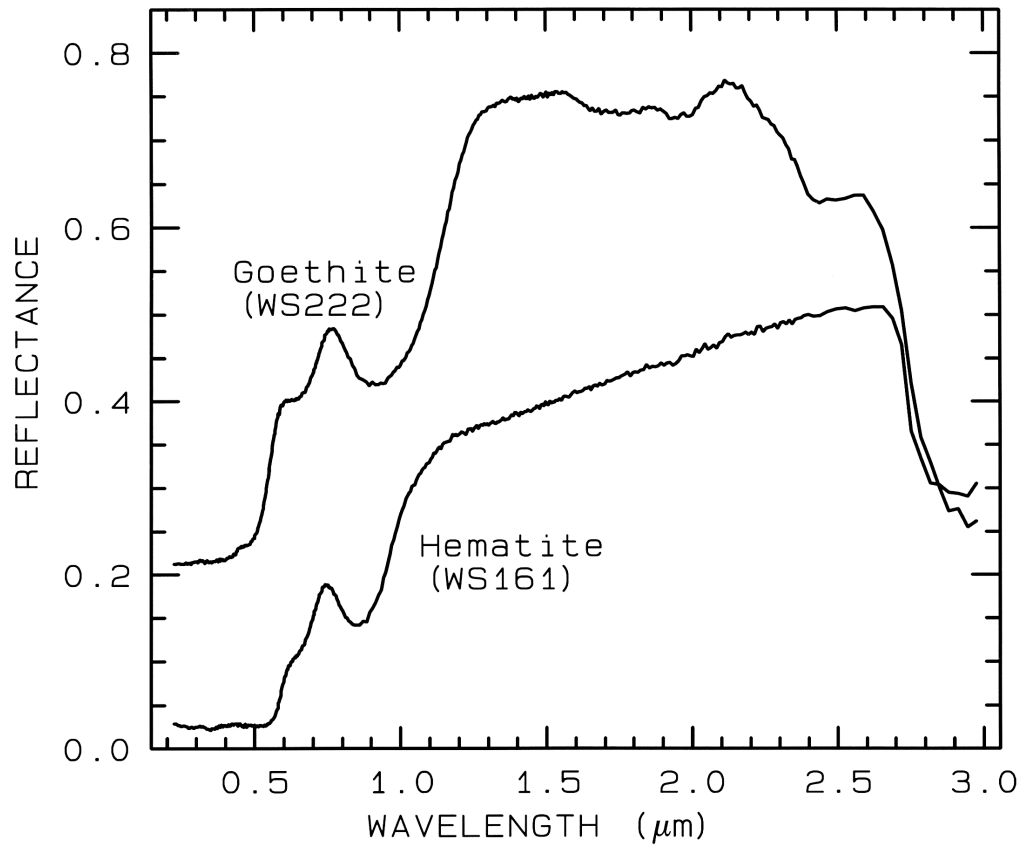


Figure 1.11: In the plot are shown the reflectance spectra of the hematite (iron oxide) and goethite (hydroxide). The absorption bands at 0.9 and 0.86 μm are due to the conduction band transitions (Clark, 1999).

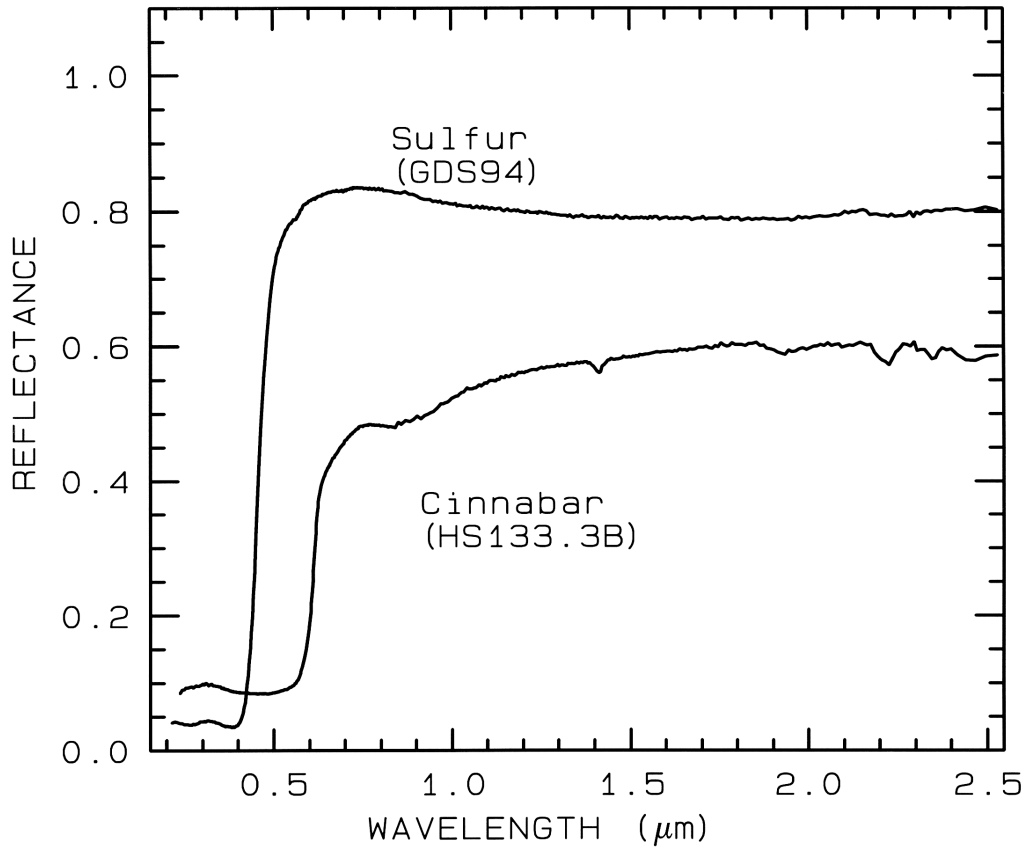


Figure 1.12: Effect of the conduction band in sulfure and cinnabar (Clark, 1999).

difference of energy between the two levels is called the *band gap*, the *band gap* which is negligible in the metal but large in the dielectrics. An example of the band gap is the color yellow effect in sulphur (Clark, 1999).

- **Color centers.** The process called *color center* is caused by irradiation of impurity of the crystal. An electron can orbit a positively-charged imperfection, and a hole negatively charged forming a hydrogen-atom-like system. This process is responsible for the yellow, purple and blue colors of fluorite (Hapke, 1993; Clark, 1999).

1.5.3 Free carriers of charge

Free carriers of charge, such as electrons and holes, can absorb light in a solid in the presence of electric fields of the incident radiation. Part of the

energy carried by the radiation is converted into lattice vibration. This kind of absorption occurs typically in the visible and near-infrared wavelengths in metal and semiconductors (Hapke, 1993).

1.5.4 Vibrational processes

The bond in a molecule or crystal lattice can be compared to a spring with attached weights (Clark, 1999). A solid can be considered to be made up of positive and negative ions arranged in a periodic array, free to vibrate around their equilibrium position (Hapke, 1993). A molecule with N atoms has $3N-6$ fundamental modes of vibration. Each vibration can occur at roughly multiples of the original fundamental frequency. The additional vibrations are called *overtone*s when they involve multiples of a single fundamental mode, and combinations when they involve different modes of vibrations. A free molecule can rotate and vibrate, but in a solid the motion is limited (Clark, 1999). The lattice vibration can be described by the equations of the motion of the ions. Both in the classical and in the quantum-mechanical case these equations have two classes of solution called the acoustical branch of the vibrational spectrum and the optical branch of the lattice vibration (Hapke, 1993). The acoustical branch describes the collective motion of the positive and negative ions. Since no dipole moment is associated with the vibrational motion, there is no interaction with the electromagnetic field. The optical branch of lattice vibration describes the case in which positive and negative ions move out of phase with each other; in this case the lattice can absorb or emit photons. The strongest interaction between electromagnetic radiation and lattice waves occur when the relative ionic displacement results in transverse dipole moments (Hapke, 1993). These motions are called lattice modes.

Vibrational absorption generate strong bands in the thermal infrared when a molecule present a dipole moment and can be associated with the water, hydroxyl (OH), and the ion CO_3^{-2} in carbonates. In Fig. 1.13 are shown some examples of reflectance spectra of minerals that present vibrational absorption bands (Clark, 1999).

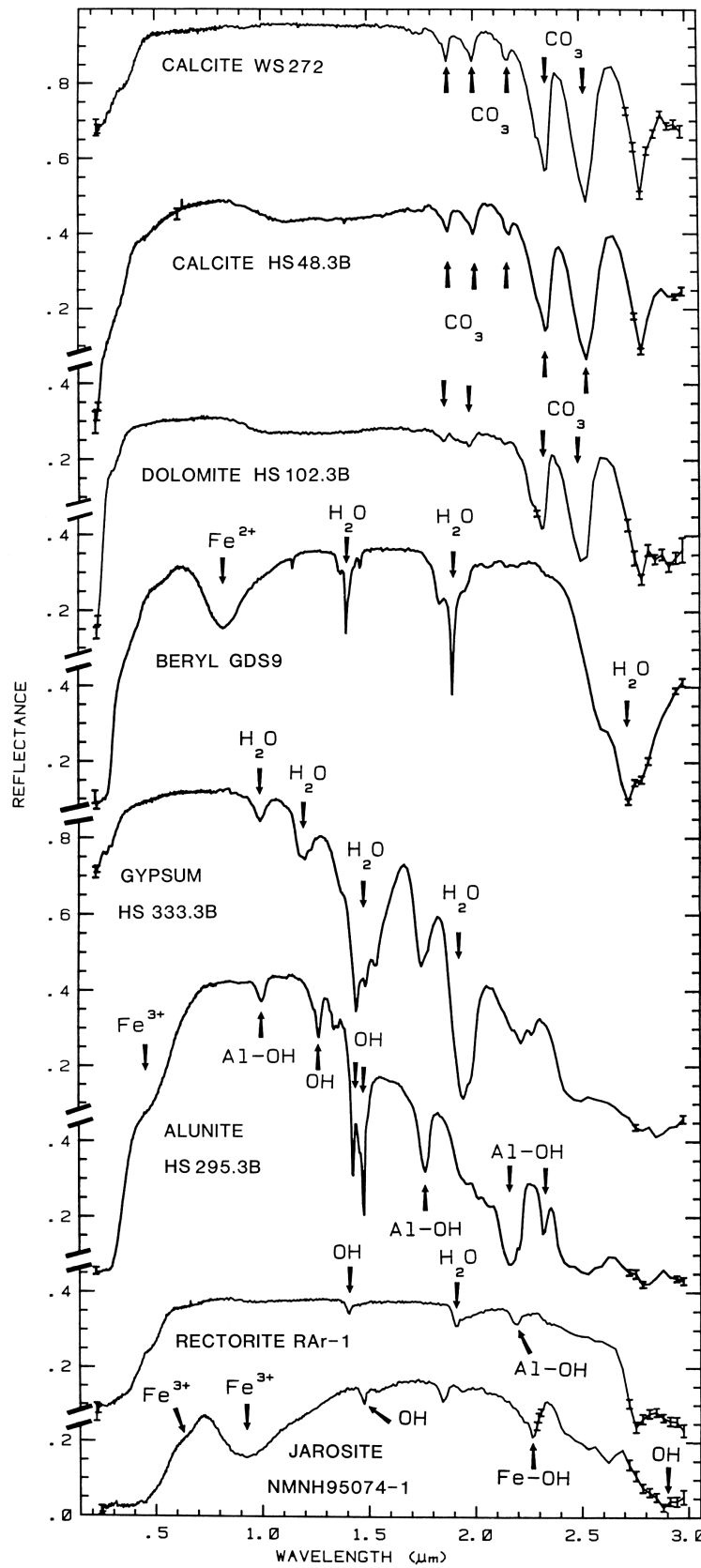


Figure 1.13: Examples of spectra of mineral that present the vibrational absorption band of H_2O , OH and CO_3^{2-} (Clark, 1999).

1.5.5 Band shape

Absorption bands caused by lattice vibration can be modeled with a Lorentian shape, (Lax, 1954; Dexter, 1956; Hapke, 1993). On the other hand, those due to the shorter wavelength electronic band are better modeled by a Gaussian shape (Hapke, 1993; Clark and Roush, 1984). The width of the electronic potential wells depend on the neighbor ions (Lax, 1954; Dexter, 1956; Hapke, 1993). The distance between the ions in the lattice varies because of the lattice vibration and this determines the shape of a band (Hapke, 1993). Increasing temperature induces an expansion of a solid and so the ion distance and the electronic potential wells increase, causing a further widening of the bands.

1.6 Continuum

The *continuum* is defined by Clark and Roush (1984) as "a mathematical function used to isolate a particular absorption feature for analysis of a spectrum. As such, it represents the absorption due to a different process in a specific mineral, or possibly, absorption from a different mineral in a multimineralic surface", while Clark (1999) defines it as "the background absorption onto which other absorption features are superimposed". Following the Clark and Roush (1984) definition, the continuum can be modeled using the mean optical path length through different materials or separated into different absorption processes using the equation:

$$e^{-\bar{k}\bar{l}} = \exp\left[-\sum_{i=1}^N k_i \bar{l}_i\right] \quad (1.7)$$

where \bar{k} is the equivalent absorption coefficient, \bar{l} is the mean optical path length of the whole surface, and k is the absorption coefficient of the i -th material having a mean optical path length l , for a multimineralic surface in an intimate mixture (Clark and Roush, 1984). In Fig. 1.14 we show the continuum for a montmorillonite and montmorillonite plus carbon black.

In addition to the absorption bands that are useful to diagnose the mineralogy of a surface, the continuum of a spectrum can also provide helpful information. For example, the slope of the continuum is typically used to study the space weathering effects. The continuum can be removed from a spectra dividing the reflectance by the continuum or subtracting the apparent absorbance (Clark and Roush, 1984).

The depth of a band and the continuum are related. Clark and Roush (1984) defined the band depth D_b as:

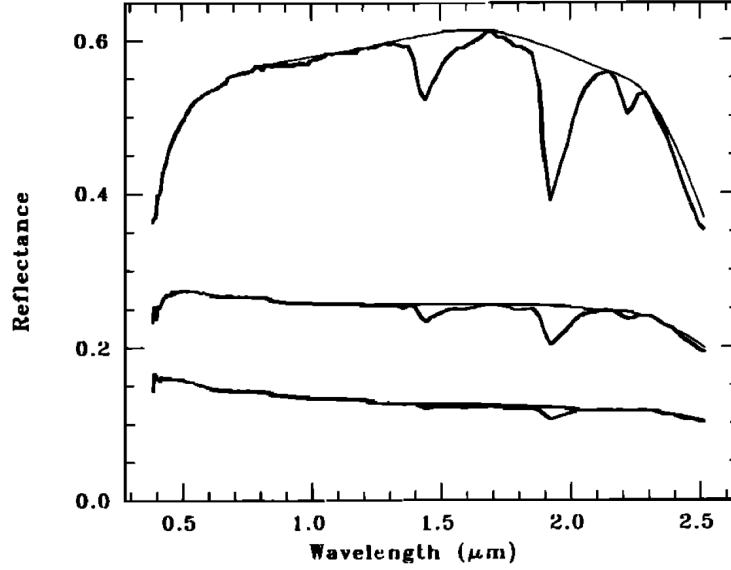


Figure 1.14: Top. Continuum for a montmorillonite spectrum. Middle. Continuum for mixtures of montmorillonite plus carbon black (0.5 wt % carbon black). Bottom. Continuum for mixtures of montmorillonite plus carbon black (0.5 wt % carbon black) (Clark and Roush, 1984).

$$D_b \equiv \frac{R_c - R_b}{R_c} \quad (1.8)$$

where R_c is the reflectance of the continuum at the band center and R_b is the reflectance of the band center. We use this definition to calculate the band depth of VIR spectra.

1.7 Main minerals in airless bodies

In this section we illustrate the characteristics of the main mineralogical phases present in airless bodies of our interest.

1.7.1 Pyroxenes

Pyroxenes are single-chain inosilicates (Burns, 1993; Klima et al., 2007, 2011) and they are composed of two units, a silicon-oxygen tetrahedra chain (Si_2O_6) linked parallel to an octahedral chain $((\text{M2})(\text{M1})(\text{Si},\text{Al})_2\text{O}_6)$. Tetrahedra chains are linked alternately to a M1 octahedra chain and M2 octahedra chain (Deer et al., 1992). M1 octahedra are connected to the silicon-oxygen

tetrahedra by the vertex producing M1 sites smaller than the M2 sites. M1 sites contain principally small cations e.g. Mg^{2+} , Na^{2+} and Li^{2+} , therefore this is more symmetric. M2 sites can contain larger cations as Fe^{2+} and Ca^{2+} hence they are more distorted. In Fig. 1.15 are shown a schematic representation of the octahedra of the M1 site. M2 site have a similar structure. The M1 and M2 sites can be of two types, (+), (-) as illustrated in Fig. 1.15. Pyroxenes are classified in two types based on the orientation of the vertexes of the M1 and M2 sites: clinopyroxenes and orthopyroxenes. Clinopyroxenes have the octahedra disposed in the same way (+) (Fig. 1.16), and the disposition modules (Fig. 1.16 green rectangle) of the elementary monocline cell have an orientation of $\neq 90^\circ$. Orthopyroxenes, have an alternate disposition on the M1 and M2 sites as shown in Fig. 1.17, and the elementary cell has an orthorhombic structure. Orthopyroxenes are calcium poor unlike clinopyroxenes (Deer et al., 1992; Burns, 1993).

Pyroxenes are characterized by two strong absorption bands in the $1\mu\text{m}$ (band I) and $1.9\mu\text{m}$ (Band II). The positions and the strength of the bands are related to the size, the symmetry and the cations occupancy (Burns, 1993). Band I and band II in pyroxenes (Fig. 1.8) are due to the presence of the cation Fe^{2+} in the M2 sites, in particular band I depend on the absorption from both M1 and M2 sites, while band II depends only on the Fe^{2+} in the M2 site (Burns, 1993; Klima et al., 2007, 2011). Studies carried out on single phase pyroxenes with different amounts of calcium magnesium, and iron show that the increasing of Ca^{2+} and Fe^{2+} in the M2 sites cause a shift of the band centers toward increasing wavelengths (Adams, 1974; Klima et al., 2007, 2011). The ternary diagram of pyroxenes in Fig. 1.18, shows the variation of the amount of calcium, magnesium and iron in the different pyroxenes.

In Fig. 1.19 are shown several spectra of pyroxenes located in opposite positions of the pyroxenes diagram (Fig. 1.18). In Fig. 1.19-A are represented three spectra of orthoferrosilite. With respect to hypersthene (Fig. 1.19-B) which is iron-poor (Fig. 1.18), orthoferrosilite band centers are shifted toward longer wavelengths, as explained before. The absorption band around $1.2\mu\text{m}$ is due to the high abundance of Fe^{2+} . This band is prominent in all pyroxenes with 20% or more total iron (Klima et al., 2007). The $1.2\mu\text{m}$ band shifts to longer wavelengths and its intensity increases with increasing total iron, as the 1 and 2 μm bands (Klima et al., 2007).

Hypersthene spectra at different grain size show an evident reduction of the intensity of the bands for grain size larger than $250\mu\text{m}$. In this case the reflectance level is low and the two bands almost disappear (Fig. 1.19-B). Plot in Fig. 1.19-C represents enstatitic pyroxene in red and diopsidic pyroxene in blue. Enstatitic pyroxene is an orthopyroxene magnesium rich,

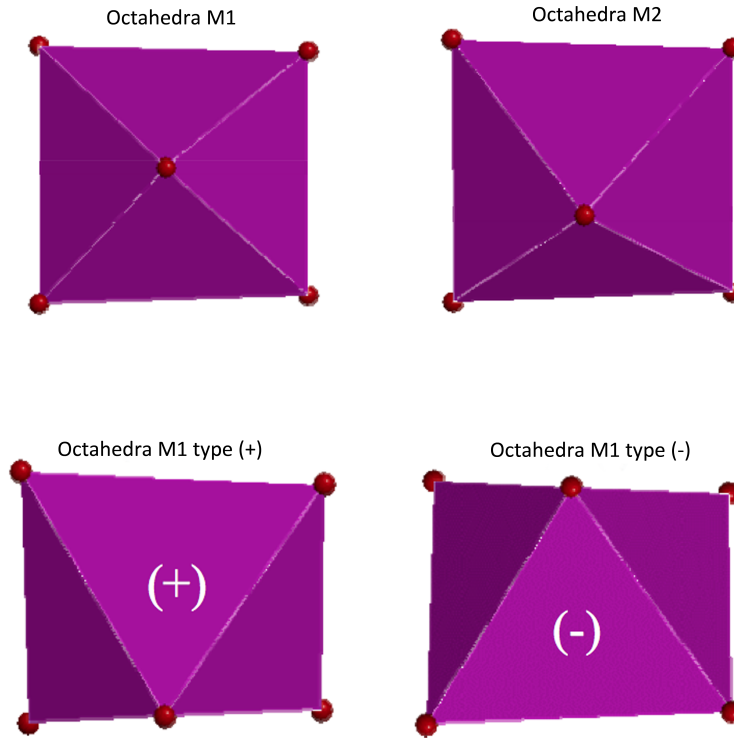


Figure 1.15: Types of octahedral in pyroxenes.

while diopsidic pyroxene is a clinopyroxene Ca^{2+} and Mg^{2+} rich. This plot which illustrates two extreme cases, highlights the large differences between the two spectra. The low content of Ca^{2+} and Fe^{2+} in the enstatitic pyroxene causes the shift of the band centers toward short wavelengths, while the presence of calcium in diopsidic pyroxene generates a very high shift of the bands: $1\mu\text{m}$ for the band I and largely below $2\mu\text{m}$ for the band two.

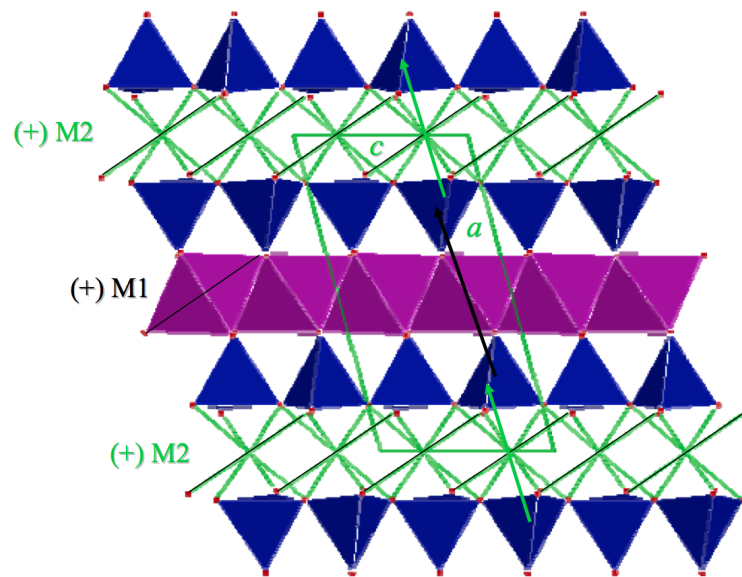


Figure 1.16: Clinopyroxenes symmetrical structure.

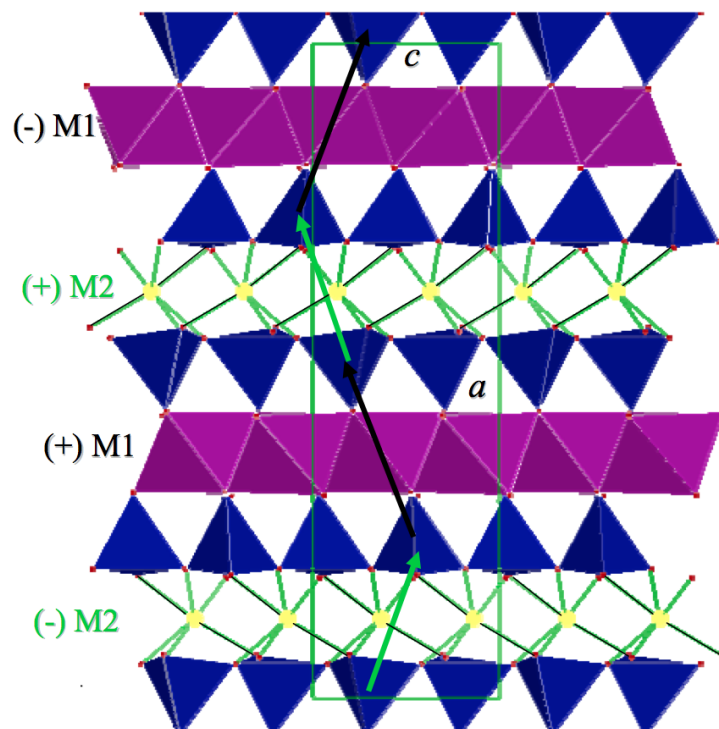


Figure 1.17: Orthopyroxenes symmetrical structure.

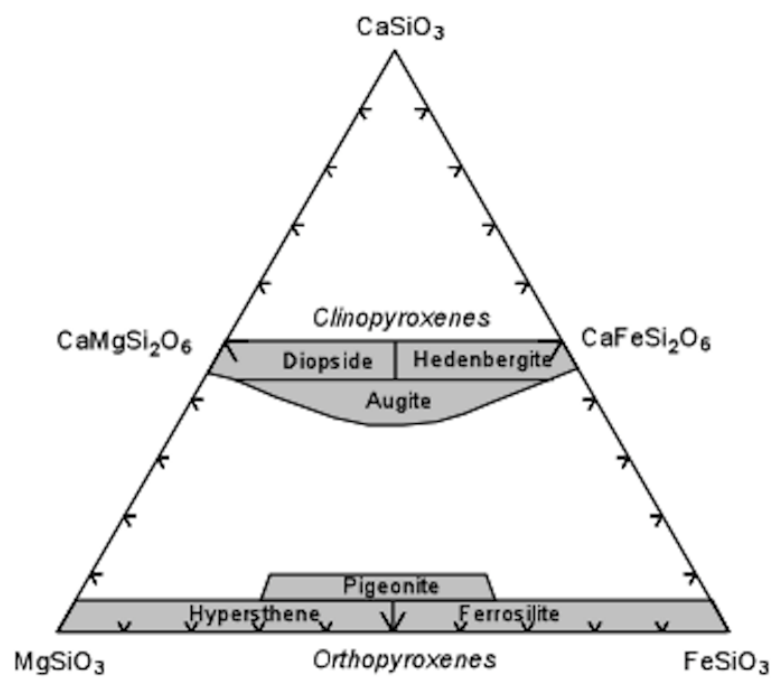


Figure 1.18: Ternary diagram of pyroxenes.

Nomenclature of Pyroxenes		
Mineral Names	Composition as endmember	Main composition as solid solution
A. Mg-Fe pyroxenes		
Enstatite (En)	$\text{Mg}_2\text{Si}_2\text{O}_6$	$(\text{Mg,Fe})_2\text{Si}_2\text{O}_6$
Ferrosilite (Fs)	$\text{Fe}_2^{2+}\text{Si}_2\text{O}_6$	$(\text{Mg,Fe})_2\text{Si}_2\text{O}_6$
Clinoenstatite		$(\text{Mg,Fe})_2\text{Si}_2\text{O}_6$
Clinoferrosilite		$(\text{Mg,Fe})_2\text{Si}_2\text{O}_6$
Pigeonite		$(\text{Mg,Fe,Ca})_2\text{Si}_2\text{O}_6$
B. Mn-Mg pyroxenes		
6. Donpeacorite		$(\text{Mn,Mg})\text{MgSi}_2\text{O}_6$
Kanoite (Ka)	$\text{MnMgSi}_2\text{O}_6$	$(\text{Mn,Mg})\text{MgSi}_2\text{O}_6$
C. Ca pyroxenes		
Diopside (Di)	$\text{CaMgSi}_2\text{O}_6$	$\text{Ca}(\text{Mg,Fe})\text{Si}_2\text{O}_6$
Hedenbergite (Hd)	$\text{CaFe}^{2+}\text{Si}_2\text{O}_6$	$(\text{Ca,Mg,Fe})\text{Si}_2\text{O}_6$
Augite		$(\text{Ca,Mg,Fe})_2\text{Si}_2\text{O}_6$
Johannsenite (Jo)	$\text{CaMnSi}_2\text{O}_6$	
Peteddunnite (Pe)	$\text{CaZnSi}_2\text{O}_6$	
Esseneite (Es)	$\text{CaFe}^{3+}\text{AlSi}_2\text{O}_6$	
D. Ca-Na pyroxenes		
Omphacite		$(\text{Ca,Na})(\text{R}2+,\text{Al})\text{Si}_2\text{O}_6$
Aegirine-augite		$(\text{Ca,Na})(\text{R}2+,\text{Fe}3+)\text{Si}_2\text{O}_6$
E. Na pyroxenes		
Jadeite (Jd)	$\text{NaAlSi}_2\text{O}_6$	$\text{Na}(\text{Al,Fe}3+)\text{Si}_2\text{O}_6$
Aegirine (Ae)	$\text{NaFe}^{3+}\text{Si}_2\text{O}_6$	$\text{Na}(\text{Al,Fe}3+)\text{Si}_2\text{O}_6$
Kosmochlor (Ko)	$\text{NaCr}^{3+}\text{Si}_2\text{O}_6$	
Jervisite (Je)	$\text{NaSc}^{3+}\text{Si}_2\text{O}_6$	
F. Li pyroxenes		
Spodumene (Sp)	$\text{LiAlSi}_2\text{O}_6$	

Table 1.3: Nomenclature and composition of pyroxenes (Morimoto et al., 1988).

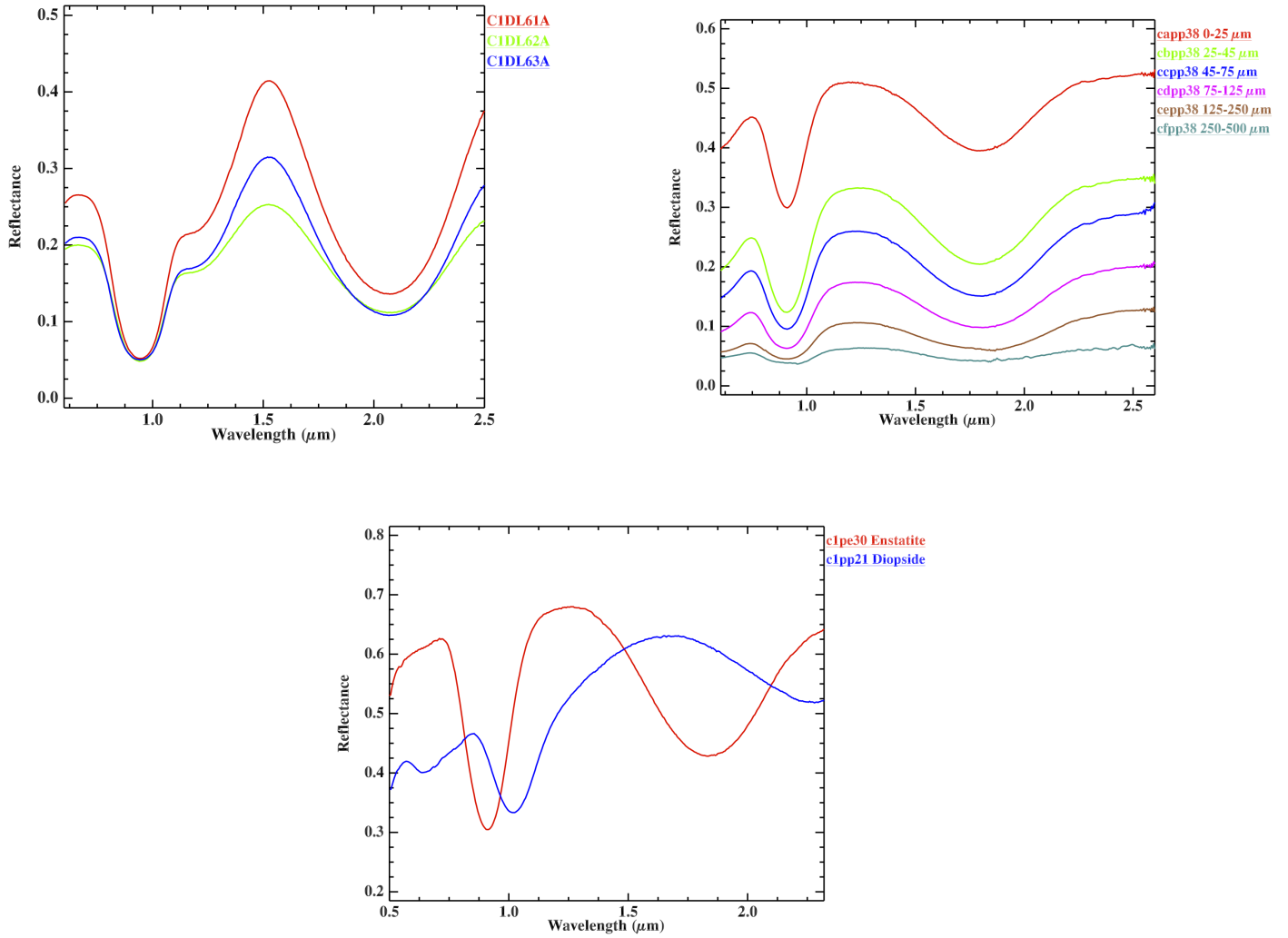


Figure 1.19: A. Orthoferrosilite RELAB spectra with a grain size <45 μm. B. Orthopyroxene RELAB spectra. Plot represents the same hypersthene sample at different grain sizes. The column on the left indicates the spectrum name with the relative grain sizes. C. Enstatitic pyroxene in red and diopsidic pyroxene in blue are represented. Spectrum name is indicated in the left column.

1.7.1.1 HED

Howardite, eucrite, diogenite (HED) meteorites represent a large sample of igneous rocks that includes basalts, cumulate gabbros, orthopyroxenes and igneous brecciated mixtures (Mittlefehldt et al., 1998). The diogenites are coarse-grained cumulates that originated from a plutonic layer deep in the crust (Mittlefehldt et al., 1998; Beck and McSween, 2010; McSween et al., 2011, 2013b). The mineralogy of diogenites is dominated by orthopyroxenes (from ~ 87 to 99 %); all diogenites contain $<5\%$ chromite and some contain olivine usually with a content $<10\%$ (McSween et al., 2011). Eucrites occur as basaltic or cumulate rocks. They are dominated by pyroxenes and plagioclase, with minor to trace amounts of metal troilite, chromite, ilmenite, and silica (Mayne et al., 2010; McSween et al., 2011). Eucrites are believed to have crystallized as lavas on the asteroid's surface or within relatively shallow-level dikes and plutons (McSween et al., 2011). Basaltic eucrites contain Fe-rich pyroxenes. Cumulate eucrites are predominantly unbrecciated and their mineralogy is similar to that of the basaltic eucrites, but richer in Mg (Mittlefehldt et al., 1998; McSween et al., 2011). The impact mixing of eucrite and diogenite produces the polymitic breccias and howardites. The howardites are a mixture of eucrite and diogenite clasts (Mittlefehldt et al., 1998; McSween et al., 2011).

Examples of HED spectra are shown in Fig. 1.20 (stack offset for clarity in the presentation). Spectral parameters of this sample are shown in Table 7.2. Diogenite is magnesium rich with respect to eucrite and thus band centers are shifted to shorter wavelengths. Howardite has an intermediate behavior, being a mixture of eucrite and diogenite.

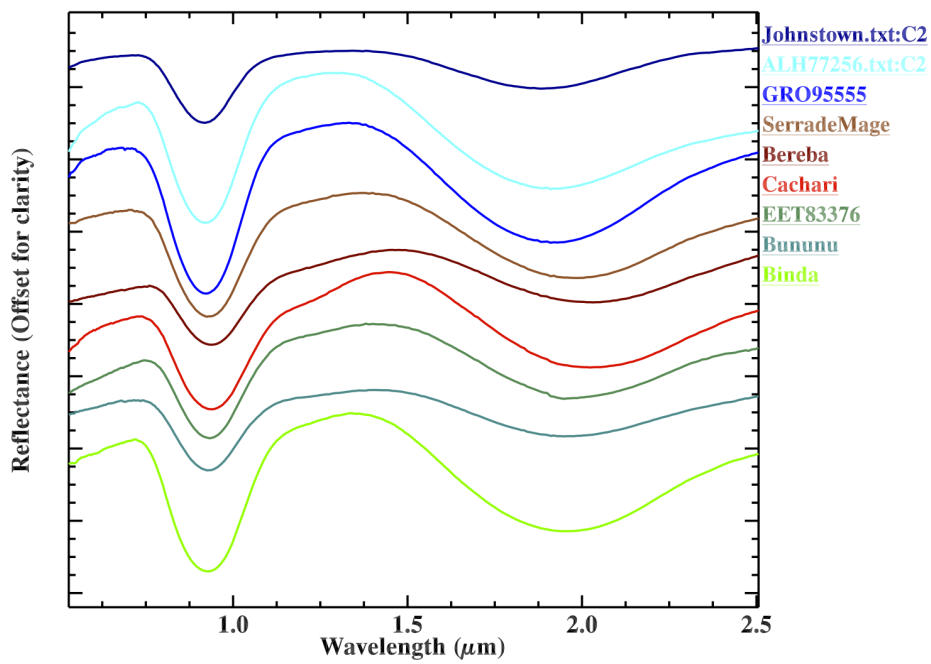


Figure 1.20: Howardite, diogenite and eucrite RELAB spectra with a grain size interval between 0 and 25 μm . Howardites are plotted in different shades of green, diogenite in blue and eucrite in red.

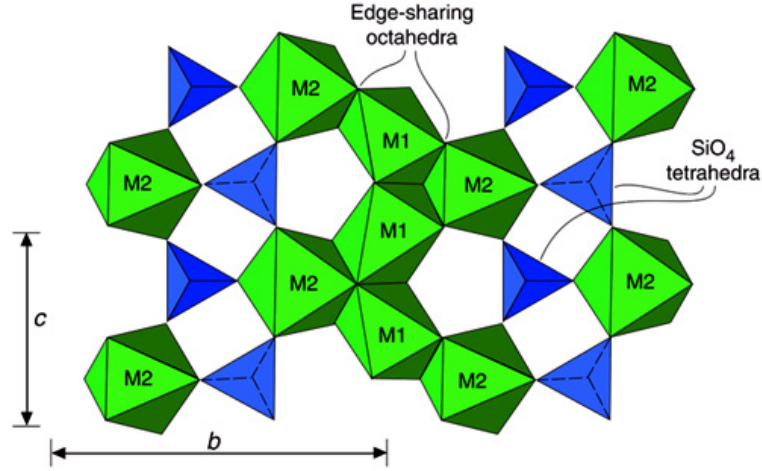


Figure 1.21: Olivine symmetrical structure.

1.7.2 Olivine

Olivine $((\text{M1}),(\text{M2}))\text{SiO}_4$ is a silicate mineral, present in many rocks and originated in the mantle. It is characterized by independent SiO_4 tetrahedra linked by divalent atoms in sixfold coordination (Deer et al., 1992; Burns, 1993), that crystallizes in orthorhombic structure (Fig. 1.21). The two symmetrically nonequivalent octahedral sites, M1 and M2 can contain Mg^{2+} , Fe^{2+} , Mn^{2+} , Ca^{2+} , Co^{2+} , Ni^{2+} and Zn^{2+} 1.4. Olivine is typically composed of two endmembers, forsterite (Mg_2SiO_4) and fayalite (Fe_2SiO_4). Olivine group can also contain manganese (tephroite), calcium-manganese (glaucochroite), calcium-magnesium (monticellite), and calcium-iron (kirschsteinite) end-members (Deer et al., 1992; Burns, 1993). In magnesium-iron olivines there is no M1 or M2 site preference for magnesium or ferric iron. However, in calcic olivines like monticellite, calcium preferentially enters the M2 site and magnesium occupies the M1 site (Deer et al., 1992). Table 1.4 summarizes the olivine types and their composition.

Olivine does not have the band at $1.9\mu\text{m}$ and band I has an asymmetric shape. In Fig. 1.22 we show some olivine RELAB spectra. Green and Magenta spectra represent fayalite and forsterite respectively (Fig. 1.22).

Nomenclature of Olivine	
Mineral Names	Composition as endmember
Forsterite	Mg_2SiO_4
Fayalite	Fe_2SiO_4
Tephroite	Mn_2SiO_4
Monticellite	CaMgSiO_4
Kirschsteinite	CaFeSiO_4
Glaucochroite	CaMnSiO_4

Table 1.4: Nomenclature and composition of olivines.

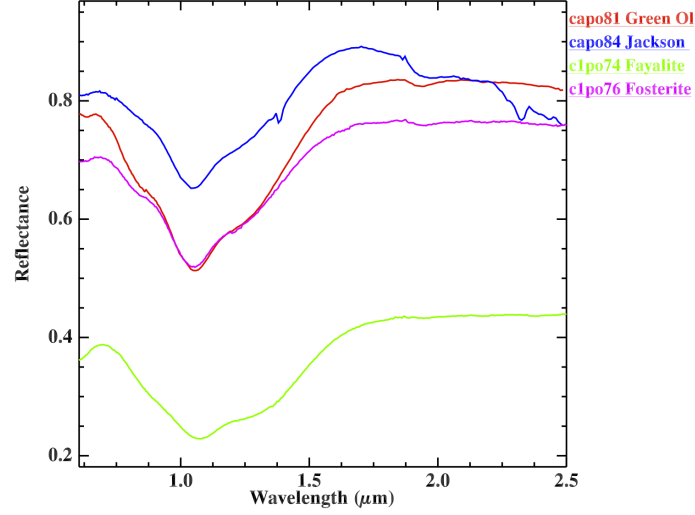


Figure 1.22: Olivine spectra selected by RELAB data base. Left column indicates the spectrum name. In green is represented the fosterite (Mg_2SiO_4) and in magenta the fayalite (Fe_2SiO_4) with a grain size range between 25 and 45 μm . The other two spectra are relative to two olivine sample with a grain size interval between 0 and 25 μm called "green olivine" and "Jackson city"

1.7.3 Feldspar

Feldspar belong to the tectosilicate group, and constitute around $\sim 60\%$ of the Earth's crust. They have a triclinic or monoclinic crystal structure, and all the oxygen SiO_4 and $(\text{Si},\text{Al})\text{O}_4$ tetrahedra are shared with other tetrahedra. This produces a cavity generally larger than the transition metal ions (Burns, 1993). Feldspars consist in three principal endmembers: Potassium-Feldspar (K-spar) endmember (KAlSi_3O_8), Albite endmember ($\text{NaAlSi}_3\text{O}_8$) and Anorthite endmember $\text{CaAl}_2\text{Si}_2\text{O}_8$. Minerals belonging to the feldspar family are: Alkali feldspars, Plagioclase feldspars, and Barium feldspars (Blatt and Tracy, 1996). Feldspar diagram (Fig. 1.23) summarizes the minerals belonging to feldspar family.

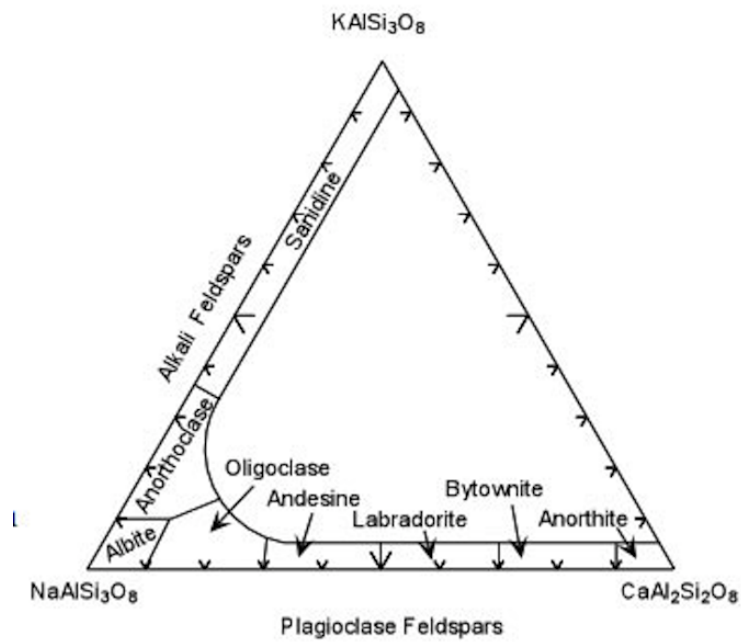


Figure 1.23: Feldspar diagram.

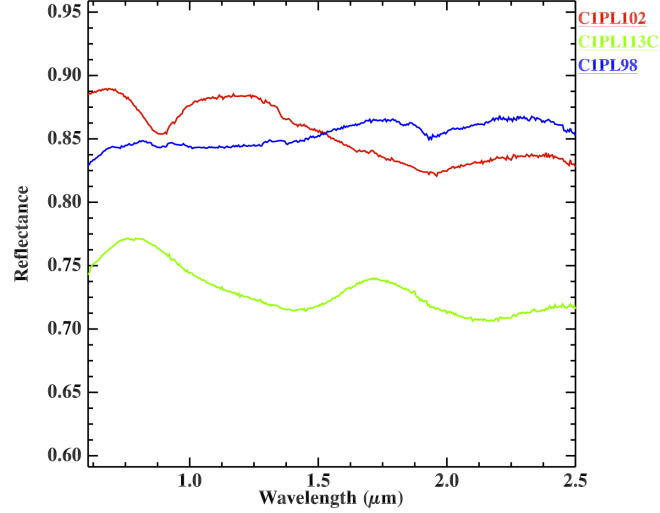


Figure 1.24: Plagioclase spectra selected by RELAB data base. Left column indicates the spectrum name.

1.7.3.1 Plagioclase

Plagioclase $((\text{Na,Ca})(\text{Si,Al})_4\text{O}_8)$, belongs to the series of feldspar minerals. It is typically light-coloured, glassy, transparent to translucent, with brittle crystals. Plagioclase has a monocline or triclinic structure. It is a major constituent mineral in the Earth's crust, and it is a mixture of two endmembers: albite (Ab) $(\text{NaAlSi}_3\text{O}_8)$, and anorthite (An) $(\text{CaAl}_2\text{Si}_2\text{O}_8)$. In Fig. 1.23 is shown the ternary diagram of plagioclase. The plot in Fig. 1.24 shows some examples of plagioclase spectra (Blatt and Tracy, 1996).

1.8 Hydrate minerals

We consider as hydrate any minerals containing H_2O or OH (Rivkin et al., 2002). Hydrate minerals include both silicates and nonsilicates (Rivkin et al., 2002). Nonsilicate hydrated minerals include, for example, brucite and goethite, the carbonate hydromagnesite, and the sulfide tochilinite, while serpentine-group, smectite-group, and chlorite-group minerals belong to phyllosilicates (Rivkin et al., 2002). Hydrate minerals are recurrent in meteorites and asteroids. H and O are among the most abundant elements in the Solar System, so their compounds are common (Rivkin et al., 2002). Both the OH and H_2O absorption bands are shallower (Clark, 1999). OH is typically at-

tached to metal ions and generally located in multiple crystallographic sites of a specific mineral (Clark, 1999). In spectra of OH-bearing minerals, an OH-signature is observed typically near 2.7 to 2.8 μm wavelengths, but can occur anywhere in the range from about 2.67 μm to 3.45 μm (Clark, 1999). OH stretches occur also at other wavelengths (e. g. first overtone may be found at 1.4 μm), while the combinations of the H-O-H bend with the OH stretches generates the absorption band at 1.9 μm . On the other hand the combination of a metal-OH bend plus an OH stretch is responsible for the absorption near 2.2 to 2.3 μm (Clark, 1999). Water absorption occurs at 2.738 μm , 6.270 μm and 2.663 μm in isolates molecules (vapor phase), or at 3.106 μm , 6.079 μm and 2.903 μm in liquid water. In Fig. 1.13 we represented spectra with OH and H₂O signatures at different positions.

Chapter 2

Data analysis methods

Data provided by different space missions are available in the Planetary Data System (PDS), an archive of data products sponsored by NASA's Science Mission Directorate, created to make available data provided by different space missions, with the aim to facilitate and encourage the use of these data (see section 2.1). We analyzed the data produced by the Visible and Infrared Spectrograph (VIRS), Mercury Dual Imaging System (MDIS) onboard Messenger, and those of Visible and InfraRed spectrometer (VIR) onboard Dawn. These instruments are different from each other (see Chapter 3), and so each type of data must be treated differently, taking into account the information that we want to derive from them. In this chapter we describe the techniques used to analyze the data produced by VIRS, MDIS and VIR. Concerning the spectral analysis, different methods are applied to different data sets, according to their characteristics. For example, Messenger Mercury spectra are featureless, do not show absorption bands and the principal differences are observed in the spectral slope. Application of particular classification methods (section 2.5) to the MASCS and MDIS data can be useful to understand how the spectral slopes varies in relation to the different type of terrains. VIR spectra of Vesta are different from those of Mercury, showing strong absorption bands. Vesta spectra can be associated with the howardite, eucrite, diogenite (HED) meteorites (section 1.7.1.1), and all the spectra present the typical iron-bearing pyroxene bands at 0.9 and 1.9 μm . In this case the analysis of the two bands through the study of the spectral parameters is indicated to understand Vesta mineralogy. Moreover, the linear unmixing method can be very useful to derive the composition of different region on Vesta (Section 2.7 and Chapter 7).

Another key characteristic of the data analyzed is the fact that they include also the gathered spatial information. Often can be useful to project the data and produce local or global maps. In section 2.3 we will describe the

projection that we used to produce the maps. The maps and the projection produced are shown in appendix A and B.

2.1 Planetary Data System (PDS)

The Planetary Data System (PDS) (<https://pds.jpl.nasa.gov/>) is an archive that includes data products from NASA planetary missions (JPL, 2008, 2009). The aim is those to have an archive in which all the NASA planetary missions data are available in a standard format, to maximize usefulness, and to make it a basic resource for scientists around the world to stimulate advanced research.

All PDS-produced products are peer-reviewed, well-documented, and easily accessible via a system of online catalogs that are organized by planetary disciplines (<https://pds.jpl.nasa.gov/>) (JPL, 2008).

Data can be released at different levels, e.g. raw data, calibrated data, and resampled data. In Fig. 2.1 we show the PDS data levels description.

PDS data nomenclature defines the rules for constructing Data Element and Data Object names and facilitates user access to the data (JPL, 2008). Naming and specification follow the international standard ISO9660. An example of VIR file name is "VIR_IR_1B_1_360823166_1_refl.QUB". The name contains the instrument name "VIR", the acquisition channel "IR", the level type "1B" corresponding to reflectance (indicated with "refl") calibrated data, and the acquisition time "360823166" a clock count value. To every data file is associated a label that contains all the information relative to the file. In Fig. 2.2 we show an example of the VIR label.

Level	Type	Data Processing Level Description
1	Raw Data	Telemetry data with data embedded.
2	Edited Data	Corrected for telemetry errors and split or decommutated into a data set for a given instrument. Sometimes called Experimental Data Record. Data are also tagged with time and location of acquisition. Corresponds to NASA Level 0 data.
3	Calibrated Data	Edited data that are still in units produced by instrument, but that have been corrected so that values are expressed in or are proportional to some physical unit such as radiance. No resampling, so edited data can be reconstructed. NASA Level 1A.
4	Resampled Data	Data that have been resampled in the time or space domains in such a way that the original edited data cannot be reconstructed. Could be calibrated in addition to being resampled. NASA Level 1B.
5	Derived Data	Derived results, as maps, reports, graphics, etc. NASA Levels 2 through 5.
6	Ancillary Data	Nonscience data needed to generate calibrated or resampled data sets. Consists of instrument gains, offsets, pointing information for scan platforms, etc.
7	Correlative Data	Other science data needed to interpret space-based data sets. May include ground-based data observations such as soil type or ocean buoy measurements of wind drift.
8	User Description	Description of why the data were required, any peculiarities associated with the data sets, and enough documentation to allow secondary user to extract information from the data.
N	N	Not Applicable

Figure 2.1: PDS data levels (JPL, 2009).

```

PDS_VERSION_ID = PDS3
LABEL_REVISION_NOTE = "MTC_11-10-2011"

/* Dataset and Product Information */
DATA_SET_NAME = "DAWN VIR CAL (RDR) VESTA INFRARED SPECTRA V1.0"
DATA_SET_ID = "DAWN-A-VIR-3-RDR-IR-VESTA-SPECTRA-V1.0"
PRODUCT_ID = "VIR_IR_1B_1_388371556_1_refl"
PRODUCT_TYPE = RDR
PRODUCER_FULL_NAME = "A. CORADINI"
PRODUCER_INSTITUTION_NAME = "ISTITUTO NAZIONALE DI ASTROFISICA"
PRODUCT_CREATION_TIME = 2013-09-06T14:03:18.220
PRODUCT_VERSION_ID = "01"

/* File Information */
RECORD_TYPE = FIXED_LENGTH
RECORD_BYTES = 512
FILE_RECORDS = 48
LABEL_RECORDS = 47

/* Time Information */
START_TIME = 2012-04-22T12:58:09.828
STOP_TIME = 2012-04-22T12:59:47.574
IMAGE_MID_TIME = 2012-04-22T12:58:58.701
SPACECRAFT_CLOCK_START_COUNT = "1/388371556.4943"
SPACECRAFT_CLOCK_STOP_COUNT = "1/388371654.2404"

/* Mission description parameters */
INSTRUMENT_HOST_NAME = "DAWN"
INSTRUMENT_HOST_ID = "DAWN"
MISSION_PHASE_NAME = "VESTA SCIENCE LAMO (VSL)"

/* Instrument description parameters */
INSTRUMENT_NAME = "VISIBLE AND INFRARED SPECTROMETER"
INSTRUMENT_ID = "VIR"
INSTRUMENT_TYPE = "IMAGING SPECTROMETER"

/* Celestial Geometry */
RIGHT_ASCENSION      = 1.438 <degrees>
DECLINATION          = -44.217 <degrees>
TWIST_ANGLE          = 240.081 <degrees>
CELESTIAL_NORTH_CLOCK_ANGLE = 299.919 <degrees>
QUATERNION            = ( 0.37704,
                          0.24896,
                          -0.88697,
                          0.09569 )
QUATERNION_DESC       = "
    Above parameters are calculated at the center time of the observation
    which is 2012-04-22T12:58:58.701. The quaternion has the form:
    w, x, y, z (i.e. SPICE format)."

```

Figure 2.2: Example of PDS label file.

2.2 Coordinate Systems

The geometrical information contained in the data package of the PDS archive are defined according to international standards. The International Astronomical Union (IAU) establishes the coordinate system for the bodies of the Solar System. The IAU and the International Association of Geodesy (IAG) have jointly established the Working Group on Cartographic Coordinates and Rotational Elements (WGCCRE) (JPL, 2009) (<http://astrogeology.usgs.gov/Projects/WGCCRE/>). The WGCCRE defines the reference surface of a body that can be of different types; the most common one is the oblate spheroid aligned with the spin axis of the body, but other reference surfaces are also considered, e.g., triaxial ellipsoid and gravitational equipotential (JPL, 2009).

The shape of the body defines the coordinate system to be used. The equatorial plane is the reference plane of the coordinate system, the rotation axes is the z axes, while the geometric center of the planet is the origin of the coordinate system. Since not all bodies of the solar system can be associated with a sphere, it is necessary to introduce two type of coordinates: **planetocentric** and **planetographic** (Fig. 2.3). Planetocentric system is indicated for irregular bodies. North and south are the same for both the systems except for the values.

Planetocentric system. Planetocentric latitude is the angle between a vector from the center of mass of the body to the point of interest and the equatorial plane (JPL, 2009) (Fig. 2.3). Planetocentric longitude is the angle between the prime meridian and the projection of the vector onto the equatorial plane and is always measured positively to the east from 0° to 360° , regardless of the direction of rotation of the body (JPL, 2009). An external observer sees the longitude decreasing with time if the rotation is prograde but increasing with time if the rotation is retrograde (JPL, 2009).

Planetographic system. Planetographic latitude is the angle between the normal to the point of interest on the surface and the equatorial plane (Fig. 2.3). Planetographic longitude is measured positively opposite to the rotation of the body. It is positive west when the rotation is prograde, and it is positive east when the rotation is retrograde. An external observer sees the longitude increasing with time (JPL, 2009).

IAU defined the reference systems to be used for the Solar System bodies (see 2.4). In the past the longitude range of -180° $+180^\circ$ has been used for the Earth, the Moon and the Sun. For the Moon this longitude range is still being used. For small bodies the longitude range is always positive east both for the planetocentric and planetographic system.

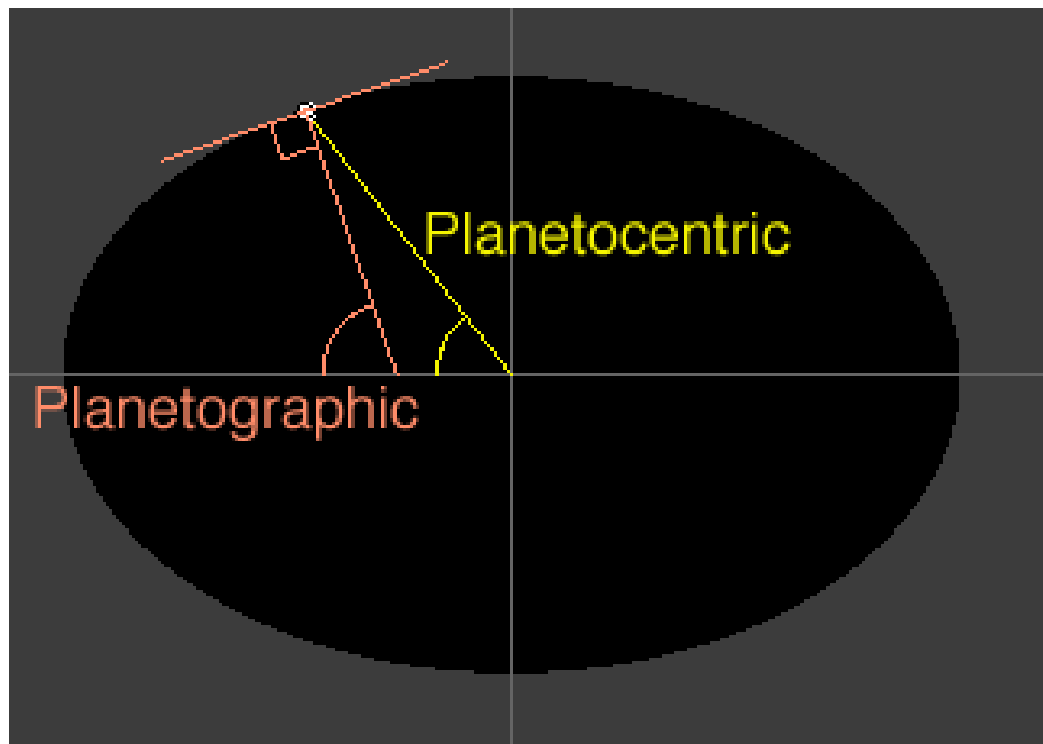


Figure 2.3: Planetocentric and planetographic coordinates (<http://planetarynames.wr.usgs.gov/Page/Website>).

The measurement of the longitude implies the choice of the prime meridian. For solid bodies the prime meridian is defined by a specific feature on the surface, typically a small crater in the equatorial region. For non-solid surface bodies the definition of the prime meridian is based on the angular velocity. For Vesta we adopt the coordinate system called "Dawn-Claudia" (Roatsch et al. (2012), Russell et al. (2012) supplementary material, Li (2013); Reddy et al. (2013). This reference system is different from that previously adopted by the International Astronomical Union (IAU) for Vesta (Roatsch et al., 2012; Archinal et al., 2009). The pole orientation is 6.2° toward the east and, the prime meridian in the "Dawn-Claudia" system has an offset of $\sim 150^\circ$ with respect to the prime meridian in the IAU system. PDS uses the "Claudia Double-Prime" system, which attempts to exactly register the prime meridian with the IAU-2000 coordinate system (Li, 2013; Reddy et al., 2013; Tosi et al., 2014a). The center of the Claudia crater in this coordinate system is: -1.6° latitude and 146.0° longitude at J2000 epoch (Li, 2013).

Target	Coordinate Systems	Control Networks
Amalthea	Planetographic, +West, 0 - 360	
Ariel	Planetocentric, +East, 0 - 360	
Callisto	Planetographic, +West, 0 - 360	
Deimos	Planetographic, +West, 0 - 360	
Dione	Planetographic, +West, 0 - 360	
Enceladus	Planetographic, +West, 0 - 360	
Epimetheus	Planetographic, +West, 0 - 360	
Europa	Planetographic, +West, 0 - 360	
Ganymede	Planetographic, +West, 0 - 360	
Hyperion	Planetographic, +West, 0 - 360	
Iapetus	Planetographic, +West, 0 - 360	
Io	Planetographic, +West, 0 - 360	Voyager/Galileo SSI
Janus	Planetographic, +West, 0 - 360	
Mars	Planetographic, +West, 0 - 360 Planetocentric, +East, 0 - 360	MDIM 2.0 MDIM 2.1
Mercury	Planetographic, +West, 0 - 360	MESSENGER Team Preliminary MESSENGER
Mimas	Planetographic, +West, 0 - 360	
Miranda	Planetocentric, +East, 0 - 360	
Moon	Planetographic, +East, -180 - 180	LOLA 2011 ULCN 2005
Oberon	Planetocentric, +East, 0 - 360	
Phobos	Planetographic, +West, 0 - 360	
Phoebe	Planetographic, +West, 0 - 360	
Proteus	Planetographic, +West, 0 - 360	
Puck	Planetocentric, +East, 0 - 360	
Rhea	Planetographic, +West, 0 - 360	
Tethys	Planetographic, +West, 0 - 360	
Thebe	Planetographic, +West, 0 - 360	
Titan	Planetographic, +West, 0 - 360	
Titania	Planetocentric, +East, 0 - 360	
Triton	Planetographic, +East, 0 - 360	
Umbriel	Planetocentric, +East, 0 - 360	
Venus	Planetocentric, +East, 0 - 360	

Figure 2.4: IAU-accepted coordinate systems for planets and satellites (<http://planetarynames.wr.usgs.gov/TargetCoordinates>).

2.3 Projections

The coordinate system is used for all the resolved Solar System bodies, and latitude and longitude define the position of a point in a surface (Fig. 2.5). A point in a surface can be represented on a bidimensional plane. For each body a reference surface is assigned, that can be spherical or ellipsoidal. Generally, Solar System bodies have an irregular surface, that differ from a sphere or an ellipsoid. In Fig. 2.6 we show a representation of different types of reference surface. The topographic surface is the real surface, the geoid is the geometric shape that takes into account the spheroid and its gravity variations, and can be defined as an equipotential surface of the gravitational field passing through the mean sea level (Snyder, 1982, 1987). To define the equation of a point in a surface it is necessary to approximate the body with a sphere or an ellipsoid. Through these equations it is possible to represent a point in a spherical or ellipsoidal body in a plane. It is necessary to transform the spherical coordinates in cartesian coordinates, thus there is a bijective correspondence between the point of the ellipsoid and the cartesian plane. This transformation is called projection and every projection causes a deformation on the map (Snyder, 1982, 1987). Every projection is characterized by a **Scale** i.e. the ratio between the distance on the map and that on the body (Snyder, 1982, 1987).

There are several types of projections, and their classification depends on the parameters that do not modify the surface projection, the position of the point of view and the orientation of the projection surface (Snyder, 1982, 1987). Projections can maintain unchanged some geometric characteristics such as angles, areas, and distances. Depending on the parameters that remain unchanged, they can be classified as:

- **Conformal or orthomorphic projection.** In these projections the angles and the shape are unchanged.
- **Equivalent projection.** Areas remain unchanged. This condition is not compatible with the previous one.
- **Equidistant of linear projection.** The ratio between the distances on the plane and those on the ellipsoid is constant.

These conditions cannot be verified together. A projection that minimize the deformations is called **afilactic**.

The surface of projection can be **azimuthal (plane)**, **cylindric** or **conic** (Fig. 2.7), while the orientation of the surface of projection can be **direct** or **normal** when the auxiliary plane or the solid axes is parallel to the

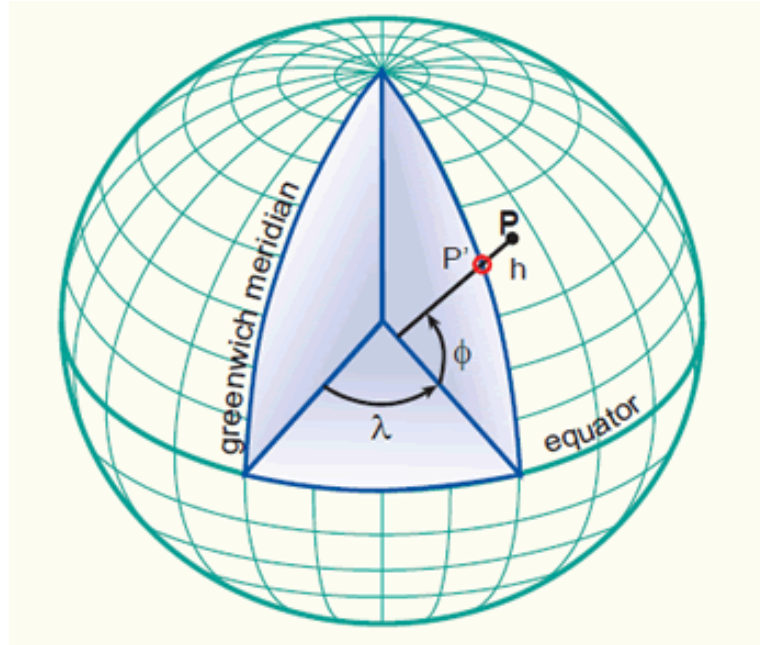


Figure 2.5: Representation of the latitude (ϕ) and longitude (λ) (<http://kartoweb.itc.nl/geometrics/coordinate%20systems/coordsys.html>).

equator, **inverse or transverse** when the auxiliary plane or the solid axes is perpendicular to the equator, and **oblique** in all the other cases (Fig. 2.7) (Snyder, 1982, 1987).

The position of the point of view (or an hypothetical source that illuminate the ellipsoid) can be **centrographic or gnomonic** if the point of view is inside the ellipsoid, **stereographic** is the point of view is in the opposite position with respect to the surface of projection, **orthographic** if the point of view is outside the ellipsoid at infinite distance and the visual ray are parallel, and **scenographic** is the if the point of view is outside the ellipsoid (Fig. 2.8).

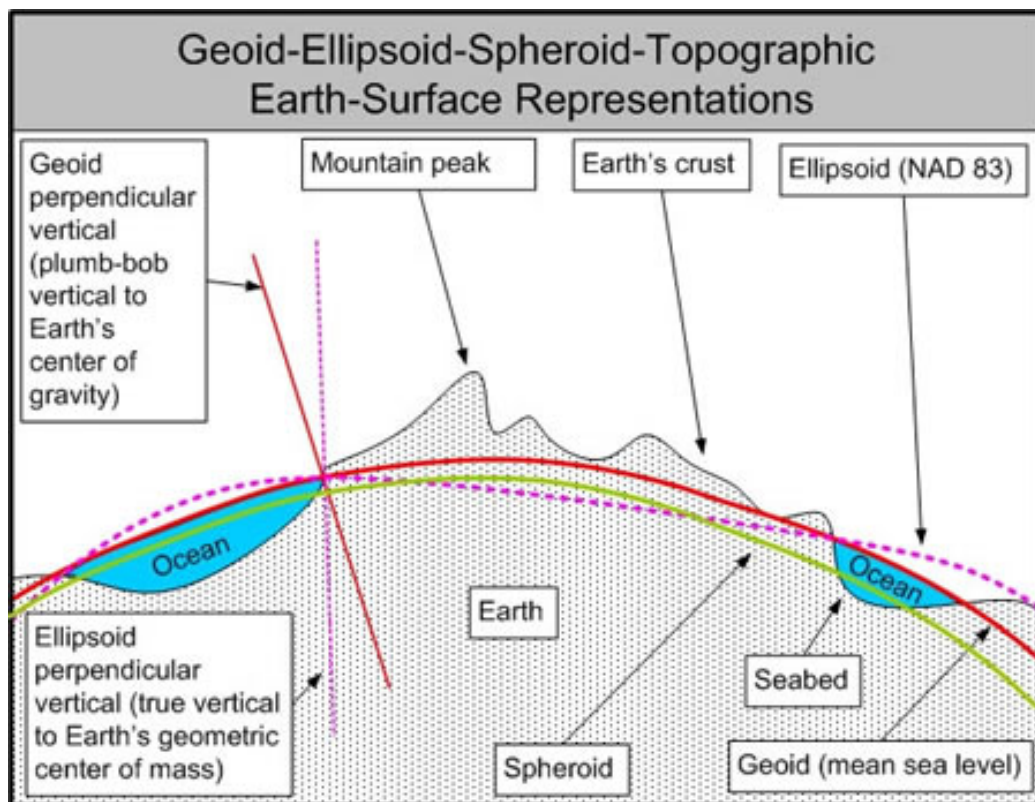


Figure 2.6: Representation of the geoid and the ellipsoid (<http://therucksack.tripod.com/MiBSAR/LandNav/Datums/MapDatums.htm>).

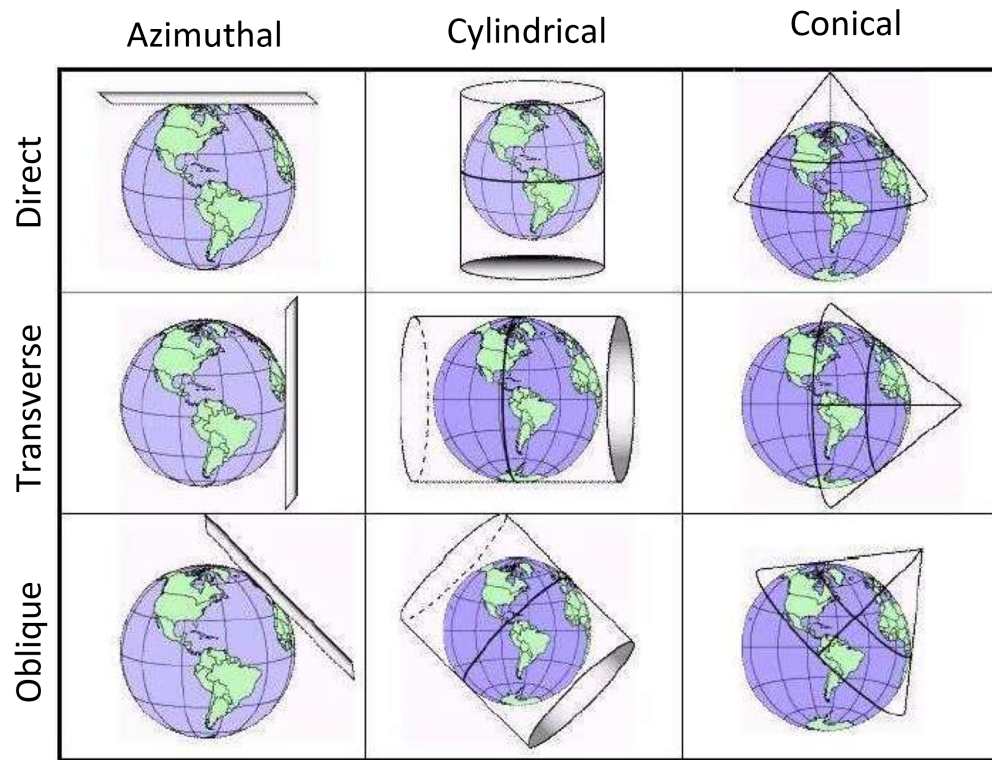


Figure 2.7: Representation of the surfaces of projection in the three different orientations.

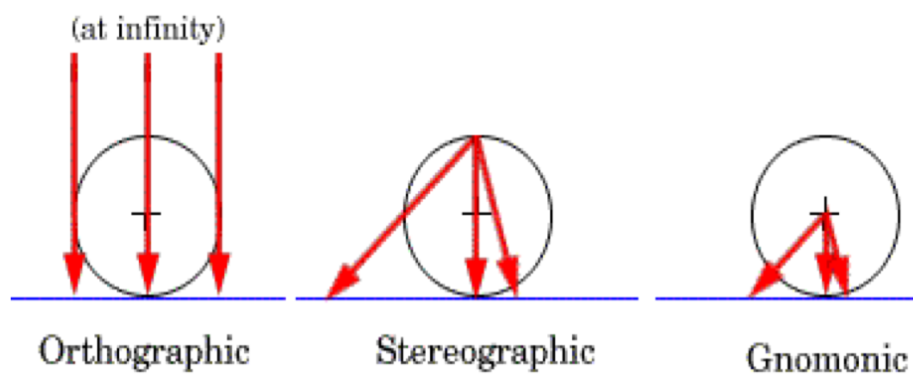


Figure 2.8: Representation of three principal point of view (http://www.geografia-applicata.it/wordpress/wp-content/uploads/2011/04/03_Proiezioni_Cartografiche.pdf).

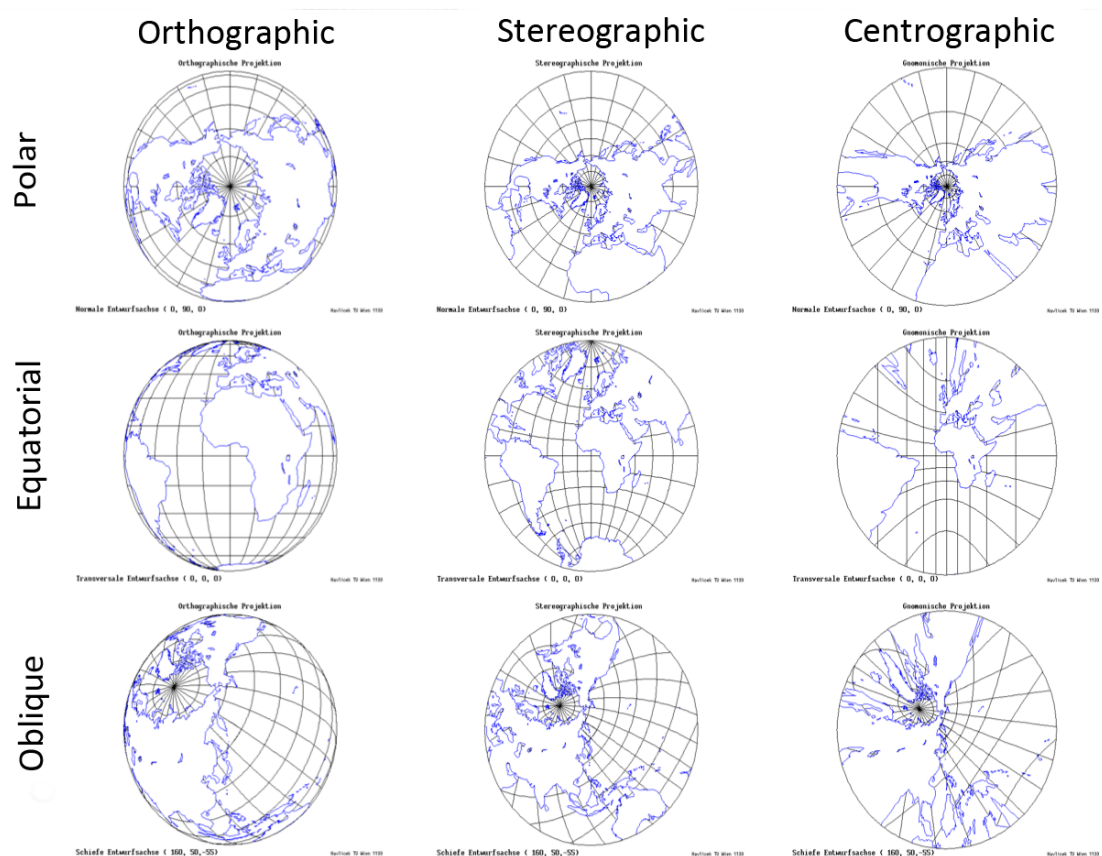


Figure 2.9: Examples of different types of projection (http://www.geografia-applicata.it/wordpress/wp-content/uploads/2011/04/03_Proiezioni_Cartografiche.pdf).

Each projection introduces a deformation. The Tissot's indicatrix is a parameter that indicates the degree of distortion. The indicatrix is an ellipse (ellipse of distortion) on the map and corresponds to a circle on the ellipsoidal surface (Snyder, 1982, 1987). Every point on the projected map has a different degree of distortion. In the conformal projections, the ellipse remains a circle, and its area indicates the expansion or the contraction generated by the projection. In the equivalent projection the circle becomes an ellipse with the same area. In Figs 2.10 and 2.11 we show the Tissot's indicatrix superimposed to different types of projection.

Many types of projection exist. We now describe those used in this work.

- **Mercator projection** was presented by Mercator in 1569; it is a cylindric and conform projection. Meridians cut parallels at right angle, and the distance between parallels increase toward the poles to compensate the deformation in east-west direction, while meridians are equally spaced straight lines. Thus poles are at infinity with great distortion of area in polar regions, and the scale is true along the Equator, or along two parallels equidistant from the Equator (Snyder, 1982, 1987). We use this map to project the Rudaki's area located in the equatorial region of Mercury (Fig. 5.12).
- **Equatorial cylindrical equidistant or equirectangular projection** was presented by Eratosthenes (275-195B.C.) or Marinus (A.D. 100). It is used only in spherical form and it is cylindrical, with no equivalent and no conformal projection. Meridians and parallels are equidistant straight lines, intersecting at right angles, and the poles shown as lines (Snyder, 1982, 1987). We use this map to produce a global map of Vesta and to project the equatorial regions (Appendix B).
- **Simple cylindrical or Plate Carree projection** is a variant of the Equirectangular projection. The equator is made of standard parallel, true to scale and free of distortion, the meridians are spaced at the same distances as the parallels, and the graticule appears square (Snyder, 1982, 1987) (Fig. A.2, A.4, A.9, A.10).
- **Orthographic projection** is known since the time of the ancient Greeks and Egyptians, and it is used only in the spherical form. It is an azimuthal projection, and all meridians and parallels are ellipses, circles, or straight lines. It is neither conformal nor equivalent, and it is represented as a globe because of the point of view at infinity distances. Only one hemisphere can be shown at a time and the greater distortion

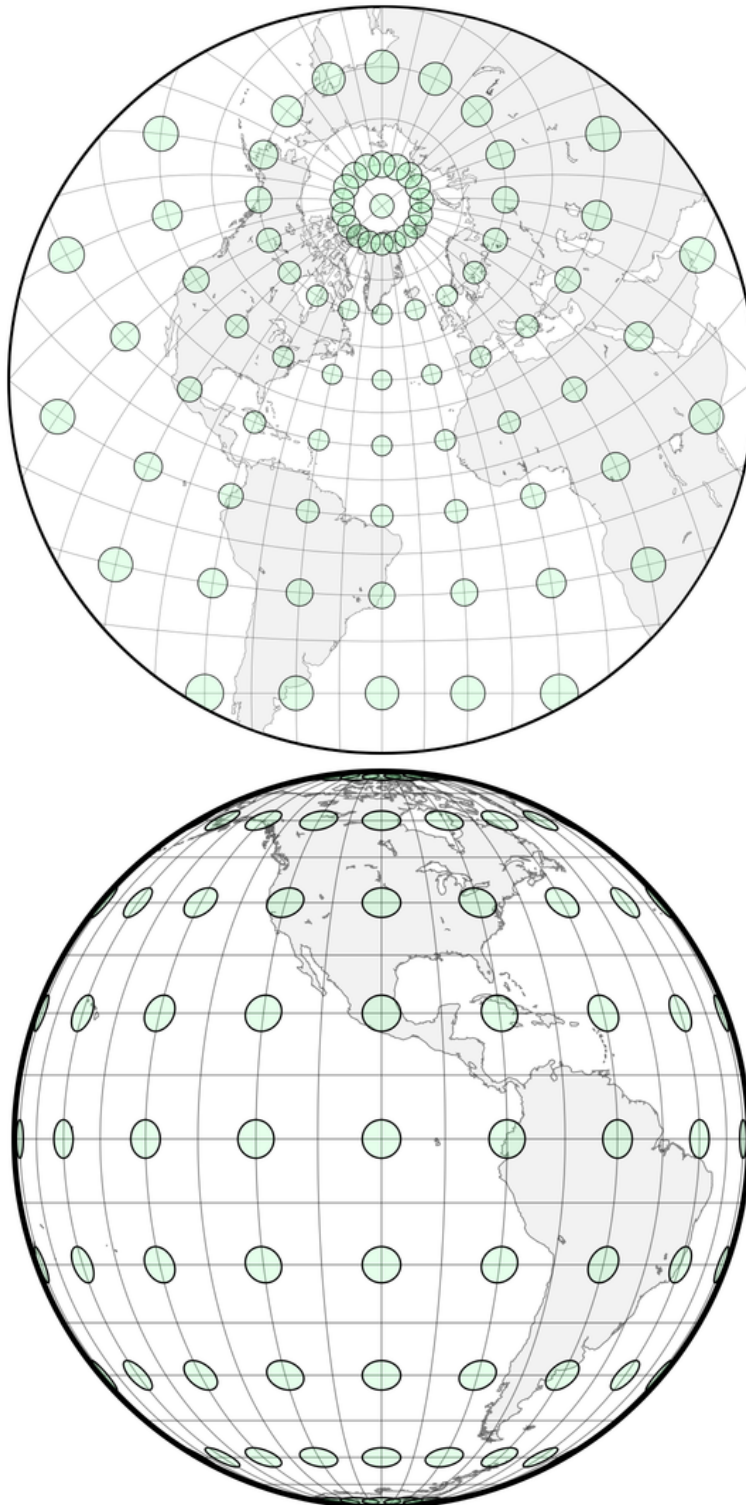


Figure 2.10: Top. Ellipses of distortion in the oblique stereographic projection. Bottom. Ellipses of distortion in the equatorial orthographic projection (C. A. Furuti - www.progonos.com/furuti)

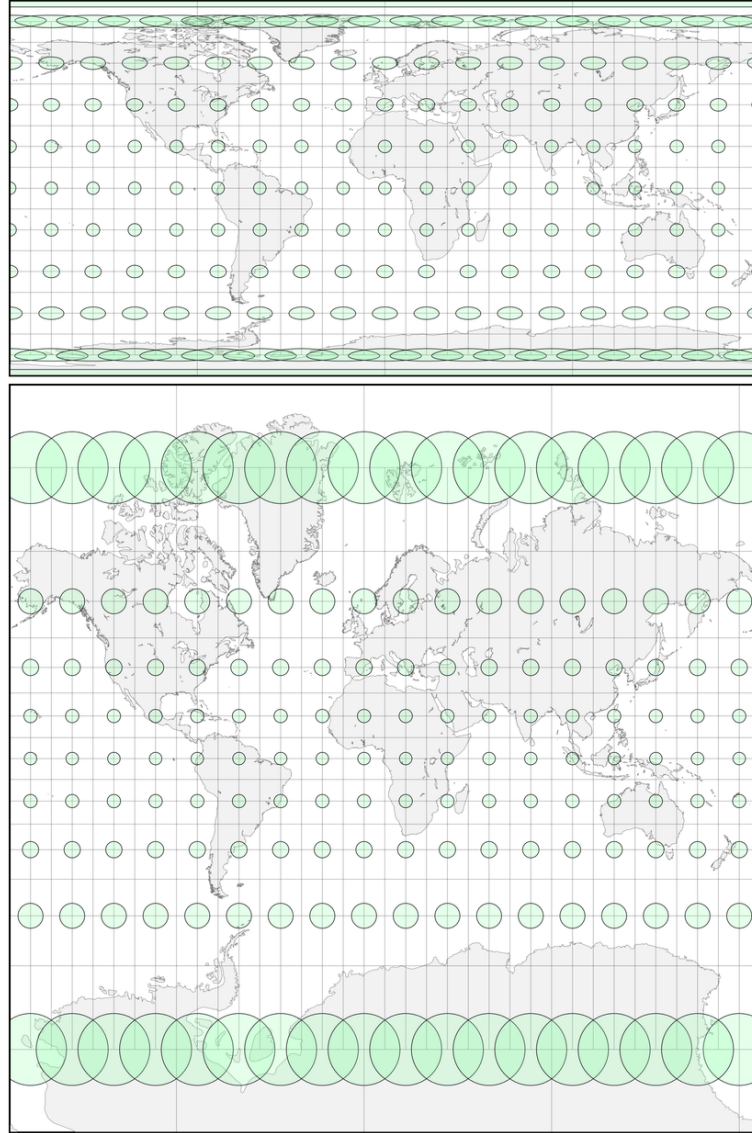


Figure 2.11: Top. Ellipses of distortion in the equatorial cylindrical equidistant projection. Bottom. Ellipses of distortion in the Mercator projection (C. A. Furuti - www.progonos.com/furuti)

is near the edge of the hemisphere shown, while no distortion is present at the center. Directions from the center are true. Radial scale factor decreases as distance increases from the center and the scale in the direction of the lines of latitude is true in the polar aspect (Snyder, 1982, 1987). We use it to produce a pictorial view of the VIR data coverage (Fig. B.1, A.8).

- **Polar stereographic projection** seems to have been invented by Hipparchus (2nd century B.C.). It is an azimuthal and conformal projection and a perspective projection for the sphere, and the point opposite the center of the projection cannot be plotted. The central meridian and a particular parallel (if shown) are straight lines, and all meridians on the polar aspect and the Equator on the equatorial aspect are straight lines. All other meridians and parallels are shown as arcs of circles. Directions from the center of the projection are true (except on ellipsoids oblique and equatorial aspects). Scale increases away from the center of the projection (Snyder, 1982, 1987). We use this projection to map the poles of Vesta (Fig. A.1, A.5, A.6).

2.4 Projections and mosaics of VIR data

In this section we show the steps to produce a mosaic with the VIR data using ISIS 3. Integrated Software for Imagers and Spectrometers (ISIS) is a powerful software developed by USGS dedicated to the reduction and the analysis of multispectral and hyperspectral data. All the mosaics and projection produced are shown in Appendix A, B. The steps to create a mosaic are the following:

1. Convert the VIR data from PDS format to ISIS format using the command *dawnvir2isis* (Fig. 2.12).
2. Georeference the data using the command *spiceinit*.



Figure 2.12: Exemple of VIR cube at $1.4\mu\text{m}$.

3. Choose the appropriate projection based on the region that must be analyzed. For equatorial regions are indicated Mercator, cylindrical or equirectangular projections, while for the polar regions the stereographic projection is preferable.
4. Generate the map that will be used to project the data with *mosrange*. Mosrange generates a file.map, containing all the information necessary for the projection, and calculates the map information according to the characteristics of the selected data. Center latitude and longitude (Fig. 2.13) of the map must be changed *a posteriori*, and must be (0°, 180°) for the equatorial regions (e.g. in Mercator, cylindrical and equirectangular projections), (-90°, 180°) for the southern regions, and (90°, 0°) for the northern regions. To create a mosaic all the image considered must be at the same resolution, so it is necessary to use the same file.map.

```

Group = Mapping
ProjectionName      = Equirectangular
TargetName         = VESTA
EquatorialRadius   = 289000.0 <meters>
PolarRadius        = 229000.0 <meters>
LatitudeType       = Planetocentric
LongitudeDirection = PositiveEast
LongitudeDomain    = 360
PixelResolution    = 185.67 <meters/pixel>
Scale              = 27.169790172 <pixels/degree>
MinPixelResolution = 161.14556499269 <meters>
MaxPixelResolution = 203.56028823661 <meters>
CenterLongitude    = 180.0
CenterLatitude     = 0
MinimumLatitude    = -46.486720476494
MaximumLatitude    = 62.083102488294
MinimumLongitude   = 0.0
MaximumLongitude   = 360.0

# Actual Parameters without precision applied
PreciseCenterLongitude = 180.0
PreciseCenterLatitude  = 0
PreciseMinimumLatitude = -46.486720476494
PreciseMaximumLatitude = 62.083102488293
PreciseMinimumLongitude = 0.0
PreciseMaximumLongitude = 360.0
End_Group
End

```

Figure 2.13: Example of a map file produced by *mosrange*

5. Project each cube with *cam2map*, using the file.map generated previously (Fig. 2.12);

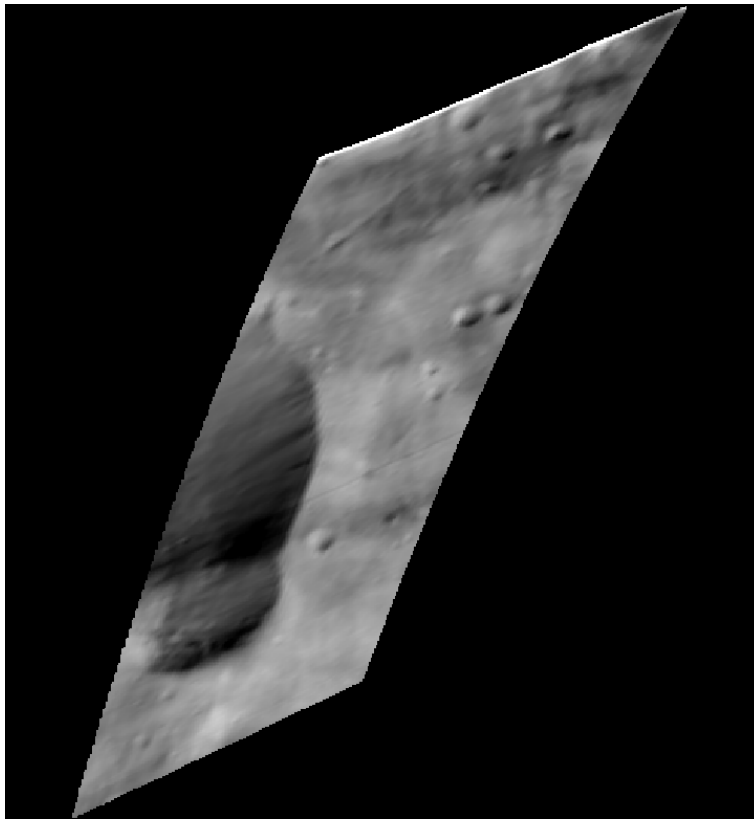


Figure 2.14: Cylindrical projection of the VIR image shown in Fig. 2.12.

6. Generate a list containing the name of the projected cube to create the mosaic, and use *automos* to generate the it. Fig. 2.15 shows an example of a mosaic created with this procedure.

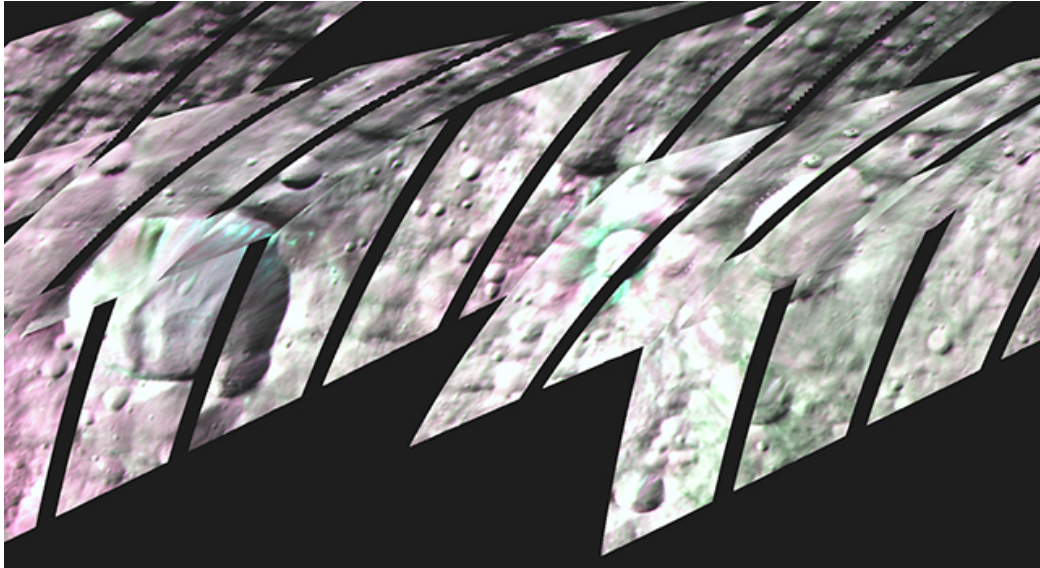


Figure 2.15: Mosaic of the Bellicia and Arruntia region in cylindric projection (Ammannito et al., 2013b).

2.5 Classification methods

When a large quantity of data are available such as in the space mission, a good way to make a rapid analysis of the dataset is to apply classification methods (Akamatsu et al., 1996; Adams and Gillespie, 2006; Richards, 2013). Classification methods are based on clustering algorithms. They are based on grouping together pixels with similar characteristics, forming classes. Classification methods are divided in two categories: unsupervised and supervised (Akamatsu et al., 1996; Adams and Gillespie, 2006; Richards, 2013). In the first case the algorithm chooses the reference classes and assigns each pixel to corresponding class. In the second case, the user chooses the reference classes or end-member and the algorithm distributes the single pixel to the corresponding class (Adams and Gillespie, 2006). To classify the MDIS and MASCS data we use ENVI (Environment for Visualizing Images), a very useful software for the remote sensing data analysis (Research System, 2004). ENVI integrates many clustering algorithms, including those used in this work. Unsupervised methods can be useful when no *a priori* information is available, and can be used to choose the reference classes for the supervised methods. The principal unsupervised algorithm are K-mean (Adams and Gillespie, 2006) and ISODATA (Iterative Self-Organizing Data Analysis Technique) (Ball and Hall, 1965; Adams and Gillespie, 2006; Memarsadeghi et al., 2007). Among the principal supervised methods there are: the parallelepiped classification method, the MINIMUM DISTANCE, and the Spectral Angle Mapper (SAM) (Adams and Gillespie, 2006). In this work we used the ISODATA unsupervised classification method to find the reference classes called endmember or training data to apply the MINIMUM DISTANCE classification method. We now describe these two techniques of classification.

2.5.1 ISODATA

ISODATA is a complex variant of the K-mean method (Ball and Hall, 1965; Memarsadeghi et al., 2007). Consider a set of N objects $X = \{X_1, X_1, \dots, X_n\}$, where X_i represents an object containing m attributes (in our case the object X_i represent the pixels, and the attributes are the bands), and $\mathbf{Q} = \{Q_1, Q_2, \dots, Q_n\}$ the set of the centroid of each reference class. Unlike the K-mean, ISODATA allows to the user to choose some setting parameters (Ball and Hall, 1965; Adams and Gillespie, 2006; Memarsadeghi et al., 2007):

- Maximum number of classes K ;
- Maximum number of iterations I ;

- Maximum number of couples P that may be merged;
- Minimum number of member for each class θ ;
- Threshold values of the standard deviation θ_s , to decide which classes can be separated;
- Minimum distance of the classes to be merged θ_c

Here are the principal steps of the ISODATA classification algorithm (Fig. 2.16), applied to a sample X of N objects:

1. Among the objects belonging to X the algorithm chooses randomly a arbitrary number of classes $\tilde{k} < K$, and a set of centroid for each class Q , chosen among the objects in X .
2. the Euclidean distance ($d(X_i, Q_j)$) between a centroid and the each pixel is calculated.
3. Each pixel is assigned to the closest centroid.
4. Classes with not enough elements are discarded, and the centroid re-calculated.
5. For each classes the mean distance d_j between the centroid and the elements of the cluster is calculated.
6. The distance D of the objects X_i and the correspondence centroid is calculated.
7. If $\tilde{k} < K/2$ there are few clusters and they must be separated. If $\tilde{k} > 2K$ the clusters must be merged.

This is an iterative process, and it will end when the class number is unchanged or if the maximum number of iterations have been achieved.

To separate the cluster is necessary to find the standard deviation vector of each class $\sigma_i^{(j)} = (\sigma_1^{(j)}, \sigma_2^{(j)}, \dots, \sigma_n^{(j)})$, where σ_{max}^j is the maximum standard deviation. If $\forall \sigma_{max}^j$ are verified concurrently the following conditions:

- $\sigma_{max}^j > \sigma_s$,
- $d_j > D$,
- $N_j > 2\theta$

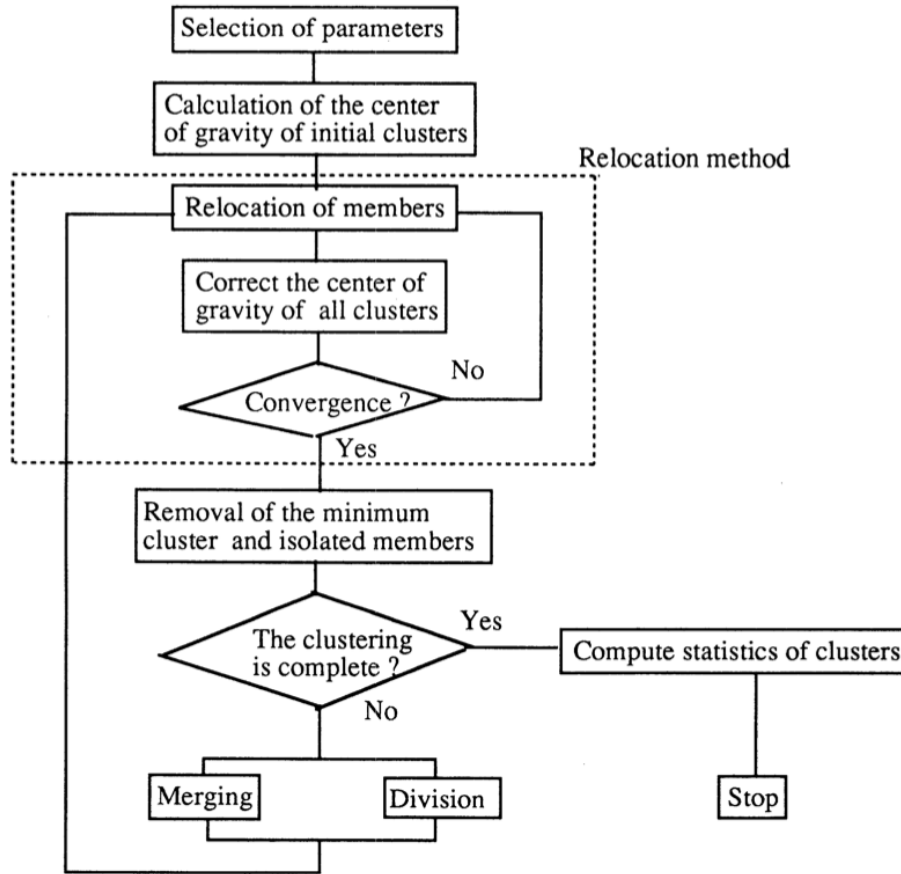


Figure 2.16: Scheme of the ISODATA algorithm (Akamatsu et al., 1996).

the two centroid Q_j^+ and Q_j^- replace Q_j , and the classes become $k + 1$. To merge the classes, distance between the centroids must be calculated. Among the distances $< \theta_c$, at most P distances are considered. They are disposed in ascending order and the classes relative to the P couples are merged, and a new centroid is calculated.

2.5.2 MINIMUM DISTANCE

The MINIMUM DISTANCE classification method is used to classify unknown image data to a class which minimizes the distance between the image data and the class in a multi-feature space (Wacker and Landgrebe, 1972; Akamatsu et al., 1996; Adams and Gillespie, 2006; Richards, 2013). Now we describe the minimum distance algorithm shown in Richards (2013). Consider the number of classes M , \mathbf{m}_i (with $i = 1, \dots, M$) the means of the M classes determined from training data, ω_i the i -th class, and \mathbf{x} the position of the pixel in the spectral space to be analyzed (Richards, 2013). The steps of the algorithm are:

1. Computation of the Euclidean distances of the unknown pixel to each of the mean class:

$$\begin{aligned} d(\mathbf{x}, \mathbf{m}_i)^2 &= (\mathbf{x} - \mathbf{m}_i)^T \cdot (\mathbf{x} - \mathbf{m}_i) = \\ &= (\mathbf{x} - \mathbf{m}_i) \cdot (\mathbf{x} - \mathbf{m}_i) = \\ &= \mathbf{x} \cdot \mathbf{x} - 2\mathbf{m}_i \cdot \mathbf{x} + \mathbf{m}_i \cdot \mathbf{m}_i \end{aligned}$$

2. Define $g(x_i) = 2\mathbf{m}_i \cdot \mathbf{x} + \mathbf{m}_i \cdot \mathbf{m}_i$, the discriminant function for the minimum distance classifier. The decision rule can be written as

$$\mathbf{x} \in \omega_i \text{ if } g_i(\mathbf{x}) > g_j(\mathbf{x}) \quad \forall i \neq j$$

The distance threshold in terms of a number of standard deviations from the class mean can be used, to ensure that a pixel is not too close to a candidate class, and also that it is within a prescribed distance of that class in spectral space (Richards, 2013).

2.6 Spectral unmixing

Spectral unmixing is a useful technique to derive information on a scene in hyperspectral data. The concept supposes that each pixel of an hyperspectral image is a physical mixture of different elements, called *endmembers*, and assumes also that the spectrum of each pixel is the linear combination of the spectrum of each endmember. The definition of endmember depends on the applications. For example, the endmembers can be different types of plants in order to discriminate the invasive plants to the other, or the grass, the trees and the soil (Bioucas-Dias et al., 2012). On the other hand, if we want to derive the mineralogical composition of a surface as in our case, we can consider different minerals as endmembers.

The mixing model can be linear or nonlinear. The linear model can be applicable if the mixing scale is macroscopic, and it is based on the approximation of single scattering between the radiation and the material (Fig. 2.17) (Bioucas-Dias et al., 2012). In this case, the endmembers are assumed to represent pure material. Many authors assume that "a proportion (abundance) is the percentage of material associated with an endmember present in the part of the scene imaged by a particular pixel. The abundances in a linear mixture represent the relative area of the corresponding endmembers in an imaged region" (Hapke, 1993; Bioucas-Dias et al., 2012).

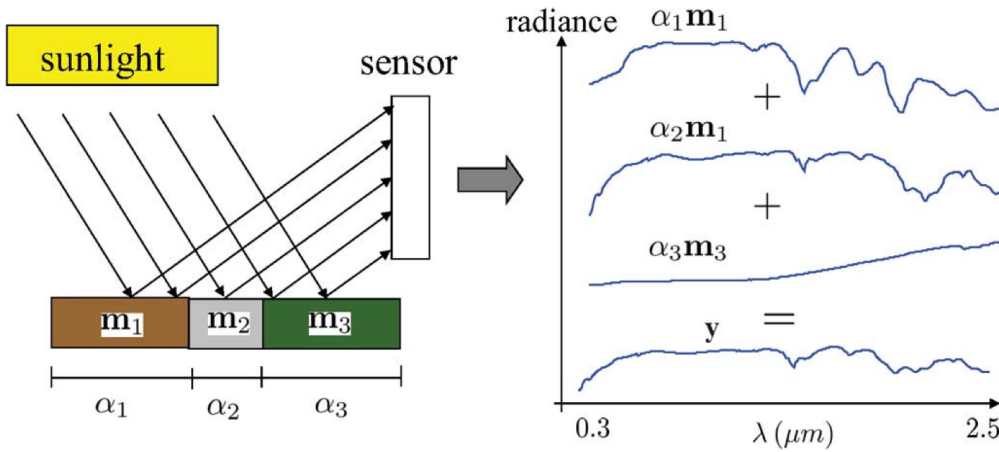


Figure 2.17: Linear unmixing concept. The radiance of each pixel is the linear combination of the different endmember (m) each one with the correspondent abundance (α) (Bioucas-Dias et al., 2012).

The nonlinear method takes into account the effects of multiple scattering due to the interaction between the radiation and the material (Fig. 2.18). The nonlinear interactions can occur at a classical, or multilayered level, or at intimate level as illustrated in Fig. 2.18 (Bioucas-Dias et al., 2012). In the first case the light scattered by one or more objects is reflected by other objects present in the scene and subsequently measured (Fig. 2.18). The second case is typical of materials homogeneously mixed. Multiple scattering occurs inside the material, photons emitted from molecules of one material interact with the molecules of another material and are emitted (Hapke, 1981, 1993; Bioucas-Dias et al., 2012). Several nonlinear mixing methods have been developed. One of the most used is the Hapke model (Hapke, 1981, 1993) (section 1.2.1).

The principal steps for hyperspectral unmixing are shown in Fig. 2.19, and consist in the atmospheric correction (if any), data dimensionality re-

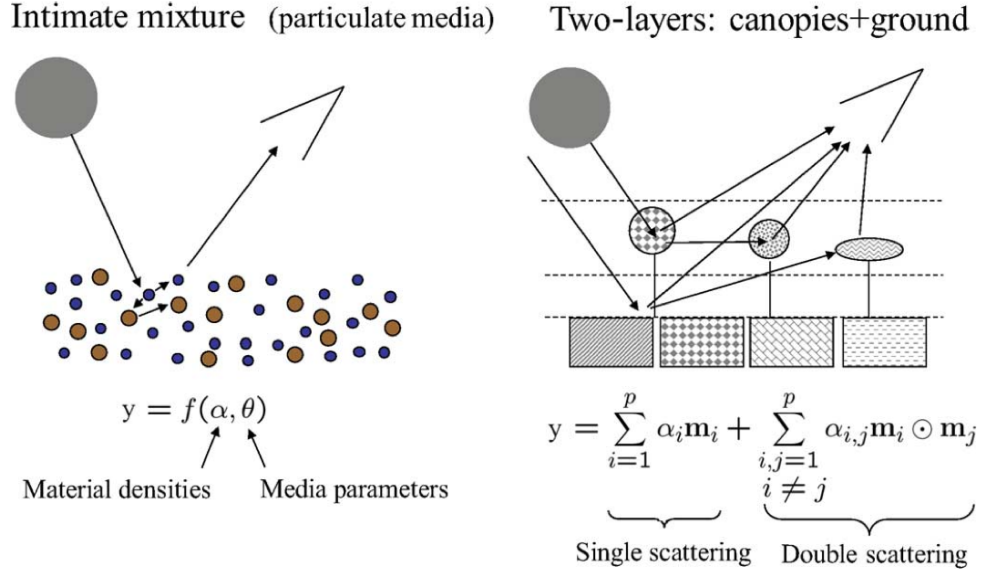


Figure 2.18: Nonlinear mixing scheme. Right. Intimate mixture scheme. Left. Multilayered scene (Bioucas-Dias et al., 2012).

duction, unmixing, i.e. identifying the endmembers in the scene and the fractional abundances at each pixel, and the inversion that consists in solving a constrained optimization problem which minimizes the residual between the observed spectral vectors and the linear space spanned by the inferred spectral signatures (Bioucas-Dias et al., 2012).

Unmixing can be approached as a geometrical problem, assuming that linearly mixed vector is in a simplex set or in a positive cone (Bioucas-Dias et al., 2012). In Fig. 2.20 is represented the concept of simplex.

Representing in a plane the pixels of two bands of a cube as shown in Fig. 2.21, if the endmembers are really representative of the scene, all the pixels must be included on in the polygon (simplex) that has the endmembers as vertex. In real case (Fig. 2.20) is not easy to define the simplex, since many pixels can be outside it, as shown in Fig. 2.21. Many classical algorithm that assume the purity pixel hypothesis are based on maximize the volume of the pixels. Other methods, such as algorithms without the pure pixel assumption, minimize the volume of the simplex (see next paragraphs) (Plaza, 2013).

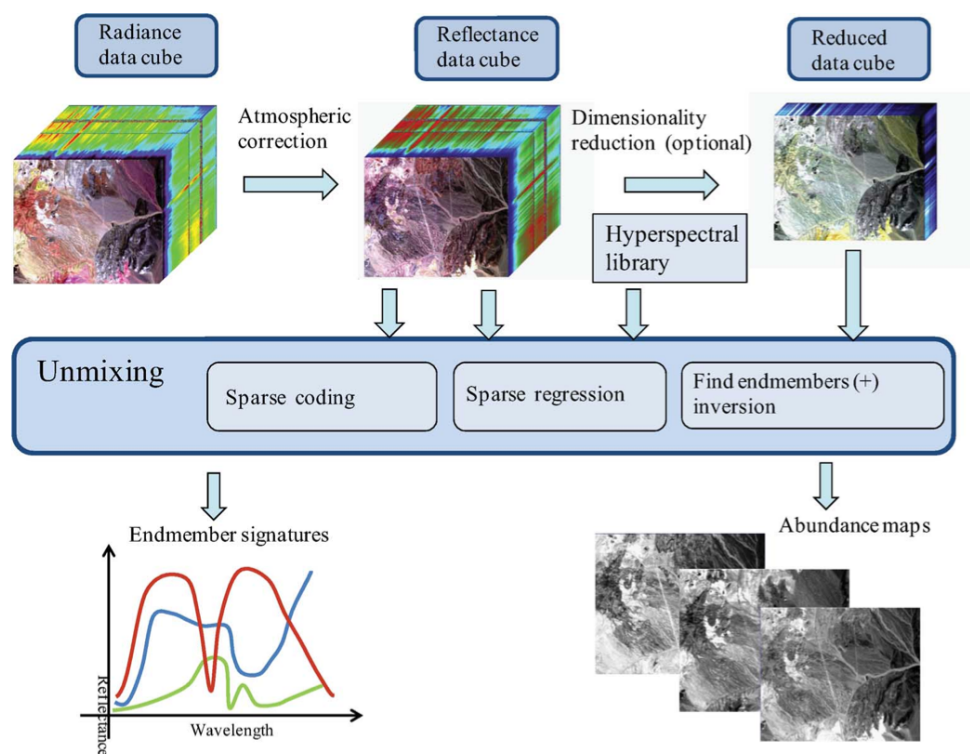


Figure 2.19: Scheme of the hyperspectral unmixing process (Bioucas-Dias et al., 2012).

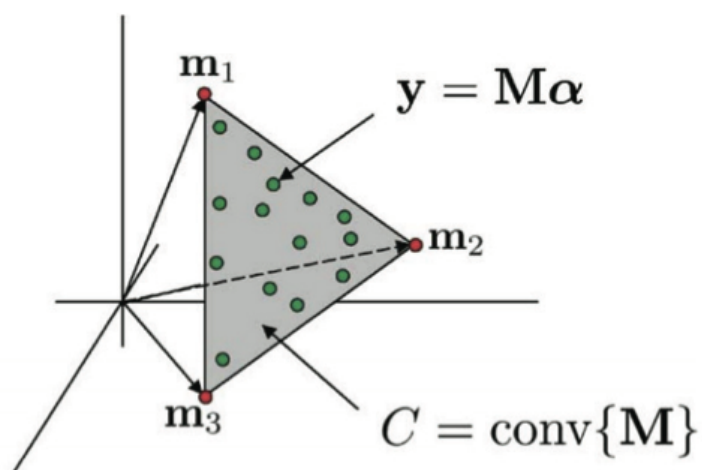


Figure 2.20: Simplex representation (Bioucas-Dias et al., 2012).

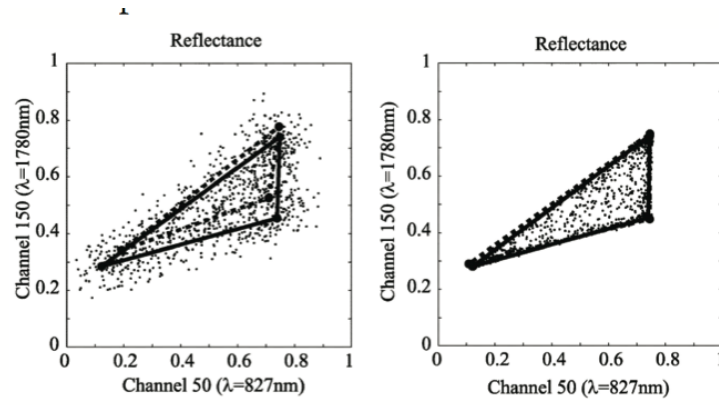


Figure 2.21: Example of simplex in the real case (Plaza, 2013).

2.7 Linear unmixing

In our work we apply linear unmixing to the bright material units on Vesta to derive their composition (Chapter 7). We neglect multiple scattering and we suppose that the surface is partitioned according to fractional abundances (Fig. 2.17). This assumption is valid because the VIR pixel size at Vesta is relatively large scale (several hundred meters). We can approximate the spectrum of each pixel as a linear mixture of endmember spectra (Adams et al., 1986; Liangrocapart and Petrou, 1998; Keshava and Mustard, 2002):

$$y_i = \sum_{j=1}^p m_{i,j} \alpha_j + w_i \quad (2.1)$$

where $m_{ij} \geq 0$ is the spectral measurement of the j -th endmember with $j \in \{1, \dots, p\}$ at the i^{th} spectral band, $\alpha_j \geq 0$ is the fractional abundance relative to the endmember j , w_i represents an additive perturbation (e.g., noise and modeling errors), and p is the number of endmembers. α_j must respect two constraints:

- Non-negativity $\alpha_j \geq 0$, $j = 1, \dots, p$;
- Sum to one $\sum_{j=1}^p \alpha_j = 1$

Sometimes the sum of the fractional abundances may be less than one. This because the algorithm cannot be able to identify all the materials present (Bioucas-Dias et al., 2012). It is not clear whether it is better to relax the constraint or to simply consider that part of the modeling error (Bioucas-Dias et al., 2012).

Formula 2.1 can be written in vectorial shape

$$\mathbf{y} = \mathbf{M}\alpha + \mathbf{w} \quad (2.2)$$

where $\mathbf{y} \in \mathbb{R}^B$ is the spectrum of the j th endmember, $\mathbf{M} \equiv [m_1, \dots, m_p]^T$ is the mixing matrix containing the signatures of the endmembers present in the covered area, α is the vector of the abundances, and $\mathbf{w} \equiv [w_1, \dots, w_p]^T$ the error (Bioucas-Dias et al., 2012).

2.8 Estimation of the number of endmembers

There are several techniques to determine the number of endmembers (Plaza, 2013). Here we give a brief description of the principal methods (Plaza, 2013; Somers et al., 2012).

- **Classic methods for subspace estimation.** A possible method to estimate the endmember is to take into account the intrinsic dimensionality of the data, i.e. the minimum number of parameters that take into account the properties of the data. Principal component analysis (PCA) can be a good method to derive the number of endmembers. The data are transformed in a new coordinate system, and the number of significant components gives the number of endmember.
- **Virtual dimensionality (VD).** Estimates the number of source present in given dataset in not so easy. VD method is used in presence of unknown signal sources. This method is based on the "pigeon-hole principle". The signal (our data) is represented by pigeon in which the signal source are represented by a pigeon, while a spectral band by a hole. The goal is associate a signal source to a spectral band. To verify if the signal source is detected in the remote sensed spectral band, the difference between data-correlation eigenvalues and covariance matrices eigenvalues (PF parameter) is calculated. If the PF parameter is positive, the signal source is present (Chang and Du, 2004; Chang, 2009; Plaza, 2013).
- **Hyperspectral subspace identification minimum error (HySime)** is based on finding the first k eigenvectors that contain most of data information. The k eigenvectors are those such that the mean square error (MSE) between remote sensed data and its projection onto the eigenvector subspace is minimum (Bioucas-Dias and Nascimento, 2008; Plaza, 2013).
- **Eigenvalue likelihood maximization (ELM)** is a fully automatic method, based on the VD concept. The eigenvalues of the noise are the same for the covariance and the correlation matrices, and the eigenvalues corresponding to the signal (the endmembers) that are larger in the correlation matrix than in the covariance matrix (Bin Luo et al., 2013; Plaza, 2013).
- **Normal compositional model (NCM)** assumes that in the remote sensed data no pure pixels are present, and the pixels of an hyperspectral image are the linear combinations of an unknown number of random endmembers (Eches et al., 2010)

2.9 Endmember extraction

After deriving the number of endmembers it is necessary to determine the endmember. Here we illustrate the principal methods for the endmember extraction.

- **Classic method.** In the classical method the endmembers are derived directly from the original data. This method consists of three steps: dimensional reduction, endmember selection and abundances estimation (Plaza, 2013). Here we illustrate the principal methods for the endmembers extraction.
 - *The pixel purity index (PPI)* is one of the most popular endmember extraction algorithms, and it is available in several software packages such as ENVI. It is based on the assumption that an endmember is an idealized pure signature for a class (Boardman et al., 1995).
 - *The N-FINDER algorithm* is another very popular algorithm for endmember extraction, also present in most software packages. It based on the assumption of the presence of pure pixels in the original hyperspectral scene and further maximizes the volume that can be formed with pixel vectors in the data cube. (Winter, 1999).
 - *Vertex component analysis (VCA)* is an iterative method, based on the projection of data onto a direction orthogonal to the subspace spanned by the endmembers which have been already determined (Nascimento and Bioucas-Dias, 2005).
- **Spatial-spectral endmember extraction** takes into account spatial and spectral information. The spatial information can be useful in the selection of endmembers, for instance, in homogeneous areas (Plaza, 2013). Several algorithms exist that use both spatial and spectral information. Here is a brief description of the principal methods:
 - *The automatic morphological endmember extraction (AMEE)* uses extended morphological transformations to integrate spatial and spectral information. This method is based on the spectral purity (eccentricity) of the pixels in spectral space. Extended morphological transformations of erosion and dilation are defined to look for the most spectrally pure and the most highly mixed pixels in

spatial neighborhoods (Plaza et al., 2002; Plaza, 2013). The algorithm performs multi-scale morphological processing using structuring elements of increased size in order to derive spatial-spectral information, and a morphological eccentricity index (MEI) at a pixel level. Mean spectra after adaptative region-growing are selected as final endmembers (Plaza et al., 2002; Plaza, 2013).

- *The spatial-spectral endmember extraction (SSEE)*. The image is processed using a local search window and applies singular value decomposition (SVD) to determine a set of eigenvectors that describe most of the spectral variance in the window (Plaza, 2013; Rogge et al., 2007). Eigenvectors of the image data have been calculated to determine candidate endmember pixels. The spatial constraints have been used to extract endmembers from spectrally similar candidate endmember pixels (Rogge et al., 2007; Plaza, 2013)
- *Spatial preprocessing prior to endmember extraction*. Spatial information can be included as a preprocessing module in spectral-based algorithms for endmember extraction (Zortea and Plaza, 2009; Plaza, 2013). Using this approach it is possible to obtain a spatial homogeneity index which is relatively insensitive to the noise present in the hyperspectral data (using Gaussian filtering) (Zortea and Plaza, 2009; Plaza, 2013). A set of pure regions used to look for endmembers are derived merging this index with a spectral-based classification (Martinez and Plaza, 2012).
- **Algorithms without the pure pixel assumption.** Commonly a pixel of an hyperspectral image does not contain a pure signature, and the pixels are located outside the simplex as shown in Fig. 2.21. Unlike classical methods, algorithms without the pure pixel assumption are based on minimizing the volume that encloses all observations. Below we list the main algorithm base on this principle (Hendrix et al., 2012).
 - **Minimum volume algorithms.** Endmembers extraction is done minimizing the reconstruction error and the volume term. The principal algorithms are the Iterative Constrained Endmembers (ICE), the Minimum Volume Transform-Nonnegative Matrix Factorization (MVC-NMF) methods, and the Sparsity-Promoting ICE (SPICE) which is an extension of the ICE algorithm (Berman et al., 2004; Miao and Qi, 2007; Zare and Gader, 2007).
 - **Statistical algorithms** When the data are highly mixed, minimum volume algorithms fail and it is necessary to use a statistical

framework as Bayesian inference. The most famous algorithms are the independent component analysis (ICA) and the dependent component analysis (DECA) algorithm (Bioucas-Dias et al., 2012).

2.9.1 Method used for the VIR data on board Dawn

Here we describe the unmixing method used for the VIR data. VIR, the spectrometer on board Dawn (see section 3.9) (De Sanctis et al., 2011; Russell and Raymond, 2011) produces data in a spectral range between $0.25\text{-}5\mu\text{m}$ (De Sanctis et al., 2011). Vesta mineralogy is known and it was largely discussed in many works, e.g. McCord et al. (1970); Feierberg and Drake (1980); De Sanctis et al. (2012a, 2013); Ammannito et al. (2013a). We are interested to estimate the abundance of the main mineralogical phases present on Vesta. At a large scale Vesta is characterized by spectra similar to those of the HED meteorites. Moreover other mineralogical phases, such as olivine and hydrate minerals, exist. In Chapter 7 we demonstrated that linear unmixing gives good results, combining eucrite, diogenite, and olivine, so we create a spectral library containing many of these spectra. As a first approach we choose two endmembers, and to choose the right ones we perform all the possible combinations of two spectra contained in the spectral library. We choose as a best fit those with the minimum χ^2 . In this way the algorithm automatically chooses the endmembers. Even if the results obtained with two endmembers are good, we need at least one other endmember to represent Vesta mineralogy. The limit of this method is high calculation time. Currently, we are exploring a ways to reduce the computation time to increase the number of endmembers. In Chapter 7 we show the results obtaining applying this method.

Chapter 3

Messenger and Dawn missions

In this Chapter we give an overview of the Dawn and Messenger (Mercury Surface, Space ENvironment, GEochemistry and Ranging) missions. Dawn is the first mission dedicated to the exploration of the two largest asteroids in the main belt: Vesta and Ceres (the last one recently reclassified as a dwarf planet). Messenger was the first mission to orbit around Mercury. Both Dawn and Messenger belong to the NASA discovery program. Dawn completed its journey around Vesta and is now going to Ceres, where it will arrive in the spring of 2015. And Messenger has now mapped the entire Mercury surface. In July 2016 is scheduled the launch of Bepi Colombo, the first European mission to Mercury, which help to answer some unsolved questions about Mercury. Here we describe in more detail the MDIS and MASCS instruments onboard Messenger and VIR, the Dawn spectrometer, which provided the data analyzed in the next chapters.

3.1 The Dawn Mission

The principal goal of the Dawn mission is to understand the processes occurring in the early Solar System as Vesta and Ceres formed and evolved, allowing us to understand the earliest epoch of the Solar System and the growth of protoplanets (Russell and Raymond, 2011).

Dawn arrived on Vesta in July 2011 and departed toward Ceres in September 2012, where its arrival is expected in the spring of 2015. The Dawn mission is divided into three principal phases, based on the altitude of the spacecraft with respect to the asteroid. These are called: Survey, HAMO (High Altitude Mapping Orbit), and LAMO (Low Altitude Mapping Orbit). The altitude of the spacecraft during the single phase changes for Vesta and Ceres. In Fig. 3.1 we show a summary of the mission phases for Vesta, while

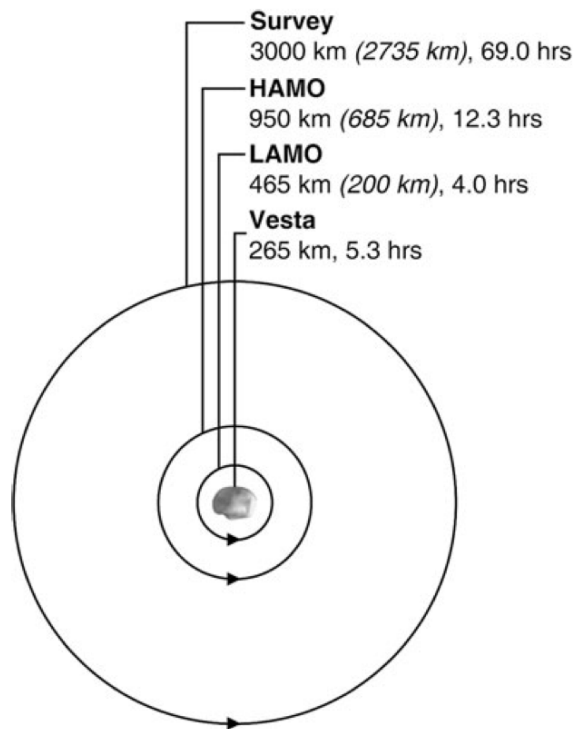


Figure 3.1: Vesta phases of the mission divided for the spacecraft altitude (Russell and Raymond, 2011).

Fig. 3.2 illustrates all the details of the Vesta's phases of the mission (Russell and Raymond, 2011). For Vesta it was possible to extend the mission with a second HAMO phase (called HAMO-2). This will not be possible for the Ceres because of the lack of hydrazine.

Science phase	Acronym	VIR start date	VIR stop date	Altitude (km)	Lat (°)	Pixel res. (km)	Φ (°)	r (AU)
Approach	VSA	Jul 23, 2011	Aug 6, 2011	2707-5497	70.0°S-59.2°N	0.677-1.374	7.85-68.5	2.230-2.242
Survey	VSS	Aug 12, 2011	Aug 31, 2011	2704-2874	90.0°S-44.6°N	0.676-0.719	12.2-78.1	2.246-2.263
HAMO	VSH	Sep 30, 2011	Oct 31, 2011	660-820	82.9°S-45.8°N	0.165-0.205	28.2-82.8	2.291-2.322
LAMO	VSL	Jan 8, 2012	Apr 29, 2012	172-298	90.0°S-26.1°N	0.043-0.075	44.9-96.0	2.390-2.488
HAMO-2	VH2	Jun 15, 2012	Jul 24, 2012	644-825	80.9°-70.7°N	0.161-0.206	27.9-66.8	2.520-2.541

Figure 3.2: Details of phases of the mission for Vesta (Russell and Raymond, 2011).

3.1.1 The Dawn spacecraft

The Dawn spacecraft contains three scientific instruments: the Framing Camera (FC), the Visible and InfraRed spectrometer (VIR) and the Gamma Ray and Neutron Detector (GRaND), with low and high gain antennas and a solar array, which provide energy for all onboard systems, including the ion propulsion system (Fig. 3.3). All these instruments are able to satisfy the main targets of the mission. The ion propulsion system of Dawn is an innovative technology. It was tested in NASA's Deep Space 1 mission, and it was fundamental for the success of the mission. Thanks to the ion propulsion system it was possible to use 10 times less propellant, reducing the spacecraft dimension (Russell and Raymond (2011), http://dawn.jpl.nasa.gov/technology/ion_prop.asp). Here we describe the scientific payload of Dawn.

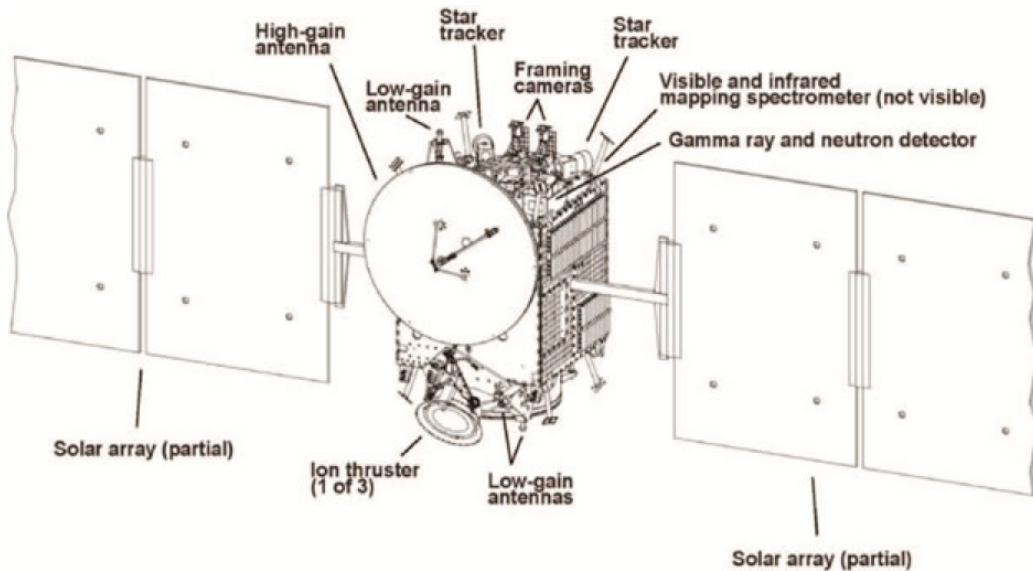


Figure 3.3: Global view of the Dawn spacecraft <http://dawn.jpl.nasa.gov/technology/spacecraft.asp>.

3.1.2 Dawn Gamma Ray and Neutron Detector (GRaND)

GRaND, the Dawn Gamma Ray and Neutron Detector has been developed by the Los Alamos National Laboratory (LANL) (Fig. 1.4). It maps the surface elemental composition of Vesta at different spatial scales depending on the spacecraft altitude (Fig. 3.4). It mapped the surface elemental composition of Vesta at different spatial scale depending on the spacecraft altitude (Prettyman et al., 2011). The target is to measure the constituents of the silicate and oxides minerals, such as O, Mg, Al, Si, K, Ca, Ti, Fe, Ni, U, Th and ices, e.g. H, C, N. GRaND is a deck-mounted instrument, designed to survive about 10 years. It consists of 21 sensors, arranged to separately measure planetary gamma rays and neutrons from backgrounds originating from the spacecraft and space environment (Prettyman et al., 2011).

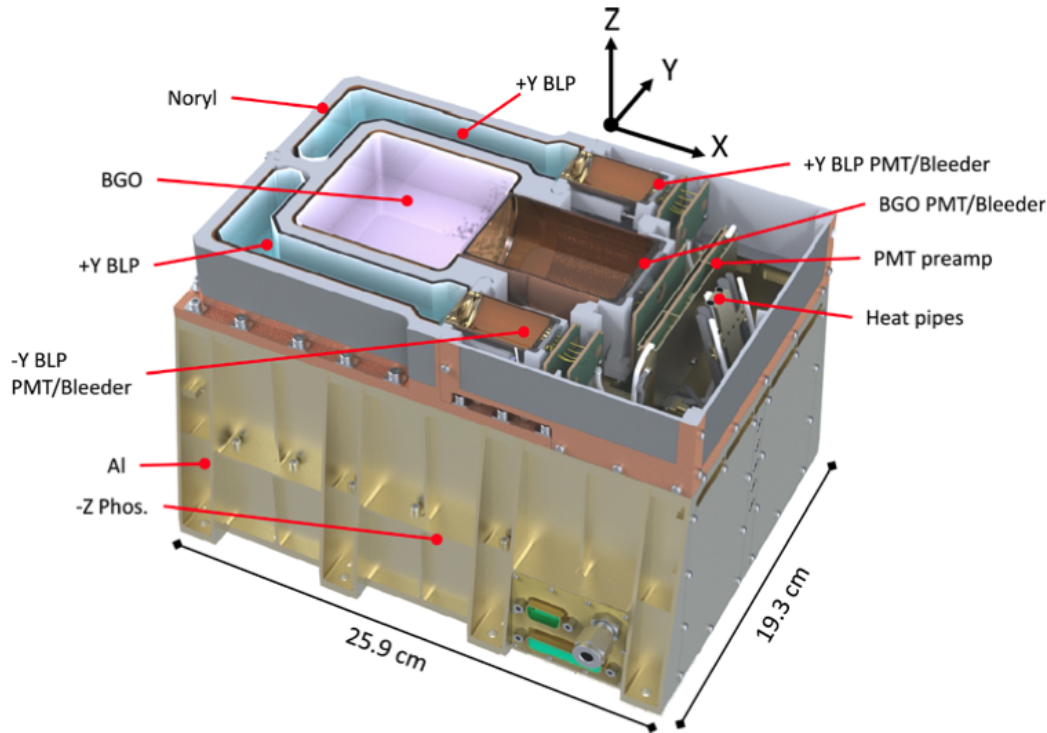


Figure 3.4: Representation of GRaND (Prettyman et al., 2011).

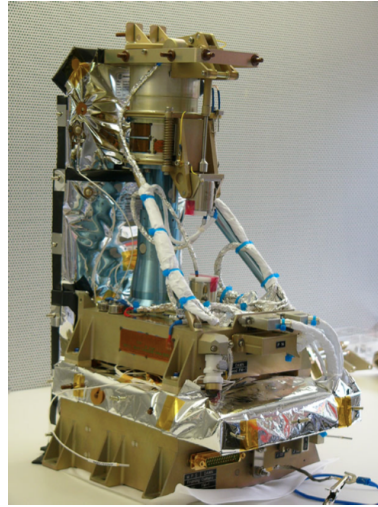


Figure 3.5: Dawn framing camera (Sierks et al., 2011).

3.1.3 Framing Camera (FC)

The Dawn camera is the German instrument onboard Dawn (Fig. 3.5). It consists of two principal components: the Camera Head (CH) and the Electronic Box (E-Box). The E-Box contains the electronics for the Data Processing Unit (DPU), the Power Converter Unit (PCU), and the Mechanism Controller Unit (MCU). The camera head contains the CCD, the electronics for CCD operation and readout (Front-End Electronics, FEE), the filter-wheel mechanism, and is thermally insulated from the E-Box. The lens system is located in the lens barrel mounted on the camera head (Sierks et al., 2011). The optical system is composed of four lenses (Fig. 3.7) that are derived from a triplet with a split third lens to allow telecentricity in image space (Sierks et al., 2011). The focal plane (CCD) is located below the lens, while the filter-wheel is positioned between the lens system and the CCD. The filter-wheel contains eight filters that cover a range of wavelength between 400 and 1050 nm. In Fig. 3.8 we illustrate the filters characteristics. The design is optimized to reduce the distortion (Fig. 3.6) (Sierks et al., 2011). The main goals of the FC are map the topography of the targets, reconstruct the global shape of the asteroids, produce a Digital Terrain Model (DTM), and study the geology of Vesta and Ceres, to contribute to understanding the internal structure and give information on the mineralogy.

Item	Specification
Focal Length	150 mm
F-Number	7.5
Encircled Energy	>80% inside a pixel of 14 μm sq.
BFL	19 mm
Focal Shift	<20 μm wrt. channel 4
Field of View	$5.5^\circ \times 5.5^\circ$
IFOV	93.7 μrad
Field Curvature	<10 μm
Distortion	<0.1%
Spectral Range	400–1050 nm
Spectral Transmission	>75%

Figure 3.6: Dawn framing camera characteristics (Sierks et al., 2011).

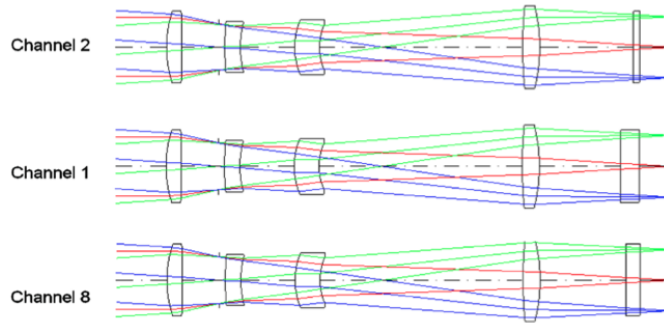


Figure 3.7: Scheme of the Framing Camera optical system (Sierks et al., 2011).

Channel No.	Center wavelength [nm]	Bandwidth [nm]	Trans-mission [%]	Filter-wheel position	Thickness [mm]
1	polychromatic	450 \pm 10 to 920 \pm 10	98	F1	6.00 \pm 0.05
2	430 \pm 2	40 \pm 5	>75	F8	2.00 \pm 0.05
3	550 \pm 2	40 \pm 5	>75	F2	5.90 \pm 0.05
4	650 \pm 2	40 \pm 5	>75	F7	6.60 \pm 0.05
5	750 \pm 2	40 \pm 5	>75	F3	6.40 \pm 0.05
6	830 \pm 2	40 \pm 5	>75	F6	5.90 \pm 0.05
7	920 \pm 2	40 \pm 5	>75	F4	5.30 \pm 0.05
8	980 \pm 2	80 \pm 5	>75	F5	4.80 \pm 0.05

Figure 3.8: Framing camera filter specification (Sierks et al., 2011).

3.1.4 Visible and Infrared spectrometer (VIR)

VIR is the Visible and Infrared spectrometer of Dawn (Fig. 3.9), and it is the Italian contribution to the Dawn mission. VIR is an hyperspectral spectrometer and it is similar to VIRTIS onboard Rosetta and VenusExpress. These instruments follow the optical layout of Cassini/VIMS-V (De Sanctis et al., 2011). VIR has 864 bands, and it is composed of two channels, one for the visible ($0.25\text{--}1.05\ \mu\text{m}$) and one for the infrared ($1\text{--}5.0\ \mu\text{m}$), each channel containing 432 bands (De Sanctis et al., 2011). The visible spectral resolution ($\Delta\lambda_{VIS} = 1.8\ \text{nm/band}$) is higher than the infrared channel ($\Delta\lambda_{IR} = 9.8\ \text{nm/band}$). In Fig. 3.10 we illustrate the VIR characteristics (De Sanctis et al., 2011).

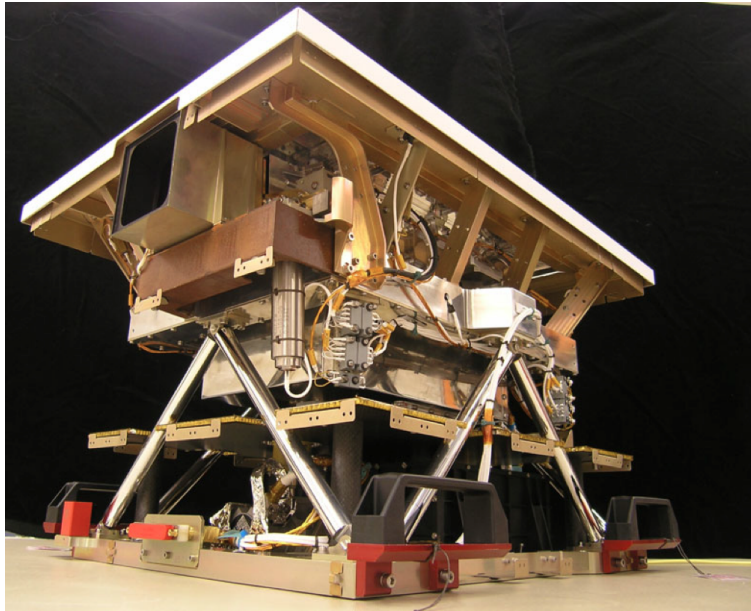


Figure 3.9: VIR (De Sanctis et al., 2011).

VIR has several scientific targets:

- Identify different materials and mixtures and determine their spatial distribution.
- Identify the silicates, hydrates and other minerals.
- Determine the overall continuum slopes of the spectra.
- Map the presence and extent of space weather.

- Produce high resolution maps of the asteroids to determine the spatial distribution of the various mineralogical types and their mixtures
- Determine the physical microstructure and nature of the surface particles by measuring the spectrophotometric phase curve.

The main goals set for Vesta are:

- Confirm of the link between Vesta and the HED meteorites.
- Obtain the first in-depth view of a planetary interior through the spectral imaging of Vesta's wide and deep impact basin.
- Mineralogical mapping at different spatial resolution of Vesta.
- Confirm of the presence of hydrated minerals.

- Detect of the presence of olivine.

The main targets for Ceres include:

- Investigate Ceres primitive surface mineralogy.
- Identify of water-bearing minerals and clay-like material.
- Identify of possible ices and map frost-covered regions.
- Detect very weak atmosphere and frost.
- Correlate surface mineralogy with the small albedo variation.

VIR is composed of several modules:

- The **Optical Head** is made of a telescope, a scanning mirror, a spectrometer, a grating and a focal plane. The telescope is in a Shafer configuration (Fig. 3.11). The primary mirror (M1) is concave and it is placed on a scan mechanism that allows it to move at steps of 250 μ rad along the slit direction (De Sanctis et al., 2011). The radiation reflected by M1 hits the convex secondary mirror (M2), and the beam reflected by M2 hits the mirror M3 to enter in the Offner configuration composed by two spherical mirrors (M4 and M5) (Fig. 3.12). The mirror M5 is placed on the optical axis, and the beam is reflected two times on M4. After the second reflection the beam is focused on a slit. The beam is reflected by the Offner mirror M6 and dispersed by the diffraction convex grating, it is again reflected by M6 mirror and sent on the focal plane (Fig. 3.12). In Fig. 3.13 we show the path of a beam

VIR main characteristics		VIR VIS	VIR IR
<i>Spectral Performances</i>	Spectral range	0.25–1.05 μm	1.0–5.0 μm
	Spectral sampling (high res)	1.8 nm/band (432 bands)	9.8 nm/band (432 bands)
	Spectral resolution $\lambda/\Delta\lambda$	100–380	70–360
<i>Spatial Performances</i>	IFOV (high res)	250 \times 250 μrad	
	FOV (high res)	64 \times 64 mrad	
<i>Telescope</i>	Configuration	Shafer with Offner relay	
	Pupil area	5.77 cm^2	17.71 cm^2
	Pupil diameter	27.1 mm	47.5 mm
	Focal length	152 mm	
	f/#	5.6	3.2
<i>Spectrometer</i>	A Ω	3.6 $\times 10^{-11}$ $\text{m}^2 \text{sr}$	7.5 $\times 10^{-11}$ $\text{m}^2 \text{sr}$
	Configuration	Offner	
	Slit dimensions	38 $\mu\text{m} \times$ 9.53 mm	
	Grating grooves density	267.9 mm^{-1}	53.8 mm^{-1}
	Dispersion on focal plane	52.6 nm/mm	263.1 nm/mm
<i>Focal Planes</i>	Type	CCD Thomson TH7896	HgCdTe Raytheon
	Active size	1024 \times 508 pixels	435 \times 270 pixels
	Frame size	432 \times 256 (bands \times sample)	
	Elemental pixel size	19 \times 19 μm	38 \times 38 μm
	Acquired pixel size	38 \times 38 μm	
	Full well capacity	10 ⁶ e [−]	2 \times 10 ⁶ el
	Readout noise	2 ADU	
	Dark current	<1 e [−] /s	<10 fA (@70 K)
	A/D converter	16 bit	
	Repetition time	5–20–60 s	
<i>Operative Temperature</i>	Focal plane	150–190 K	65–90 K
	Telescope and spectrometer	100–150 K	
<i>Mass</i>	Optical Head and ME	20 kg	
<i>Power</i>	Average power	52 W	

Figure 3.10: VIR principal characteristics (De Sanctis et al., 2011).

in the VIR optical head (De Sanctis et al., 2011).

The grating (Fig. 3.14) is realized on a convex NG5 glass element. It is designed to disperse with optimal efficiency the light in the range of the wavelength 0.25–5 μm . It is done using two concentric circles (Rowland's circles). It is designed with rectangular-shaped grooves with a linear density of 267.9 mm^{-1} . The internal circle (Fig. 3.14) corresponds to 33% of the surface dispersing the light in the visible range the remaining 67% is dedicated to the infrared (Fig. 3.14) (De Sanctis et al., 2011). The focal plane has two detectors: the visible sensor is a 1024X1024 pixels CCD (by Thomson) with frame transfer design, while the IR sensor is a HgCdTe array.

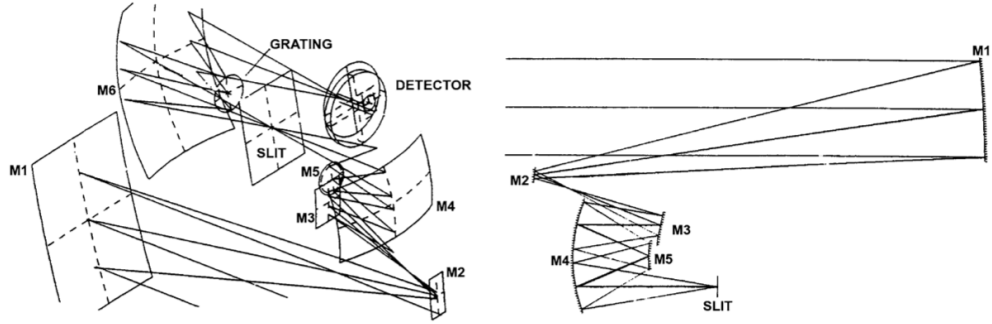


Figure 3.11: Right. Scheme of the Shafer configuration in VIR telescope. Left. VIR optical layout (De Sanctis et al., 2011).

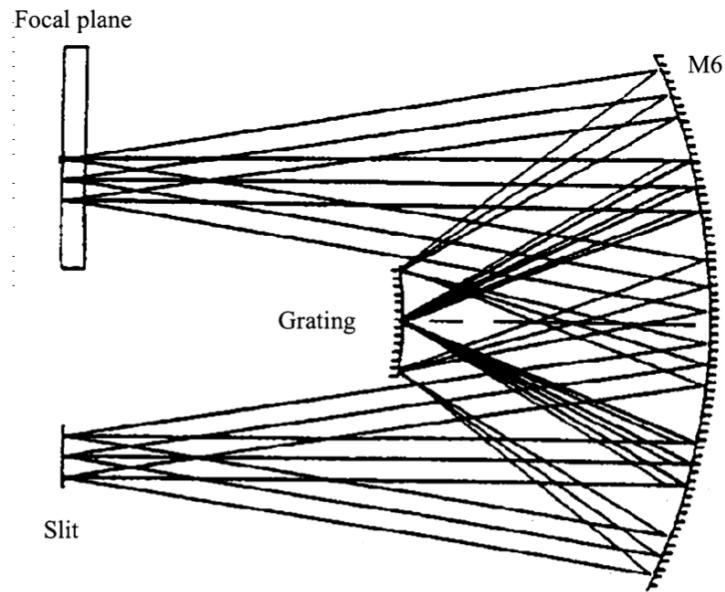


Figure 3.12: Scheme of the Offner configuration for VIR (De Sanctis et al., 2011).

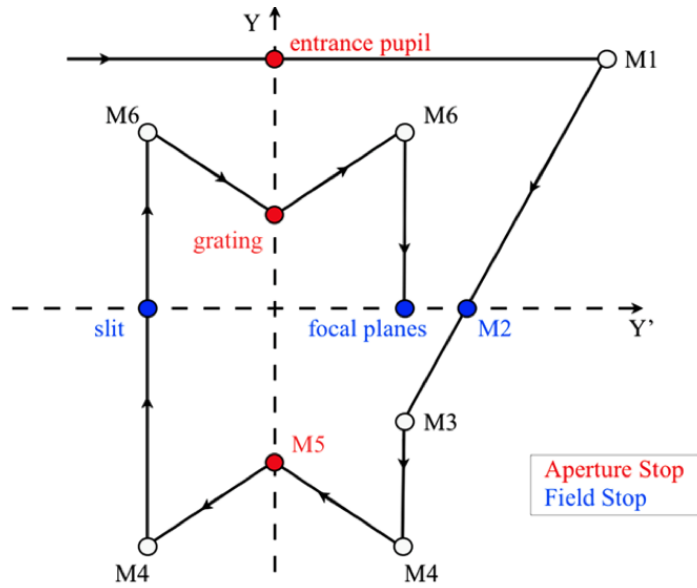


Figure 3.13: Scheme of a beam inside VIR telescope (De Sanctis et al., 2011).

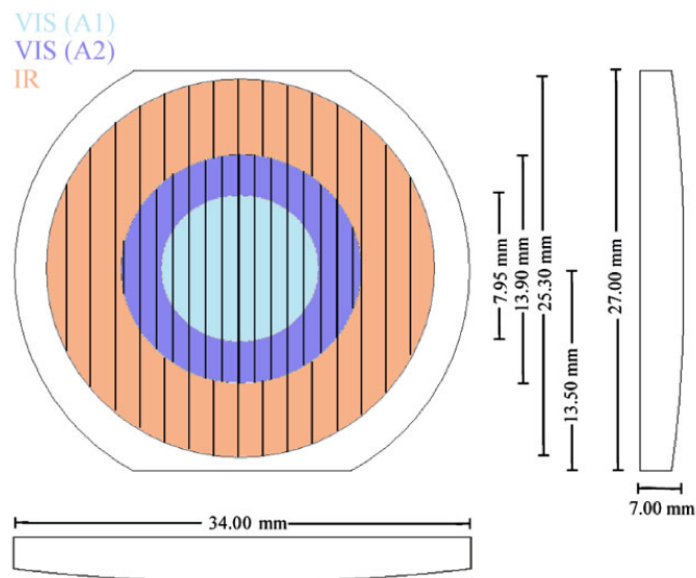


Figure 3.14: VIR grating (De Sanctis et al., 2011).

- **Thermal Control.** The right operative temperature is guaranteed by two different systems. VIR is equipped with an external radiator placed on top of the optical head that allows it to have an operative temperature around 130-150 K. The visible sensor is cooled at 150 K, while the infrared needs an operative temperature of 70-80K. To achieve these temperatures, it was necessary to equip VIR with a cryocooler located below the optical bench (De Sanctis et al., 2011).
- The **Internal Calibration Unit** is necessary to verify the accuracy of the spectral registration, verify the stability of the flatfield, monitor the evolution of the defective pixels, and check the relative stability of the radiometric response. This unit is composed of two lamps designed to optimize a high flux for both the visible and infrared channels. The lamps are composed of a paraboloid concentrator in titanium which contains a filament in tungsten. This lamp can be used to illuminate the internal side of the cover. The internal calibration sequence can be produced combining the use of cover and shutter and switching on-off the lamp (De Sanctis et al., 2011).
- **Electronics Modules.** VIR has two electronic modules: the Proximity Electronics Module (PEM) and the Main Electronics (ME). The PEM is located close to the optical head, and it allows it to command, read and digitalize the signals coming from the two focal planes, to generate the housekeeping data, and to command the scan unit mechanism and the cover's actuator. ME is placed in the internal bay of the spacecraft, and it commands and monitors the instrument subsystems (De Sanctis et al., 2011).

3.2 VIR data

VIR data are hyperspectral cubes (section 1.3). They are 3D arrays with each pixel corresponding to a spectrum (Fig. 3.15). VIR acquires data in pushbroom mode (section 1.3), or using the scanning mirror, and it is able to acquired million spectra, allowing a good coverage of the surface. *Raw data* are formed by a core structure, which stores the scientific data, and a side-plane, which stores all the instrument housekeeping informations related to each frame (De Sanctis et al., 2011). *Calibrated data* contain a core with acquisitions in radiance physical units ($\text{Wm}^{-2}\mu\text{m}^{-1}\text{sr}^{-1}$). The side-plane contains also the SCET (SpaceCraft Elapsed Time) computed for the central time of each acquisition (Fig. 3.15). The last three planes of a cube contain information about the calibration processes. Both raw and calibrated date are available in PDS format. VIR data have been calibrated by the VIR team and are available in the PDS node small bodies (http://sbn.pds.nasa.gov/data_sb/missions/dawn/index.shtml) (De Sanctis et al., 2011).

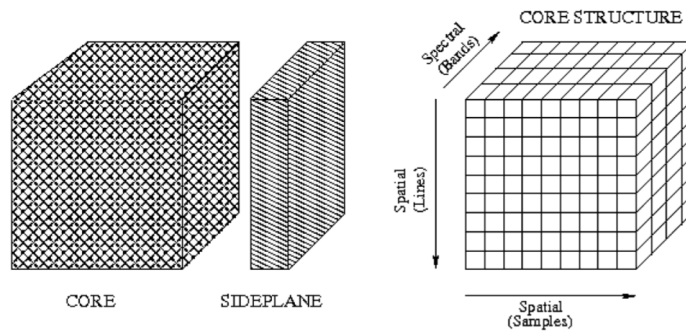


Figure 3.15: Scheme of a VIR cube (De Sanctis et al., 2011).

3.3 The Messenger mission

Messenger (Mercury Surface, Space ENvironment, GEochemistry and Ranging) is one of the NASA discovery missions. It was launched 3 August 2004 and it entered orbit around Mercury in March 2011. During its journey, the spacecraft carries out several flybys: one of the earth, two of Venus and three of Mercury. Fig. 3.16 shows the Messenger journey (<http://messenger.jhuapl.edu>).

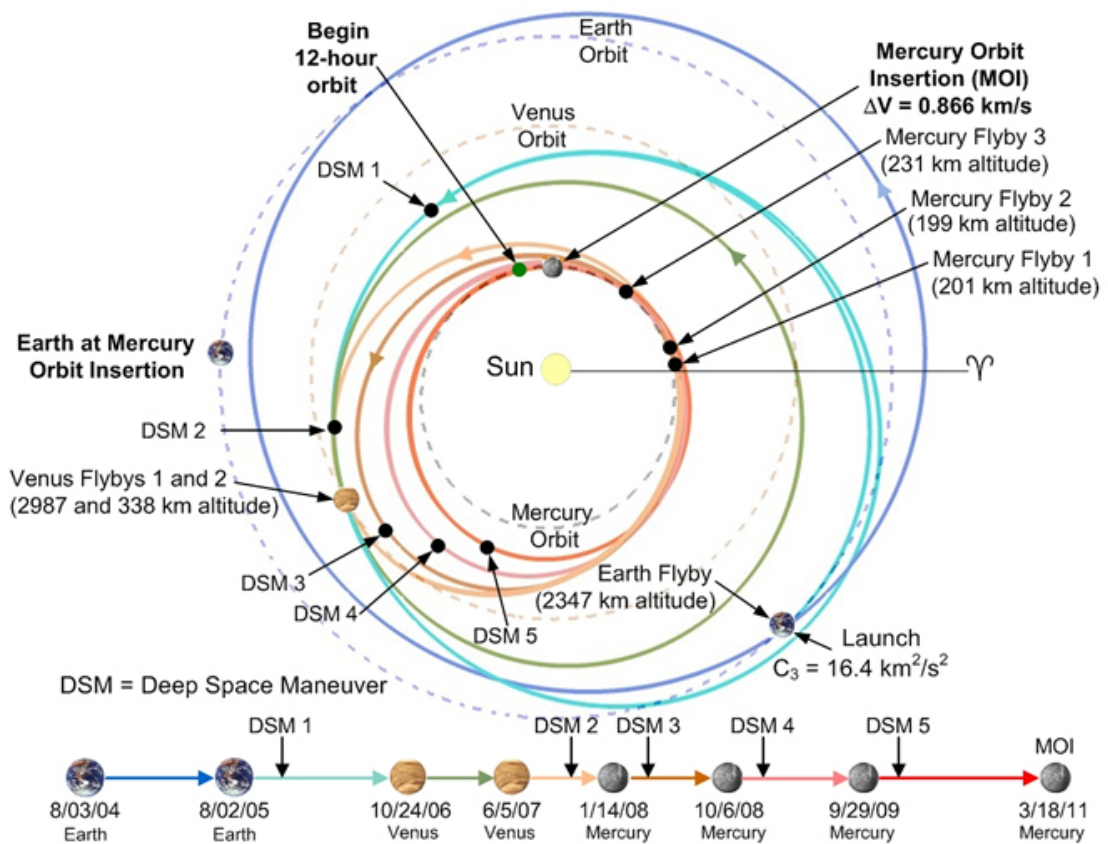


Figure 3.16: Journey stages of Messenger (<http://messenger.jhuapl.edu>).

3.3.1 The spacecraft

The design and the fabrication of the spacecraft was performed by the *John Hopkins University Applied Physics Laboratory*. The principal problem faced during the design phase was to find an efficient and economical way to protect the spacecraft from extreme temperatures. In fact in the vicinity of the planet, the spacecraft can exceed the 400°C . Therefore engineers and scientists planned for a carbon structure heat-resistant material and at the same time for light. Moreover, they have adopted devices such as shields and ceramic heat radiators, to minimize the exposure time in the hotter regions, avoiding complicated and expensive cooling systems <http://messenger.jhuapl.edu>). The spacecraft (Fig. (3.17)) measures $1.9 \times 1.4 \times 1.3$ m e with a weight of 1100 kg, including 600 kg fuel used for orbital maneuvers <http://messenger.jhuapl.edu/spacecraft/overview.html>). It is equipped with:

- Solar panels with a surface of 2.5 mq.
- A sunscreen of 2.5 m x 2 m.
- A propulsion system.
- Communication systems.
- Drive and control systems.
- An electronic system for data management.

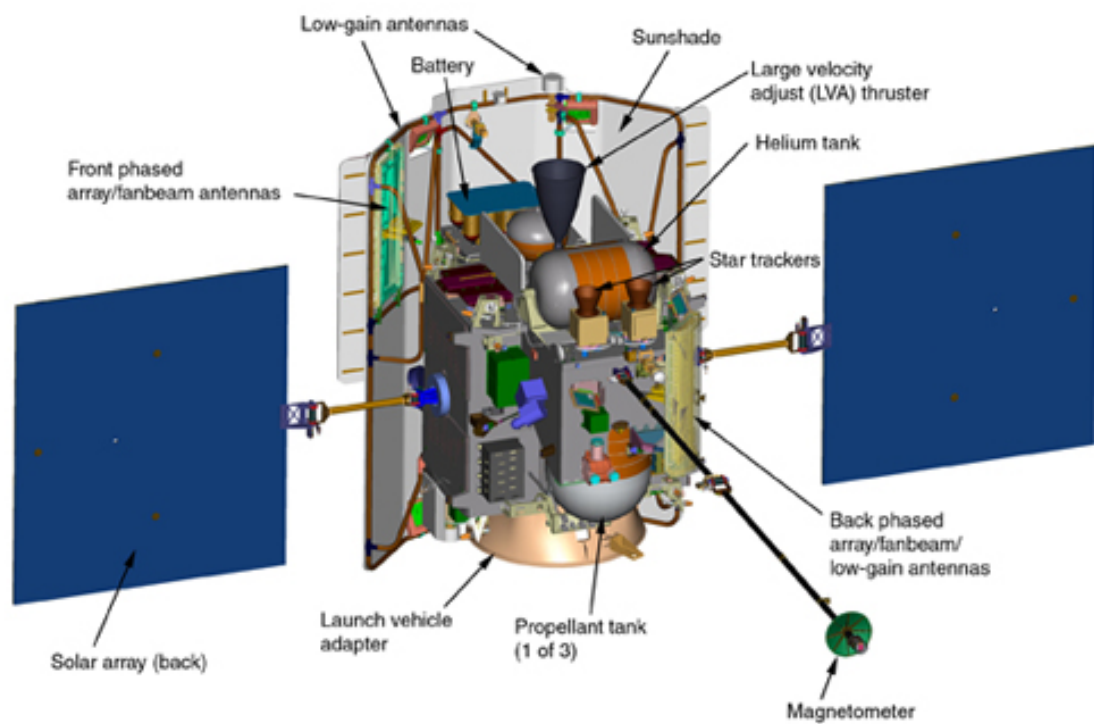


Figure 3.17: Representation of the Messenger spacecraft (<http://messenger.jhuapl.edu/spacecraft/overview.html>).

3.3.2 Scientific instruments

The payload (Fig. 3.18) contains seven scientific instruments:

- MDIS (Mercury Dual Imaging System),
- GRNS (Gamma-Ray and Neutron Spectrometer),
- XRS (X-Ray Spectrometer), MAG (Magnetometer),
- MLA (Mercury Laser Altimeter),
- EPPS (Energetic Particle and Plasma Spectrometer) ,
- MASCS (Mercury Atmospheric and Surface Composition Spectrometer).

In the next sections we discuss only the instruments that provided the data analyzed.

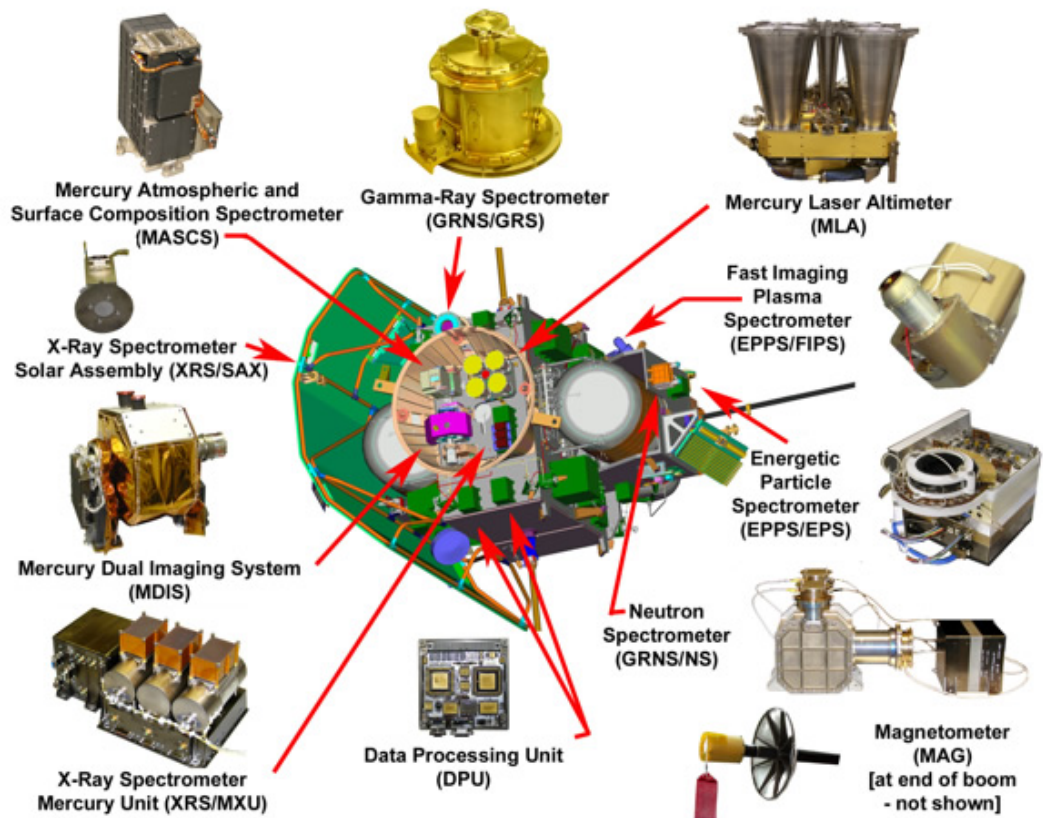


Figure 3.18: Messenger Payload (<http://messenger.jhuapl.edu>).

3.3.3 MDIS (Mercury Dual Imaging System)

MDIS is a multispectral camera (Figure 3.19), and is composed of two instruments: the WAC (Wide Angle Camera) and the NAC (Narrow Angle Camera) (Mick et al., 2013).

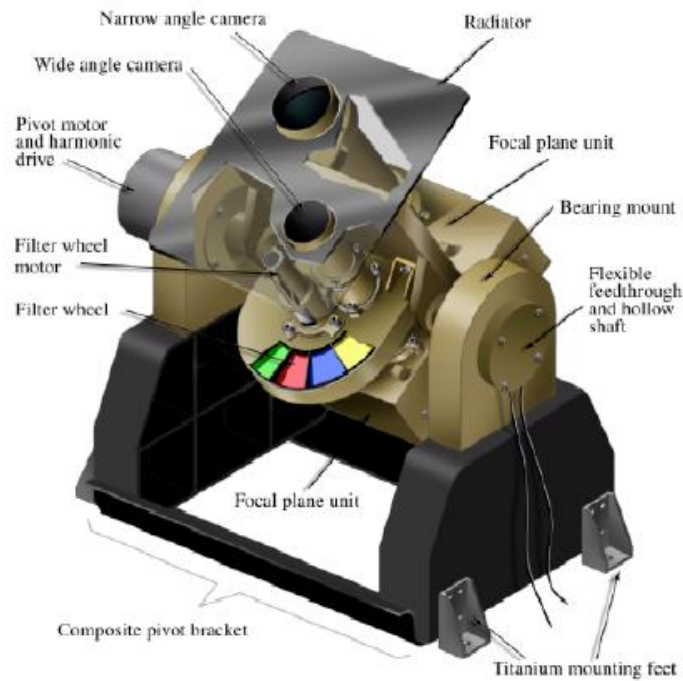


Figure 3.19: Representation of MDIS camera (Mick et al., 2013).

- The **Wide Angle Camera (WAC)** has wide field $10.5^\circ \times 10.5^\circ$, and it is equipped with a system of 12 monochromatic filters (Fig. 3.20) that covers a range of wavelengths from 395 nm to 1040 nm. The optical layout is composed of a 4-element refractive telescope and has a focal length of 78 mm and a collecting area of 48 mm^2 . The detector is an Atmel (Thomson) TH7888A frame-transfer CCD of 1024×1024 pixels and is located on the focal plane. The filter wheel is placed before the focal plane (Fig. 3.22). Eleven filters (Fig. 3.20) were chosen to perform an optimal analysis of the Hermean surface. The filter B at 700 nm is a broadband filter for optical navigation. The NAC is a high-resolution camera with a field of view of $1.5^\circ \times 1.5^\circ$ and can show details less than 18 m. The characteristics of the WAC are illustrated in Fig. 3.21.

Filter Number	Filter Filename letter	Wavelength (Flight) (nm)	FWHM (Flight) (nm)	Total Thickness (mm)	Focal length (mm)	Scale change (%)
1	A	698.8	5.3	6.00	78.218	-0.104
2	B	700	600.0	6.00	78.163	-0.104
3	C	479.9	10.1	6.30	77.987	-0.329
4	D	558.9	5.8	6.30	78.023	-0.283
5	E	628.8	5.5	6.20	78.109	-0.173
6	F	433.2	18.1	6.00	78.075	-0.216
7	G	748.7	5.1	5.90	78.218	-0.033
8	H	947.0	6.2	5.20	78.449	0.262
9	I	996.2	14.3	5.00	78.510	0.340
10	J	898.8	5.1	5.35	78.390	0.186
11	K	1012.6	33.3 0	4.93	78.535	0.372
12	L	828.4	5.2	5.60	78.308	0.082

Figure 3.20: Wide angle camera filters Mick et al. (2013).

- The **Narrow Angle Camera (NAC)** is the high resolution camera of MDIS. It has a unique filter centered at 747 nm, that matches to the corresponding WAC filter for monochrome imaging (Mick et al., 2013). The NAC optical design consists in an off-axis reflective telescope with an effective 550-mm focal length with a collecting area of 462 mm^2 (Fig. 3.22) (Mick et al., 2013). The NAC focal plane is identical to the WAC's, providing a $25\text{-}\mu\text{rad}$ IFOV (Mick et al., 2013). All Details of the NAC camera are reported in Fig. 3.21.

	Narrow Angle	Wide Angle
Field of view	$1.5^\circ \times 1.5^\circ$	$10.5^\circ \times 10.5^\circ$
Pivot range (observational)	-40° to $+50^\circ$ (Sunward) (Planetward)	
Exposure time	1 ms to ~ 10 s	
Frame transfer time	<4 ms	
Image readout time[†]	1 s	
Spectral filters	1	12 positions
Spectral range	721–770 nm	395–1040 nm in clear filter
Focal length	550 mm	78 mm
Collecting area	462 mm ²	48 mm ²
NAC-WAC coalignment knowledge	0.01 deg (179 μ rad)	
Spacecraft pointing knowledge	0.1 deg (1.75 mrad)	
Spacecraft knowledge	0.02 deg (350 μ rad)	
Detector-TH7888A	CCD 1024 \times 1024, 14- μ m pixels	
IFOV	25 μ rad	179 μ rad
Pixel FOV	5.1 m at 200-km altitude	35.8m at 200-km altitude
Quantization	12-bits per pixel	
Compression	Lossless, multi-resolution lossy, 12-to-8 bits	

Figure 3.21: Characteristics of the WAC and NAC cameras (Mick et al., 2013).

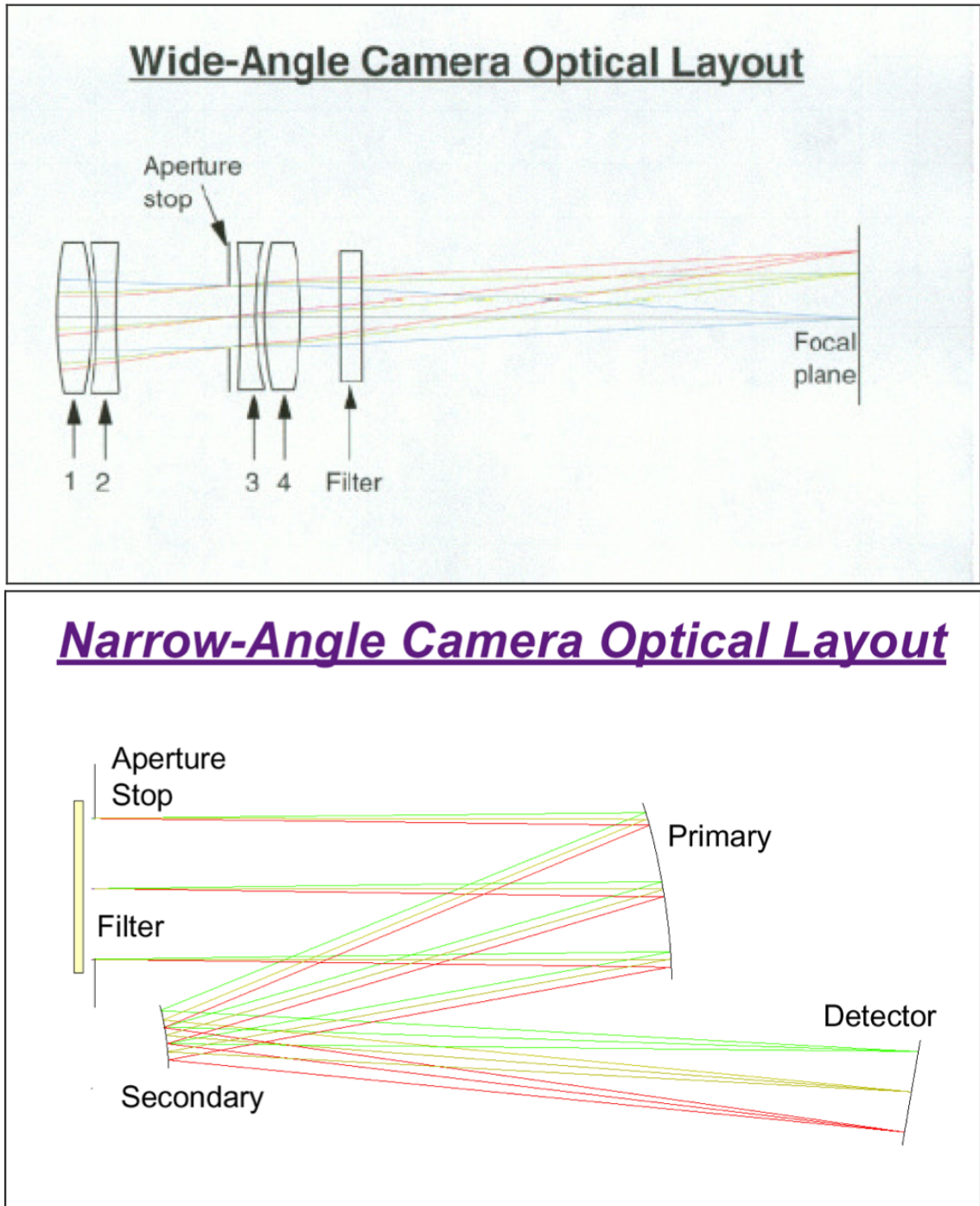


Figure 3.22: WAC and NAC optical layout (Mick et al., 2013).

3.3.4 MASCS (Mercury Atmospheric and Surface Composition Spectrometer)

MASCS (Figure 3.24) is the Messenger spectrometer devoted to the study of the amounts of atmospheric gases and the surface mineralogy. It contains two instruments: UVVS (Ultraviolet and Visible Spectrometer), and VIRS (Visible and Infrared Spectrometer) (<http://messenger.jhuapl.edu/instruments/MASCS.html>). UVVS studies the composition, the structure, the density, and the emission of atmospheric neutral gases and it detects the presence of known elements such as H, O, Na, K and Ca and assumptives (e.g. S, Si, Al, Mg, Fe and OH) in the exosphere (Espiritu and Malaret, 2012). VIRS is a spectrometer operating in the visible and near-infrared range of wavelength and is able to diagnose the presence of iron, titanium, silicates and other minerals such as pyroxene, olivine and ilmenite on the surface. The complementary work of these two instruments allow us to understand the processes that hold together the exosphere, the connection between surface and atmospheric composition, the dynamics of volatile materials and the nature of the radar reflective elements located at the poles (Espiritu and Malaret, 2012).

MASCS is composed of a Cassegrain telescope with a 50 mm diameter and a focal length of 257 mm connected simultaneously to UVVS and VIRS (who do their work separately). The characteristics of UVVS and VIRS are reported in Fig. 3.23.

- **UVVS** is a *scanning grating* spectrometer Ebert-Fastie type with a focal length of 125 mm (the optical scheme shown is in figure 3.26). It is equipped with three photomultipliers tubes that cover the length of the far-UV from 115 nm to 180 nm, the mid-UV from 160 nm to 320 nm and 250 nm, and the visible range up to 600 nm, with an average spectral resolution of 0.6 nm (<http://messenger.jhuapl.edu/instruments/MASCS.html>).
- **VIRS** (Fig. 3.25) is a spectrograph fixed concave grating (Fig. 3.26) with focal length of 210 mm, and a spectral resolution of 5 nm. The light through the fiber optics of the telescope arrives on the grid and is sent to a beam splitter that separates it into two beams. One beam goes to hit a solid-state detector with 512 elements silicon for the visible channel (215-1050 nm), and the second beam hits the indium-gallium-arsenide near infrared detector (850-1450 nm) of 256 elements (Espiritu and Malaret, 2012).

		VIRS	UVVS
Focal length		210 mm	125 mm
Grating		120 g/mm blazed at 600 nm	1800 g/mm blazed at 300 nm
Spectral resolution	FUV channel	N/A	0.5 nm
	MUV channel	N/A	1.0 nm
	VIS channel	4 nm	1.0 nm
	IR channel	4 nm	N/A
Wavelength range	FUV channel	N/A	115 - 190 nm (2 nd order)
	MUV channel	N/A	160 - 320 nm (1 st order)
	VIS channel	300-1050 nm	250 - 600 nm (1 st order)
	IR channel	850-1450 nm	N/A
Detector	FUV channel	N/A	Hamamatsu R 1081 PMT - CsI
	MUV channel	N/A	Hamamatsu R 759 PMT - CsTe
	VIS channel	Hamamatsu S3902-512 Si Diode Array	Hamamatsu R 647 PMT - Bi Alkali
	IR channel	Hamamatsu G8052-256 InGaAs Diode Array	N/A
Field of view	Surface	0.023° diameter	0.05° x 0.04°
	Atmosphere	N/A	1.0° x 0.04°

Figure 3.23: Technical characteristics of UVVS and VIRS (Espiritu and Malaret, 2012).



Figure 3.24: MASCS overview (Espiritu and Malaret, 2012).

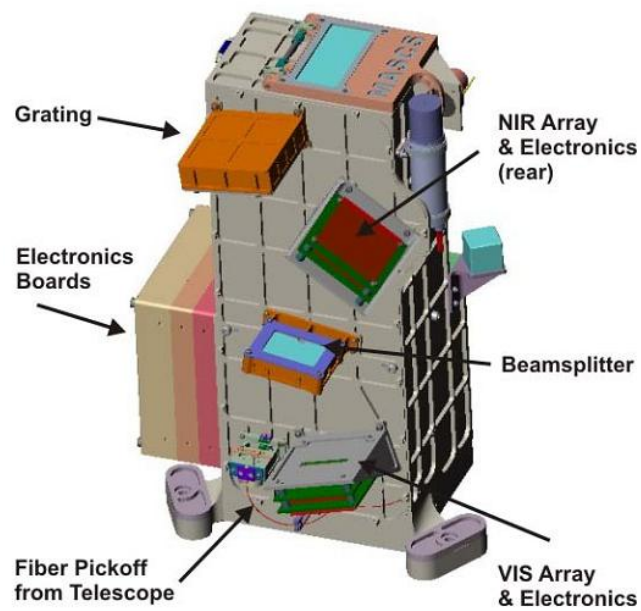


Figure 3.25: VIRS scheme (Espiritu and Malaret, 2012).

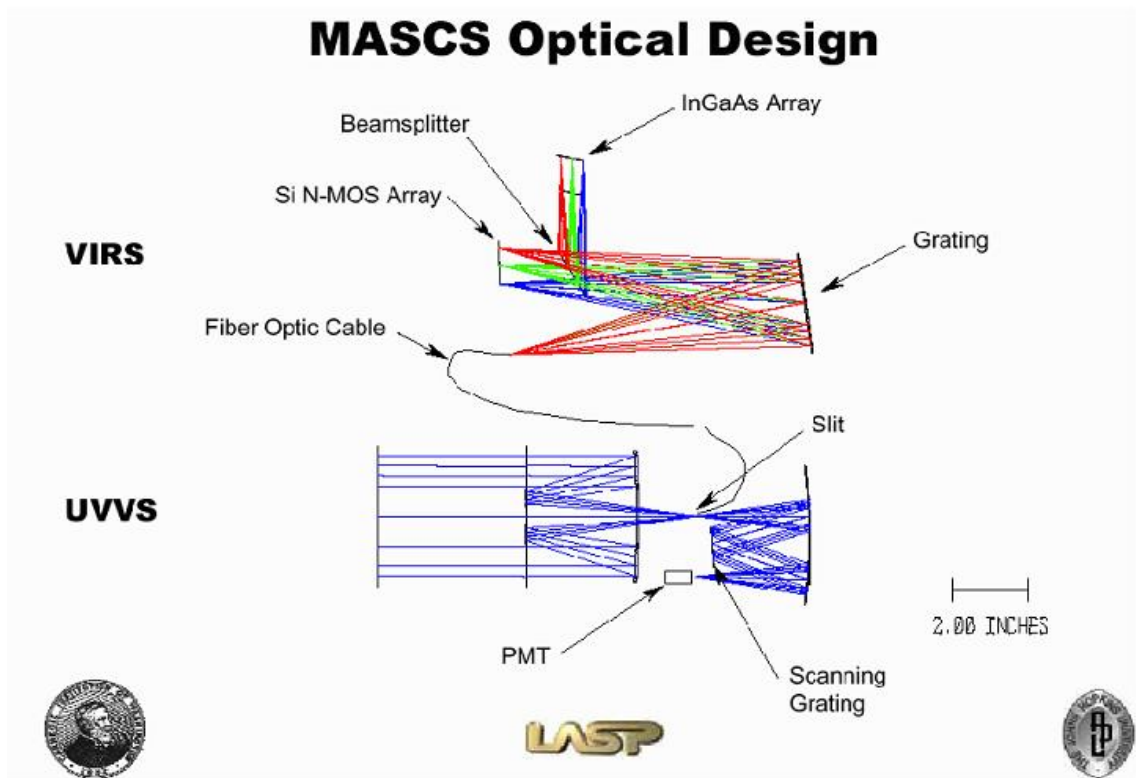


Figure 3.26: Optical scheme of UVVS and VIRS (Espiritu and Malaret, 2012).

3.4 VIRS and MDIS data

Data produced by VIRS are stored in two EDR (Experimental Data Records), one for the visible and one for the near-infrared spectrums, and are all available in a PDS standard format. Unlike VIR, MASCS is a punctual spectrometer and acquires data in whiskbroom mode (Section 1.3), namely pixel by pixel. VIRS produces three typologies of data:

- CDR (Calibrated Data Records) are the calibrated data.
- RDR (Reduced Data Records) are the raw data.
- Housekeeping data gives information about the instruments and hardware.

The calibration has been done directly by the team of VIRS and consists of the following steps:

- Calculation of the integration time for each spectrum for each observation.
- Correction of the magnitude of the detector of the visible.
- Determination and subtraction of the dark data.
- Various types of corrections such as subtraction of the scattered light and temperature.
- Determination of the geometrical parameters (i.e. ground reference) for each spectrum.
- Assignments of flags and indicators for the quality of the data.

Labeling of the data follows the PDS standard (Section 2.1). For each set of data is associated with its own label, is shown all the information of the data set. Tables 3.1 and 3.2 shows information relating to the data of the first two flybys (<http://starbrite.jpl.nasa.gov>).

Characteristics of the data of the flyby I		
	VIS	NIR
PRODUCT ID	<i>VIRSVCMF1_08014_191254.DAT</i>	<i>VIRSNCMF1_08014_191254.DAT</i>
PRODUCT CREATION TIME	2009/02/05T19 : 50 : 43	2009/02/05T19 : 26 : 08
PRODUCT TYPE	CDR	CDR
INSTRUMENT ID	MASCS	MASCS
DETECTOR ID	VIRS	VIRS
START TIME	2008/01/14T19 : 12 : 55	2008/01/14T19 : 12 : 55
STOP TIME	2008/01/14T19 : 28 : 37	2008/01/14T19 : 28 : 37
SPACEC. START COUNT	108825356.405	108825356.405
SPACEC. STOP COUNT	108826298.924	108826298.924
INTERCHANGE FORMAT	BINARY	BINARY
ROW BYTES	9506	4898
ROWS	755	755

Table 3.1: Table showing the main information related to the EDR of the first flyby for the two data sets VIS and NIR.

Characteristics of the data of the flyby II		
	VIS	NIR
PRODUCT ID	<i>VIRSVCMF2.08280.084654.DAT</i>	<i>VIRSNCF2.08280.084654.DAT</i>
PRODUCT CREATION TIME	2009/02/05T19 : 57 : 41	2009/02/05T19 : 31 : 08
PRODUCT TYPE	CDR	CDR
INSTRUMENT ID	MASCS	MASCS
DETECTOR ID	VIRS	VIRS
START TIME	2008/10/06T08 : 46 : 55	2008/10/06T08 : 46 : 55
STOP TIME	2008/10/06T08 : 55 : 38	2008/10/06T08 : 55 : 38
SPACEC. START COUNT	131770259.125	131770259.125
SPACEC. STOP COUNT	131770782.885	131770782.885
INTERCHANGE FORMAT	BINARY	BINARY
ROW BYTES	9506	4898
ROWS	420	

Table 3.2: Table showing the main information related to the EDR of the first flyby for the two data sets VIS and NIR.

The MDIS archive contains different data for different levels of processing. In Fig. 3.27 are summarized the MDIS data processing levels (Mick et al., 2013).

NASA	CODMAC	Description
Packet data	Raw - Level 1	Telemetry data stream as received at the ground station, with science and engineering data embedded.
Level-0	Edited - Level 2	Instrument science data (e.g., raw voltages, counts) at full resolution, time ordered, with duplicates and transmission errors removed.
Level 1-A	Calibrated - Level 3	Level 0 data that have been located in space and may have been transformed (e.g., calibrated, rearranged) in a reversible manner and packaged with needed ancillary and auxiliary data (e.g., radiances with the calibration equations applied).
Level 1-B	Resampled - Level 4	Irreversibly transformed (e.g., resampled, remapped, calibrated) values of the instrument measurements (e.g., radiances, magnetic field strength).
Level 1-C	Derived - Level 5	Level 1A or 1B data that have been resampled and mapped onto uniform space-time grids. The data are calibrated (i.e., radiometrically corrected) and may have additional corrections applied (e.g., terrain correction).
Level 2	Derived - Level 5	Geophysical parameters, generally derived from Level 1 data, and located in space and time commensurate with instrument location, pointing, and sampling.
Level 3	Derived - Level 5	Geophysical parameters mapped onto uniform space-time grids.
	Ancillary – Level 6	Data needed to generate calibrated or resampled data sets.

Figure 3.27: MDIS data processing levels (Mick et al., 2013).

From MDIS data can be derived several products (Mick et al., 2013):

- **Calibrated Data Record (CDR)** are calibrated images in units of radiance, I/F, or reflectance corrected to $i = 30^\circ$, $e = 0^\circ$ and not geometrically corrected.
- **Derived Data Record (DDR)** consists in five bands containing latitude, longitude, incidence angle, emission angle, and phase angle.
- **Map Projected Basemap RDR (BDR)** data is a global reflectance monochrome map.
- **8-color Map Projected Multispectral RDR (MDR)** data are a

set of a uncontrolled, mosaicked global color map of 8-color image sets derived from eight of the eleven WAC filters.

- **The 3-color Map Projected Multispectral RDR (MD3)** data are a set of a uncontrolled, mosaicked global color map of 3-color image sets derived from three of the eleven WAC filters.

The WAC and NAC data are archived together, they have the same dimensions (1024X1024 pixels), and they are not coregistered. MDIS and all the Messenger data are available in the PDS geoscience node (<http://ode.rsl.wustl.edu/mercury/index.aspx>).

Chapter 4

Mercury and Vesta

In this Chapter we illustrate the general results obtained for Mercury and Vesta, after the Messenger and Dawn missions. In particular, we report the results obtained from VIR data regarding Vesta mineralogy. These results are described in several papers, with contribution by the author Francesca Zambon (De Sanctis et al., 2012a,b, 2013; Ammannito et al., 2013a,b).

4.1 Mercury

Mercury is the closest planet to the Sun, but because of its position it is particularly difficult to observe from the Earth. The extreme thermal environment makes it difficult to explore onsite. Observations of Mercury from the Earth are possible only when its elongation is sufficiently high (the maximum elongation is 28.3°). In 1974, *Mariner 10*, the first mission dedicated to Mercury, during of the three Hermean flybys covered 45% of the surface (Solomon et al., 2007).

For about 30 years after Mariner 10, no missions to Mercury have flown. Many unresolved issues need an answer, and in recent years the interest about Mercury has increased. Messenger contributed to understand, Mercury's origin, its surface structure, and the nature of its magnetic field, exosphere, and magnetosphere (Solomon et al., 2007).

The planned BepiColombo project, the next ESA-JAXA mission to Mercury, will soon contribute to improve the knowledge of the planet.

Mercury physical and orbital parameters	
Semi-major axis	0.38709893 AU
Perihelion	0.30749951 AU
Aphelion	0.46669835 AU
Orbital period	87.96935 days
Inclination	7.00487°
Eccentricity	0.20563069
Mean radius	2439 km
Mass	3.302 10^{23} kg
Mean density	5.430 10^3 kg/m ³
Sidereal rotation period	58.6462 days
Axis inclination	0.01°
Max surface temperature	700 K
Min surface temperature	100 K
Mean surface temperature	440 K

Table 4.1: Mercury physical and orbital parameters

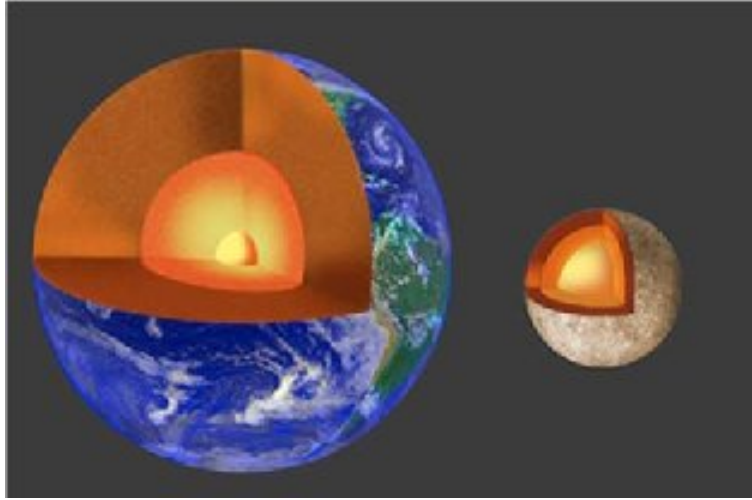


Figure 4.1: Mercury internal structure compared with the Earth (Solomon et al., 2007).

4.1.1 Mercury origin and structure

The structure and evolution of Mercury are related to its thermal history and depend on two processes: the growth caused by impacts with planetesimals which is the major source of heat, and the release of gravitational potential energy during the differentiation of metal from silicates. The principal characteristic of Mercury is its density ($5430/10^3 \text{ kg/m}^3$), the highest among the terrestrial planets. The high density suggests that the amount of metal is double with respect to that of the other terrestrial planets. This property should involve a very extensive and dense core. The core occupies most of the volume of Mercury (Harder and Schubert, 2001), with a radius which is about 70% of the total. In the case of a large dense core, the mantle would have a thickness of about 600 km, and the crust is extended between 100 and 300 km (Breuer et al., 2007) Fig. 4.1). The average high density of Mercury is probably due to a greater amount of iron within the core. To explain the high ratio of Fe/S has been hypothesized that Mercury may have formed from the Solar nebula, and its proximity with the Sun caused the evaporation of the volatile elements such as sulphur (Harder and Schubert, 2001).

Another possibility is that during its formation Mercury was in another position in the solar nebula and the fraction of the initial sulfur may have been lost because of impacts with other objects (Breuer et al., 2007). The percentage of sulfur influences the radius of the core. Models indicate that if Mercury was composed entirely of FeS its average density would differ by

only 0.5% with respect to a core completely composed of iron (Harder and Schubert, 2001). A recent model for Mercury's internal structure forecasts a solid silicate crust, a mantle overlying a solid iron-sulfide layer and an iron-rich liquid outer core and perhaps a solid inner core (Smith et al., 2012). Mercury appears morphologically similar to the Moon with a large part of planet heavily craterized (Spudis and Guest, 1988). Mercury surface is characterized by mountain chain, *lobate scarps*, extended between 10 and 100km, generated by the movement of the faults (Watters et al., 1998). Their irregular distribution indicates that they could have originated as the result of a possible reduction of the radius of about 1-2km, due to the cooling of the planet occurring after the accretion age. The extent of the contraction is related to the presence of sulfur in the core. However if the sulfur content was low, we would have seen a contraction greater than that observed (Watters et al., 1998; Solomon et al., 2007). Smooth plains are widespread on Mercury, and cover around $\sim 27\%$ of the surface. A large number of them seem to have had volcanic origin (Denevi et al., 2013). Most of the smooth planes have a composition similar to the northern smooth planes, suggesting a magnesian alkali-basalt-like composition. A small number of the smooth planes are interpreted to be different, characterized by low reflectance and shallower spectral slope, suggesting more ultramafic compositions (Denevi et al., 2013). Particularly extended planes are located in the region of the Caloris basin. These knobby and hummocky planes, called Odin-type plains, occupy 2% of Mercury's surface (Denevi et al., 2013). They probably formed as Caloris ejecta, although such an origin is in conflict with a straightforward interpretation of crater-size frequency distributions (Denevi et al., 2013). Measures obtained by Neutron Spectrometer on Messenger combined with radar data revealed the presence of possible pure water ice deposits in the north polar region. The total mass of water at Mercury's poles is inferred to be 2×10^{16} to 10^{18} grams and is consistent with delivery by comets or volatile-rich asteroids (Lawrence et al., 2013). Radioactive elements such as potassium (K, 1150 T 220 parts per million), thorium (Th, 220 T 60 parts per billion), and uranium (U, 90 T 20 parts per billion) have been detected in the northern hemisphere by GRS. Amounts of K, Th, and U indicate that internal heat production has declined substantially since Mercury's formation, consistent with widespread volcanism shortly after the end of late heavy bombardment 3.8 billion years ago and limited, isolated volcanic activity (Peplowski et al., 2011).

4.1.1.1 Surface composition

During the orbit around Mercury, MASCS (section 3.24) provided more than 1.6 million spectra. Reflectance spectra of the Hermean surface do not show evident absorption bands, in particular the $1\mu\text{m}$ band associated with ferrous iron in silicates. Mercury's surface is darker than the laboratory mixture of iron silicates, and seems to be dominated by low-Fe phases, that appear bright when freshly excavated (e.g., enstatite, feldspar). Modeling results indicate that mafic silicates on Mercury have no more than $\sim 1.4\text{ wt}\%$ Fe^{2+} ($\sim 1.8\text{ wt}\%$ FeO) (Izenberg et al., 2014). Some higher-UV regions observed by VIRS correspond to areas with XRS-derived upper limits on iron amounts near $2\text{ wt}\%$ Fe (Izenberg et al., 2014). No sulfide absorption bands have been detected, even in the region such as hollows (Blewett et al., 2011, 2013) in which this bands are expected. Hollows are irregular, shallow, rimless depressions inside bright deposits within impact craters (Blewett et al., 2011, 2013). Moreover, no hydroxylated silicates have been detected. The low Signal Noise Ratio (SNR) in the spectral region around $1.4\mu\text{m}$ do not allow detection of weak features.

Although no spectral features have been observed, there is a systematic spectral variation associated with morphological boundaries, indicating different composition of the geologic units (Izenberg et al., 2014). Mercury reflectance spectra are characterized by spectral slope variation. Spectral slope are indicative of the maturation of the soil, with shallower slope indicating young terrain and vice versa. VIRS spectra are characterized by "red" spectral slope, steeper than those of the Moon, indicating some combination of more rapid optical maturation with respect to the Moon, possibly due to the intense "space weathering" and a different average composition (e.g., Warell and Valegard (2006); Holsclaw et al. (2010); Riner and Lucey (2012); Izenberg et al. (2014)).

4.1.2 The magnetic field

The presence of a weak internal magnetic field was discovered by *Mariner 10* during its flyby (Breuer et al., 2007). Its structure is similar to the magnetic field of the Earth (Fig. 4.2). Its origin is linked to the evolution of Mercury and the presence of iron in the core. The cooling of the nucleus is mainly due to the precipitation towards the center of metallic solid iron coming from the overlying areas, forming a solid inner core. The growth rate of the inner core depends on the rate of cooling of the core. The magnetic field suggests that the core is partially fluid. In fact a liquid core does not justify completely a magnetic field of this type (Breuer et al., 2007). The evolutionary models of

Mercury forecast the possibility of a dynamo that generates the field. The magnetometers onboard MESSENGER allowed the separation of internal and external magnetic field contributions (Anderson et al., 2011). The global planetary field is represented as a southward-directed, spin-aligned, offset dipole centered on the spin axis (Anderson et al., 2011).

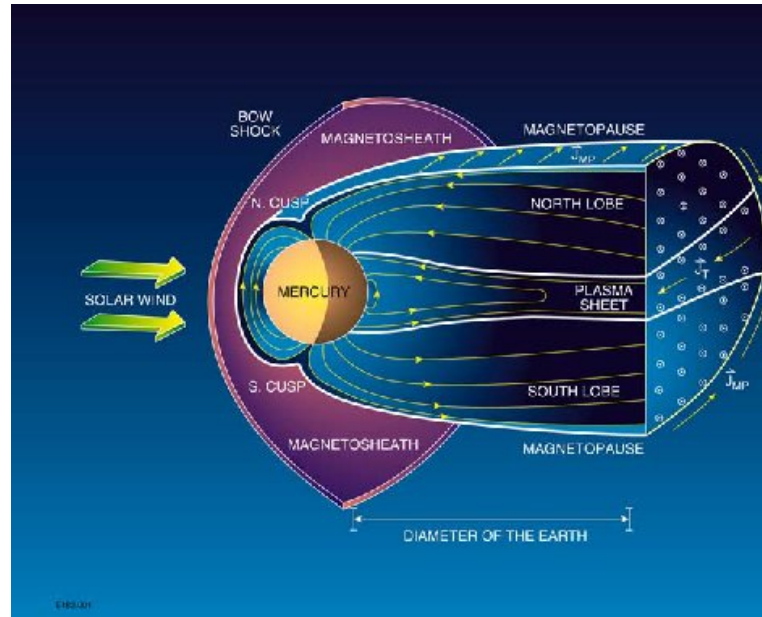


Figure 4.2: Representation of Mercury's magnetosphere (Solomon et al., 2007).

4.1.3 The exosphere

Observations of Mercury's exosphere between 1997 and 2003 revealed that sodium is its main component. The Na distribution varies day by day, and this non-uniformity is probably due to the solar wind (Potter et al., 2006). Furthermore, variations with the latitude have been observed. Sometimes sodium is concentrated at high latitudes in the northern and southern hemispheres. This could be due to the entrance of sodium particles through the polar regions. In some regions, the concentration of sodium in the rocks is higher and when illuminated by sunlight generates an increase in the amount of sodium in the exosphere. For instance, in the southern hemisphere near the terminator, an increase in sodium concentration caused by its depletion in the regions illuminated by the Sun has been observed (Potter et al., 2006).

4.2 Vesta

Vesta and Ceres, the two targets of the Dawn mission, are among the largest members of the Main Asteroid Belt. They are very different from each other. Vesta is a rocky body while Ceres is an ice-rich body (McCord and Sotin, 2005; Coradini et al., 2011; McCord et al., 2011a). They can be considered a relic of the protoplanetary disk that orbited the young Sun (Coradini et al., 2011). For this reason Vesta and Ceres are fundamental to understand the formation and evolution of the Solar System (Coradini et al., 2011).

Vesta is melted and differentiated. It is formed by a metal-rich core surrounded by a rocky mantle (Hewins and Newsom, 1988; Righter and Drake, 1997). The surface has been covered with a basaltic crust, probably due to serial magmatism (Wilson and Keil 1996) or the solidification of an extensive magma ocean (Righter and Drake, 1997; Ruzicka et al., 1997; Warren, 1997). Fig. 4.3, 4.4 illustrates Vesta structure model (Thomas et al., 1997a,b; Zuber et al., 2011).

4.2.1 Vesta composition

Dawn, for the first time, acquired high resolution images of Vesta's asteroid. Fig. 4.6 shows a global map of Vesta with official nomenclature of the International Astronomical Union (IAU). In the other Chapters we refer to this nomenclature to indicate the crater and the features present on Vesta.

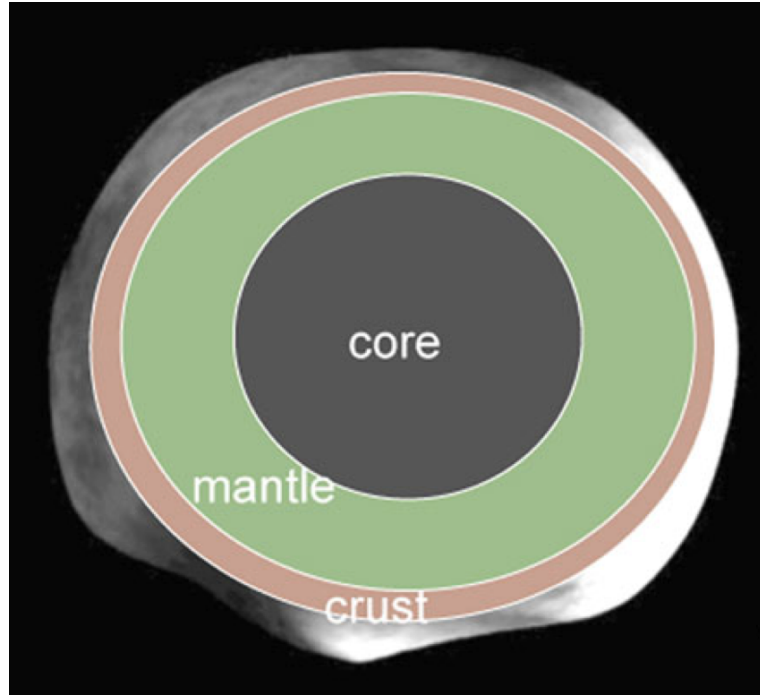


Figure 4.3: Representation of Vesta's internal structure (Zuber et al., 2011).

	Thickness (km)	Density (kg m^{-3})	Mass ($\text{kg}/10^{19}$)
Upper crust	Shape-214 ^a	2800	8.0
Lower crust	14	3200	2.6
Mantle	80	3976	10.4
Core	120	7870	5.7

Figure 4.4: Base model of the internal structure of Vesta (Thomas et al., 1997a,b; Zuber et al., 2011).

Table 1 Vesta parameters

Parameter	Value	Reference
Mean heliocentric distance, AU	2.3619	JPL Small-body Data Browser (2003)
Orbital eccentricity	0.0886	JPL Small-body Data Browser (2003)
Orbital period, yr	3.63	Millis and Elliot (1979)
Rotational period, h	5.342	Harris et al. (2006)
GM , $\text{km}^3 \text{s}^{-2}$	17.66 ± 0.2	Konopliv et al. (2011b)
Mass, $10^{-12} M_{\text{Sun}}$	133.1 ± 1.5	Konopliv et al. (2011b)
Mean radius	258 ± 5	Thomas et al. (1997b)
Axes of shape, km	280 ± 5 $\times 272 \pm 5$ $\times 227 \pm 5$	Thomas et al. (1997b)
Volume, 10^7 km^3	7.19 ± 0.87	Thomas et al. (1997b)
Mean density, kg m^{-3}	3760	Konopliv et al. (2011b)
g , m s^{-2}	0.32	
Spectral type	V	(Zellner et al. 1985)

Figure 4.5: Vesta parameters (Zuber et al., 2011).

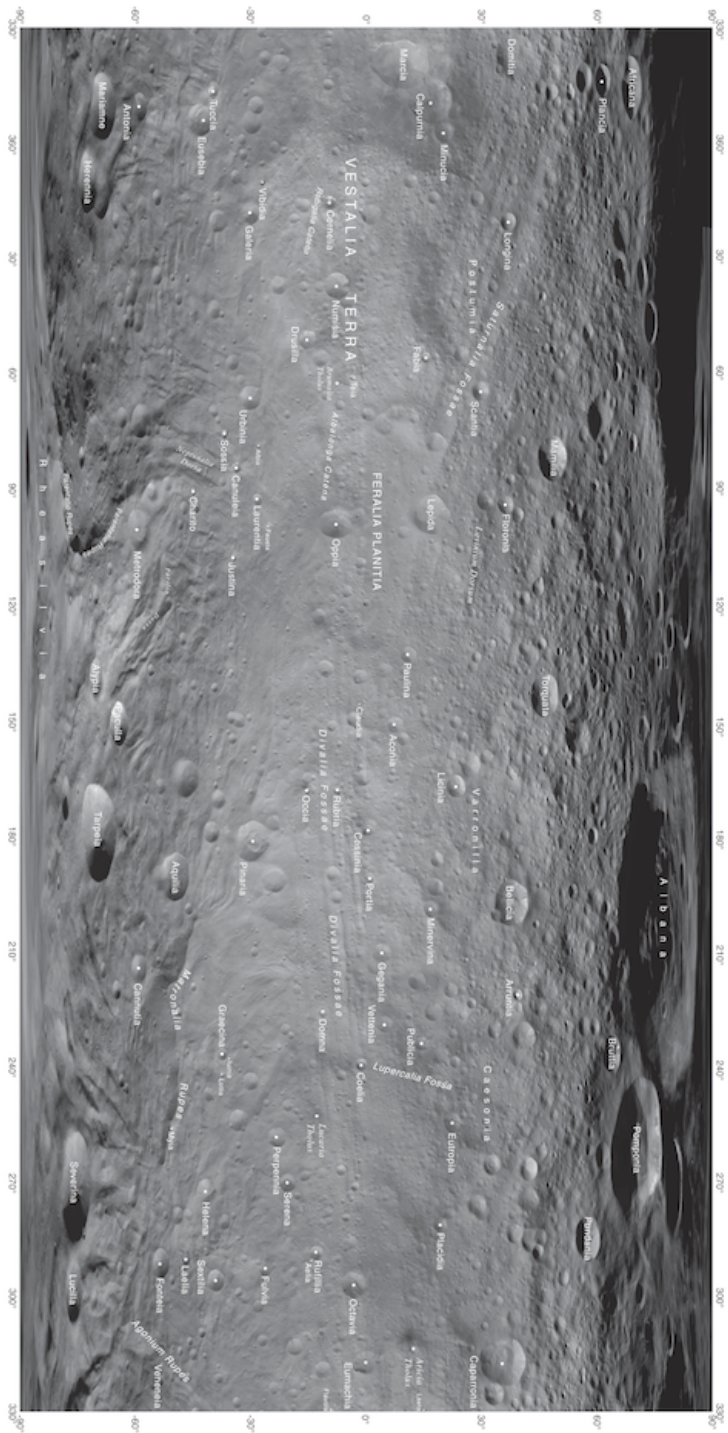


Figure 4.6: Vesta map with the names of the principal features. The coordinate system used for this map is claudia double prime (Section 2.2) <http://planetarynames.wr.usgs.gov/images/vesta.pdf>.

4.2.2 Vesta's surface

Vesta mineralogical diversity was already known from Hubble Space Telescope (HST) observation of Vesta. Li et al. (2010) show two different RGB maps which highlight Vesta global diversity (Fig. 4.7). Reddy et al. (2012a) reported the Clementine color ratios mosaic of the Vesta disk resolved, which highlight the compositional diversity of Vesta (Fig. 4.8B). The map in Fig. 4.8D shows in red the diogenite-rich areas and in blue the eucritic regions, while the map in 4.8C highlights in red high band depth regions (Reddy et al., 2012a).

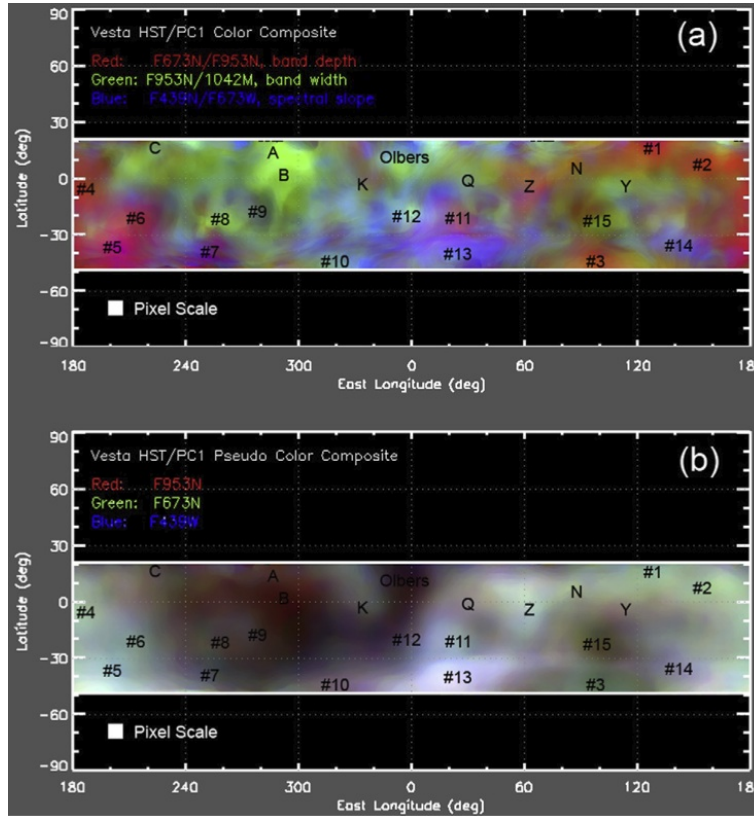


Figure 4.7: RGB images of Vesta observed by Hubble highlight Vesta mineralogical diversity (Li et al., 2010).

Vesta presents a complex topography at all spatial scales (Fig. 4.9) (Jaumann et al., 2012). Full disk images of HST revealed a large south polar basin with a central mound (Thomas et al., 1997a; Jaumann et al., 2012), subsequently named Rheasilvia (301°E and 75°S) (Fig. 4.6). This feature is an approximately circular impact basin with a diameter of 500 ± 20 km, while

the diameter of the mound is ~ 180 km (Jaumann et al., 2012). The Rheasilvia region shows an apparent lower crater density (Marchi et al., 2012) and smoother texture distinctive from the surrounding terrain (Jaumann et al., 2012). Vestalia Terra ($\sim 25^\circ\text{N}$ to 35°S and $\sim 200^\circ\text{E}$ to 300°E) is the highest topography area with an elevation of $\sim 20\text{km}$ (Jaumann et al., 2012). The southern part is merged with the rim area of the Rheasilvia basin. In the western part of Vestalia Terra border there are the Marcia border, Marcia, Calpurnia and Minuccia craters, and in the eastern side Veneneia (170°E and 52°S), the second largest older basin of Vesta ($400 \pm 20\text{km}$ wide) (Jaumann et al., 2012).

A Vesta albedo map (Schröder et al., 2013) reveals the presence of dark, bright and intermediate terrain (Fig. 4.10) (Jaumann et al., 2012; Mittlefehldt et al., 2012). Presence of different albedo regions is connected to the mineralogy. Dark material is dominated by the pyroxene, as the other regions of Vesta, but presents weaker absorption features. This could imply the presence of opaque materials that reduce the albedo and the bands (Palomba et al., 2014). Palomba et al. (2014) observed that the large part of the dark materials (90%) show the OH-signature at $2.8\mu\text{m}$. A comparison between laboratory and dark material spectra reveals that the darkening agents are compatible with eucritic material mixed with 10-30 vol% of carbonaceous chondrite materials (Palomba et al., 2014). Bright areas are studied in detail in Chapter 6.

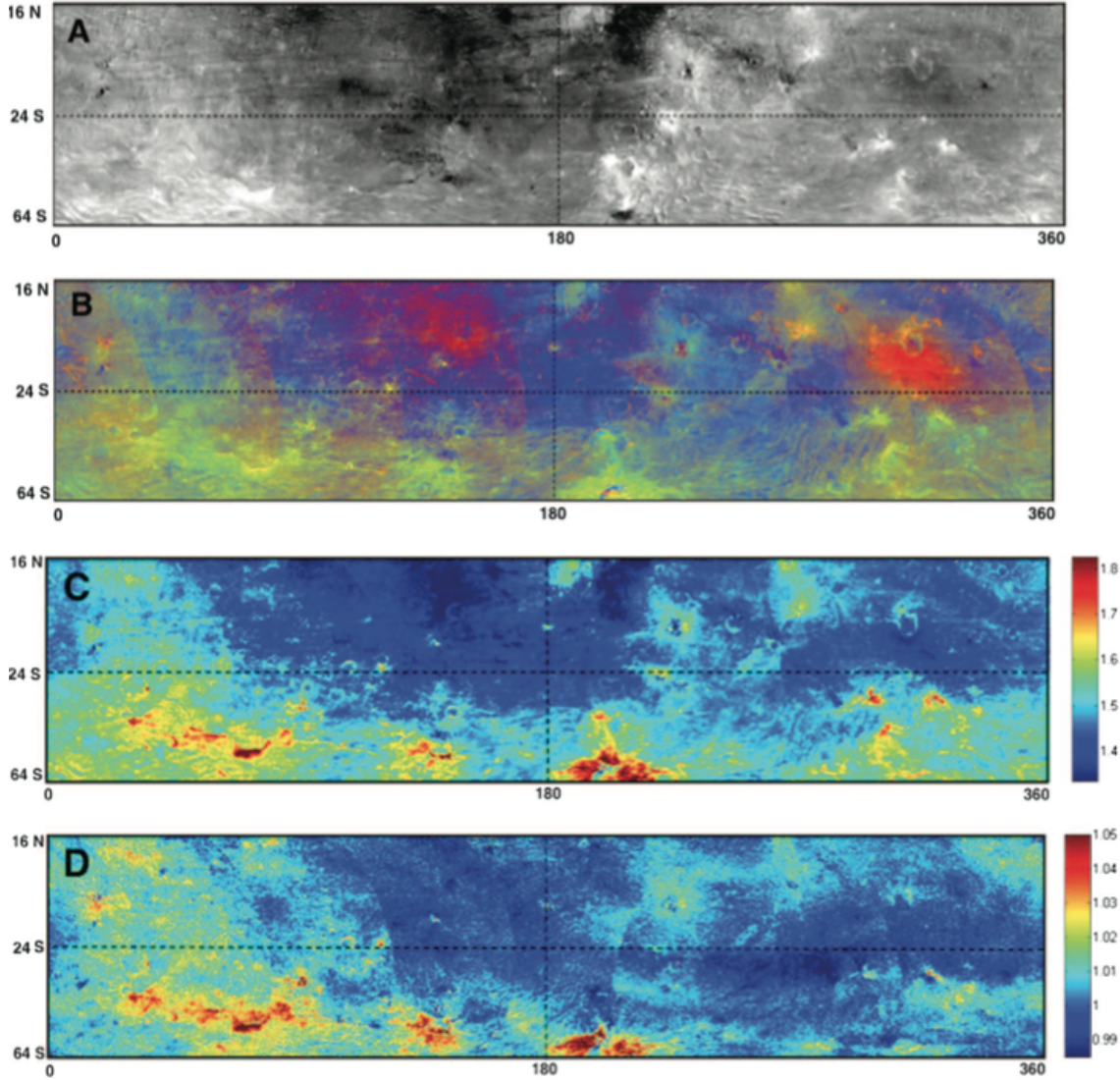


Figure 4.8: Cylindrical projections of Vesta color mosaics relative to the approach phase (~ 480 m/ pixel), derive from the Framing Camera images. A. Photometrically corrected 0.75-mm filter global mosaic showing east- west and north-south dichotomies in reflectance. B. Clementine color ratios mosaic ($CR = R(0.75)/R(0.45)$, $CG = R(0.75)/R(0.92)$, and $CB = R(0.45)/R(0.75)$). C. Rainbow-color coded map of $R(0.75)/R(0.92)$ ratio. C. Rainbow-color coded map of $R(0.98)/R(0.92)$ ratio (Euclite-Diogenite) showing diogenite-rich regions as red and euclite-rich regions as blue (Reddy et al., 2012a).

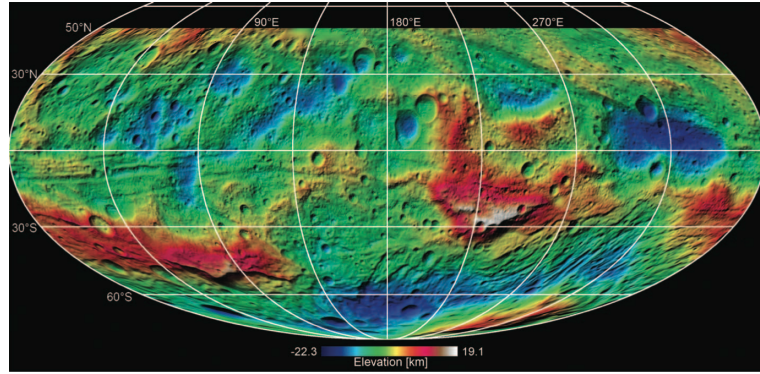


Figure 4.9: Vesta digital terrain model in Mollweide projection (Jaumann et al., 2012).

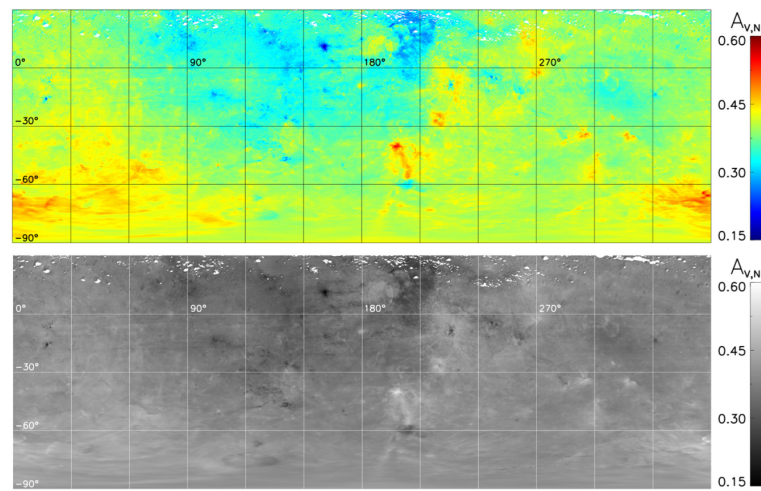


Figure 4.10: Vesta albedo map. Top. Albedo map in false color. Bottom. Albedo map in grayscale (Schröder et al., 2013).

4.2.3 Vesta mineralogy

Data from the Dawn mission allowed deriving the mineralogy of Vesta at different resolutions. McCord et al. (1970) observed that Vesta spectra are characterized by pyroxenes bands at 0.9 and 1.9 μm , while Feierberg and Drake (1980) found a connection between the HED meteorites and Vesta. All VIR spectra contain the two pyroxene bands. The first mineralogical maps derived from the Survey data (spatial resolution $\sim 700\text{m}/\text{pixel}$) (section 3.1) have been published in De Sanctis et al. (2012a). In Fig. 4.12 we show the maps of the band centers and those of the band depth. Band centers are indicative of the mineralogy, small band centers correspond with a higher content of diogenite, while longer band centers are representative of the eucrite content. Band center maps show that the diogenite, that is typical of the underlying layer of the surface, is present in small restricted areas, in the south pole in correspondence to the large impact basin Rheasilvia. Diogenitic material is also present in some regions of the northern hemisphere in correspondence to the Rheasilvia ejecta (De Sanctis et al., 2012a; McSween et al., 2013a). A large part of Vesta's surface is dominated by howardite rich in eucrite (De Sanctis et al., 2012a). Band depths are associated with the abundance of the absorbing mineral, the grain size and the presence of opaque material (Clark, 1999). Band depth maps of Vesta show an increase of the band depth for the diogenitic areas of the south pole, while they are shallower in the equatorial region. In general, band I depths in the equatorial region are ~ 0.35 to 0.4 , whereas those in the Rheasilvia basin are commonly 0.45 to 0.55 . Similarly, band II depths in the equatorial region are typically ~ 0.15 to 0.2 , whereas in the southern region they are ~ 0.25 to 0.3 (De Sanctis et al., 2012a). VIR data suggest that the Rheasilvia basin is richer in pyroxene than the equatorial regions and that the regolith in this region has a larger average grain size distribution and/or contains fewer opaque minerals. A larger grain size is consistent with less impact comminution in the southern region because of the younger age of the Rheasilvia basin (De Sanctis et al., 2012a). Ammannito et al. (2013a) present high resolution mineralogical maps of Vesta relative to the HAMO and HAMO2 phase of the mission (spatial resolution $\sim 180\text{m}/\text{pixel}$). The maps confirm the results obtained in (De Sanctis et al., 2012a), better emphasize the different lithologies present on Vesta (Fig. 4.13, 4.14, 4.15). In Fig. 4.11 we show a scatter plot of the band II center vs. band I center relative to the whole Survey phase. Band centers are diagnostic of the mineralogy, and plotting together both band I centers and band II centers of all the VIR spectra, and we can have an idea of the global mineralogy and of the dominant lithologies of Vesta. This plots shows that most of the points are in the howardite that is the dominant

lithology on Vesta.

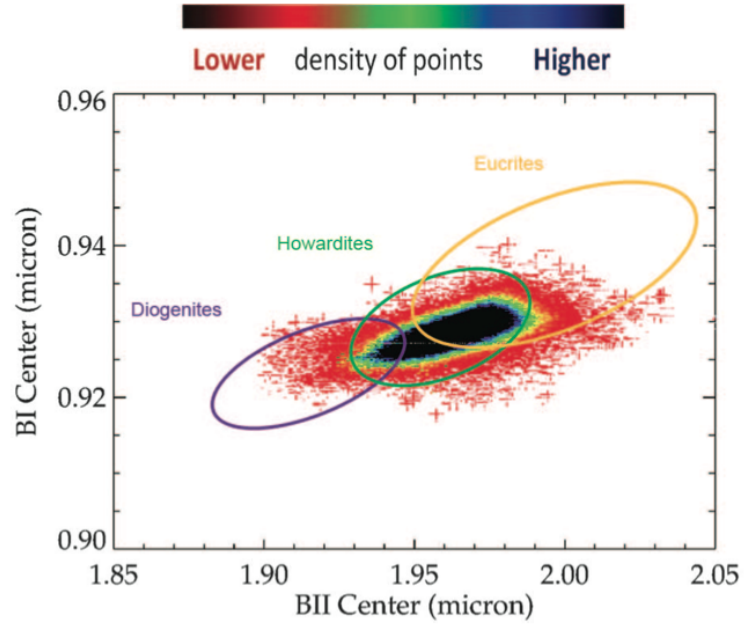


Figure 4.11: Band II center vs. band I center scatter plot relative to the Survey phase of the mission. The colored circles delimit the diogenite (violet), howardite (green) and eucrite (yellow) regions (De Sanctis et al., 2012a).

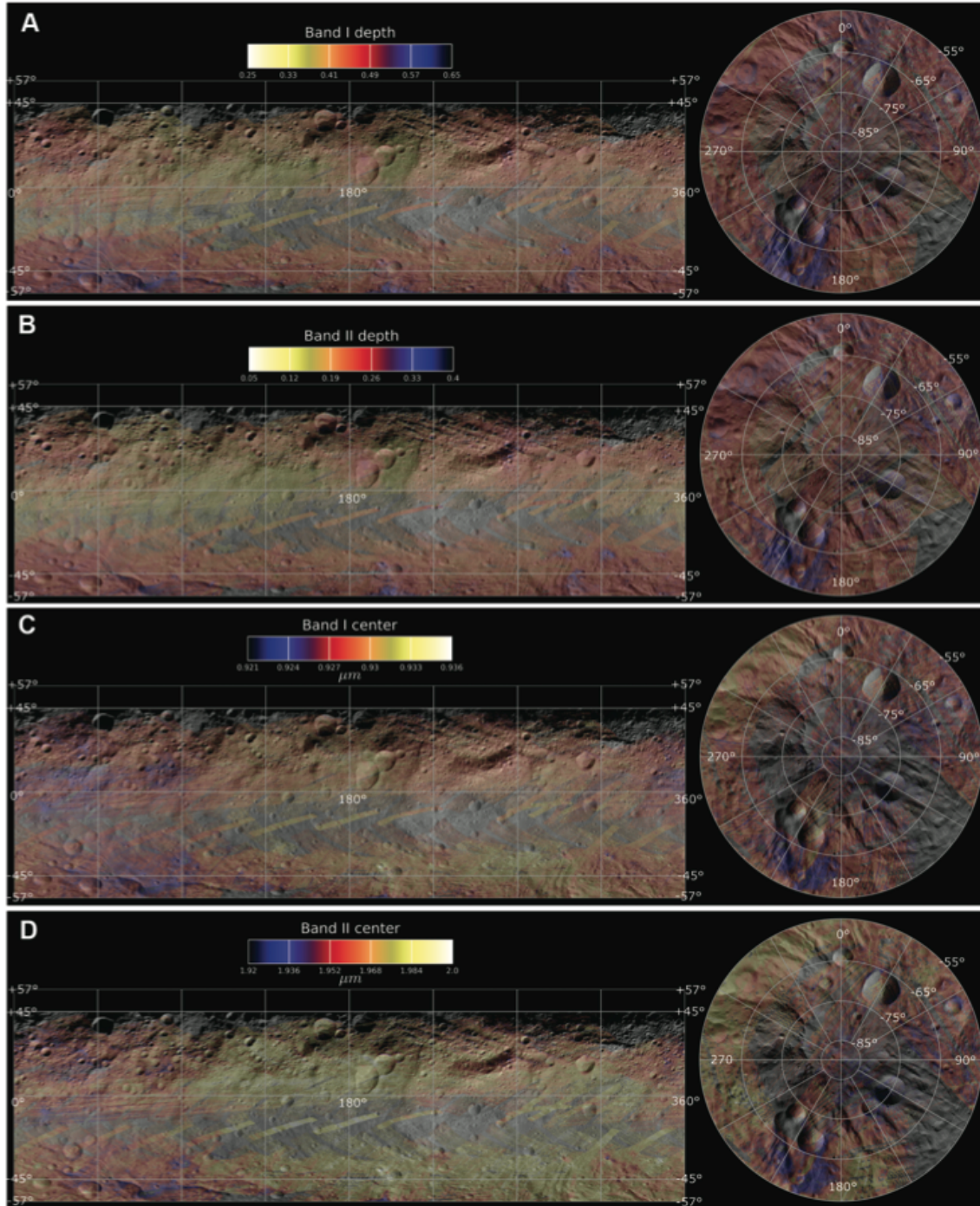


Figure 4.12: Band center and band depth maps of Vesta relative to the Survey phase of the mission (De Sanctis et al., 2012a).

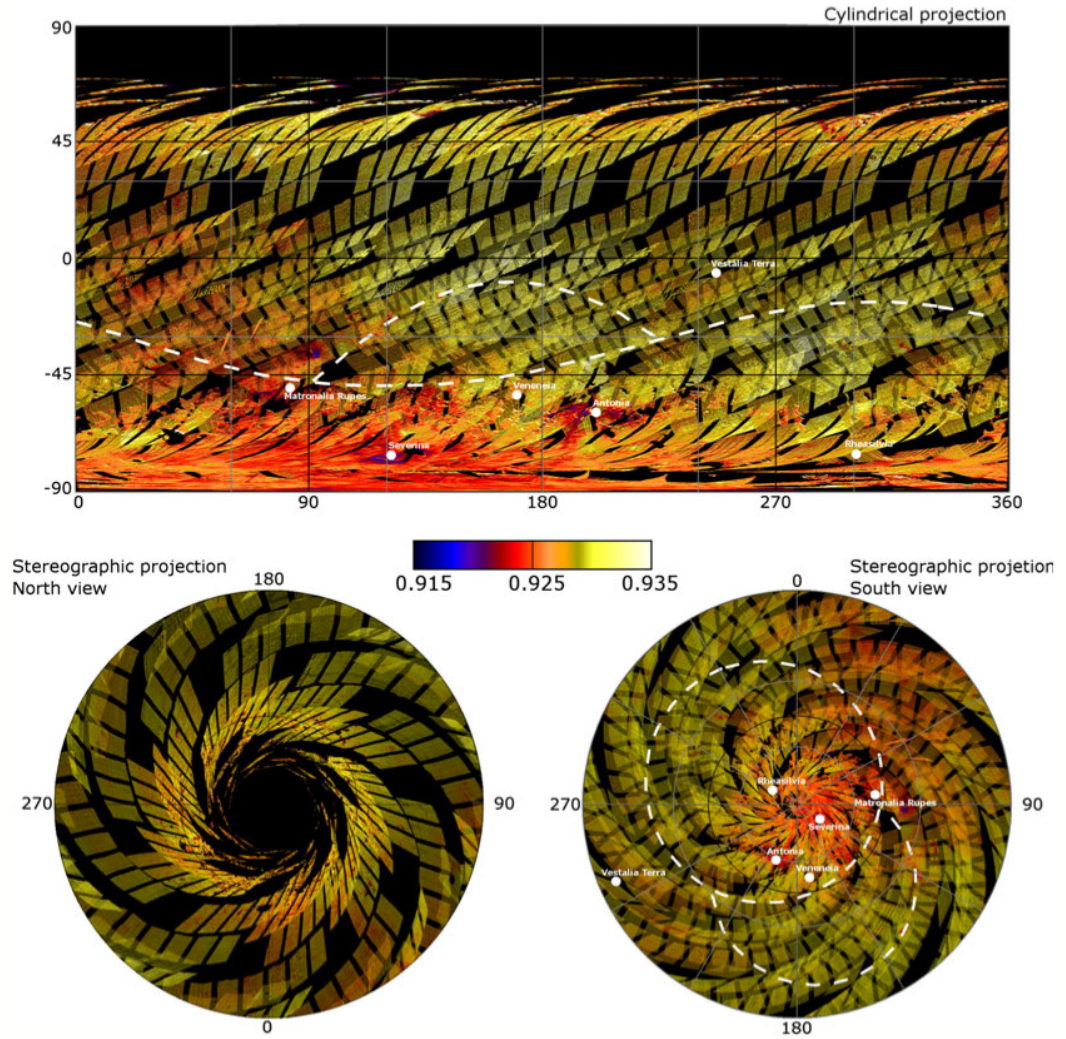


Figure 4.13: Band I center maps of Vesta relative to the HAMO and HAMO2 phase of the mission (Ammannito et al., 2013a).

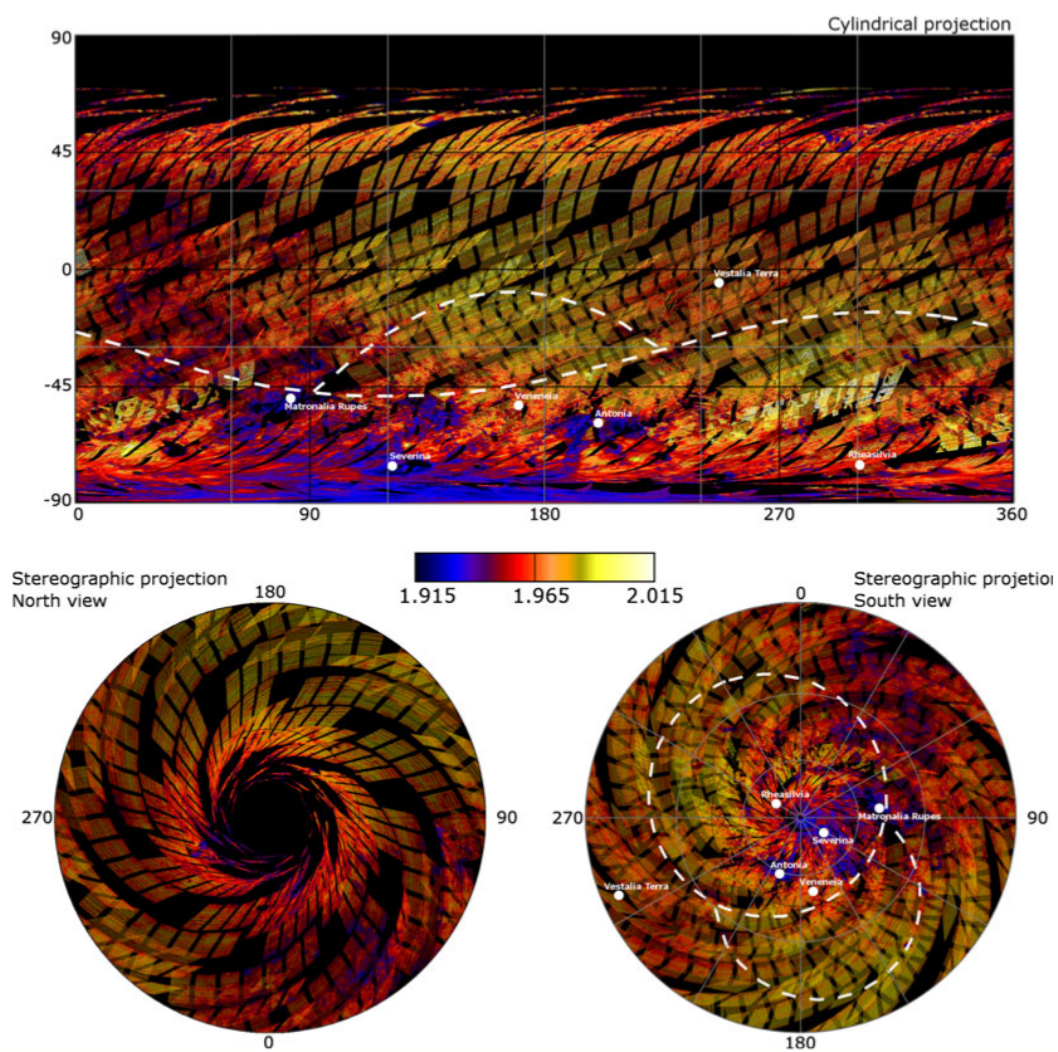


Figure 4.14: Band II center maps of Vesta relative to the HAMO and HAMO2 phase of the mission (Ammannito et al., 2013a).

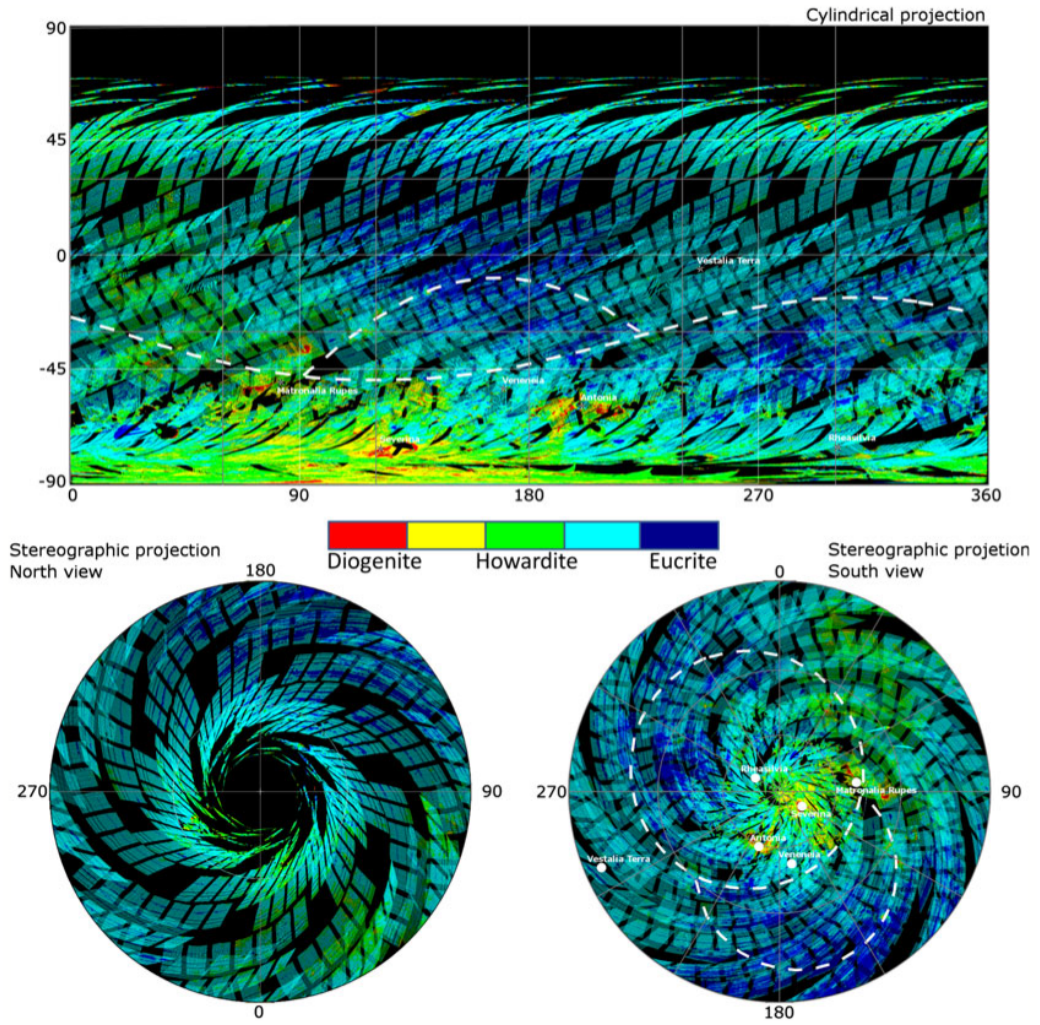


Figure 4.15: Lithologies present on Vesta's surface (Ammannito et al., 2013a).

4.2.4 Hydrate material on Vesta

Here we illustrate the results obtained by (De Sanctis et al., 2012b) on study of the hydrated materials on Vesta. Presence of absorption bands in the spectral region around 2.8 and 3 μm is indicative of the presence of hydrated OH and H_2O (Clark, 1999), (Section 1.8). These features are present in carbonaceous chondritic clasts and can be frequently found in howardites (Zolensky et al., 1996; Gounelle et al., 2003), showing different degrees of aqueous alteration. These chondritic clasts can contain H_2O in the form of hydrated, hydroxylated, or oxyhydroxylated mineral phases. De Sanctis et al. (2012b) derived the 2.8 μm map for Vesta associated with an OH signature (Fig. 4.16). A weak hydration signature in the 3 μm region has been reported for Vesta from telescopic data, but this discovery has not been independently confirmed (Rivkin et al., 2006; Hasegawa et al., 2003). Generally OH signatures are associated with low albedo areas (dark materials) (McCord et al., 2012; Jaumann et al., 2012; Palomba et al., 2014), in correspondence to the dark region OH-bearing absorption band increase, indicating that dark material is plausibly responsible for OH signatures De Sanctis et al. (2012b).

OH-bearing on Vesta has been detected in two large regions: OH-Rich Terrain 1 (OHRT1) a very large region located between 70°E to 20° E and 30°N to 30°S, that contains the strongest absorptions of hydrated materials (De Sanctis et al., 2012b); and a smaller region in Oppia crater areas (OHRT2), not associated with dark materials, in which a weak absorption has been detected. Because of the poor illumination conditions of the northern hemisphere, OHRT1 may extend farther north than currently mapped (see De Sanctis et al. (2012b)). OHRT1 presents a gap of a weak OH-absorption band in correspondence to the young Marcia crater (190°E, 10°N). The results obtained are in agreement with the measure obtained by GRAaD, that found the highest concentration of H in the OHRT1 and the lowest average H concentrations in the Rheasilvia basin (Prettyman et al., 2012).

Presence of hydrated material may be endogenic, and could have been supplied by OH-bearing impactors, or could be due to the interaction of solar-wind protons with the surface, forming superficial OH bonds as on the Moon (Pieters et al., 2009; Sunshine et al., 2009; McCord et al., 2011b; De Sanctis et al., 2012b). On the Moon the OH and H_2O signature increases dramatically with latitude beyond 45° and appear to vary as a function of the local time of day (Pieters et al., 2009; Sunshine et al., 2009; McCord et al., 2011b). This process has not been observed for Vesta, and no correlation with the temperature or illumination condition has been found. OH spatial distribution on Vesta is stable over time De Sanctis et al. (2012b). The stronger OH-bearing on Vesta is associated with howarditic and eucritic

material. Regions of rich of diogenitic and eucritic materials with no $2.8\ \mu\text{m}$ signature have been found, so the correspondence with mineralogy is not clear.

The origin of the OH signature on Vesta is different with respect to the Moon. This signature seems to be related to contamination of Vestan primordial material due to OH-bearing low-velocity impactors, that is consistent with evidence of CM OH-rich clast observed in the howardite meteorites (De Sanctis et al., 2012b). The Vestan OH distribution reveals that an important primordial process, such as the delivery of hydrated material in the main belt, may have played a role in the terrestrial planets evolution in the early stages of the solar system. This process could have also provided a way to transport organic compounds and water to main belt asteroids and terrestrial planets (De Sanctis et al., 2012b).

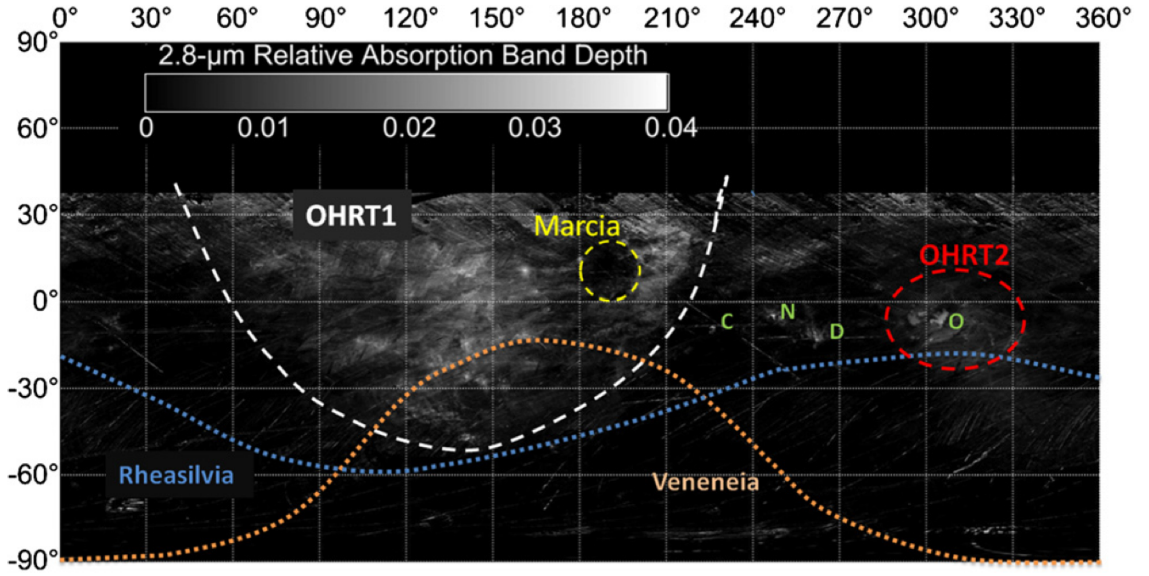


Figure 4.16: Map of the $2.8\mu\text{m}$ band on Vesta (De Sanctis et al., 2012b).

4.2.5 Olivine on Vesta

Here we illustrate the work done by (Ammannito et al., 2013b) concerning the discover of the olivine on Vesta. Magma-ocean models for Vesta predict a eucritic crust with an underlying diogenitic layer, with olivine-rich mantle rocks and a metallic core in the deep interior (Righter and Drake, 1997; Ruzicka et al., 1997). These models predict mineralogical variations on a large vertical scale, with olivine-rich cumulates occurring below olivine-poor

diogenite (Ammannito et al., 2013b). Alternative models, more consistent with the diverse trace-element geochemistry of diogenites, posit that diogenitic plutons occur at the crust-mantle boundary or within the basaltic crust (Mittlefehldt, 2000; Barrat et al., 2010), resulting in association of olivine-rich and orthopyroxene-rich diogenites mixed on smaller scales (Ammannito et al., 2013b). Pyroxenes features are dominant when mixed with olivine, and only the olivine amounts $>50\text{vol}\%$ affect the band I and cause clear reduction of the band II. Band I position, reduction of the band II and low Band Area Ratio values are indicative of the presence of a high amount of olivine (Cloutis et al., 1986; Gaffey et al., 1986). Evidence of olivine in the VIR spectra has been found in two unexpected regions at the north pole: at the Bellicia crater wall and in the ejecta blanket of the Arruntia crater (Fig. A.9, A.10). The other regions of Vesta appear to be poor in olivine, including the large impact basin Rheasilvia region in which olivine may be present in modest amounts ($\approx 25\text{ vol}\%$). Olivine content for the Bellicia and Arruntia regions is consistent with a mixture of 50-80-vol% olivine (Fig. 4.17). Results of the linear spectral unmixing in this regions show an amount of olivine for this regions up 55% (section 7.3). Generally olivine is present in the diogenitic meteorites, but on Vesta it is present in an howarditic background.

Origins of olivine on Vesta can be either endogenous or exogenous. There are two main models for the endogenic origin of the olivine on Vesta: serial-magmatism models that consider fractional crystallization in diogenite plutons emplaced at the base of, or within, the Vestan crust (Mittlefehldt, 2000; Barrat et al., 2010), and magma-ocean models that predict an olivine-dominated mantle at depths of 20-40 km underlying an orthopyroxene-dominated (diogenitic) lower crust (Richter and Drake, 1997; Ruzicka et al., 1997; Ammannito et al., 2013b). The large exposures of olivine-rich material and their association with howardite may favour a magma-ocean model for the origin of the olivine. However, the apparent absence of olivine concentrations in Rheasilvia, where the excavation depth is greater, may suggest that the internal distribution of lithologies was heterogeneous, perhaps supporting the serial-magmatism model, or that the crust-mantle boundary was deeper in the region excavated by Rheasilvia than in the Bellicia-Arruntia region (Ammannito et al., 2013b). A generalized geologic history for these olivine-rich materials could be as follows: ancient large impacts excavated and incorporated large blocks of diogenite-rich and olivine-rich material into the eucritic crust, and subsequent impacts exposed this olivine-rich material in Arruntia and Bellicia. This produced olivine-rich terrains in a howarditic background, with diogenite-rich howardites filling nearby, eroded, older basins. The hypothesis of an exogenous origin seems to be unlikely, since olivine-rich asteroids in the main belt are rare and xenocrystic (chondritic) olivine is in

howardites are uncommon (Ammannito et al., 2013b).

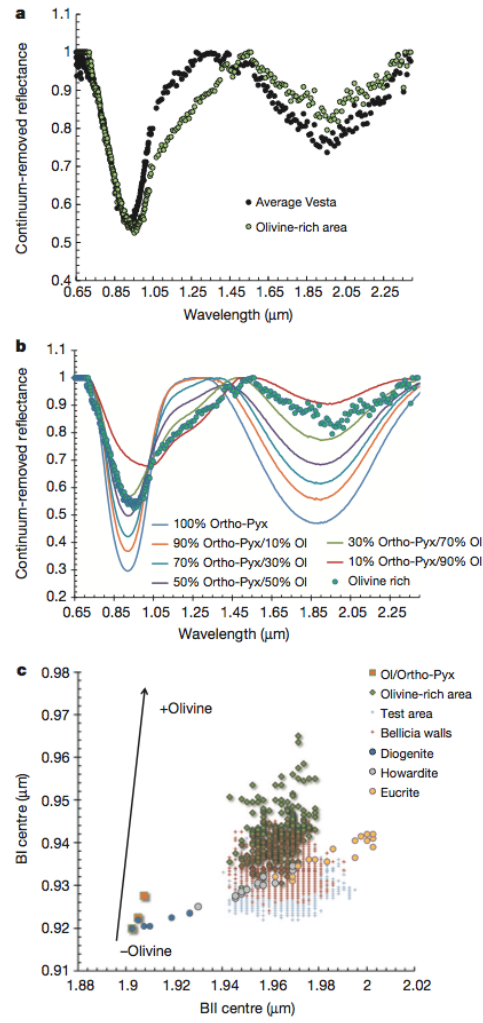


Figure 4.17: A. Olivine rich area on Vesta compared with Vesta average spectrum. B. Olivine-rich area compared with laboratory mixture with different amount of olivine. C. Band II center vs band I center of the HED, olivine and pyroxenes mixture and the olivine-rich area on Vesta (Ammannito et al., 2013b).

Results of the analysis of VIRS, MDIS-WAC and VIR data

Chapter 5

Classification of VIRS and MDIS data

In this chapter we show the results of the classification of VIRS and MDIS data (sections 3.24, 3.3.3) of the region near the Rudaki Crater (Fig. 5.12).

5.1 Reduction of VIRS-MASCS spectra

VIRS, during the the first two flybys, acquired about 1175 spectra distributed in a large portion of the Hermean surface.

The data, already calibrated, must be treated appropriately to extract the information necessary for the analysis. VIRS is not an imaging spectrometer, and the single spectra are acquired in whiskbroom fashion (section 1.3). Thus in addition to the file containing the spectral radiance, those containing the coordinates and the geometry of the pixels are also needed. The radiance file is bi-dimensional and contains n pixels (number of spectra) \times n bands (wavelengths). The coordinates file contains n pixels \times 5 bands for each spectrum, in particular the coordinates of the center and those of the four corners of the pixel. The geometric information (e.g. incidence and emission, and phase angle) are contained in a file of n pixels \times 13 bands (Tables 5.1, 5.2). In Table 5.2 and 5.2 are reported the characteristics of the radiance and the geometries file.

To identify the position of the spectra on Mercury surface it is necessary to project the spectra on the camera images. During the data elaboration we find that, unfortunately, VIRS pixels positions reported in the auxiliary files of the first flyby do not match the topography, as shown in Fig. 5.2. This problem is probably due an inappropriate geometric reconstruction, that make the data of the first flyby unusable.

File dimension for the VIRS data of the first two flyby		
radiance	fb1: 755 pixels (or spectra) X 768 bands	fb2: 420 pixels (or spectra) X 768 bands
coordinates	fb1: 755 pixels (or spectra) X 5	fb2: 420 pixels (or spectra) X 5 bands
geometries	fb1: 755 pixels (or spectra) x 13	fb2: 420 pixels (or spectra) X 13 bands
wavelength	fb1: 768 bands	fb2: 768 bands

Table 5.1: Characteristics of the file of the first two of Mercury flybys carried out by Messenger.

Geometry files bands	
column	content
0	dimension of the mapped region
1	dimension of the mapped region
2	azimuth
3	incidence angle
4	emission angle
5	phase angle
6	inclination
7	spacecraft latitude
8	spacecraft longitude
9	nadir
10	subsolar latitude
11	subsolar longitude
12	true anomaly

Table 5.2: Characteristics of the geometries file.

To verify the correspondence of the spectra with the topography we plot the radiance of the points shown in Fig. 5.1, with those of the corresponding regions in the MDIS-NAC image (Fig. 5.2). We find that the radiance of the camera image and those of the VIRS spectra are not related. We have done the same test for flyby II, and in this case we find a good correspondence between VIRS spectra and the camera image (Figs 5.3, 5.4). For these reasons we decide to use only VIRS data of the second flyby of Mercury.

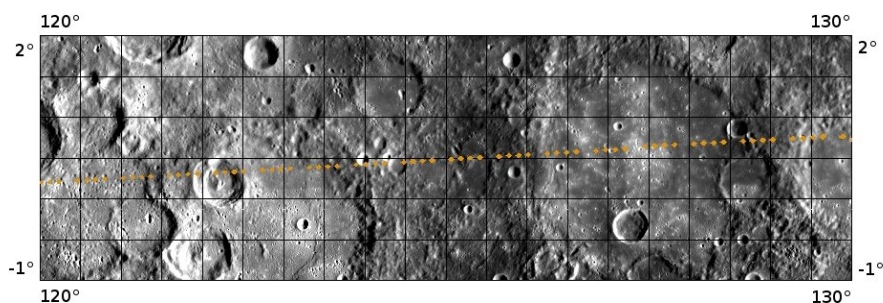


Figure 5.1: Portion of a region covered by VIRS data in the first flyby.

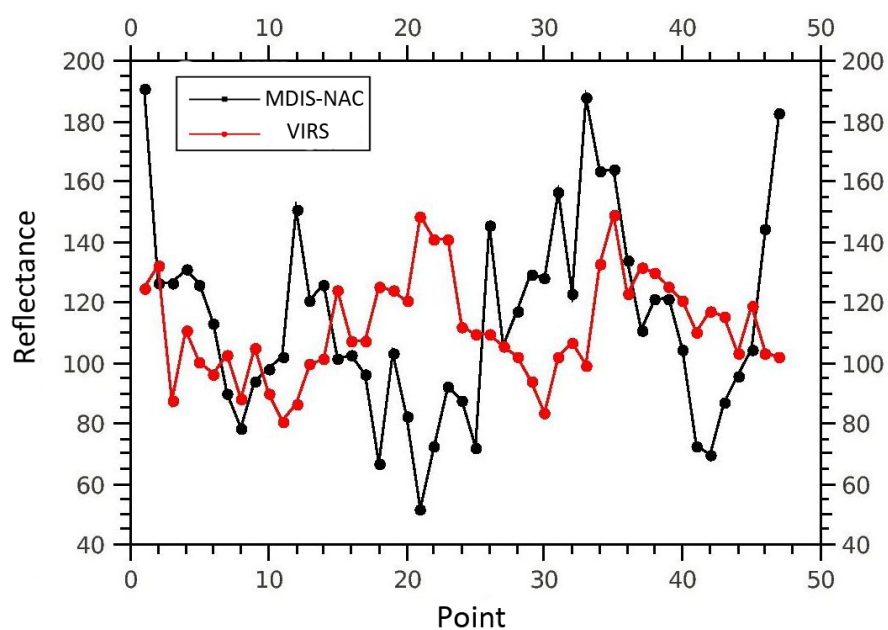


Figure 5.2: Comparison between the radiance ($\text{W}/\text{m}^2 \text{sr}^{-1} \text{nm}$) of the MDIS-NAC image and that of the VIRS spectra does not show any correlation.

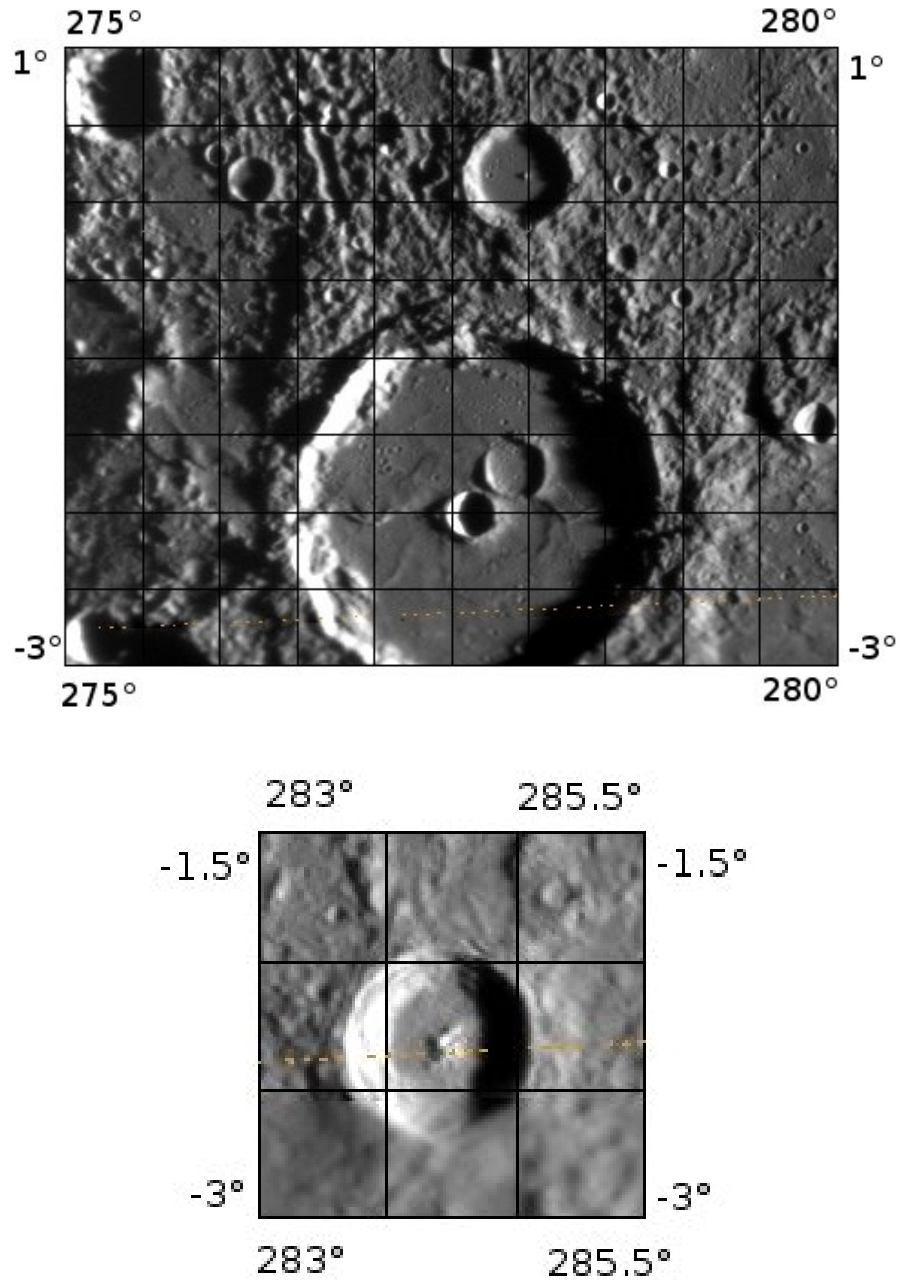


Figure 5.3: Portions of two regions of the flyby II covered by VIRS.

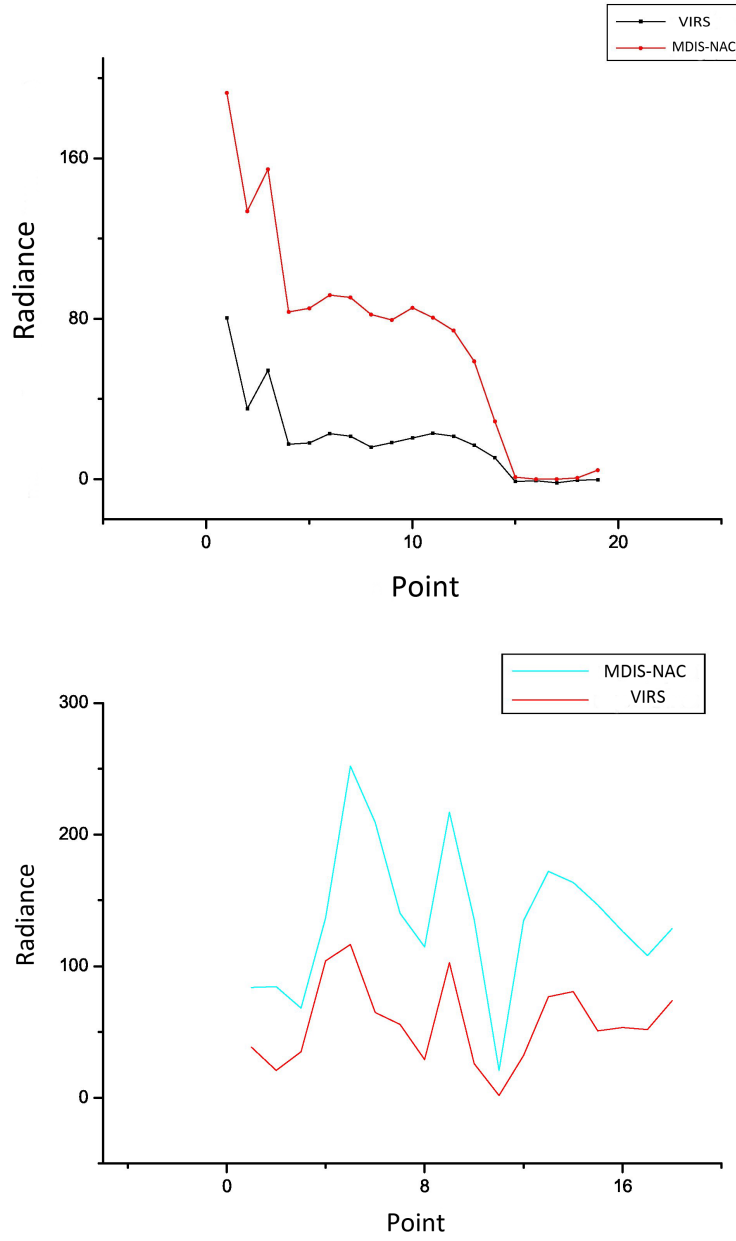


Figure 5.4: Comparison between the radiance ($\text{W/m}^2 \text{ sr}^{-1} \text{ nm}$) of the MDIS-NAC image and that of the VIRS spectra shows a good correlation.

The visible and the infrared parts of the spectrum are contained in two separated files of different bands, 512 bands for the visible (215-1050 nm) and 256 bands for the infrared (850-1450 nm). During the observations, VIRS acquired spectra of dark space periodically (dark) (Fig. 5.5), that must be removed from the data.

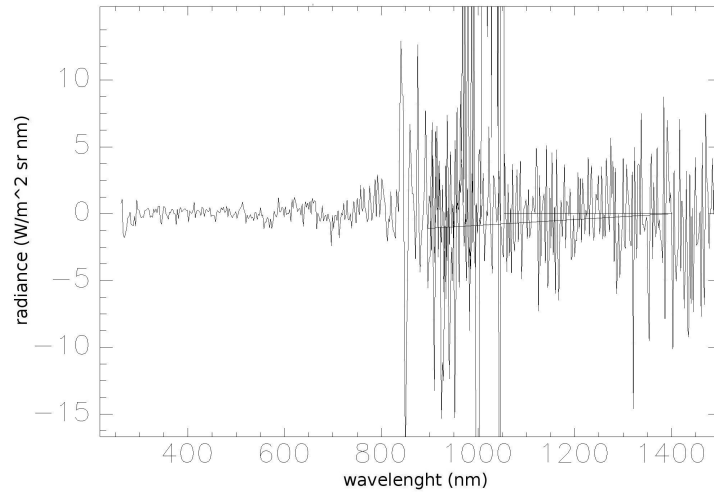


Figure 5.5: Dark spectrum.

To prepare the data for the analysis we write an appropriate algorithm using IDL (Interactive Data Language) (<http://www.exelisvis.com/ProductsServices/IDL.aspx>) a programming language for data analysis. The procedure consists in:

1. Removal of the dark spectra;
2. Extraction of the coordinates;
3. Removal of the noisy bands from the visible part of the spectrum (Fig. 5.6);
4. Removal of the solar radiance and computation of the reflectance;
5. Merging of the visible and infrared channels.

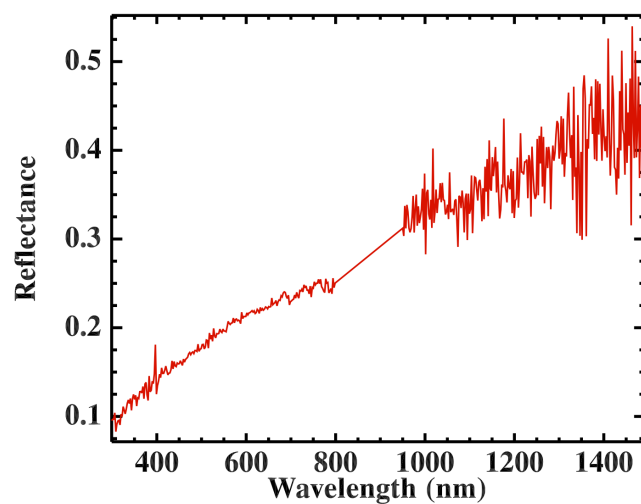


Figure 5.6: Example of VIRS reflectance spectrum.

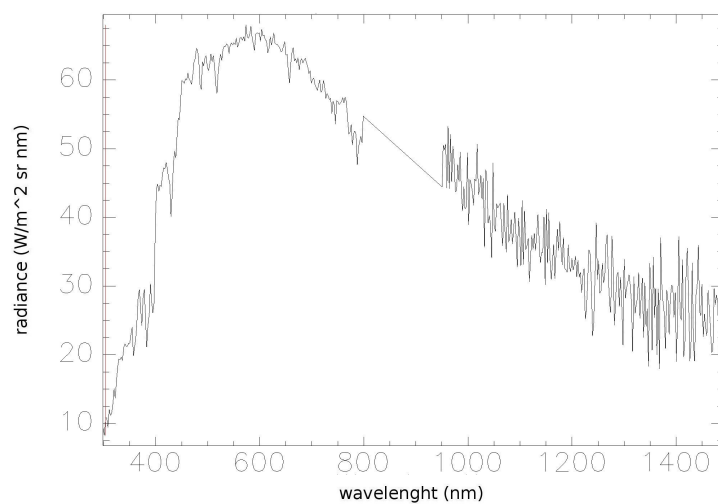


Figure 5.7: Radiance spectrum of the two merged channels (VIS+NIR). The noisy bands of the visible channel have been removed.

5.1.1 Classification of VIRS data

VIRS spectra appear to lack evident absorption bands, but present only spectral slope variations. In this condition it is difficult to extract information about the mineralogy. For this reason we decide to apply classification methods on VIRS data. Clustering methods are useful when no *a priori* information is available, as in our case. Since we are not able to identify the endmembers, we decide to use an unsupervised classifier, ISODATA (Section 2.16), with the constraint that the number of classes must be included between 3 and 10, a reasonable interval in our case.

The classifier identifies 6 different classes. In Figs 5.9, 5.10 and 5.11, we show the classes obtained by the classification of the VIRS data projected on the MDIS-NAC image. In Table 5.3 we show the results of the classification. Magenta and red classes are the less populated, and represent respectively the shadows and the illuminated regions. Blue and yellow classes are the more populated and are associated to intermediate terrain. It is interesting to note the correspondence between the yellow class and the smooth plane in the Rudaki area (Fig 5.10). Cyan class is associated with the bright areas in the camera image and the green with darker regions. In Fig. 5.8 mean spectra of each class are shown.

Although no absorption bands have been observed, however, the spectral slope can give information about the type of material present. The slope is an indicator of the maturity of the soil; thus higher spectral slopes (cyan spectra) are indicative of a fresher terrain less affected by space weathering.

ISODATA classification results	
Classes	Frequency
Red	12 (3.5 %)
Green	39 (11.3 %)
Blue	152 (43.9%)
Yellow	106 (30.6%)
Cyan	19 (5.5 %)
Magenta	18 (5.2 %)

Table 5.3: Classes obtained from the ISODATA classification of the VIRS data.

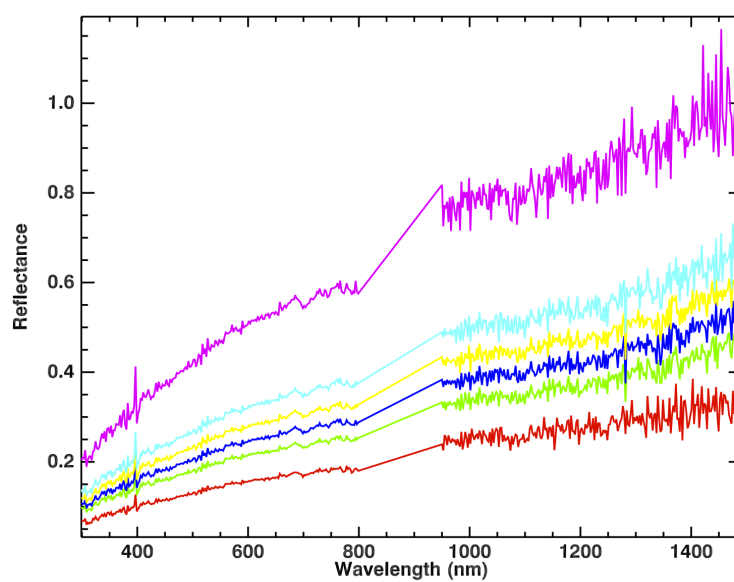


Figure 5.8: Spectral modes of the obtained classes for reflective data VIS+NIR relative to flyby II.

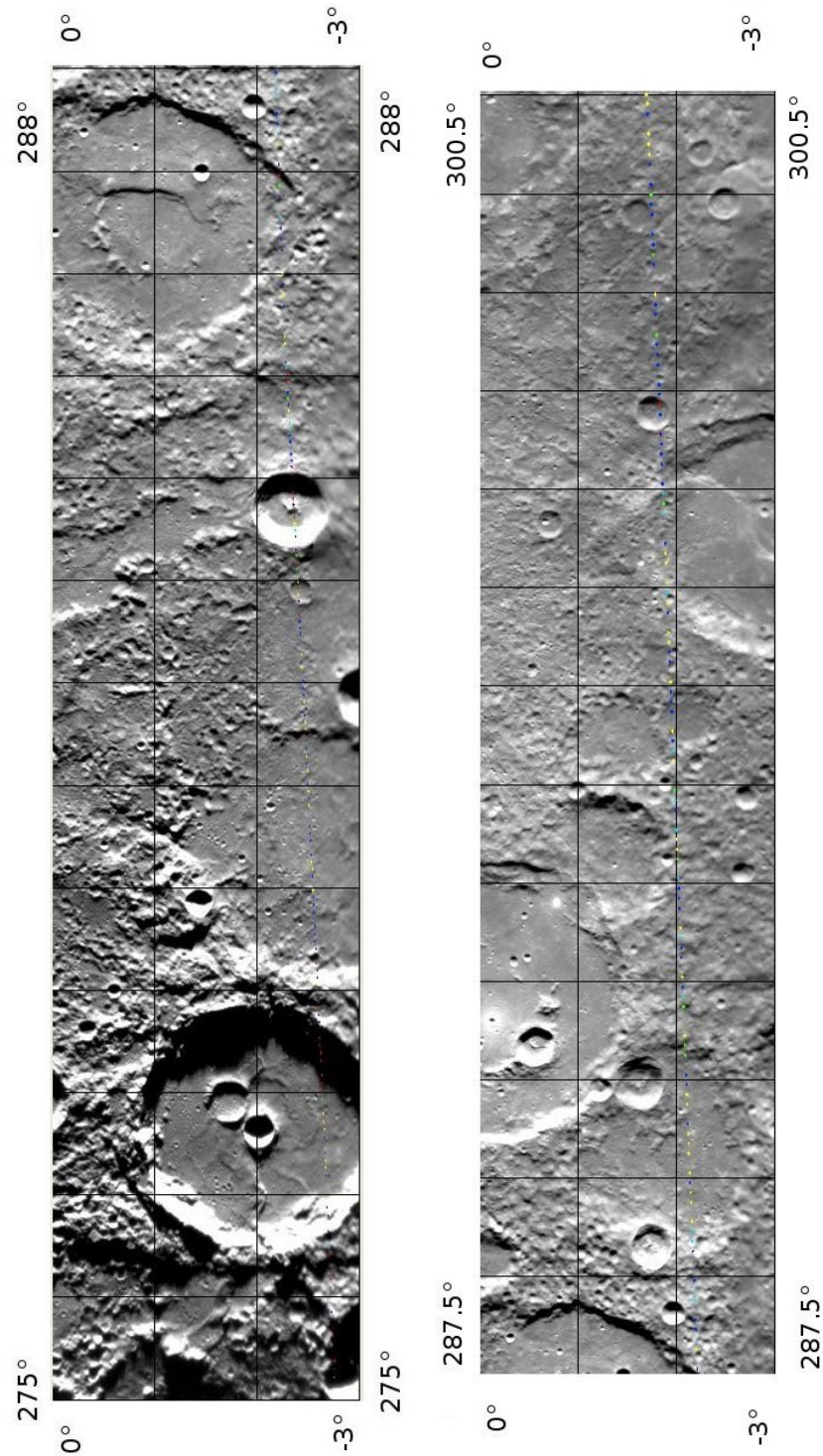


Figure 5.9: Projection of the classes on Mercury's surface.

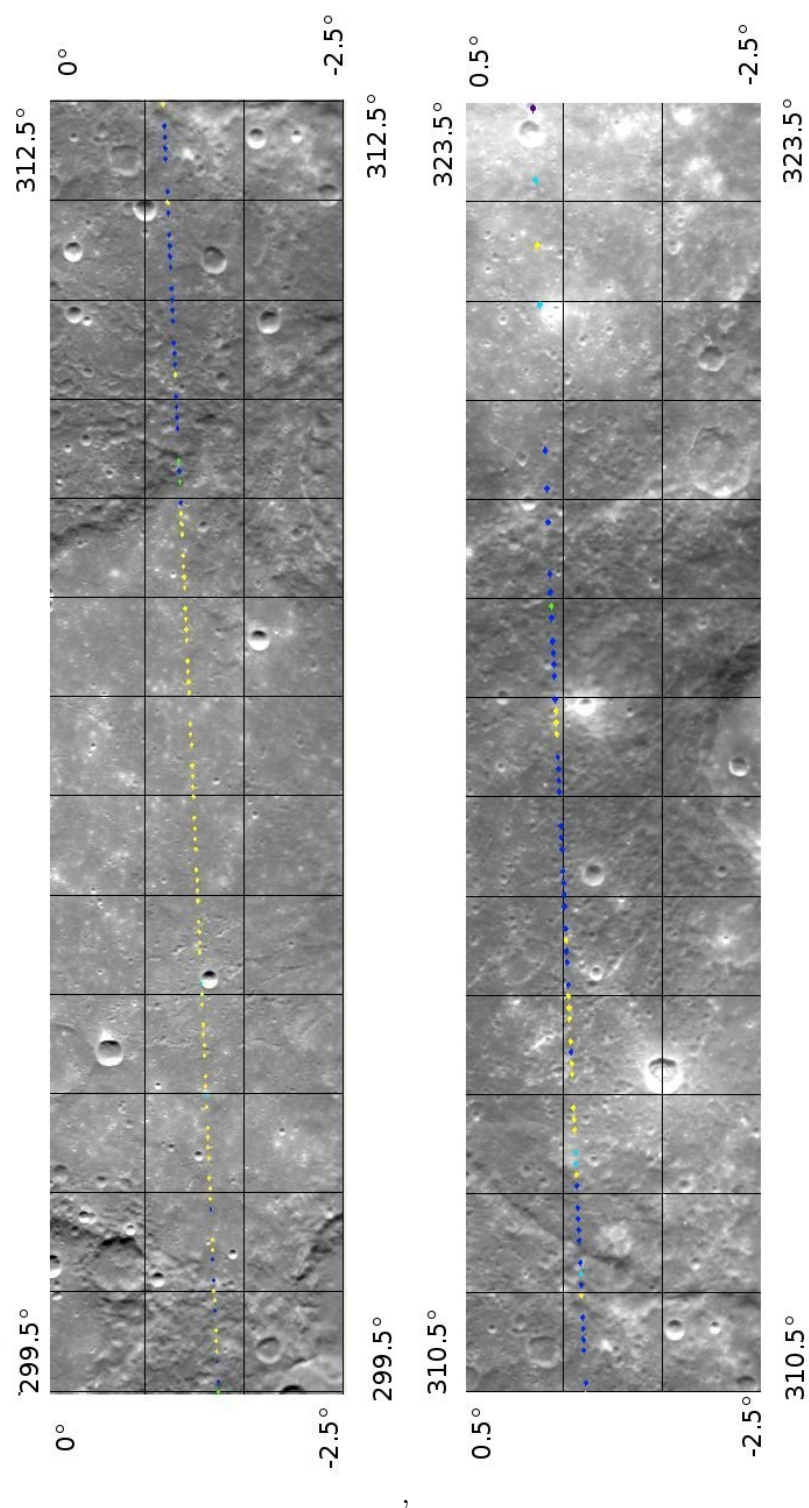


Figure 5.10: Projection of the classes on Mercury's surface.

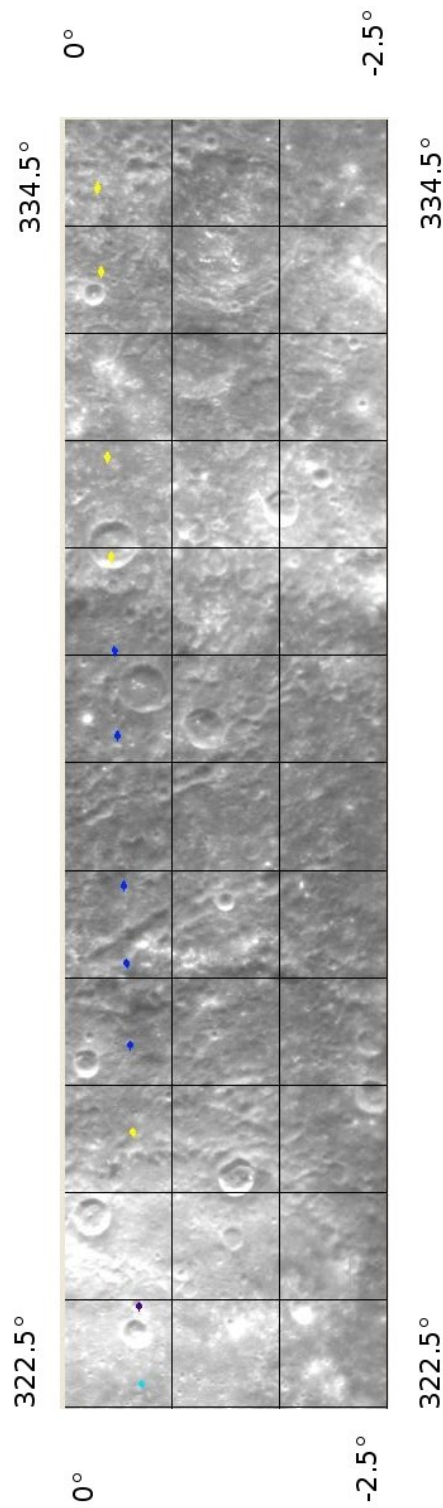


Figure 5.11: Projection of the classes on Mercury's surface.

5.2 Reduction of MDIS-WAC images

To complete the analysis of the Rudaki region, we use WAC calibrated images of this area relative to the second flyby of Messenger. To prepare the data for the analysis we use ISIS 3 (Integrated Software for Imagers and Spectrometers), a software developed by USGS very useful for to prepare images and hyperspectral images (<http://isis.astrogeology.usgs.gov/index.html>). With ISIS 3 we create a multispectral cube of eleven filters in order of increasing wavelength, we coregister and georeference the data, and we project the cube with the Mercator projection. We create a multispectral cube with a resolution of 447m/pixel (Fig 5.12).

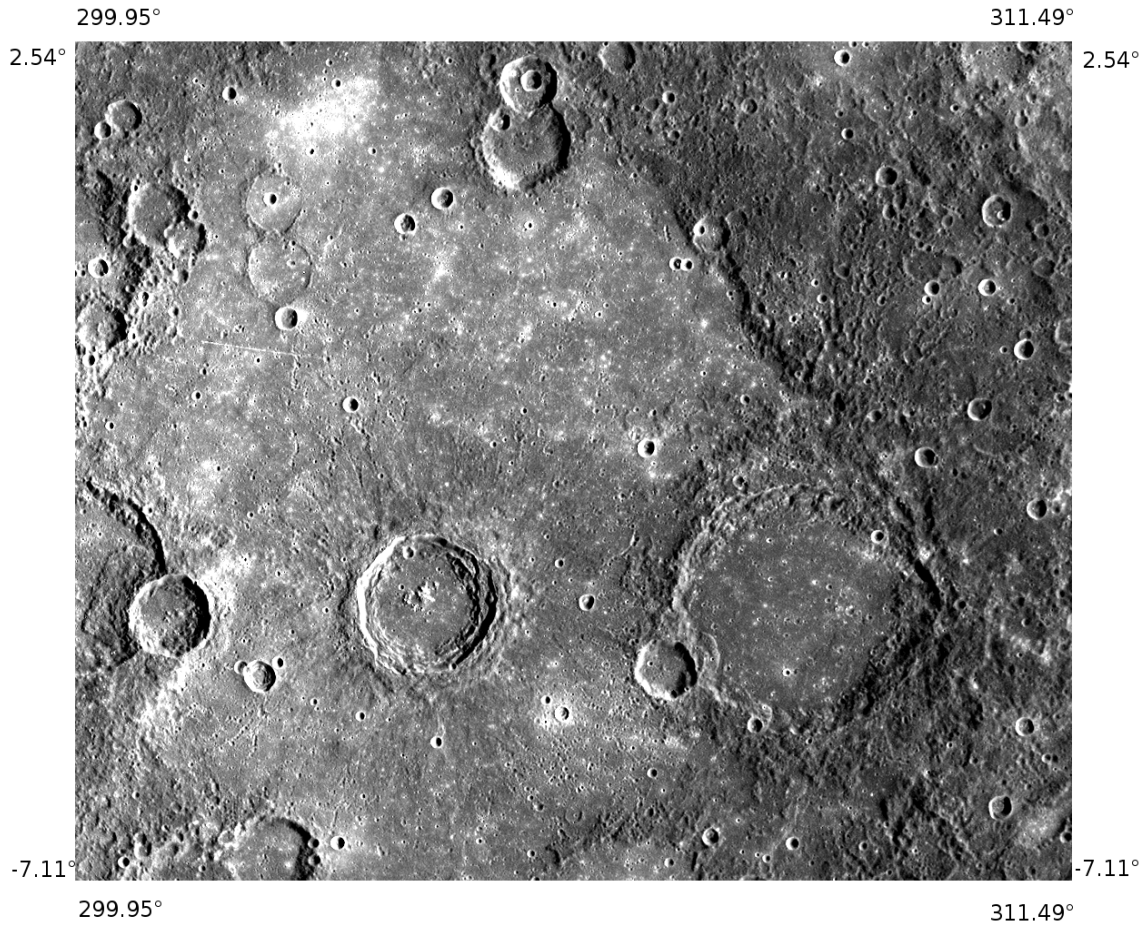


Figure 5.12: Image of the WAC Rudaki area at 433nm.

5.2.1 Classification of MDIS-WAC data

In this case we use first the ISODATA unsupervised classification method, to determine the principal classes, and subsequently we apply the MINIMUM DISTANCE supervised method to improve the classification (sections 2.16, 2.5.2). We apply ISODATA with the constraint that the number of classes must be included between 3 and 10. ISODATA identifies 4 classes, yellow for the bright regions, blue for the smooth plane, green for the rough areas and red for the darker region (Fig. 5.13, 5.14). In this case ISODATA is not able to distinguish the shadows from the low reflectance and the bright region from the illuminated edge of the craters. To solve the question, we apply ISODATA separately to the region corresponding to the yellow and the red class. The classification produces two classes for each region, separating the shadows from the intrinsically dark regions and the illuminated edge of the crater from the bright regions.

To refine the classification of the Rudaki area, we apply the MINIMUM DISTANCE classification method, choosing as endmembers the green, the blue and the yellow class derived by ISODATA (Fig. 5.13, 5.14), and the two classes obtain by the ISODATA classification obtained by the bright and the dark areas, related to the shadow and the illuminated edge of the craters. MINIMUM DISTANCE classification method allows to remove the classes not representative for the analysis (red and cyan classes). MINIMUM DISTANCE identifies three principal classes each one representative of a different terrain. Green for the low reflectance rough areas, yellow for the bright regions and blue for the smooth plane (Fig. 5.15, 5.16).

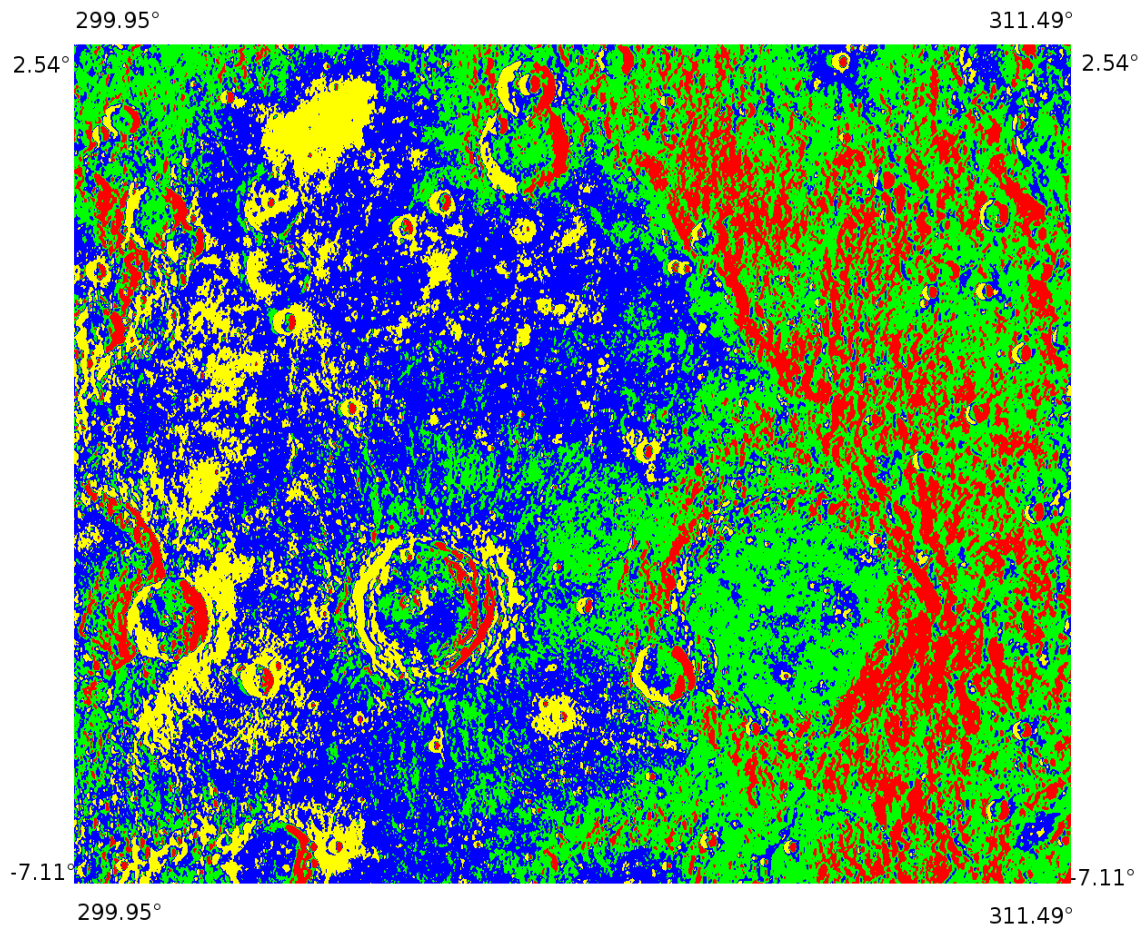


Figure 5.13: Result of the ISODATA classification method.

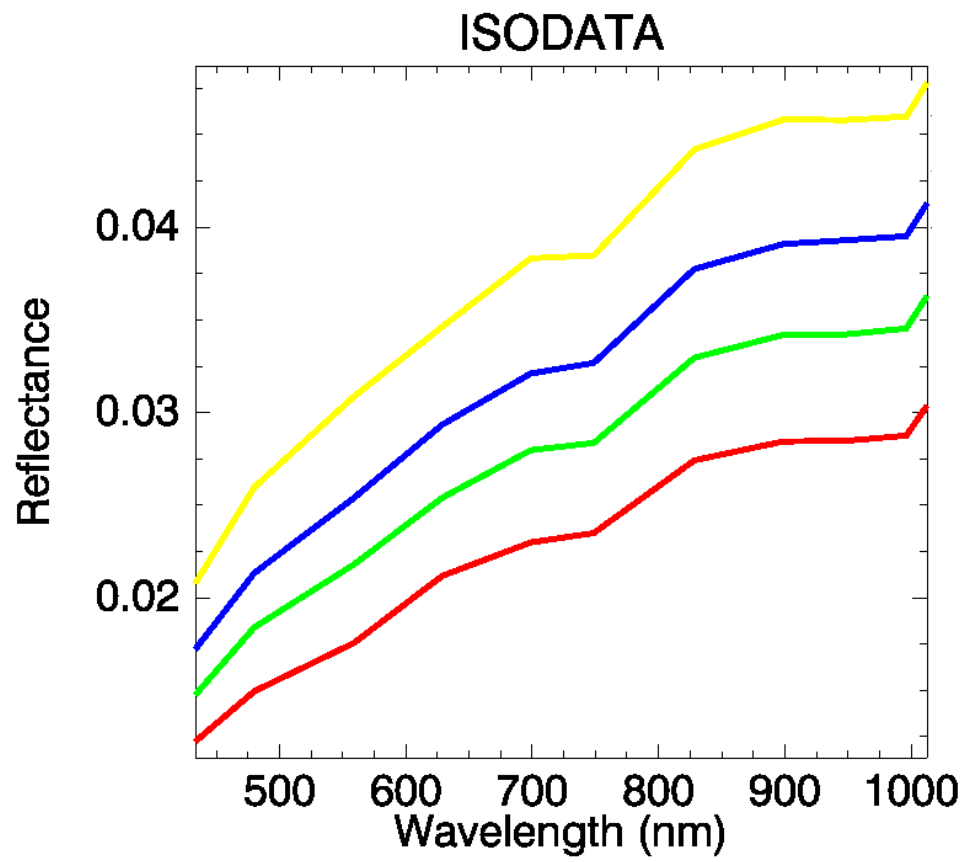


Figure 5.14: Mean classes obtain by ISODATA classification.

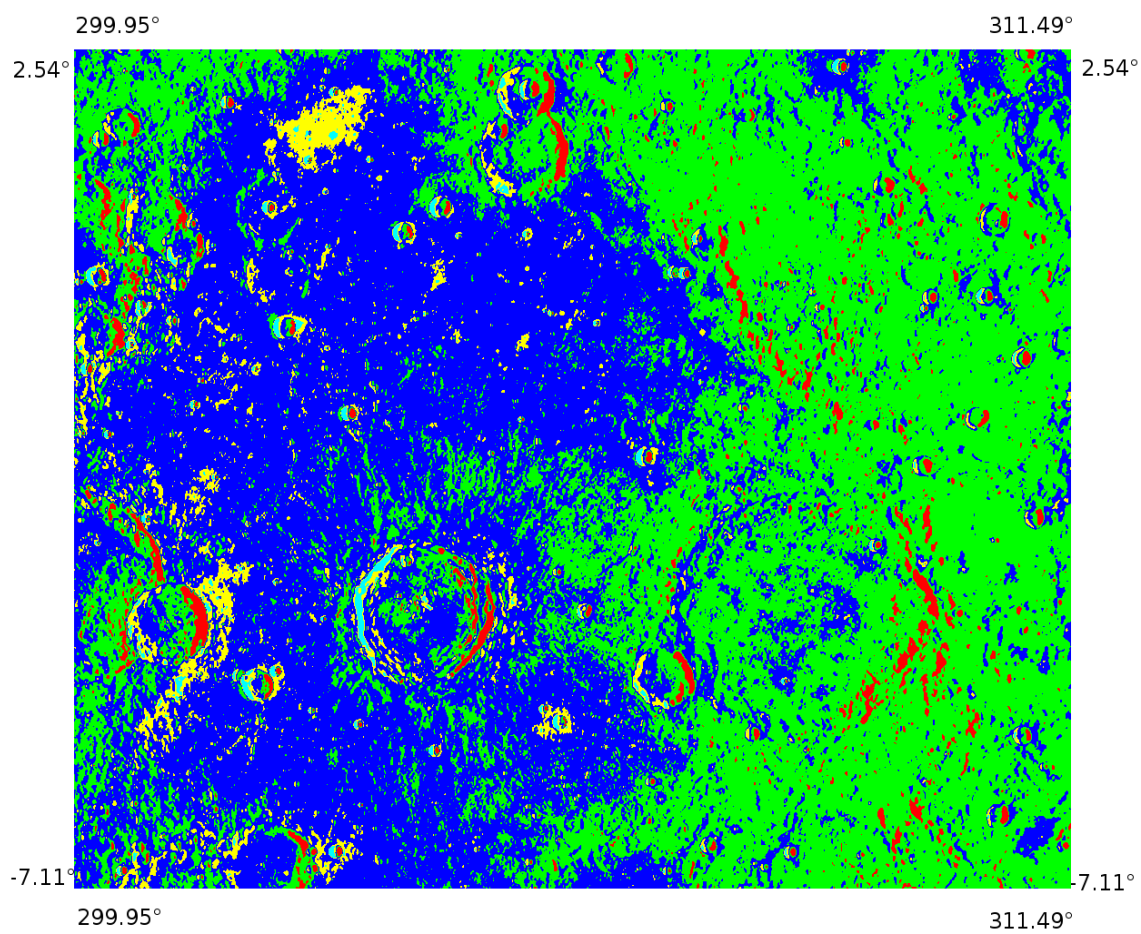


Figure 5.15: Result of the MINIMUM DISTANCE classification method.

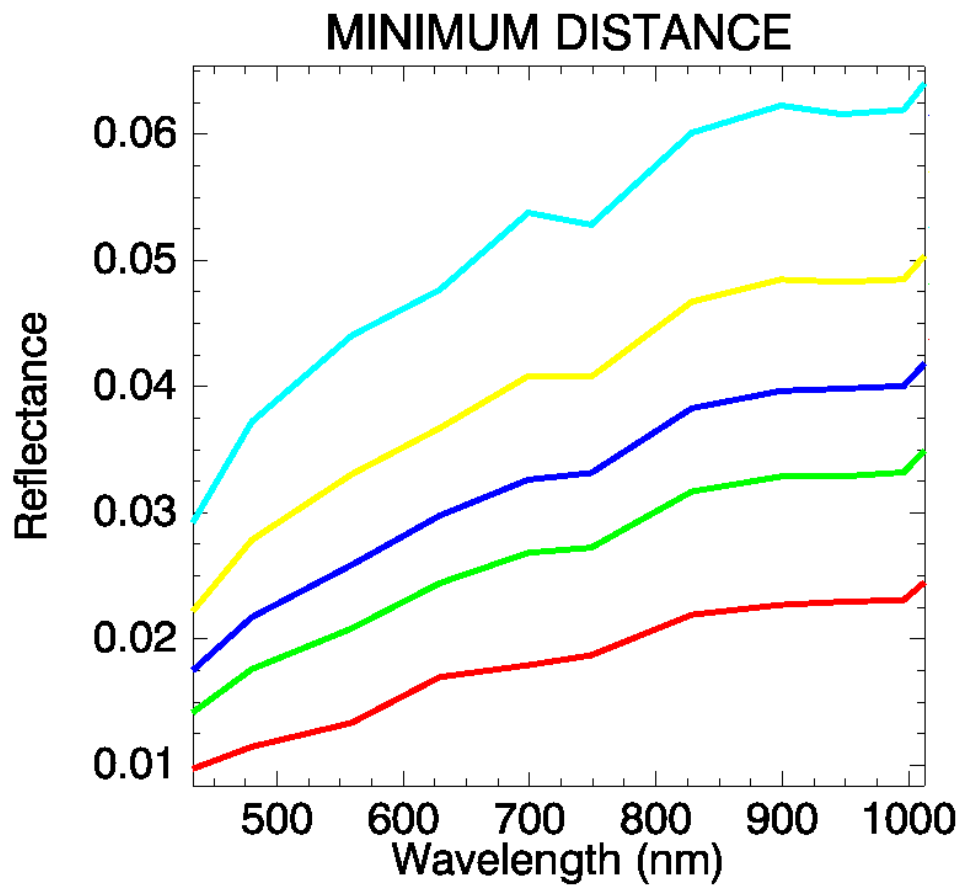


Figure 5.16: Mean classes obtain by MINIMUM DISTANCE classification method.

5.3 Comparison between VIRS and MDIS-WAC results

Although we are not able to determine the mineralogy of the analyzed areas, due to the lack of absorption bands in VIRS spectra, application of classification methods on VIRS and MDIS data produce satisfactory results. For VIRS data we find six classes that, when projected on the camera mosaic, highlight a good correspondence between VIRS spectra and the topography. Classification of MDIS data permit excluding classes affected by illumination conditions from classes indicative of intrinsic characteristics of the surface. MINIMUM DISTANCE classifier finds three principal classes, related to smooth plains, bright areas, and rough region. It is interesting to note the correspondence between the classification of VIRS spectra (Fig. 5.10) and the result obtained by MDIS-WAC. Classes individuated by MDIS correspond to those of VIRS spectra of the same region. Thus, we can associate the spectral information to the correspondence terrain. The spectral slope variations found for the VIRS data indicate that rough areas correspond to mature terrain more affected by space weathering, in contrast to smooth plane (intermediate terrain) and bright areas that represent fresher, and thus younger regions.

Chapter 6

Spectral analysis of the BM units on Vesta

In this chapter we describe the results of the spectral analysis of the bright units on Vesta, published in (Zambon et al., 2014b).

6.1 Classification of the BM units

Based on a relative criterion, BM units are defined as areas with higher reflectance than their surroundings. Detection and morphological classification of BM units was performed by Mittlefehldt et al. (2012). We studied most of the BM units mapped by Mittlefehldt et al. (2012). The geographic distribution and classification were improved, and we considered the latest version of the map (Mittlefehldt and Li, personal communication). The distribution of BM units is non-uniform. Large areas in the northern hemisphere appear to lack BM compared with the southern hemisphere, due to poorer data coverage resulting from shadows at northern latitudes during the time of Dawn's orbital mission (Mittlefehldt et al., 2012). Four morphological classes of BM have been defined. Type 1 contains two subgroups: Type 1a and Type 1b. Type 1a represents Crater Wall Material (CWM), discontinuous outcrops or large blocks of rock; Type 1b, called Slope Material (SM), generally has a wedge/tongue shape and often occurs as debris found downslope from the CWM (Mittlefehldt et al., 2012; Li et al., 2012). Most of Type 1a and 1b appear together on the walls of the craters, suggesting a common origin (Li et al., 2012). Type 2 is the Radial Material (RM), always associated with the ejecta of large craters. Type 3 is Spot Material (SpM), frequently associated with the ejecta of the small craters (diameter < 100m). Type 4, diffuse material, is present in six sites and is not correlated with impact craters. Here we

analyze the spectral properties of Types 1 and 2, which are the most abundant types on Vesta and are easily recognized in the VIR data, while Type 3 is typically too small for analysis at the spatial resolution of VIR data.

In Fig. 6.1, some examples of Type 1 and 2 BM units are shown. SM is particularly evident in Cornelia (green arrow), Tuccia and Myia craters are a clear example of RM (blue arrows), while Cornelia, Aelia and Myia provide an example of the coexistence of bright and dark material (Stephan et al., 2014; Palomba et al., 2014).

In this paper, we have carried out a classification based on the normal visual albedo (Table 6.1). Normal visual albedo of each candidate BM occurrence was compared with the Vesta geometric albedo of 0.38 (Tedesco et al., 1989; Li et al., 2010; Schröder et al., 2013). We recognize five albedo level classes: BM units with albedo that exceeds Vesta’s geometric albedo of Vesta by up to 10%, between 10% and 20%, between 20% and 30%, more than 30%. A fifth class consists of bright regions that instead have an albedo lower than the Vesta average (Table 6.1). It is important to note that in some cases there is a coexistence of bright and dark material, thus BM units on Vesta are currently not defined on the basis of an absolute criterion, but rather a relative criterion: if a region is brighter than the surroundings, then it is tagged as a BM unit. For this reason, we have some BM units whose albedo is lower than the geometric albedo of Vesta. Values of normal visual albedo were derived from the Vesta albedo map (Schröder et al., 2013) and are available in the latitude range from -90° to 30° . Fig. 6.2 shows the locations of the BM occurrences studied in this paper (Tables C.7, C.8, C.9).

We assign names to the BM sites according to the name of the crater in which they are located. Bright Units in unnamed craters are assigned a "BU" followed by a progressive number.

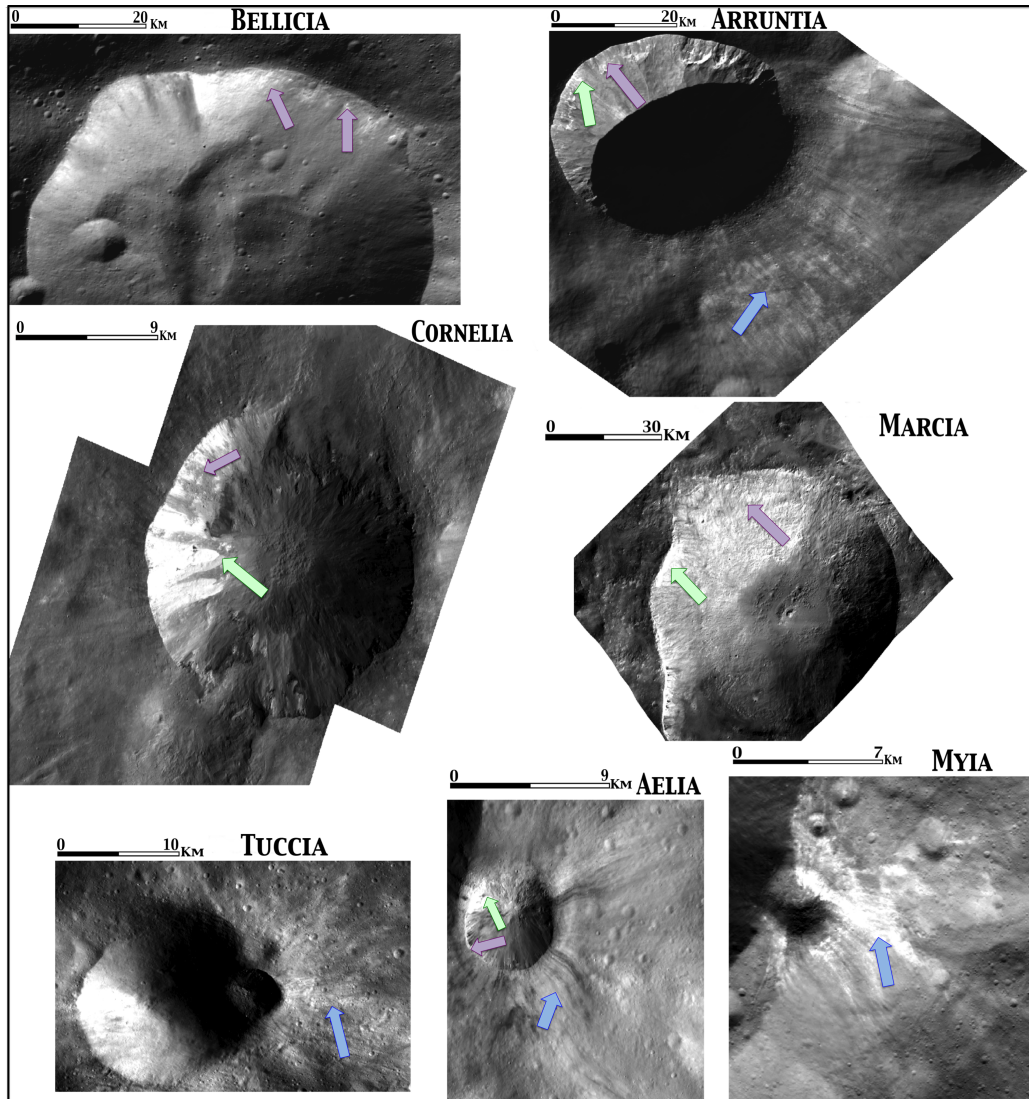


Figure 6.1: Equirectangular projection of the Framing Camera clear filter images relative to the bright material units of Types 1 and 2. Violet arrows represent the CWM, green arrows the SM, and the blue arrows the RM. Images credit: NASA/JPL-Caltech/UCLA/MPS/DLR/IDA

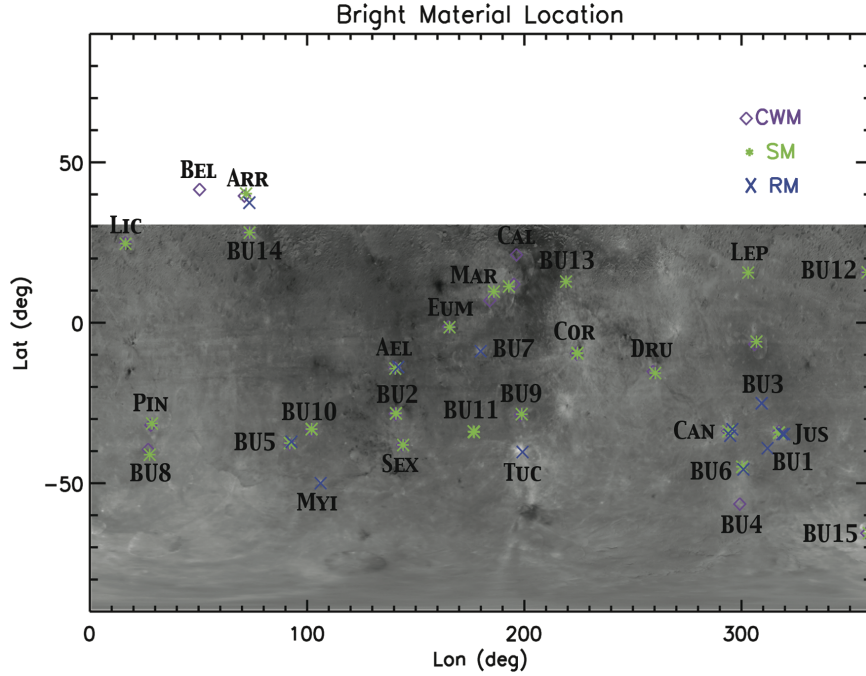


Figure 6.2: Location of the BM on Vesta global albedo map. As in Fig. 6.1, we represent in violet the CWM, in green the SM, and in blue the RM. BM names are indicated with the first three letters of the crater name in which they are found. BM in unnamed craters are indicated with the letters "BU" followed by a progressive number. We employ the Claudia coordinates system.

Normal Visual Albedo Classification			
%	CWM	SM	RM
<0%	BU14, Calpurnia, Eumchia, Oppia	Eumachia, Oppia, Aelia	Aelia
0%-10%	Licina, BU12, Marcia-1, Marcia-2, BU2-2, BU9, D10-1, BU10-2, Sextilia, BU8	BU14, Licinia, Lepida, BU12, Marcia-1, Marcia-2, Cornelia-1, Drusilla, BU9, BU11-1, BU11-2, BU11-3, BU5, Sextilia, BU8	BU5
10%-20%	Drusilla, Pinaria, Canuleia Justina-1, Justina-2, BU15	BU13, Cornelia-2, Cornelia-3, BU2-1, BU2-2, Pinaria, BU10-1, BU10-2, Canuleia, Justina-1, Justina-2, BU6	BU7, Canuleia-1, Canuleia-2, BU1 Justina-1, Justina-2, BU6
20%-30%	Cornelia-1, Cornelia-2, BU4		BU3, Myia
>30%		BU15	Tuccia

Table 6.1: Classification of the BM according to the normal visual albedo. The bright regions are classified in five categories. The first column indicates how much BM units are bright, with respect to Vesta geometric albedo.

6.2 Dataset description

In this work we used VIR data calibrated to reflectance from $0.4\mu\text{m}$ to $2.5\mu\text{m}$, focusing our analysis on the two pyroxene bands. The bridging between the two VIR channels is performed in post-processing. A break in the spectra near $1.1\mu\text{m}$ seen in Figs. 6.3 and 6.4 is due to the junction between the visible and infrared channels. To reduce the noise, we removed recurring spikes and smoothed the spectra before deriving the spectral parameters. A detailed description of the band parameter computation is given in Ammannito et al. (2013a) and De Sanctis et al. (2012a) supplementary material.

For this study, we chose VIR data from the HAMO and HAMO-2 phases of the mission. This dataset provides good coverage of most of the Vesta's surface at good spatial resolution, except for latitudes north $> 70^\circ$. The HAMO and HAMO-2 VIR coverage obtained by VIR is shown in Ammannito et al. (2013a). VIR data with the highest spatial resolution (LAMO) are limited, covering only very small portion of the surface near the south pole. In the case of the BU15 BM location, only LAMO data are available. We selected 75 bright material locations for analysis: 29 observations of CWM, 32 observations of SM and 14 observations RM. The choice of the BM sites to be analyzed was made according to the quality and availability of the VIR data. During the different phases of the mission, some areas were mapped more than one time. In this case, we refer to the acquisitions as follows: BU10-1, BU10-2, Marcia-1, Marcia-2, etc. The identification of the bright units within the VIR data was done using the coordinates reported by Mittlefehldt et al. (2012). Subsequently, we selected as bright pixels those with albedo 20% greater than their surroundings. The final spectrum for each bright area is the average of those pixels (Fig. 6.3, 6.4). The locations of the BM units are given in the coordinate system known as "Claudia" (Section 2.2)(supplemental material of Russell et al., 2012; Li et al., 2012; Roatsch et al., 2012)

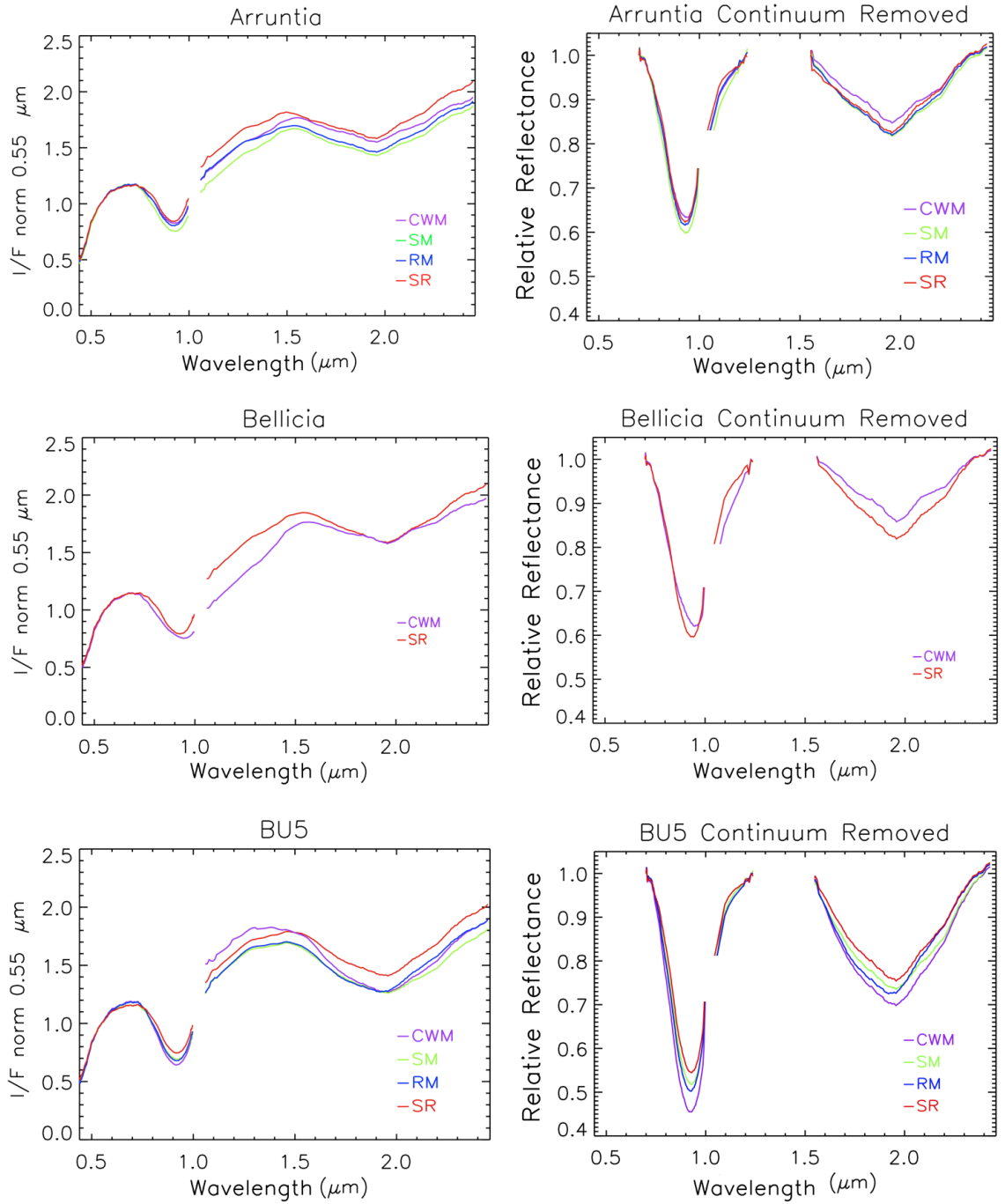


Figure 6.3: Spectra for the Arruntia, Bellicia, and BU5 BM locations. CWM are plotted in violet, SM are green, RM are in blue, the surrounding region (SR) are in red. Left column: Reflectance spectra normalized at $0.55\mu\text{m}$. Right column: Continuum-removed spectra. Arruntia and Bellicia are olivine-bearing locations, while BU5 is a more typical example of BM. The gap at $1.1\mu\text{m}$ is the connection between the VIR visible and infrared channels.

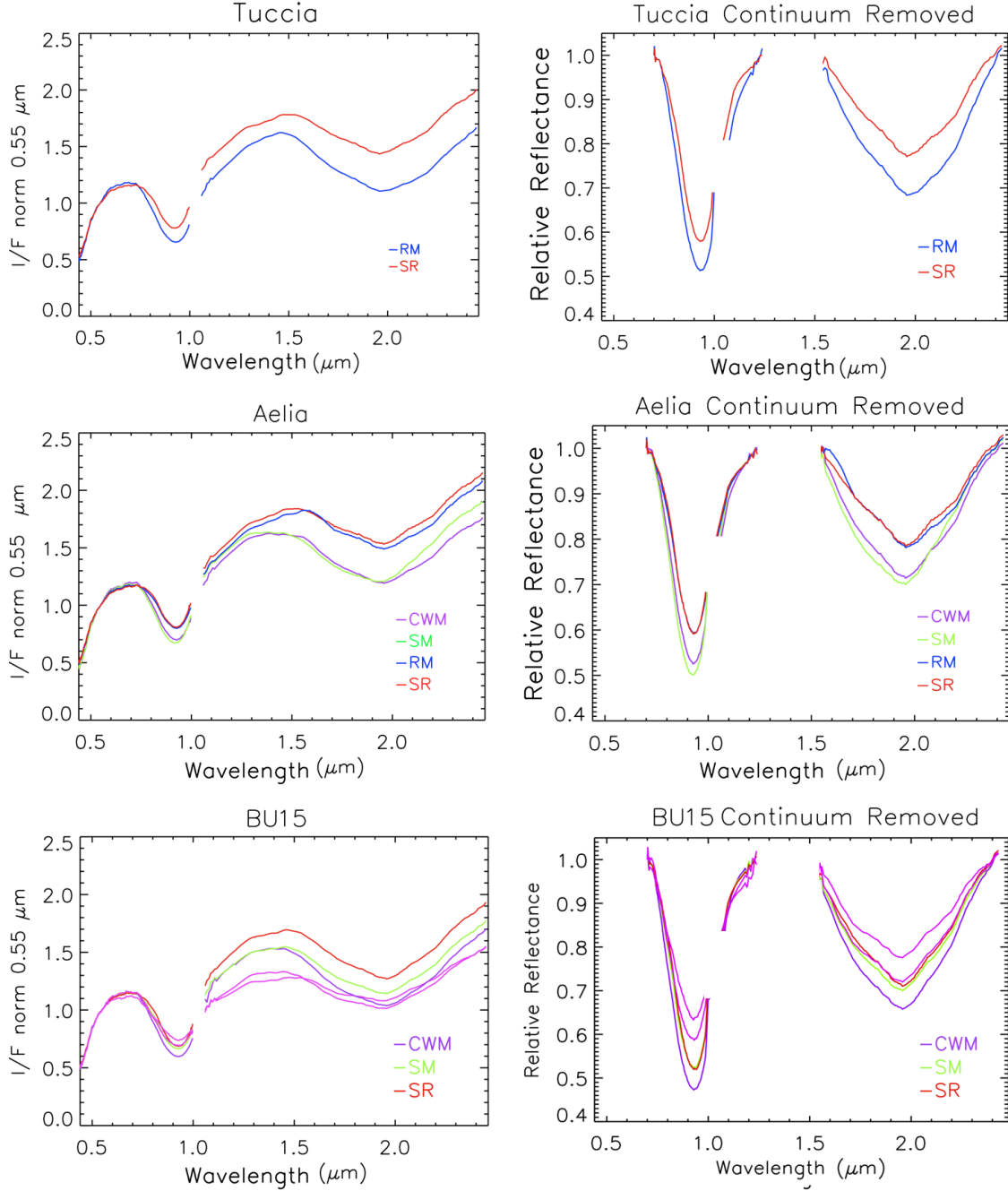


Figure 6.4: The mean spectra of Tuccia, Aelia and BU15 BM units. Tuccia and BU15 are the brightest BM units in our study set. BU15 contains a very bright streak (region bounded by the black circle in Fig. 6.11) that has band depths shallower than the surroundings, unlike the other bright units. The magenta spectra in BU15 plot are an example of spectra of the very bright streak. In Aelia, the reduction of the bands in the RM is due to the presence of admixed dark material. The colors of the spectra are indicative of the BM types, as described in Fig. 6.3. Left column: Reflectance spectra normalized at $0.55\mu\text{m}$. Right column: Continuum-removed spectra. The gap at $1.1\mu\text{m}$ is the connection between the VIR visible and infrared channels.

6.3 Description of the spectral parameters

The aim of this work is to gather information about the spectral characteristics of the BM and to highlight possible differences with respect to the other Vesta terrains. We chose three spectral parameters that are diagnostic for mineralogical composition and physical properties of the material: band center (BC), band depth (BD), and band area ratio (BAR). Band centers and BAR do not strongly depend on the viewing and illumination geometry (Cloutis et al., 1986), but they can show small shifts in case of relevant temperature changes (Hinrichs et al., 1999; Moroz et al., 2000; Hinrichs and Lucey, 2002; Burbine et al., 2009; Moskovitz et al., 2010). As we will show later, in our case temperature variations are small, thereby they do not affect the evaluation of the composition of the BM.

Band depth is the only spectral parameter that we considered that can vary depending on the illumination conditions. In our case, we select observations with phase angles between 28° and 52° and incidence angles less than 60° . Longobardo et al. (2014) show that in this range, band depths are only weakly dependent on the phase angle. Hence a photometric correction is not mandatory for our purposes (for more details see Longobardo et al., 2014).

To calculate the spectral parameters, we used the method described in Ammannito et al. (2013a), to be consistent with previously published work (De Sanctis et al., 2012a, 2013; Ammannito et al., 2013a). In this approach, the band I continuum was fitted by a straight line between the reflectances at $0.7\mu\text{m}$ and at $1.238\mu\text{m}$; while the band II continuum was fitted between $1.513\mu\text{m}$ and $2.487\mu\text{m}$. We have verified that changing the way in which the continuum is computed (small deviations in the wavelength location of the two fit points) does not alter the band centers substantially; changes are within the uncertainties associated with the band center computation. All the band parameters discussed in the present work were calculated after the removal of the spectral continuum. The band center is taken as the minimum of the second-order polynomial that provides a best fit with the measured absorption band (Ammannito et al., 2013a). Band depth is calculated following the definition by Clark and Roush (1984) (Formula 1.8). For more details, see the supplementary material of De Sanctis et al. (2012a) and Ammannito et al. (2013a).

The Band Area Ratio (BAR) is defined as the ratio of the band area II and band area I (Cloutis et al. 1986). We calculate the band area as the area enclosed by the band and the continuum line.

6.3.1 Error estimation and temperature correction

For each location, we consider the average values of the spectral parameters for the selected VIR pixels, and we take the standard deviation as an estimate of the uncertainty. Furthermore the uncertainty associated to the spectral parameters, is similar to the standard deviation, for example the error associated with the band centers is $0.004 \mu\text{m}$ for the Band I and $0.02 \mu\text{m}$ for the band II (Ammannito et al., 2013a). Since we consider average values, it may happen that in some cases the BM are mixed with dark material at very small spatial scales or that the bright regions are represented by only a few pixels. The largest STD values are found for those BM that are mixed with dark material at a small local scale because of the difficulty in selecting "pure" BM-only pixels. Representative cases are Aelia, Arruntia and Sextilia. High STD values are also found for the CWM, which are usually very small and more difficult to isolate in VIR data.

Laboratory data show that band center positions are subject to temperature variations (e.g., Roush and Singer, 1986; Hinrichs et al., 1999; Moroz et al., 2000; Hinrichs and Lucey, 2002; Burbine et al., 2009). A thorough analysis of the temperatures of BM units found on Vesta as retrieved from VIR infrared data (Tosi et al., 2014a) concluded that they have surface temperatures in the range from 198 to 269 K. Limiting the analysis only to the period of maximum daily insolation, the average temperatures of BM units are between 252 and 265 K with maximum values between 255 and 266 K (Tosi et al., 2014a). Due to Dawn's observational planning, aimed at optimizing the level of signal reflected from the surface of Vesta, most BM units were observed by VIR in a relatively narrow range of local solar times, during which only small thermal excursions were recorded. Studies carry out on pyroxenes sample (bronzite and enstatite) show that the band center depend on the temperature (Burbine et al., 2007, 2009; Moskovitz et al., 2010). Burbine et al. (2009), calculated the formulas to correct the band center for the temperature using the results obtained by Moroz et al. (2000) that measured the band centers position of two sample of orthopyroxenes (one sample for bronzite and one for enstatite) at three temperature (80 K, 173 K and 293 K). The formulas obtained are:

$$\Delta BI(\mu\text{m}) = 0.00505 - 0.000017 \ T(K)$$

$$\Delta BII(\mu\text{m}) = 0.0544 - 0.000185 \ T(K)$$

Taking into account the assumption made before, we have applied this method to the VIR data. The BM sample considered have a temperature interval between 223°K and 264°K (Tosi et al., 2014a). Applying this method

to the VIR data we obtained a shift of about $0.001\mu\text{m}$ for the band I center and $0.01\mu\text{m}$ for the band II center towards higher wavelengths. The results obtained are in accordance with Burbine et al. (2007, 2009); Moskovitz et al. (2010). Recently (Longobardo et al., 2014) have developed a method based on the VIR data to correct the band center position:

$$BCIL = BCI - (0.000055)(T(K) - 300K)$$

$$BCIIL = BCII - (0.00018)(T(K) - 300K)$$

The formulas referred to a temperature of 300 K. In both cases, considering the temperature correction, band centers are shifted towards longer wavelengths, therefore the howarditic units move toward the eucrite region and diogenitic units toward the howarditic region. The Longobardo et al. (2014) correction provides the same results for the band II center, while the band I center shift is slightly larger (up to $0.004\mu\text{m}$). The possible thermal shifts of the band centers are comparable with the STD of the BM data, therefore confirming that, for the purpose of mineralogical analysis, temperature variations are not relevant.

6.4 Bright Material spectral analysis

In this section we describe the results of the spectral analysis performed on BM units. We used these parameters to derive information on the origin and nature of the BM units on Vesta.

6.4.1 Band centers

Band centers of the BM units, computed as explained above, have been analyzed in comparison with other quantities such as albedo, band depths and laboratory analogue band centers values.

A classical way to infer the mineralogy of a sample is to plot band I and band II centers positions (Fig. 6.5). The values obtained for the 75 observations of BM analyzed are shown in Tables C.1, C.2 and C.3. Most of the band I and band II centers lie on a linear correlation trend, as expected if variations are caused by changes in pyroxene chemistry (Adams, 1974; Gaffey et al., 2002). The only clear deviation from the linear correlations is shown by the Bellicia site, described in later sections. Therefore, in the next section we discuss the band centers in relationship to HED mineralogy.

6.4.1.1 Bright Material Mineralogy and relation with HED

From laboratory data analysis it is known that band centers of pyroxenes increase with increasing iron content (Klima et al., 2007, 2011). HED meteorites show similar trend in a plot of band I center versus band II center (Gaffey, 1997; De Sanctis et al., 2012a; McSween et al., 2013b). The band I and II centers occur at shorter wavelengths in diogenites than in eucrites, due to a higher abundance of Mg-rich pyroxenes with lower Ca concentrations in diogenites (Gaffey, 1976). Howardites overlap the band-center fields of diogenites and eucrites. The areas occupied by each subgroup have been outlined in Fig. 6.5 with different colors: red for diogenites, green for howardites, and yellow for eucrites. The definition of the HED regions is given by Ammanito et al. (2012, 2013a) and De Sanctis et al. (2012a, 2013). The values of the band centers derived from the BM units plot in different regions, spanning from diogenites to eucrites, suggesting a large range of mineralogies present among the different BM units. However, the values of the band centers of the BM units show that most of them are compatible with eucrite-rich howardites, and only a few bright areas are diogenite-rich howardites (Figs. 6.5, 6.6). In particular, among the 75 observations analyzed, 42 can be associated to eucrite-rich howardites, 24 to eucrites, 2 to howardites and 5 to diogenite-rich howardites while only 2 are diogenitic (Fig. 6.6). The proportion of the different mineralogies among the BM units is similar to the proportion found on Vesta, where VIR data show a preponderance of eucrite-rich howardite, indicating that eucritic lithologies dominate, as they do among the HEDs on Earth (De Sanctis et al., 2013). Diogenites are the less abundant class among HEDs, and VIR spectral data confirm that they are the less common lithology on Vesta (De Sanctis et al., 2013) as well as among the BM units.

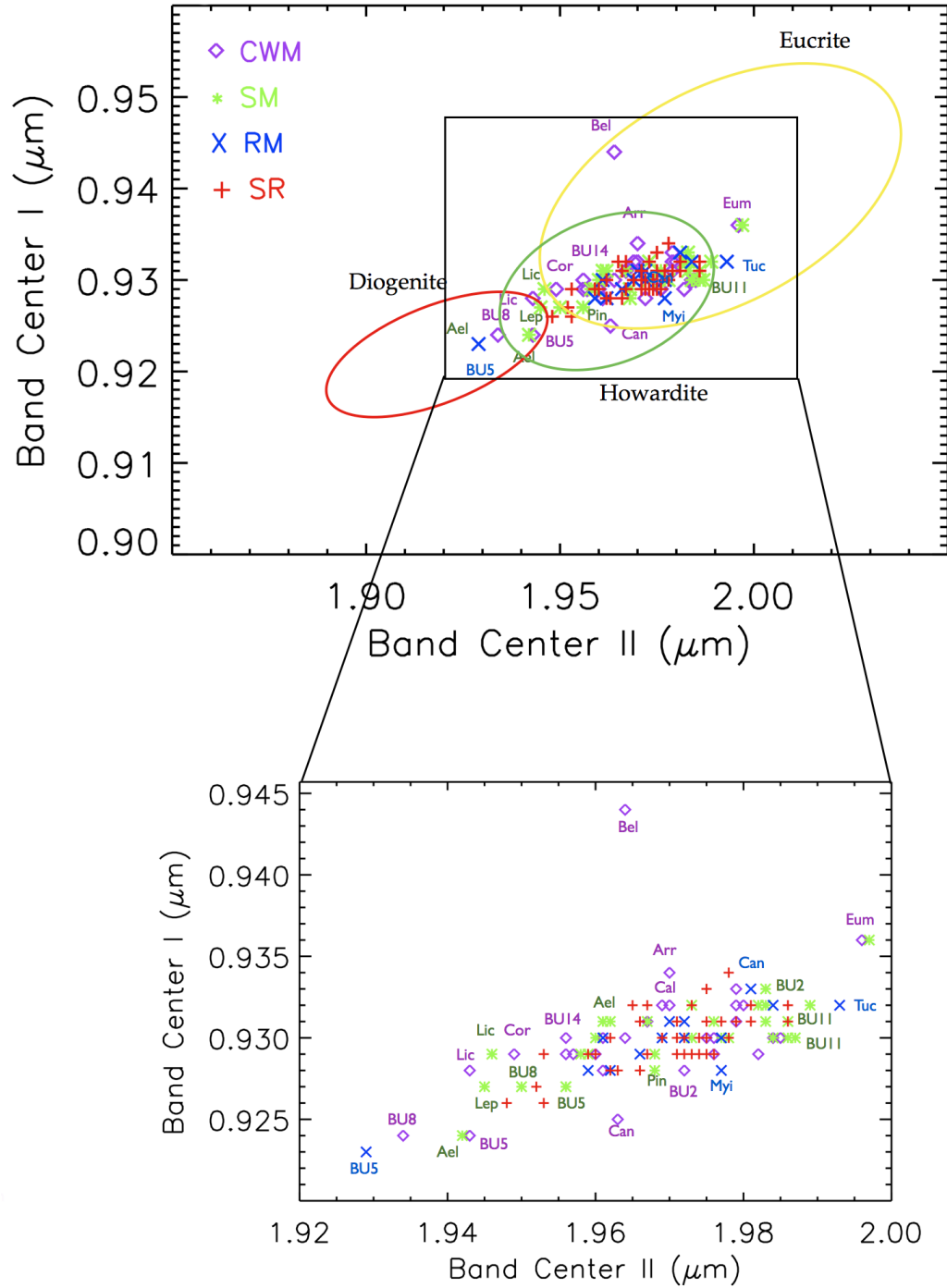


Figure 6.5: Plot of Band I vs. Band II centers of the BM. Symbols and colors designate the BM types. The colored circles delimit the HED regions.

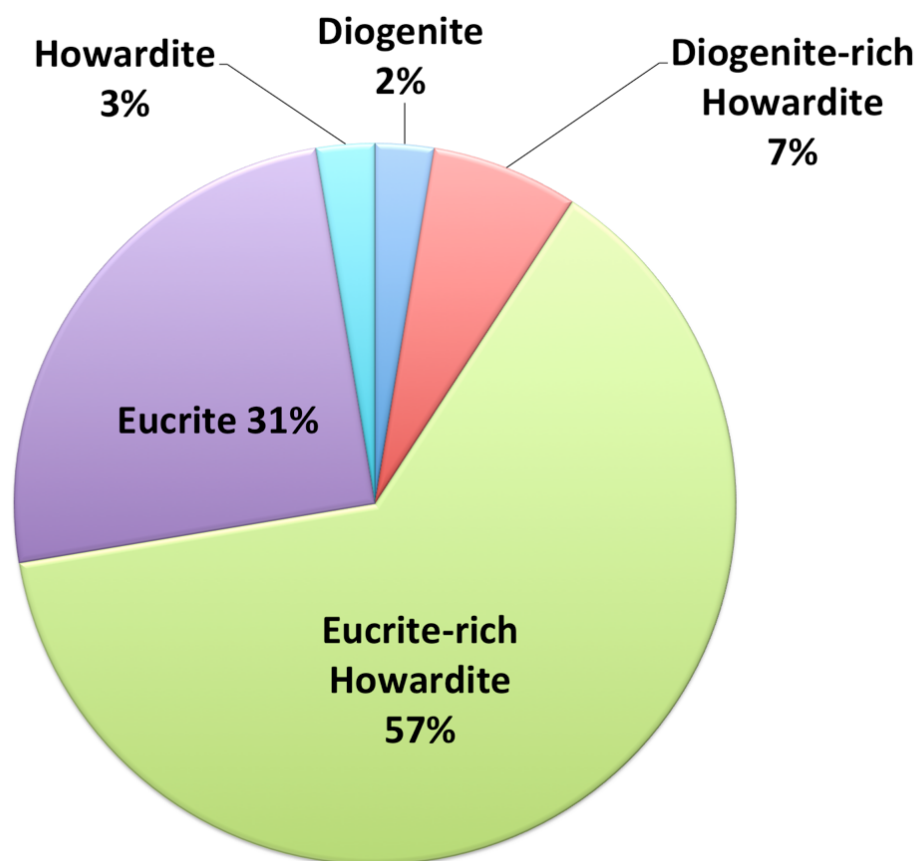


Figure 6.6: Summary diagram of the bright material composition. Each color represents the percentage of diogenitic, howarditic and eucritic BM units.

6.4.1.2 Band centers and albedo

We analyzed potential relationships between the band center position and the normal visual albedo for each BM, but we do not find any clear dependence of the two parameters. In Fig. 6.7-A is represented the normal visual albedo vs. band II center. Similarly, no correlation is found for the band I center normal visual albedo. This means that Vesta has both eucritic and diogenitic bright units, and also that the two lithologies do not exhibit major differences in terms of reflectance (6.7-A).

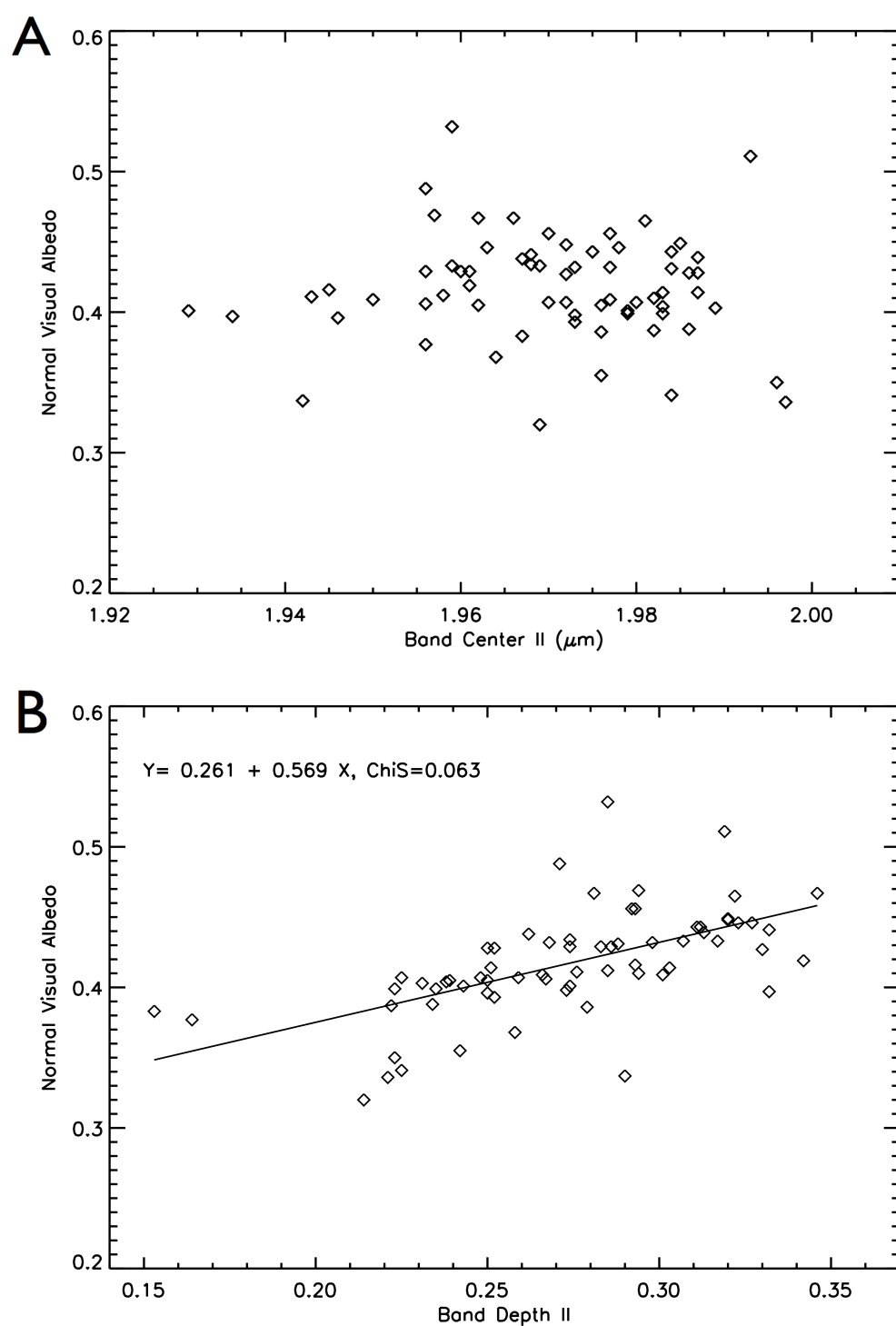


Figure 6.7: (A): The plot of normal visual albedo vs. band II center does not show a relationship between albedo and band centers. (B): Plot of normal visual albedo vs. band II depth. Solid line represents the best fit.

6.4.2 Band depth analysis

Band depths are indicative of content of the pyroxene, opaque minerals or other mineralogical phases, the iron content, and the grain size distribution (Adams, 1974; Clark, 1999; Mayne et al., 2010; Serventi et al., 2013). The values of the band depths of the BM units are reported in Table C.7, C.8 and C.9. A key characteristic of BM units is the their greater band depths compared with their surroundings (Pieters et al., 2012; Reddy et al., 2012b). We calculated band I and band II depths of the different types of BM to determine if there are differences between different classes of BM and if all the BM units show this increased band depth (Fig. 6.8-A). We found that only a few units, namely BU14, Arruntia, Bellicia and Aelia-RM, depart from the general trend for their BM type. Those cases have shallower band depths with respect the surrounding areas. Band I depth and band II depth are related by a linear law and to emphasize the differences among the BM types, we calculated the best-fit line for each BM type (Fig. 6.8-A). We found that the best-fit line for RM has a lower slope than the other BM types, suggestive of greater degrees of mixing between RM and the surrounding regions. In Fig. 6.8-B, we show band depths of the different BM units and band depths of HED meteorites at different grain size (Table C.11). Pyroxene absorption bands have been studied by many authors (e.g., Crown and Pieters, 1987; Craig et al., 2007, 2008; Pompilio et al., 2009), and it well known that both the band I and band II depths increase with increasing grain size. Thus band depths can be used to infer information of the grain size of the observed unit. The band depths of the BM units are similar to band depths of HEDs with smaller grain sizes (0-25 μm). Only a few BM examples are consistent with slightly larger grains (25-45 μm) (Fig. 6.8-B and Tables C.7, C.8, C.9 and C.11). This correspondence could indicate that the BM units are composed of small particles. On the other hand, the BM generally have band depths larger than those of the surrounding terrains, suggesting that the nearby regolith may have grain size even smaller. Only a very few BM cases show a reduction of one or both the bands compared with the surroundings.

6.4.2.1 Agents that modify the band depths

In the analyzed dataset, we found some bright regions with band depths shallower than the average. Below we discuss possible causes that can reduce or enhance the band contrast in order to understand why most of the BM have larger band depths and only some BM units show a behavior different from the rest of the sample.

- *Presence of other mineralogical phases.* A possible reason for the re-

duction of the bands could be relatively larger abundances of minerals with weak or no absorption bands, like plagioclase. Alternately, the presence of a mineral like olivine could modify the band I shape and reduce the band II depth (see for example Bellicia spectrum in Fig. 6.3).

- *Grain Size.* Band depth is a function of the grain size. If multiple scattering dominates, as is usually the case in the visible and near-infrared, then the reflectance decreases as the grain size increases, up to particle sizes of $\sim 100 \mu\text{m}$ (Clark, 1999; Harloff and Arnold, 2001; Craig et al., 2007, 2008; Cloutis et al., 2013), and vice versa. Hiroi et al. (1994) reported a grain size $< 25 \mu\text{m}$ for Vesta's regolith based on analysis of telescopic spectra. Fig. 6.8-B shows the variation of the band depth of HED samples provided by the Reflectance Experiment Laboratory (RELAB) for different grain sizes (the values are reported in Tables C.11). The plot indicates a good correspondence between the band depths of the finer HED grain sizes ($< 45 \mu\text{m}$) and those of the BM units.
- *Opaque Material.* The presence of low-reflectance carbon grains or other opaque phases reduces the brightness and the band depth in a mixture. Studies made on intimate mixtures with different amount of dark carbon grains, demonstrate the relationship between the band depth and the presence of dark material (e.g., Clark, 1983; Le Corre et al., 2011; Cloutis et al., 2013). The relationship between the band depth and the amount of opaque materials is generally not linear and so small quantities of opaques can drastically reduce the band depth (Clark, 1983). Carbonaceous material on Vesta is suspected to be the cause of observed dark regions, that present very shallow bands (McCord et al., 2012; Reddy et al., 2012b; Palomba et al., 2014). In our BM cases, we can exclude a reduction of the band depth due to a high abundance of opaques because of the high reflectance of these areas except for few cases like Aelia-RM, where bright and dark materials are mixed at small scale.

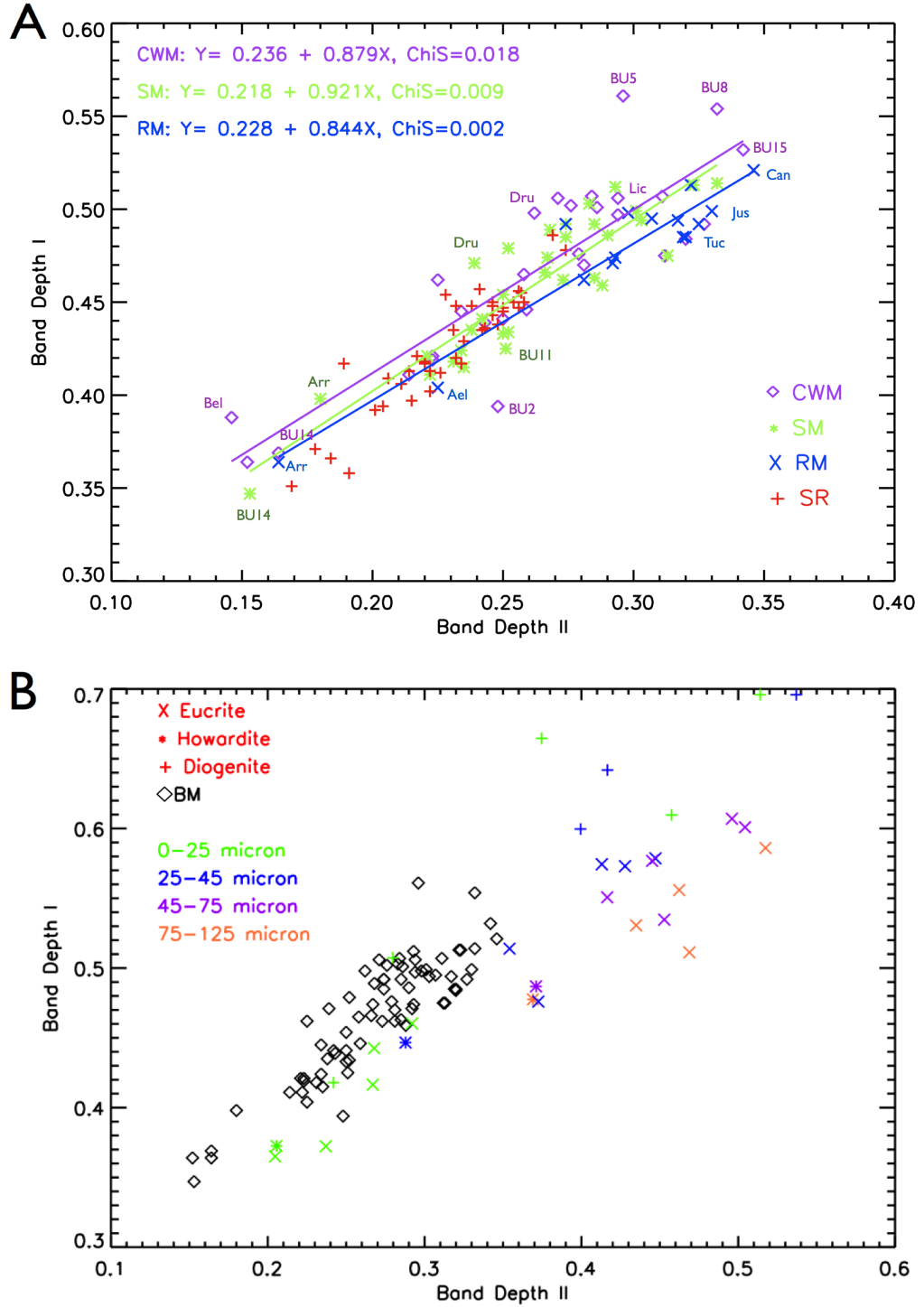


Figure 6.8: (A): Band I vs. Band II depth for the BM units. The corresponding best fit line is shown. (B): Band depths of the BM regions compared with those of the HED RELAB samples at different grain size.

6.4.2.2 Normal visual albedo and band depth of the bright material

BM units generally have an albedo greater than the average value for Vesta. We found a linear relationship between normal visual albedo and band depths for the BM units (Fig. 6.7-B), contrary to what was expected if the stronger bands were due to larger grain sizes. In fact, Fig. 6.7-B shows that albedo increases for greater band depths II. For the band I depth we have similar results. Albedo, band depth and grain size are related. The small particle size of the BM units should indicate high albedo values with decreasing band depth. This is contrary to what we see for BM units. Hence grain size is not the most important cause affecting the band depths.

Thus, excluding the few case in which BM units show smaller band depths, we can infer that the band depths of BM regions principally depend on the abundance of pyroxenes and the amount of Fe^{2+} .

6.4.2.3 Space weathering effects

Space weathering could be a further cause for the reduction of the band depth. On the Moon this process is linked to the presence of nanophase metallic iron (npFe^0), which causes darkening of the soil, and a reduction of the band depth. The "classical" space weathering, like the processes affecting the lunar soils, introduces a strong red slope in the near-infrared continuum between ~ 0.7 and $1.5 \mu\text{m}$ and reduce the pyroxenes bands and the reflectance (Pieters et al., 2012; Marchi et al., 2012; McSween et al., 2013b). As mentioned earlier, Vesta is one of the brightest airless silicate bodies in the Solar System, and Vesta's spectra have prominent absorption bands, especially for the bright regions. Vesta does not show the characteristics typical of lunar-style space weathering (Pieters et al., 2012). However, the space-weathering environment is different on Vesta than at the Moon. The evolution of Vesta's surface appears to be dominated by large- and small-scale impacts, that produce and redistribute particulate material (Bottke et al., 1994; Pieters et al., 2012). Moreover, the low average velocity ($<5\text{km/s}$) of impacts in the main asteroid belt lead to a dominance of mechanical brecciation over melting and vaporization (Pieters et al., 2012) while micrometeoroid bombardment causes a continuous redistribution of the regolith (Pieters et al., 2012; McSween et al., 2013b). This leads to a different style of space weathering on Vesta, mainly due to mixing of different endogenic and exogenic materials.

6.4.3 Band Area Ratio analysis

The Band Area Ratio (BAR) is a linear function of the abundance of pyroxenes, and is good parameter with which to identify the presence of olivine (Cloutis et al., 1986). Since the olivine lacks an absorption near $2\ \mu\text{m}$, an increase in the olivine content of a mixture with pyroxenes causes the BAR value to decrease. Thus very small BAR values, could represent a high amount of olivine in a pyroxene-olivine mixture (Cloutis et al., 1986). We evaluated the BAR of the BM units and the BAR of RELAB samples of HED meteorites with grain size smaller than $25\ \mu\text{m}$. The plot in Fig. 6.9 shows the distribution of the BAR vs. band I center of the BM compared with those of the HEDs. Most of the BM have BAR comparable to those of the diogenites, howardites and some eucrites. Moreover, we see that the BM do not have BAR value exceeding 1.7, while some eucrites show values larger than 1.7. However, the eucrites with larger BAR also have Band I centers at longer wavelengths that we do not find among the BM units on Vesta. It is interesting to see that some bright units, such as Arruntia, BU14 and specially Bellicia have small values of BAR and relatively long BI centers. This behavior is indicative of the presence of olivine in the pyroxene mixture. Band I shapes of these units are atypical for pyroxenes (Fig. 6.3). Moreover, the spectra of these regions have a smaller band depth II, that cause the small BAR values. These characteristics are compatible with the presence of an amount of olivine $> 50\%$, as reported in Ammannito et al. (2013b). Tables C.7, C.8, C.9 and C.12 show the BAR values of the BM units and those of the HED used in the analysis.

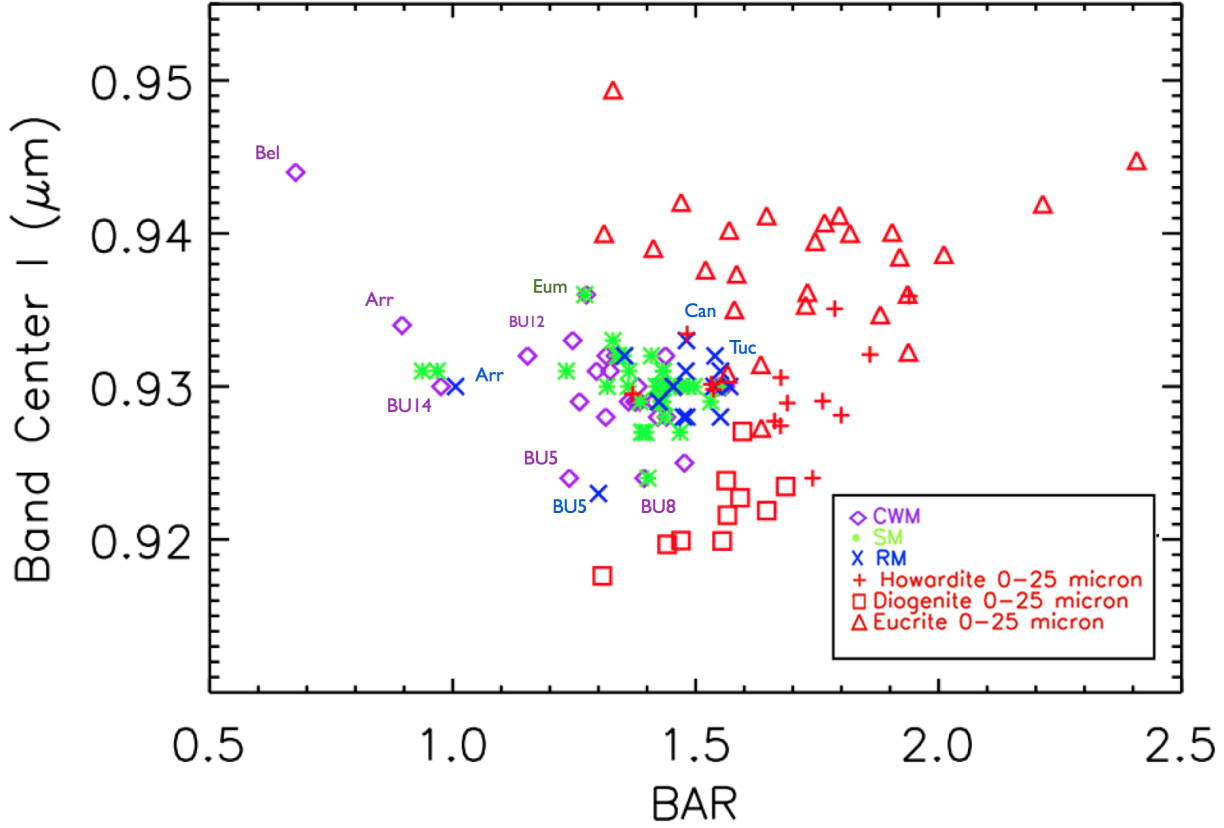


Figure 6.9: Plot of Band I center vs. BAR for the different types of BM units along with those for the HED RELAB samples of grain size $<25\mu\text{m}$.

6.4.4 Molar content of Wo and Fs in the bright material

Indirect methods based on the band center position allow us to derive the average molar content of Wollastonite (Wo) (CaSiO_3), Ferrosilite (Fs) (FeSiO_3), and Enstatite (En) (MgSiO_3) in pyroxenes, thereby revealing relative variations of Ca, Mg and Fe.

Gaffey et al. (2002) and Burbine et al. (2007) addressed this issue in two different ways. Gaffey et al. (2002) derived from pyroxene data several formulas to predict the abundance of Wo and Fs using an iterative method; each formula is valid for a given interval of Wo and Fs. Burbine et al. (2007), consider a restricted number of HEDs, and found simpler relations valid for all abundances of Wo and Fs (Burbine et al., 2007; Moskovitz et al., 2010). We derived the molar content of Wo and Fs with both the methods and we

found similar results. In particular, we see that the mean differences between the values obtained with the two methods are $\sim 1\%$ for Wo and $\sim 5\%$ for Fs. In Fig. 6.10, we show the results obtained by using the approach of Burbine et al. (2007) (see also Tables C.4, C.5 and C.6). For ease of presentation, we show the results plotted on a pyroxene quadrilateral (Fig. 6.10). Such a pyroxene diagram is in general used for single mineralogical phases, while the Vesta spectra are characterized by mixtures of several minerals, dominated by pyroxenes of various compositions. In particular, we note that that Bellicia-CWM has a very different behavior compared with the rest of the BM units, a result of its high olivine content, and thus its presence in this diagram is inappropriate. Nonetheless, the location of Bellicia-CWM in the pyroxene diagram highlights the unusual spectral properties (and composition) of this location.

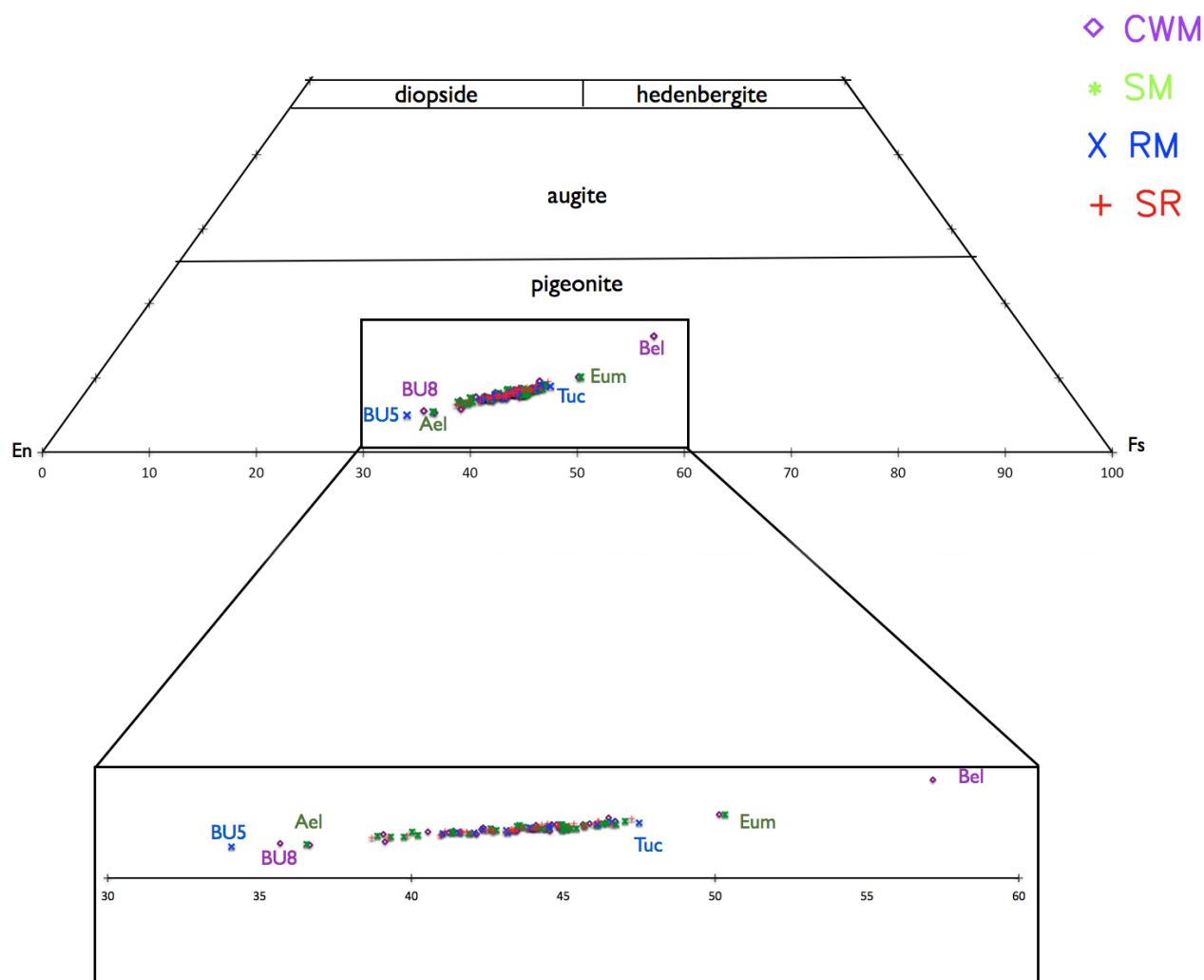


Figure 6.10: Pyroxene diagram for Vesta's BM units and the surrounding regions. Tuccia and Eumachia, the most eucritic BM units exhibit high amounts of Wo and Fs, while BU8, BU5 and Aelia are those with the lowest content of Wo and Fs. Bellicia's position in the plot is not representative of its pyroxenes because of the presence of large amounts of olivine. We include it in the diagram, only to show the strong contrast between Bellicia and the other BM.

6.5 Peculiar cases of Bright Material units

Some bright areas show peculiar characteristics compared with other regions. Below we describe these units in detail.

6.5.1 Diagenitic Bright Material units

A few BM units (BU5 - CWM and RM, BU8 - CWM, Aelia - SM,) exhibit spectral properties consistent with diogenite-rich howardite composition: their band centers are at the shortest wavelength in the entire considered dataset. Except for one case of radial material (BU5- RM), all the diagenitic BM regions belong to the Crater Wall Material (CWM) and Slope Material (SM) morphological classes. These BM are located in the longitude range of 0° to 100° E and latitude range -50° to $+50^\circ$ (Fig. 6.2) corresponding to a region possibly covered with Rheasilvia ejecta (De Sanctis et al., 2012a; Ammannito et al., 2013a; McSween et al., 2013a). BU5-RM and BU8-CWM are the most diagenitic BM with the lowest amount of Fs and Wo. The low abundance of Fs and Wo, which result in a high amount of En (up to 60%) indicating a more Mg-rich lithology. Their spectra (Fig. 6.3, 6.4) have very prominent bands, that are among the deepest of all the BM sample analyzed (Fig. 4, Fig. 8A). Nevertheless, BU5-CWM and BU8-CWM have an albedo that is only 10% higher than the average of Vesta.

Another diogenite-rich site is Aelia, a small crater located at longitude 140.6° E and latitude -14.3° . The ejecta of Aelia contains both dark and bright materials (Stephan et al., 2014; Palomba et al., 2014). Band depths for this diagenitic BM region are similar to those of the other BM, except for the Aelia-RM, which has band depths similar to the surroundings (Fig. 6.8-A). However, in interpreting of the results obtained for the Aelia region, we must consider the difficulty in selecting the BM areas, due to the small dimensions of the crater, and the presence of dark material. For the same reasons, the normal visual albedo appears to be lower than the Vesta's average.

Diagenitic BM are very rare on Vesta's surface. Diogenite is generally less abundant than howardite and eucrite, being mainly concentrated in the southern Rheasilvia basin (De Sanctis et al., 2012a) and in a few other locations in the northern hemisphere (Ammannito et al., 2013a). According to the classical magma ocean models (Bowman et al., 1997; Righter and Drake, 1997; Ruzicka et al., 1997; McSween et al., 2011; Beck et al., 2012), diogenite is formed in the lower crust/upper mantle and not on the surface. In this scheme, diogenite is exposed only by large impacts, such as the event that formed the prominent Rheasilvia basin. The deep excavation permitted the diogenite to be incorporated in the ejecta that was deposited near the

basin rim, with some ejecta reaching higher latitudes. Normally, areas surrounding the bright units do not show diogenite. An exception is the BU8 surrounding regions implying that at this location the crater interior exposes a higher quantity of diogenite that is less reworked.

6.5.2 Low band depth Bright Material units

A common characteristic of the BM is to have prominent absorption bands, generally higher than Vesta's average band depths. However, three of the BM units analyzed here, (Arruntia, Bellicia and BU14) have shallower band depths, similar to those of their surroundings (Fig. 6.3, Fig. 6.8-A). These BM units were identified by Ammannito et al. (2013b) as howarditic regions rich in olivine. The Bellicia spectrum is very different from the average of the other BM spectra. The band I center (0.944 ± 0.009), band I shape, and the low BAR value (0.677 ± 0.077) are indicative of the presence of olivine, while the Band II center value is typical of howardite (1.964 ± 0.009). Arruntia and BU14 have characteristics similar to those of Bellicia, but less extreme (Fig. 6.3). For Arruntia and BU14, band I is more similar to those of the other BM units, and the band center position are in the howarditic region.

The Bellicia bright units are small CWM and small fresh craters in Bellicia ejecta field. Arruntia crater has extended ejecta, while BU14 is a small unit near Arruntia. Arruntia, Bellicia and BU14 are located in the same region in the northern hemisphere and the similarity of their spectral parameters suggests a common origin. Their spectra have been interpreted as a mixture of howardites and olivine in different proportions (Ammannito et al., 2013b). A possible explanation for the presence of olivine in this area is as follows: an ancient large impact excavated and incorporated large blocks of diogenite-rich and olivine-rich material into the eucritic crust. Afterwards, subsequent impacts exposed the olivine-rich material in this area, producing olivine-bearing terrains in a howarditic background (Ammannito et al., 2013b).

6.5.3 High albedo Bright Material units

Tuccia and BU15, the highest-reflectance features on Vesta, are located in the southern hemisphere. The albedo of these two locations is about 40% greater than the geometric albedo of Vesta. In addition to its very high albedo, Tuccia is one of the most eucritic of the BM units. Band I center is similar to the average of the other BM (BCI $0.932 \pm 0.002 \mu m$), while its band II center ($1.993 \pm 0.006 \mu m$) is longer than the other BM, indicating a higher content of iron and calcium (Wo 8.8 ± 0.8 , Fs 43.1 ± 1.3) (Fig. 6.10). The very high albedo and prominent bands suggest that Tuccia is an example of

unweathered Vestan soil, considering that the Vesta style space-weathering reduce the albedo and band depths without reddening of the spectra (Pieters et al., 2012). BU15-SM (Fig. 11) is the brightest BM unit with a normal visual albedo of 0.531 ± 0.013 , and it is located in the southern hemisphere at -65° latitude and 358°E longitude. For this BM unit, we analyzed only LAMO data, because of the lack of HAMO and HAMO-2 data. The derived composition of the BU15-SM is eucrite-rich howardites (Table C.10), and the band depths of the BU15-CWM are among the deepest in the entire BM study set (Fig. 6.8-A). The SM band depths are similar to those of the surroundings. A very bright streak of ~ 1 km long extends inside the SM (Fig. 6.11); the band depth of this steak is lower than that of the surrounding terrain (Fig. 6.4, Table C.10) (Schröder et al., 2013). The very bright streak in BU15 is peculiar because it has the highest albedo of Vesta, but band depths similar or shallower than its surroundings. This anomalous behavior can be due to the presence of a high-albedo featurless mineral (e.g. plagioclase) that will increase the albedo of mixtures rich in it (Crown and Pieters, 1987; Harloff and Arnold, 2001; Mayne et al., 2010; Serventi et al., 2013).

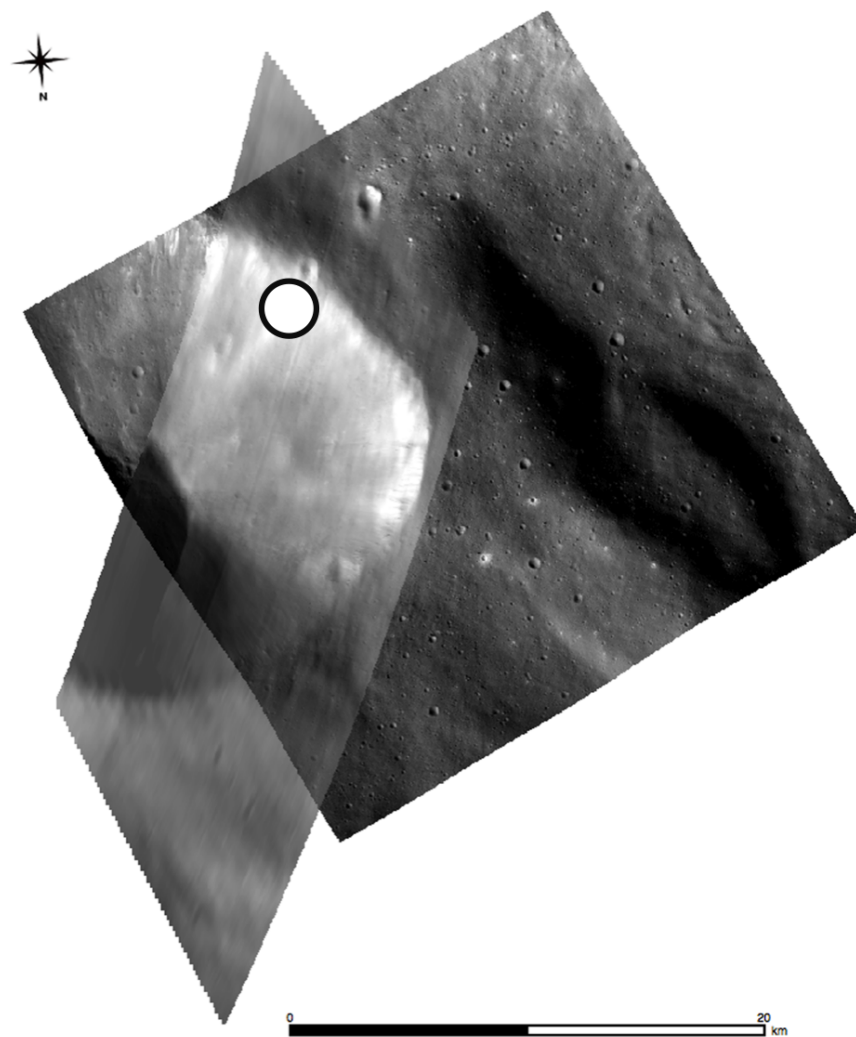


Figure 6.11: VIR LAMO image of BU15 at $0.55\ \mu\text{m}$ (VIR cube 385962328) overlapped with the corresponding Framing Camera image (FC21B0015548_11361091538F1D). The images are represented in stereographic projection. The black circle indicates the very bright streak inside the BU15-SM.

Chapter 7

Linear unmixing applied to VIR data

In this chapter we describe the application of linear spectral unmixing to laboratory spectra, to test the accuracy and the limits of this method (Zambon et al., 2014a). Then we use the same approach to determine the amounts of eucrite, diogenite and olivine in the bright units on Vesta. Here we describe the technique used, and we report the results of the tests for the laboratory mixtures and the results of the application of the linear unmixing for the VIR spectra of the bright material units.

7.1 Description of the method

To determine the composition of the bright material units on Vesta, we hypothesize that the average spectrum of each unit is a linear combination of different mineralogical phases. Mineralogical studies of the bright regions on Vesta (Zambon et al., 2014b) (Section 2.9.1) indicate that bright regions are dominated by eucrite, diogenite, howardite and by the presence of olivine in some regions. Before applying linear unmixing on VIR and laboratory spectra, we make some preliminary operations on the spectra in order to remove the influence of illumination conditions and topography. The selected spectra have been removed of the spectral continuum and normalized at $0.55\mu\text{m}$. In this way, we no longer have the information related to the albedo and the spectral slope, but instead the information on the bands characteristics (e.g. center, depth, areas). We select a sample of eucrites, diogenites and olivines, and we hypothesize that Vesta spectra are a linear combination of two endmembers, chosen from this sample. We exclude howardite because it is a breccia made of eucrite and diogenite in different proportions (Mit-

tlefehldt et al., 1998; Beck and McSween, 2010; McSween et al., 2011); thus the information contained in it is already included in combinations of eucrite and diogenite. We perform all the possible combinations of two endmembers with an accuracy of two decimal places within the error of estimation of the abundances (Section 7.2), and we chose the abundances corresponding to the minimum χ^2 value. We choose the spectrum that is the best approximation of the measured spectrum. To verify the reliability of the choice of the endmembers, we analyze the ten least χ^2 values, to see if for small χ^2 variations the endmembers remain the same (section 7.3.1).

7.2 Linear unmixing applied to laboratory mixtures

To test the limits of the linear approach, we consider three types of mixtures of two mineralogical phases: mixtures of two pyroxenes (enstatite (en) and diopside (ds)), mixtures of olivine (ol) and pyroxenes (px), and mixtures of plagioclase (pl) and pyroxene. We choose the pyroxenes and olivine and pyroxenes mixtures from the Reflectance Experiment Laboratory (RELAB) database (www.planetary.brown.edu/relabdocs/relab_disclaimer.htm), while the pyroxenes and plagioclase mixtures are those used in Serventi et al. (2013). We apply the linear spectral unmixing method to each spectrum of the defined mixture and we compare the results of the unmixing method with the laboratory data. In Table 7.4 we show the laboratory mixtures selected. We combine linearly the two endmember of each mixtures:

$$f_{mix} = a_1 f_1 + a_2 f_2 \quad \text{with} \quad f_1 + f_2 = 1$$

where f_1 and f_2 are the two endmembers and a_1 and a_2 are the coefficients relative to the abundances of each endmember.

In Figs. 7.1, 7.2, 7.3 we show the results of the linear unmixing applied to the different mixtures. Table 7.1 summarizes the results obtained.

From these tests we find that mixtures of pyroxenes are well represented by a linear unmixing (Fig. 7.1). The amounts of each phase are estimated with a mean accuracy of 3%. In the case of 50% diopside and 50% enstatite we find exactly the same amounts. The worst result is obtained for the highest content of diopside (85%) yielding a difference between the real value and the estimated value of 6%. Results obtained in the case of the olivine and pyroxenes mixture indicate that in this case the linear approach is reliable for olivine content up to 50%. For higher olivine content, the computed spectra show deviations from the laboratory spectra (the bands shape differs

from that of the physical mixture measured in laboratory). However, the method is able to identify the olivine content within an average value of 5% with respect to the real one. Despite the appearance of fit, larger differences between real and retrieved amounts values are found in mixture with the smaller content of olivine (9%) (Fig. 7.2). Thus, the linear approach can still be used to determine the olivine amount, taking into account the limitations of this method. Conversely, in the plagioclase and pyroxenes mixtures the linear method does not provide satisfactory results. The mean discrepancy between the laboratory amounts and the estimated amounts is about 17%, with a maximum of 22%. Thus pyroxenes and plagioclase mixtures cannot be modeled with linear methods (Table 7.1, Fig. 7.3). Results obtained by linear unmixing applied to mixtures indicate that the linear approach is useful to describe surfaces dominated by pyroxenes (Table 7.4, Figs 7.1), and thus to describe the Vesta composition at a global scale. At the local scale where other minerals like olivine are present, we can still use linear unmixing, but taking into account its limitations.

Results of the linear spectral unmixing for laboratory mixtures				
Mixture	a_{m1} (%)	a_{m2} (%)	$ a_m - a_l $ (%)	χ^2
15% En+85% Ds	21	79	6	0.087
50% En+50% Ds	50	50	0	0.068
60% En+40% Ds	56	44	4	0.073
75% En+25% Ds	77	23	2	0.104
85% En+15% Ds	88	12	3	0.045
10% Ol+90% Px	19	81	9	0.483
30% Ol+70% Px	31	69	1	0.475
50% Ol+50% Px	31	69	1	0.954
70% Ol+30% Px	37	63	7	0.935
90% Ol+10% Px	86	14	4	1.453
20% Pl+80% Px	93	7	13	0.029
30% Pl+70% Px	56	44	14	0.335
80% Pl+20% Px	42	58	22	0.224
90% Pl+10% Px	29	71	19	0.330

Table 7.1: Results obtained for mixtures of enstatite and diopside, olivine and pyroxene, and plagioclase and pyroxenes. The first column reports the amount of each endmember in the laboratory mixtures. The second and third columns show the value of the coefficients obtained by linear mixing relative to each endmember. The fourth column reports the difference between the amount of coefficients for laboratory mixtures and those obtained by the mixing. In fifth column, χ^2 values indicative of the fit accuracy are reported.

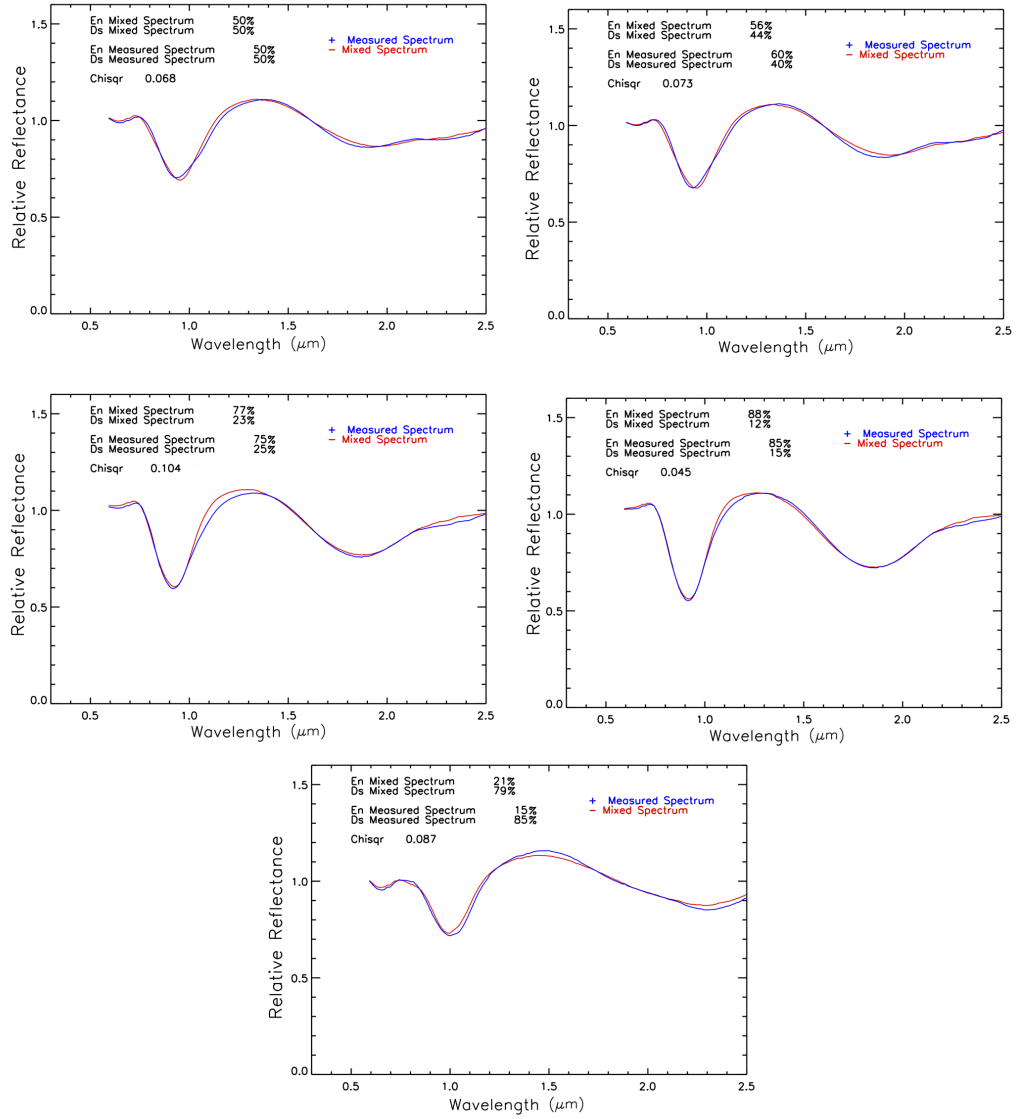


Figure 7.1: Mixtures of two pyroxenes, enstatite and diopside. In this case the linear approach gives good results with small differences between the laboratory data and the retrieved coefficients.

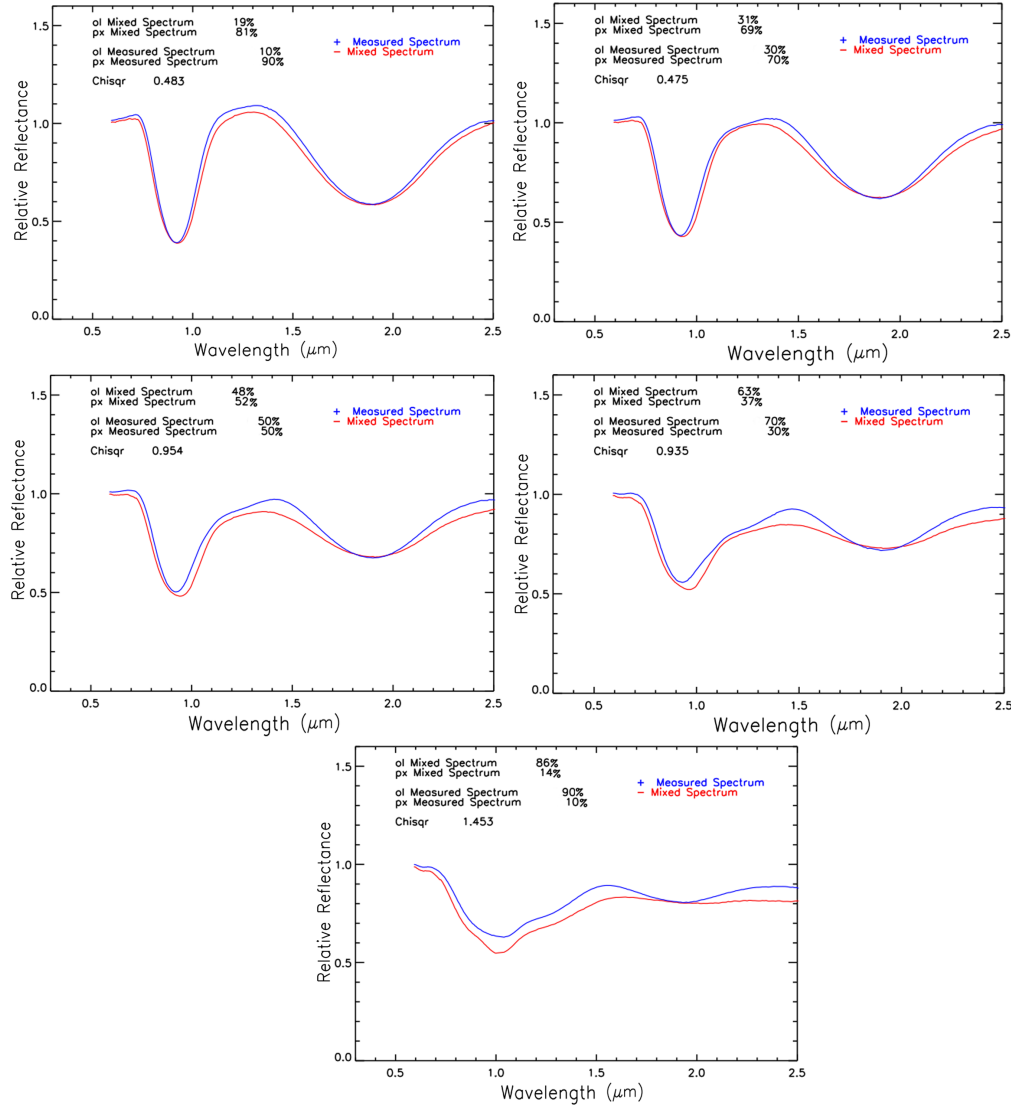


Figure 7.2: Mixtures of pyroxenes and olivine. For high olivine content the mixed spectrum (red) does not match the laboratory spectrum (blue) perfectly; in particular the second band totally disappears in the mixed spectrum for very high olivine content. Despite a high χ^2 value, the amount of olivine is correctly estimated within 4%, in the mixture with the highest content of olivine.

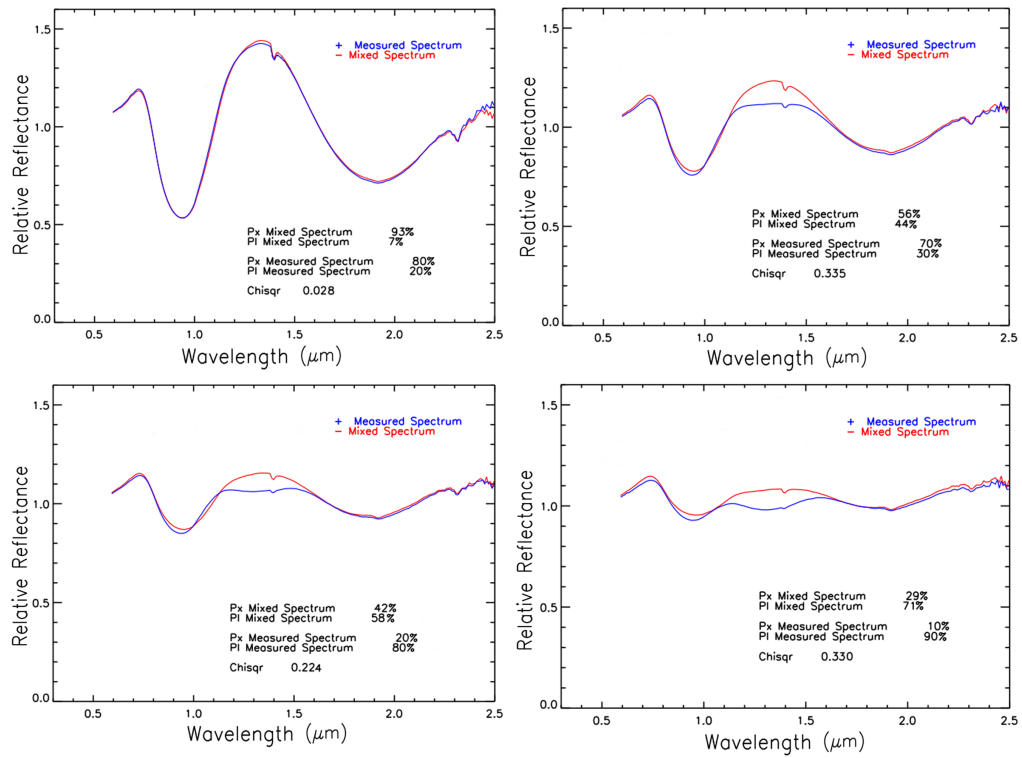


Figure 7.3: Mixtures of pyroxenes and plagioclase. For high content of plagioclase the linear approach is unsuited to describe the mixture. The amount of plagioclase is underestimated by 19% respect to the real value, and the fit curve (red) does not match the laboratory mixture (blue) in the continuum range between the first and the second band.

7.3 Linear unmixing applied to the bright regions

The results obtained in the previous section define the limit of applicability of the linear method. Considering the results obtained, we selected a sample of 26 eucrites, 10 diogenites and 2 olivines (Table 7.2), available on the RELAB database with a grain size up to $25\mu\text{m}$, typical of the Vesta's bright areas (Hiroi et al., 1994; Zambon et al., 2014b) (Chapter 6). Among the bright materials analyzed in Chapter 6, we select 59 of them to apply linear spectral unmixing. The amounts derived by linear spectral unmixing are in agreement with the mineralogy of the bright regions (Zambon et al., 2014b) (Chapter 6). Larger band center values correspond to bright units richer in eucrite, while for low band center values we find higher diogenite content (Fig. 7.15). Our method is also able to highlight the presence of olivine and to determine its amount (Fig. 7.11, 7.12), always considering the limits of the linear approach. In Table 7.4 and in Figs 7.7, 7.8, 7.9, 7.10, 7.11, 7.12, 7.13, 7.14 are shown all the abundances obtained for the bright regions. A large part of the bright units (70%) contains eucrite, while the 25% contains diogenite and only 5% contains olivine (Fig. 7.4). Among the HED meteorites sample selected, our method identified 10 eucrite and 3 diogenite types in bright material units (Table 7.2). Large part of the eucrites in BM units (45%) are identified as cumulate, 40% as monomict breccia, 9% as polymict breccia and 5% as brecciated eucrite (Fig. 7.5) (Deer et al., 1992; Burns, 1993; Mittlefehldt et al., 1998) (section 1.7.1.1).

Only three types of diogenite have been detected. 57% of the diogenite correspond with the GRO95555 diogenite. GRO95555 diogenite is a peculiar diogenite: it has less compositional variability for minor and trace elements in the minerals than most other diogenites, and shows a unique texture in the diogenite suite (Stimpfl and Ganguly, 2002). No sign of the brecciation and shock deformation characteristic of other diogenites are present (Papike et al., 2000).

Some bright units (e.g. Myia, Eumachia and Tuccia), are the combinations of 2 eucrites, no diogenite is contained in them (Fig. 6.5) according with the results obtained in section 6. Aelia-SM, that is one of the most diogenitic bright unit, contains the largest amount of diogenite (71%) (Table 7.4, Fig. 7.12). Despite the shortest band centers (Fig. 6.5), BU5-RM has only 29% of diogenite (Table 7.4, Fig. 7.9). The highest amount of olivine is found in Bellicia (54%), in BU14-SM (55%), and in Arruntia-SM (41%). Small amounts of olivine have also been found in BU14-CWM (26%) and in Arruntia-SM (32%).

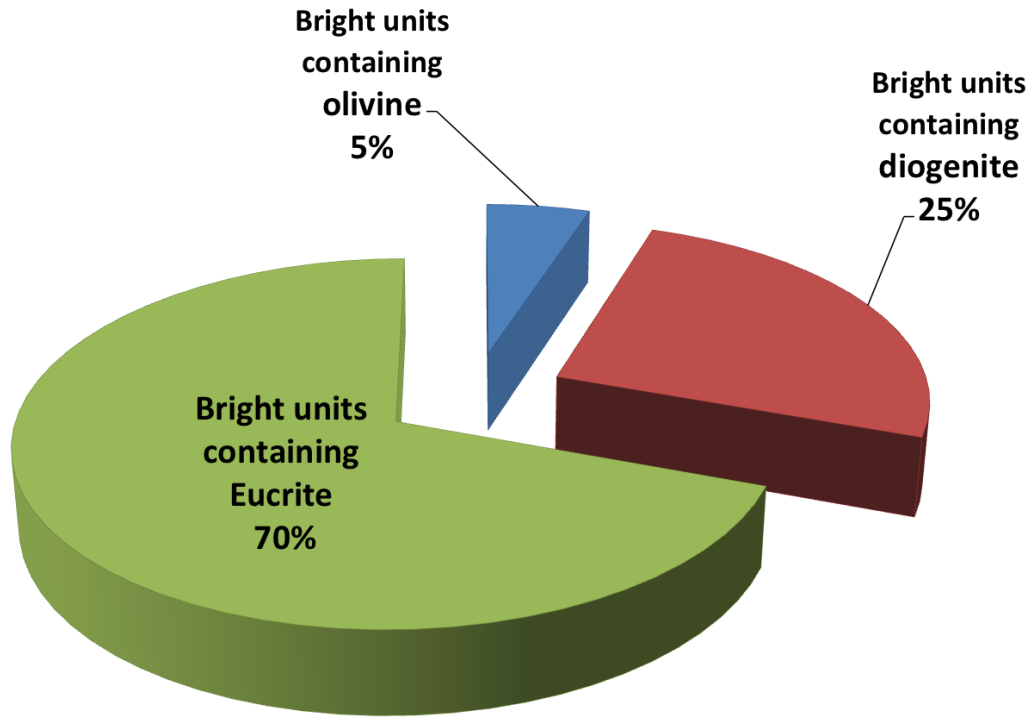


Figure 7.4: Amounts of eucrite, diogenite and olivine of the retrieved by linear spectral mixing.

The method hitherto used leads to satisfactory results, generally in agreement with those obtained in Chapter 6 and in (Zambon et al., 2014b), allowing one to determine the bright units composition. Results of the linear unmixing indicates the presence of an high amount of eucrites and almost half of the eucrite in the BM is cumulate. The most recurrent endmember is the cumulate eucrite called *Serra de Mage*, that is found in 35 bright unit spectra (Fig. 7.6).

Not all of the mineralogical phases can be mixed linearly, but we can use this technique to mix the principal components of Vesta's surface (eucrite, diogenite and olivine). Some spectra do not perfectly fit with the mixed spectra, which is probably due to the insufficient number of endmembers. We can improve our results by increasing the number of endmembers, and by considering other minerals in addition to those considered here (bearing in mind the limits of the linear approach). Furthermore, we can choose different grain size intervals and we can extend the study to larger portions of the surface.

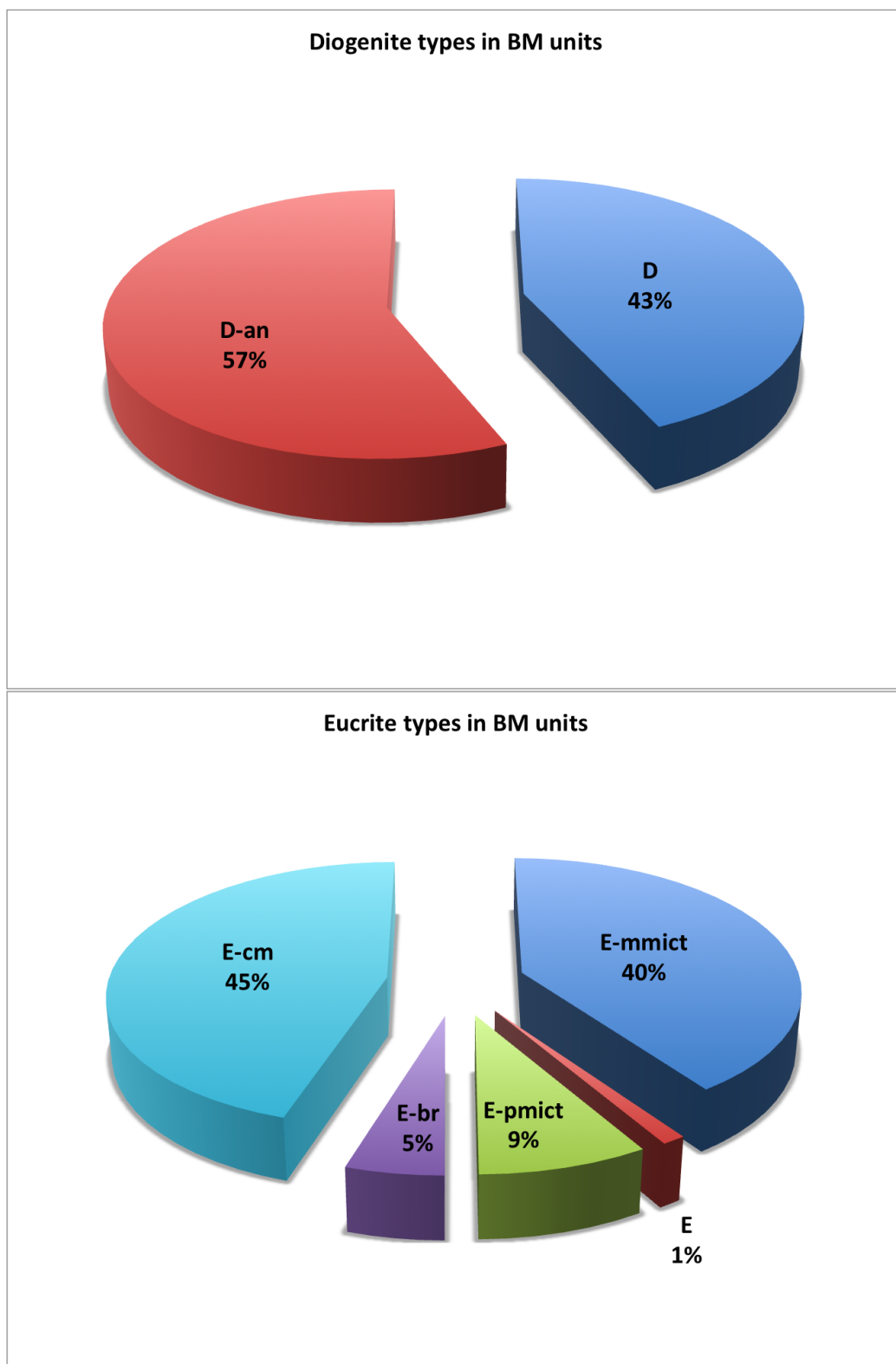


Figure 7.5: Amounts of the different eucrite and diogenite types in the bright units on Vesta.

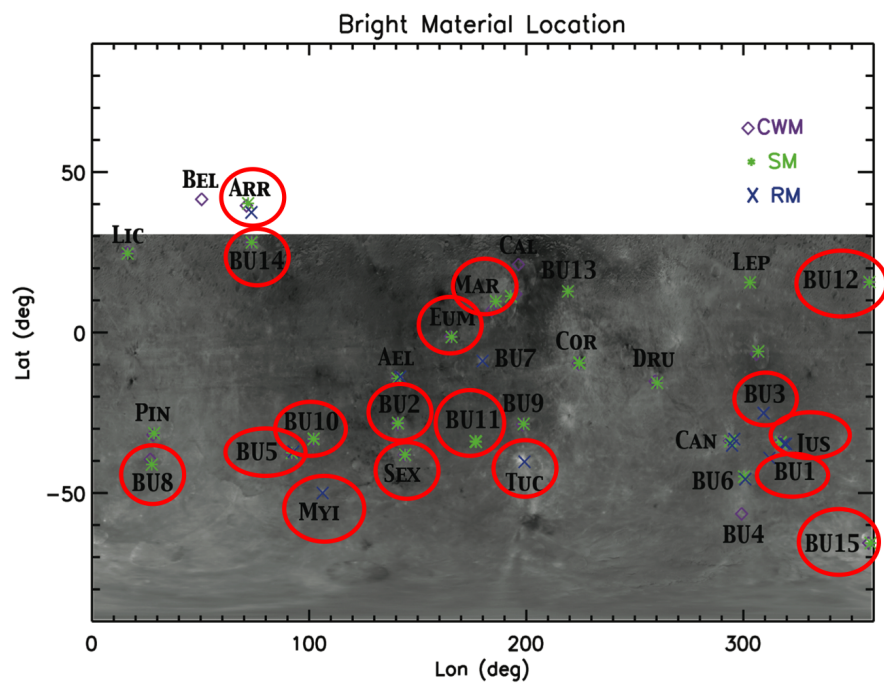


Figure 7.6: Locations of the bright units containing cumulate eucrite.

Endmember considered							
name	type	#	%	BCI	BCII	BDI	BDII
A-87272	Eucrite-mmict	0	0	0.940	2.001	0.537	0.343
A-881819	Eucrite	1	1.2	0.931	1.969	0.477	0.288
ALH78132	Eucrite-pmict	0	0	0.932	1.962	0.420	0.267
ALH85001	Eucrite-Mg rich	0	0	0.927	1.950	0.430	0.254
ALHA76005	Eucrite-pmict	0	0	0.936	1.980	0.375	0.238
Bereba	Eucrite-mmict	11	13.4	0.941	2.017	0.411	0.259
Bouvante	Eucrite-mmict	9	11	0.9448	2.008	0.432	0.325
Cachari	Eucrite-mmict	11	13.4	0.939	1.999	0.528	0.357
EET 87542	Eucrite-br	4	4.9	0.942	1.998	0.245	0.129
EET 90020	Eucrite-unbr	0	0	0.940	2.005	0.497	0.270
EETA79005	Eucrite-pmict	0	0	0.935	1.972	0.462	0.297
GRO 95533	Eucrite-br	0	0	0.940	2.014	0.473	0.321
Ibitira	Eucrite-mmict	0	0	0.939	1.994	0.581	0.339
Jonzac	Eucrite-mmict	0	0	0.939	2.002	0.527	0.369
Juvinas	Eucrite-mmict	1	1.2	0.936	1.995	0.462	0.292
LEW 87004	Eucrite-pmict	0	0	0.935	1.976	0.421	0.255
Millbillillie	Eucrite-mmict	0	0	0.937	2.005	0.444	0.268
Moore County	Eucrite-cm	2	2.4	0.938	1.985	0.588	0.364
PCA 82502	Eucrite-unbr	0	0	0.94	2.012	0.458	0.330
Padvarninkai	Eucrite-mmict	0	0	0.949	2.035	0.230	0.103
Pasamonte	Eucrite-pmict	0	0	0.940	2.002	0.469	0.314
SerradeMage	Eucrite-cm	35	42.7	0.931	1.967	0.440	0.271
Stannern	Eucrite-mmict	0	0	0.938	2.007	0.399	0.258
Y74450	Eucrite-pmict	0	0	0.935	1.983	0.368	0.205
Y792510	Eucrite-mmict	1	1.2	0.941	2.010	0.496	0.317
Y792769	Eucrite-pmict	7	8.5	0.941	2.011	0.397	0.232
A881526	Diogenite	0	0	0.920	1.900	0.646	0.383
ALH77256	Diogenite	9	30	0.922	1.895	0.588	0.359
Aioun el Atrouss	Diogenite-pm	0	0	0.924	1.915	0.629	0.387
EETA79002	Diogenite	2	6.7	0.920	1.886	0.509	0.275
GRO95555	Diogenite-an	17	56.7	0.923	1.918	0.624	0.383
Johnstown	Diogenite	0	0	0.918	1.885	0.447	0.226
LAP 91900	Diogenite	0	0	0.922	1.912	0.623	0.377
Tatahouine	Diogenite	2	6.7	0.920	1.904	0.628	0.382
Y74013	Diogenite	0	0	0.923	1.918	0.421	0.243
Y75032	Diogenite	0	0	0.927	1.944	0.512	0.299
Jackson cty	Olivine	1	16.7	-	-	-	-
Green olivine	Olivine	5	83.3	-	-	-	-

Table 7.2: A list of the endmembers considered. We select 26 eucrites, 10 diogenites and 2 olivines samples, with a grain size up to $25\mu\text{m}$, typical of Vesta bright regions. In the first column we report the name of the sample while in the second column the type. The third column indicates how many time each sample has been identified as endmember. The fourth column reports the percentage of the presence of the single sample relating to the type. For example, Bereba appears 11 times as endmember, and corresponds to 13% of all the eucrite sample.

Euclite and diogenite classification	
Type	description
Euclite-mmict	Achondrite from the euclite group; the meteorite is a monomict breccia.
Euclite	Achondrite from the euclite group
Euclite-pmict	Achondrite from the euclite group; the meteorite is a polymict breccia
Euclite-Mg rich	Achondrite from the euclite group; the meteorite contains magnesian pyroxene
Euclite-br	Achondrite from the euclite group; the meteorite is brecciated
Euclite-unbr	Achondrite from the euclite group; the meteorite is unbrecciated
Euclite-cm	Achondrite from the euclite group; the meteorite is a cumulate euclite
Diogenite	Achondrite from the diogenite group
Diogenite-pm	Achondrite from the diogenite group, which is a polymict breccia
Diogenite-an	Achondrite from the diogenite group, with anomalous properties

Table 7.3: Classifications of the euclite and diogenite. For definitions please refer to the "Meteoritical society bulletin" (<http://www.lpi.usra.edu/meteor/about.php>).

7.3. LINEAR UNMIXING APPLIED TO THE BRIGHT REGIONS 233

Result of the linear spectral unmixing for Bright Material on Vesta						
VIR cube	BU name	EndM1	Abundance EndM1	EndM2	Abundance EndM2	χ^2
385962327	BU15-CWM	SerradeMage E	0.46	GRO95555 D	0.54	0.286
385962327	BU15-SM	SerradeMage E	0.79	GRO95555 D	0.21	0.173
371632826	BU12-CWM	Cachari E	0.18	SerradeMage E	0.82	0.465
371632826	BU12-SM	SerradeMage E	0.88	ALH77256 D	0.12	0.474
371727131	Pinaria-CWM	Y792769 E	0.51	GRO95555 D	0.49	0.351
371727131	Pinaria-SM	Y792769 E	0.52	GRO95555 D	0.48	0.290
371813008	Cornelia-CWM	Bereba E	0.52	GRO95555 D	0.48	0.361
371813008	Cornelia-SM	Bereba E	0.57	GRO95555 D	0.43	0.283
371815732	BU11-SM	SerradeMage E	0.68	Y792769 E	0.32	0.208
371816828	Sextilia-CWM	Cachari E	0.33	SerradeMage E	0.67	0.457
371816828	Sextilia-SM	Cachari E	0.31	SerradeMage E	0.69	0.543
371904187	Justina-SM	Cachari E	0.38	SerradeMage E	0.62	0.337
371905283	Canuleia-RM	Bouvante E	0.44	Tatahouine D	0.56	0.627
371986649	BU13-SM	Bereba E	0.61	GRO95555 D	0.39	0.298
371992493	BU10-CWM	Bouvante E	0.20	SerradeMage E	0.80	0.356
371992493	BU10-SM	Bouvante E	0.17	SerradeMage E	0.83	0.317
371993041	BU5-RM	SerradeMage E	0.71	ALH77256 D	0.29	0.266
371993041	BU5-SM	SerradeMage E	0.72	ALH77256 D	0.28	0.363
372078317	BU6-SM	Y792510 E	0.64	ALH77256 D	0.34	0.395
372212906	BU4-CWM	Bereba E	0.48	GRO95555 D	0.52	0.488
372300571	Myia-RM	Cachari E	0.39	SerradeMage E	0.61	0.515
372385964	BU3-RM	SerradeMage E	0.70	ALH77256 D	0.30	0.335
372430301	BU9-CWM	SerradeMage E	0.62	Y792769 E	0.38	0.202
372520864	Justina-RM	SerradeMage E	0.68	ALH77256 D	0.32	0.320
372521396	BU1-RM	SerradeMage E	0.72	ALH77256 D	0.28	0.209
372565807	Tuccia-RM	Cachari E	0.41	SerradeMage E	0.59	0.327
372609208	BU10-SM	Bouvante E	0.14	SerradeMage E	0.86	0.259
372741836	BU2-CWM	Cachari E	0.11	SerradeMage E	0.89	0.386
372741836	BU2-SM	Bouvante E	0.03	SerradeMage E	0.97	0.286
372874554	BU11-SM	SerradeMage E	0.66	Y792769 E	0.34	0.280
393308781	Bellicia-CWM	MooreCounty E	0.46	Jackson cty Ol	0.54	0.412
373313780	Cornelia-CWM	Bouvante E	0.39	Tatahouine D	0.61	0.486
373313780	Cornelia-SM	Bereba E	0.51	GRO95555 D	0.49	0.298
393441792	BU14-CWM	SerradeMage E	0.74	Green olivine Ol	0.26	0.193
393441792	BU14-SM	GRO95555 D	0.45	Green olivine Ol	0.55	0.155
393750391	Arruntia-RM	Juvinas E	0.71	Green olivine Ol	0.29	0.409
393750738	Arruntia-CWM	A881819 E	0.68	Green olivine Ol	0.32	0.307
393750738	Arruntia-SM	MooreCounty E	0.59	Green olivine Ol	0.41	0.281
393801089	BU11-SM	SerradeMage E	0.69	Y792769 E	0.31	0.334
393931377	Drusilla-CWM	Bereba E	0.61	GRO95555 D	0.39	0.361
393931377	Drusilla-SM	Bereba E	0.66	GRO95555 D	0.34	0.310
394155284	BU8-CWM	SerradeMage E	0.51	ALH77256 D	0.49	0.329
394198127	Canuleia-RM	EET87542 E	0.42	GRO95555 D	0.58	0.487
394683501	Cornelia-CWM	Cachari E	0.46	EETA79002 D	0.54	0.163
394683501	Cornelia-SM	SerradeMage E	0.75	ALH77256 D	0.25	0.140
394859589	Eumachia-CWM	Bereba E	0.63	SerradeMage E	0.37	0.314
394859589	Eumachia-SM	Bereba E	0.47	SerradeMage E	0.53	0.281
394860977	Aelia-CWM	EET87542 E	0.40	GRO95555 D	0.60	0.283
394860977	Aelia-SM	EET87542 E	0.29	GRO95555 D	0.71	0.212
394993455	Aelia-RM	EET87542 E	0.22	SerradeMage E	0.78	0.260
395256929	Lepida-SM	Bouvante E	0.09	SerradeMage E	0.91	0.586
395301166	Marcia-CWM	Bouvante E	0.14	SerradeMage E	0.86	0.347
395301166	Marcia-SM	Bouvante E	0.14	SerradeMage E	0.86	0.381
395301549	Marcia-CWM	Cachari E	0.24	SerradeMage E	0.76	0.282
395301549	Marcia-SM	Cachari E	0.20	SerradeMage E	0.80	0.318
395387692	Licinia-CWM	Bereba E	0.54	GRO95555 D	0.46	0.269
395387692	Licinia-SM	Bereba E	0.49	GRO95555 D	0.51	0.192
395611823	BU2-CWM	EET87542 E	0.28	SerradeMage E	0.72	0.239
395611823	BU2-SM	SerradeMage E	0.75	Y792769 E	0.25	0.242

Table 7.4: Results of the linear unmixing applied to the bright material VIR data. In the third and fifth columns letter E indicates eucrite, D diogenite, Ol olivine.

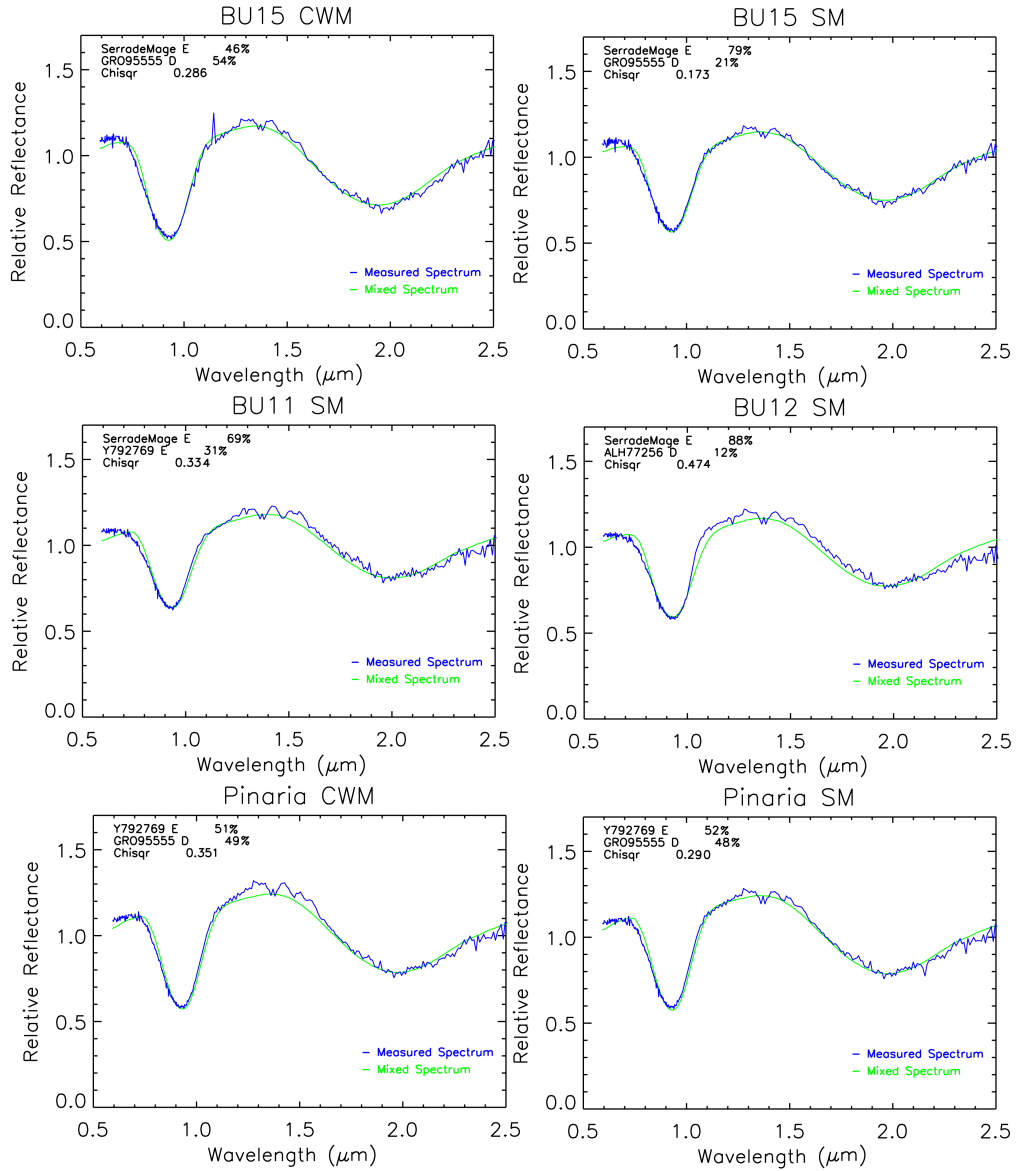


Figure 7.7: VIR spectra of different BM units compared with the best mixed spectra. In each plot we indicate the endmember with the relative amounts and the χ^2 value. The green spectrum represents the mixed spectrum, while the blue spectrum is the average spectrum of the correspondent BU provided by VIR.

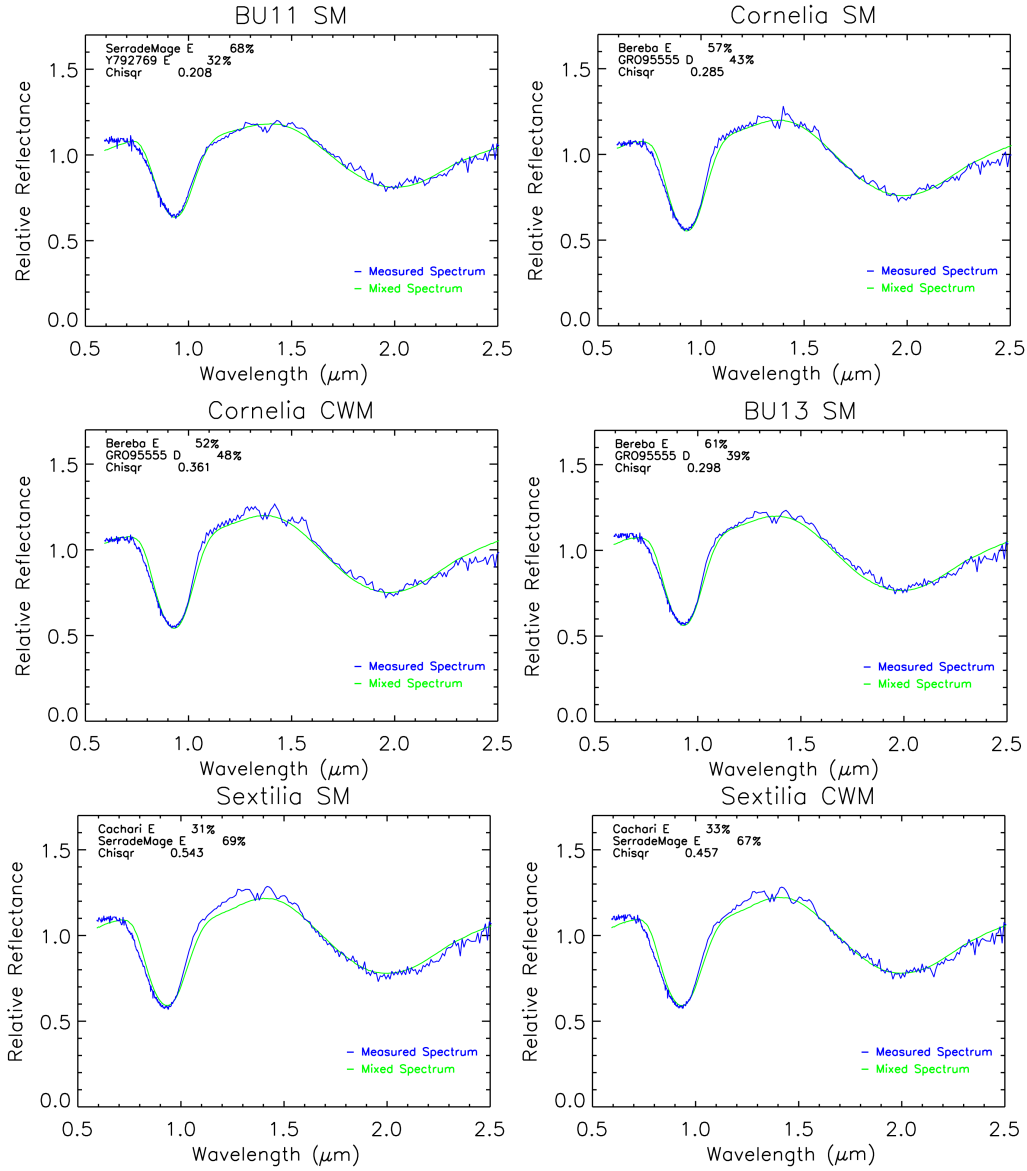


Figure 7.8: VIR spectra of different BM units compared with the best mixed spectra. In each plot we indicate the endmember with the relative amounts, and the χ^2 value. The green spectrum represents the mixed spectrum, while the blue spectrum is the average spectrum of the correspondent BU provided by VIR.

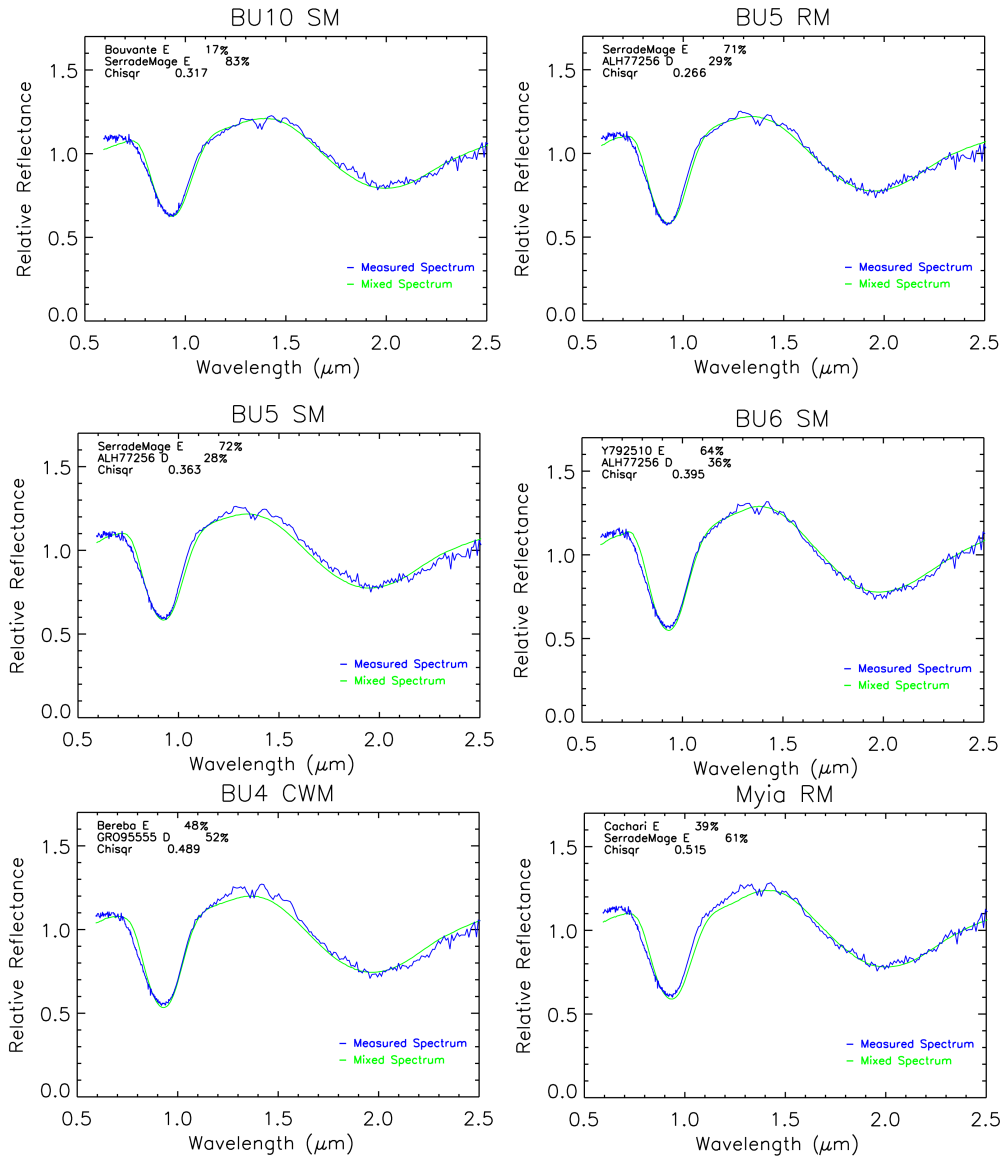


Figure 7.9: VIR spectra of different BM units compared with the best mixed spectra. In each plot we indicate the endmember with the relative amounts, and the χ^2 value. The green spectrum represents the mixed spectrum, while the blue spectrum is the average spectrum of the correspondent BU provided by VIR.

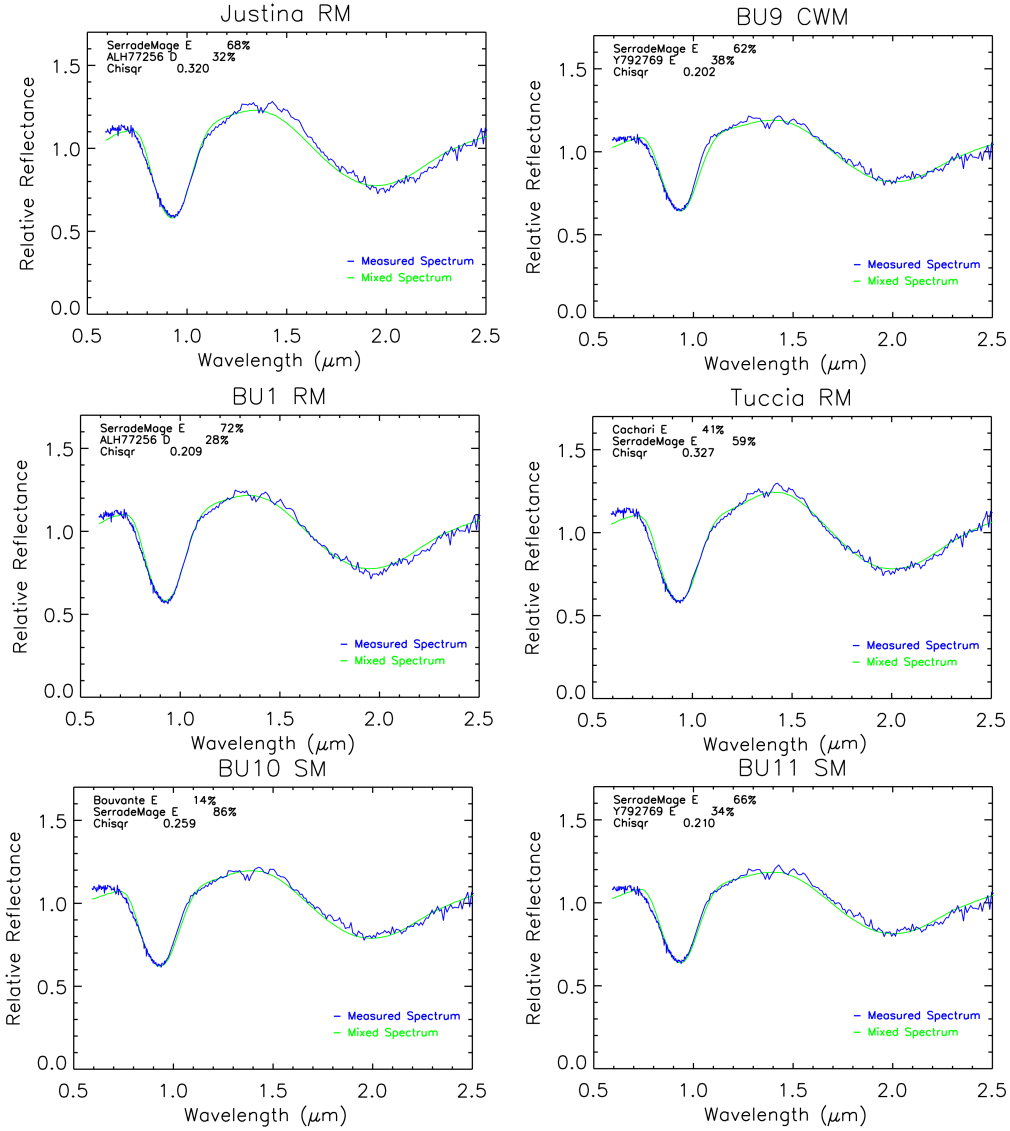


Figure 7.10: VIR spectra of different BM units compared with the best mixed spectra. In each plot we indicate the endmember with the relative amounts, and the χ^2 value. The green spectrum represents the mixed spectrum, while the blue spectrum is the average spectrum of the correspondent BU provided by VIR.

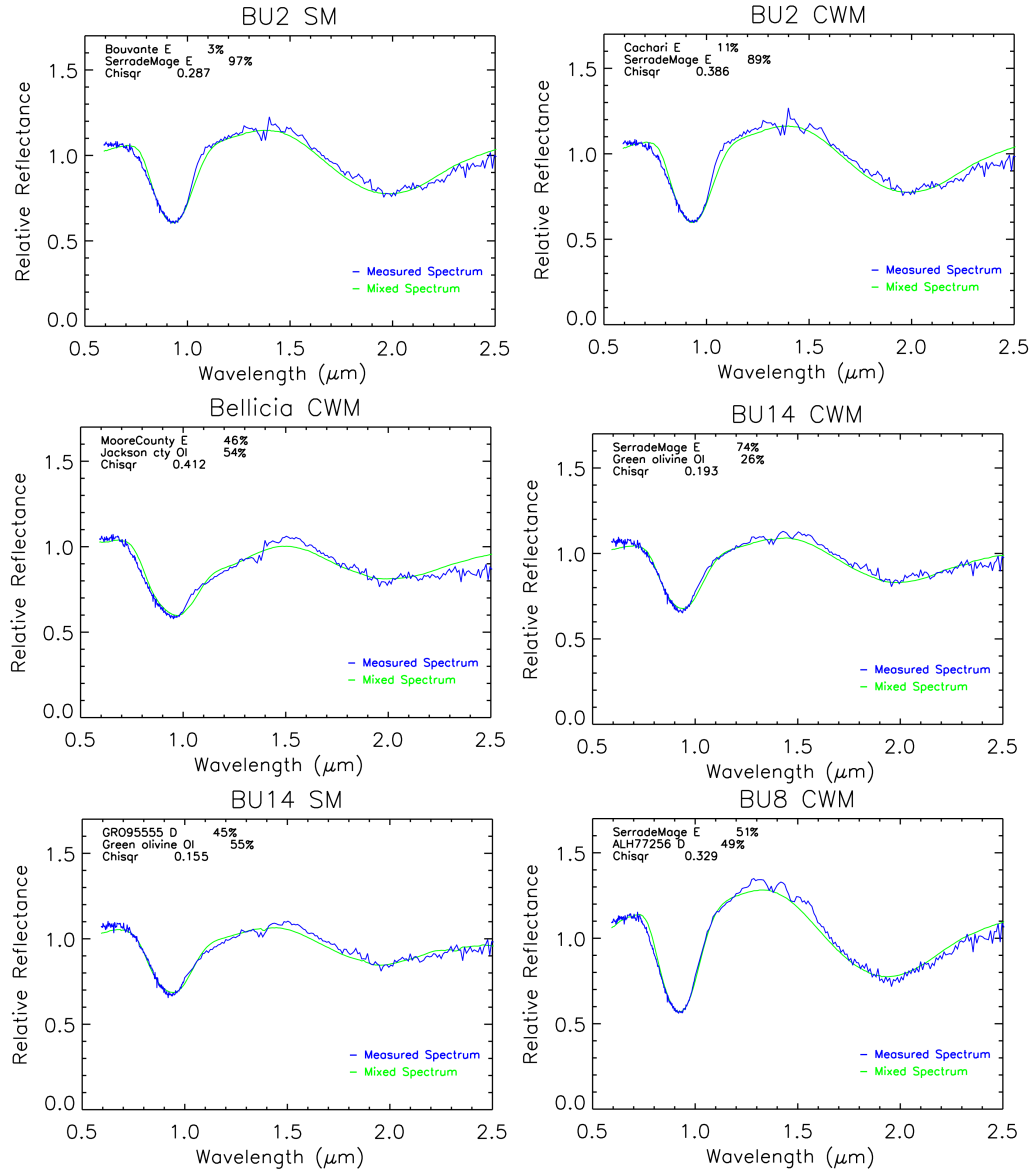


Figure 7.11: VIR spectra of different BM units compared with the best mixed spectra. In each plot we indicate the endmember with the relative amounts, and the χ^2 value. The green spectrum represents the mixed spectrum, while the blue spectrum is the average spectrum of the correspondent BU provided by VIR.

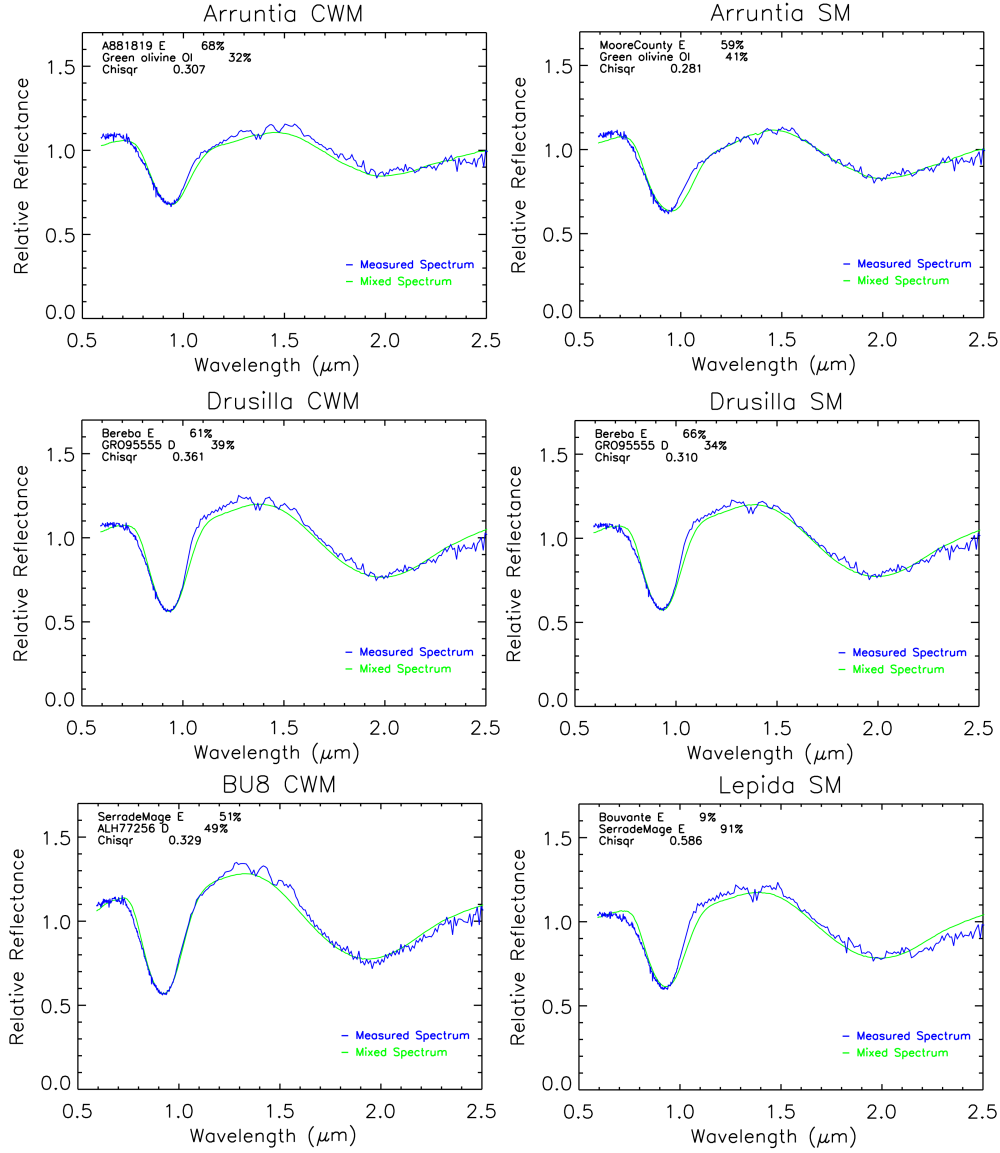


Figure 7.12: VIR spectra of different BM units compared with the best mixed spectra. In each plot we indicate the endmember with the relative amounts, and the χ^2 value. The green spectrum represents the mixed spectrum, while the blue spectrum is the average spectrum of the correspondent BU provided by VIR.

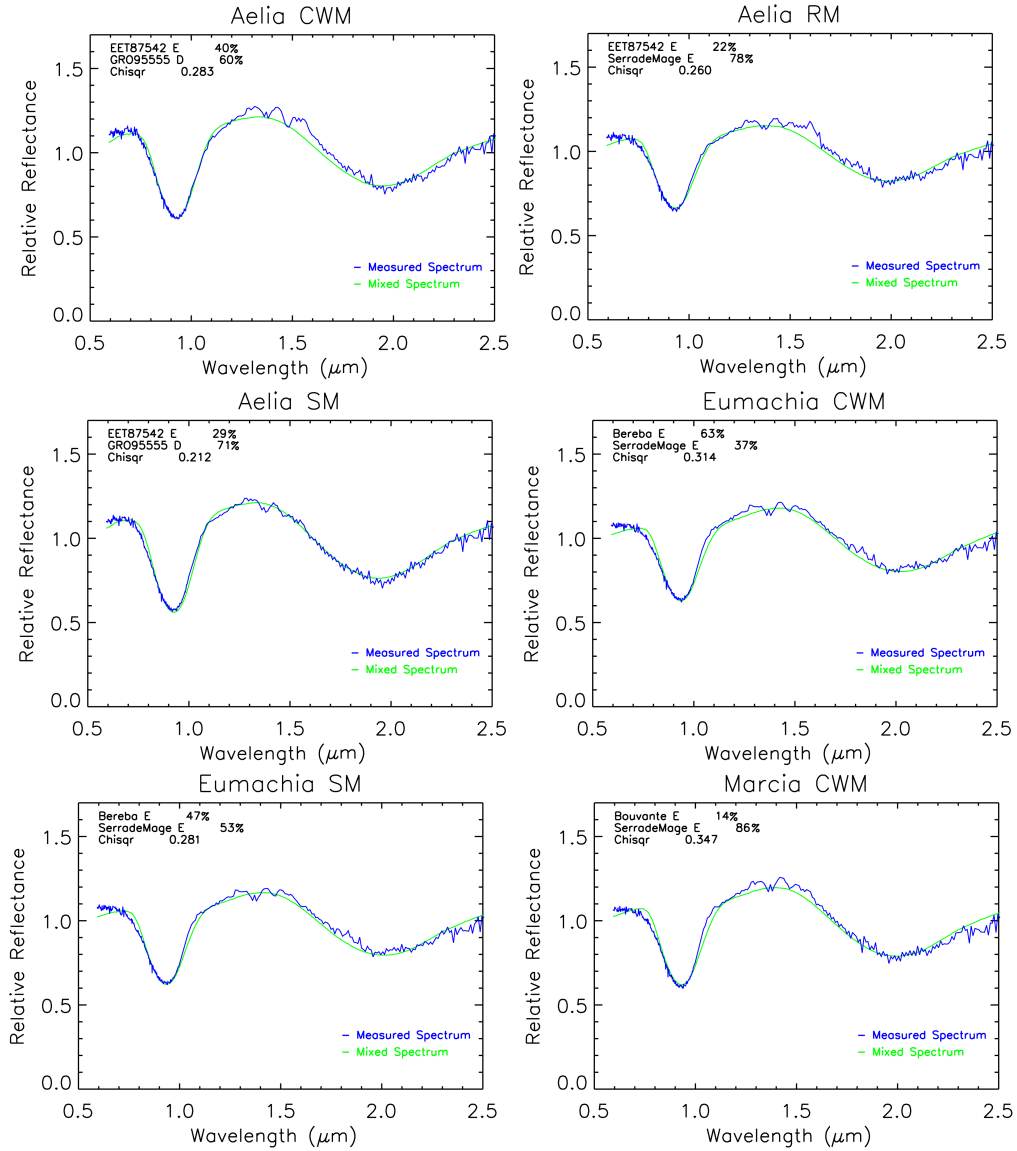


Figure 7.13: VIR spectra of different BM units compared with the best mixed spectra. In each plot we indicate the endmember with the relative amounts, and the χ^2 value. The green spectrum represents the mixed spectrum, while the blue spectrum is the average spectrum of the correspondent BU provided by VIR.

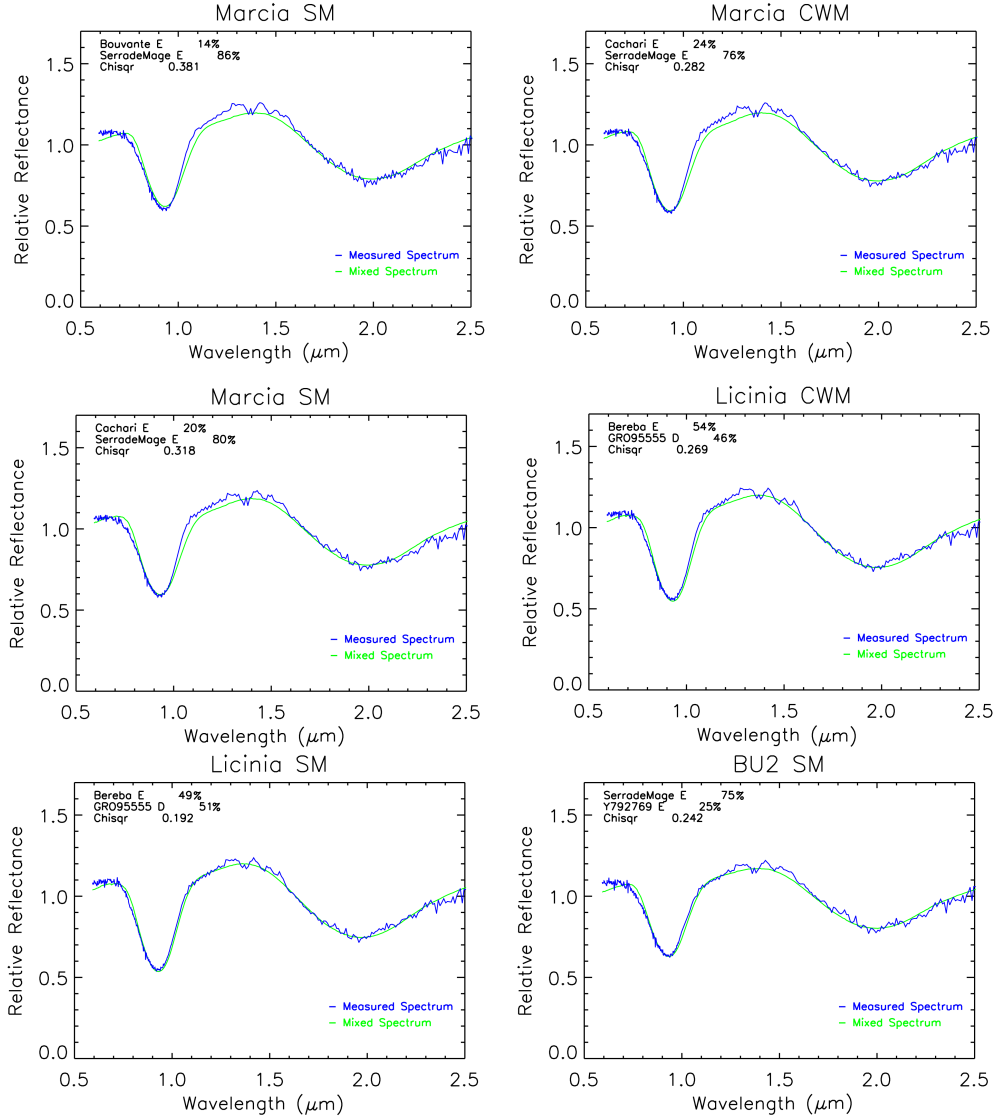


Figure 7.14: VIR spectra of different BM units compared with the best mixed spectra. In each plot we indicate the endmember with the relative amounts, and the χ^2 value. The green spectrum represents the mixed spectrum, while the blue spectrum is the average spectrum of the correspondent BU provided by VIR.

7.3.1 Evaluation of the method

In the previous section we have established the endmembers present in the bright units and their relative abundance. Now we discuss the reliability of the results obtained with this method. First of all, we considered the trend of the diogenite and eucrite content related to the band center, that gives informations on the mineralogy. Short band centers correspond to high content of diogenite and vice versa for eucrite (Burns, 1993; Mittlefehldt et al., 1998). In Fig. 7.15 we show trends of eucrite and diogenite abundances retrieved by linear unmixing with the band II center. We observe that the amount of diogenite decreases when the band II center increase, and we find an opposite trend for the eucrite, as expected.

To test the reliability of the choice of endmembers, we calculate the band centers and band depths of the sample considered. We find that the cumulate eucrite *Serra de Mage* is the endmember most found with our method. It is generally the dominant component with spectral parameters comparable with those of the bright units.. It is generally the dominant component with spectral parameters comparable with those of the bright units. The other recurrent eucrites are *Bereba*, *Cachari* and *Bouvante*; they have the band depths comparable with those of the bright units, but present band centers at longer wavelengths. They are the minor component, in the eucrite-eucrite mixture, when *Serra de Mage* is the other endmember, while they are the higher abundance components in the eucrite-diogenite mixture, when the diogenite is second endmember. Eucrites *Bereba*, *Cachari* and *Bouvante* have the band centers at longest wavelengths within the eucrite sample; thus, when they are combined with the diogenite, the result is a spectrum compatible with those of the bright units.

To study the properties of the endmembers chosen by our algorithm, we analyze the spectra of the endmembers and we compare their spectral parameters with those of the BM units (Figs 7.17, 7.18, 7.19). For the eucrite we observe that *Serra de Mage* differs from the other eucrite and thus can be considered as a representative endmember (Fig. 7.18). For the diogenite we observe that the most frequent *GRO95555* has a spectrum very similar to *Tatahouine*; thus, the selection of this endmember could not be representative (Fig. 7.17).

To verify if the endmembers are representative of the mineralogy, we consider the amounts corresponding to the ten lowest χ^2 values. If for small χ^2 variations we find the same endmembers we can consider them good endmembers, which can represent the real mineralogy. If small χ^2 variations lead to different endmembers, then they can not be considered representative of the composition. Here we find that when the mixed spectrum is very

similar to the measured spectrum and thus the χ^2 value is small, the endmembers corresponding to the ten lowest χ^2 remain the same, with similar amounts. If the fit is not optimal, the endmembers may change. In Figs. 7.20, 7.21, 7.22 and 7.23 we show an example of two different representative cases. In the case of BU12-SM (Figs 7.20, 7.21), where the χ^2 is large, we find that for small χ^2 variations the endmembers change. In this case, the two endmembers cannot be considered representative of the mineralogy, so it can be useful to increase the number of endmember or to consider other endmembers. On the other hand, in BU1-RM, the χ^2 values are lower and we find always the same endmember for the first ten χ^2 (Figs. 7.22, 7.23); thus, in this case the endmember can be considered representative of the real composition.

Application of linear unmixing of VIR spectra produces good results in agreement with the mineralogy. Using this method we have been able to estimate the amounts of eucrite, diogenite and olivine of bright material on Vesta. The results can be improved increasing the number of endmembers. Although the results obtained with two endmembers are satisfactory, at least one other endmember is necessary to detect the howardite amount when one of the endmembers is different from eucrite and diogenite.

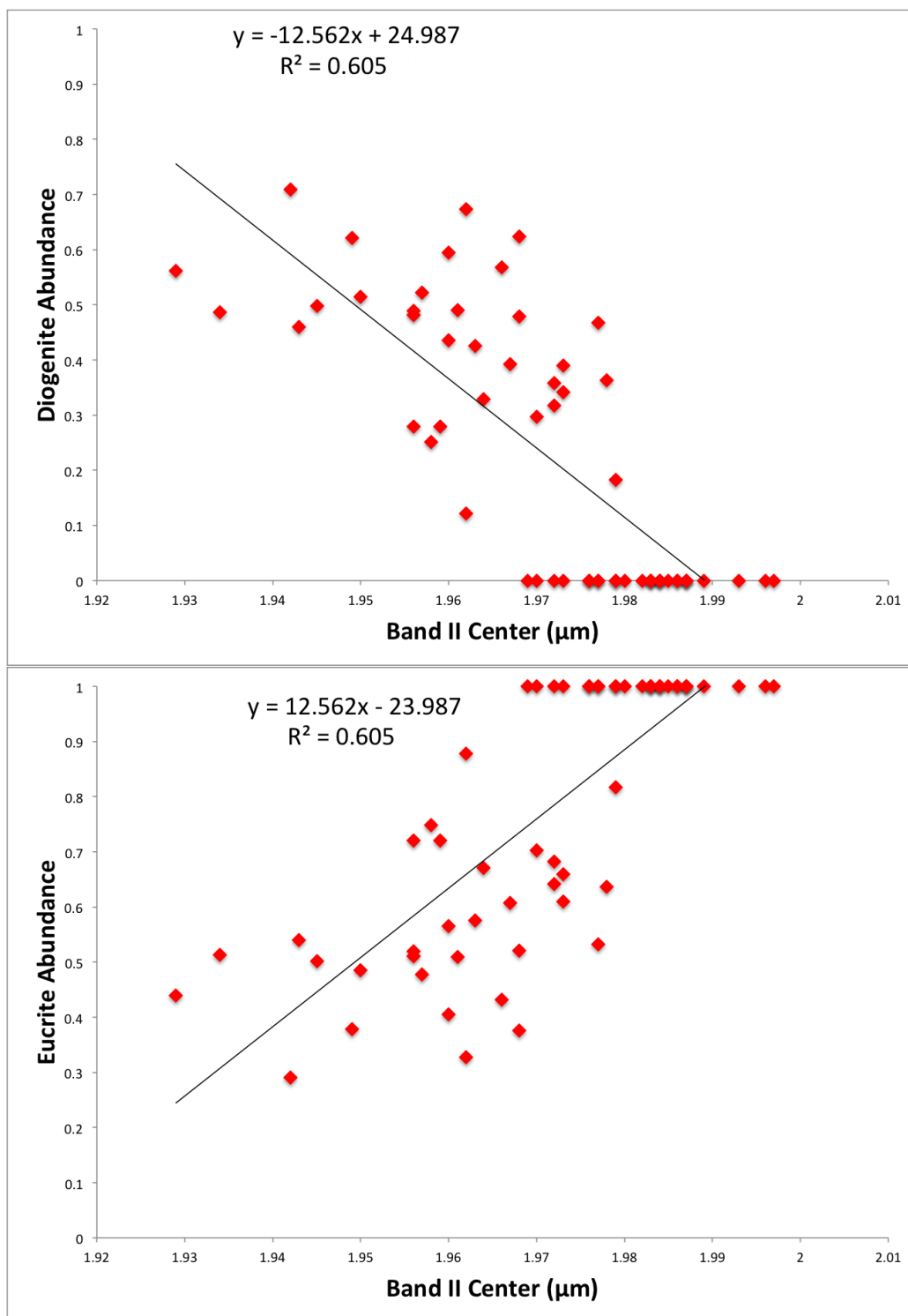


Figure 7.15: Top: Diogenite abundances vs band II center. The linear relation between band II center and abundance of diogenite indicates that diogenite abundance decreases as the band II center decreases, according with the pyroxenes mineralogy. Bottom: Eucrite abundances vs band II center. Eucrite abundance increases with increasing band II center, as expected. When the two endmembers are both eucrite the total amount of eucrite is 1 which correspond to an amount of diogenite equal to zero.

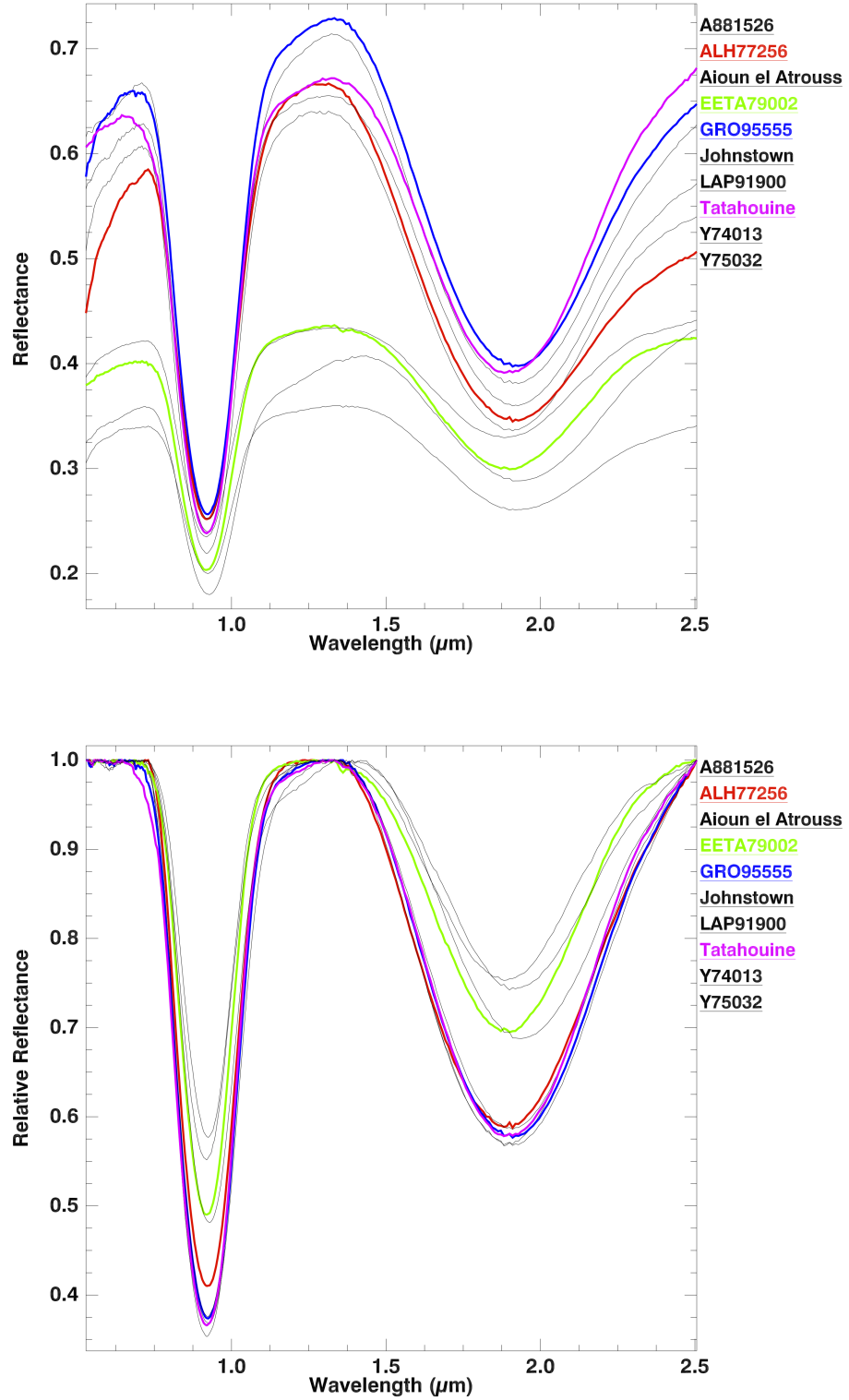


Figure 7.17: Top: Spectra of the whole diagenite sample. Colored spectra are those selected as endmembers. Bottom: Spectra of the whole diagenite sample with continuum removed.

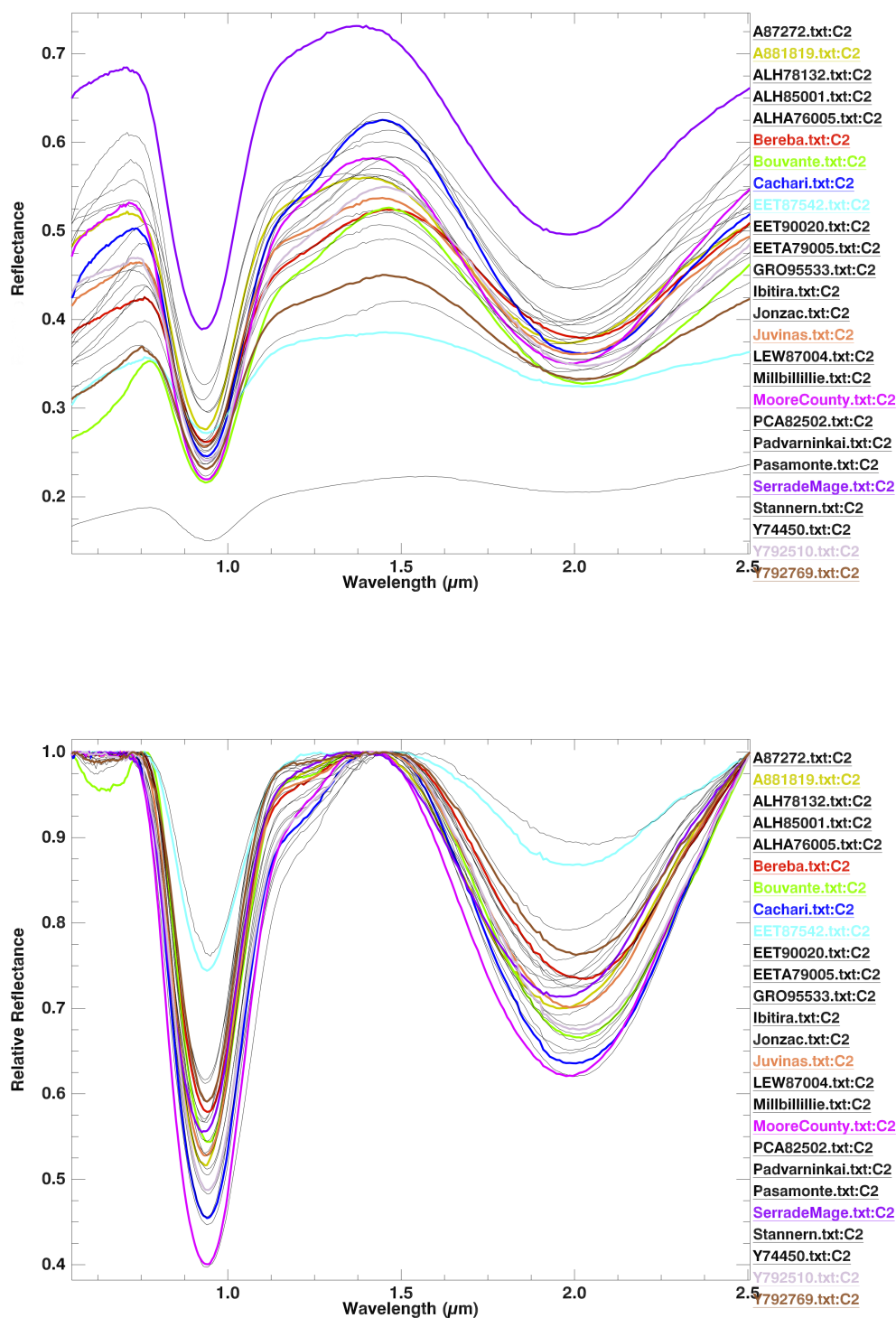


Figure 7.18: Top: Spectra of the whole eucrite sample. Colored spectra are those selected as endmembers. Bottom: Spectra of the whole eucrite sample with continuum removed.

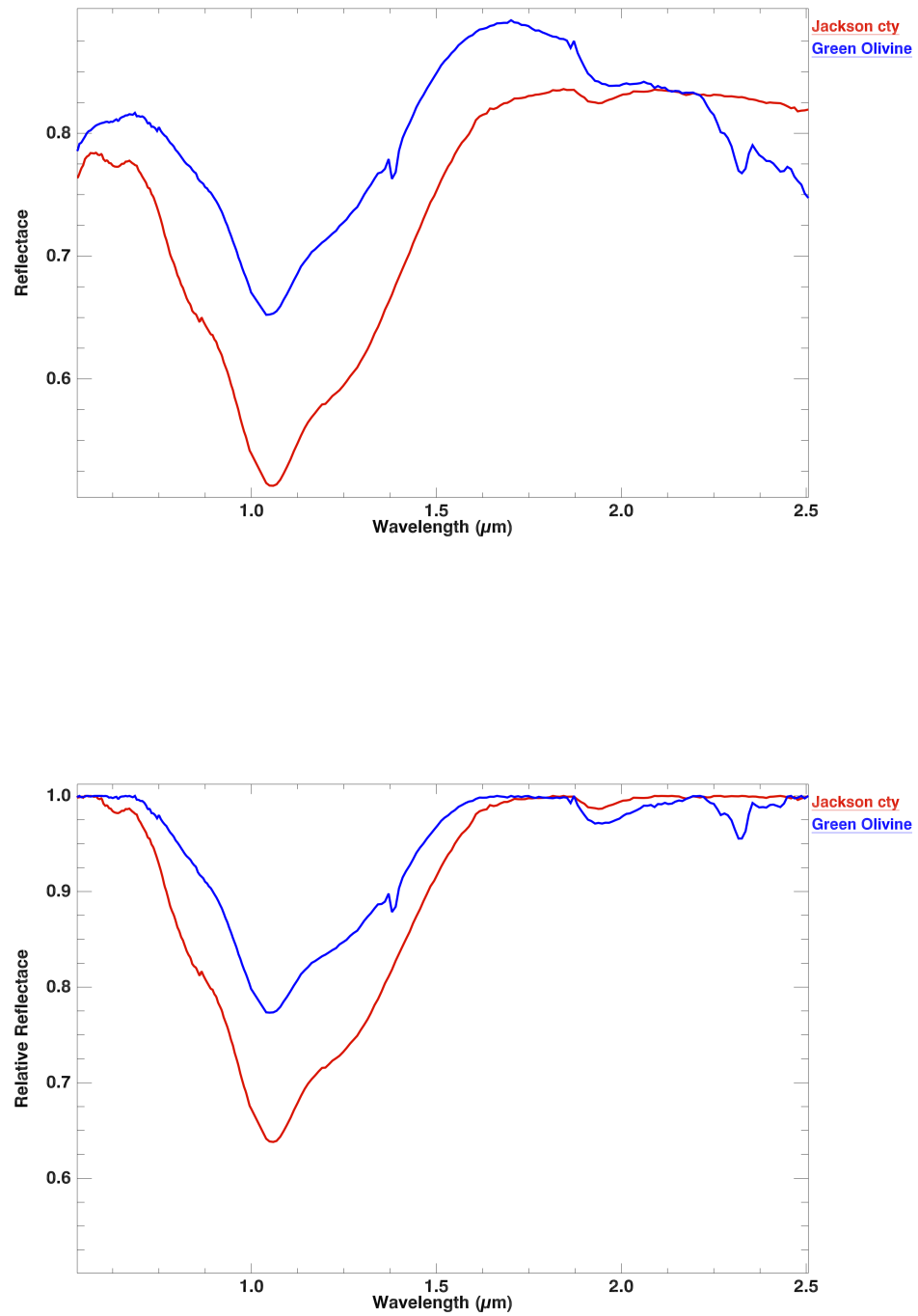


Figure 7.19: Top: Spectra of the selected olivine. Bottom: Spectra of selected olivines with continuum removed.

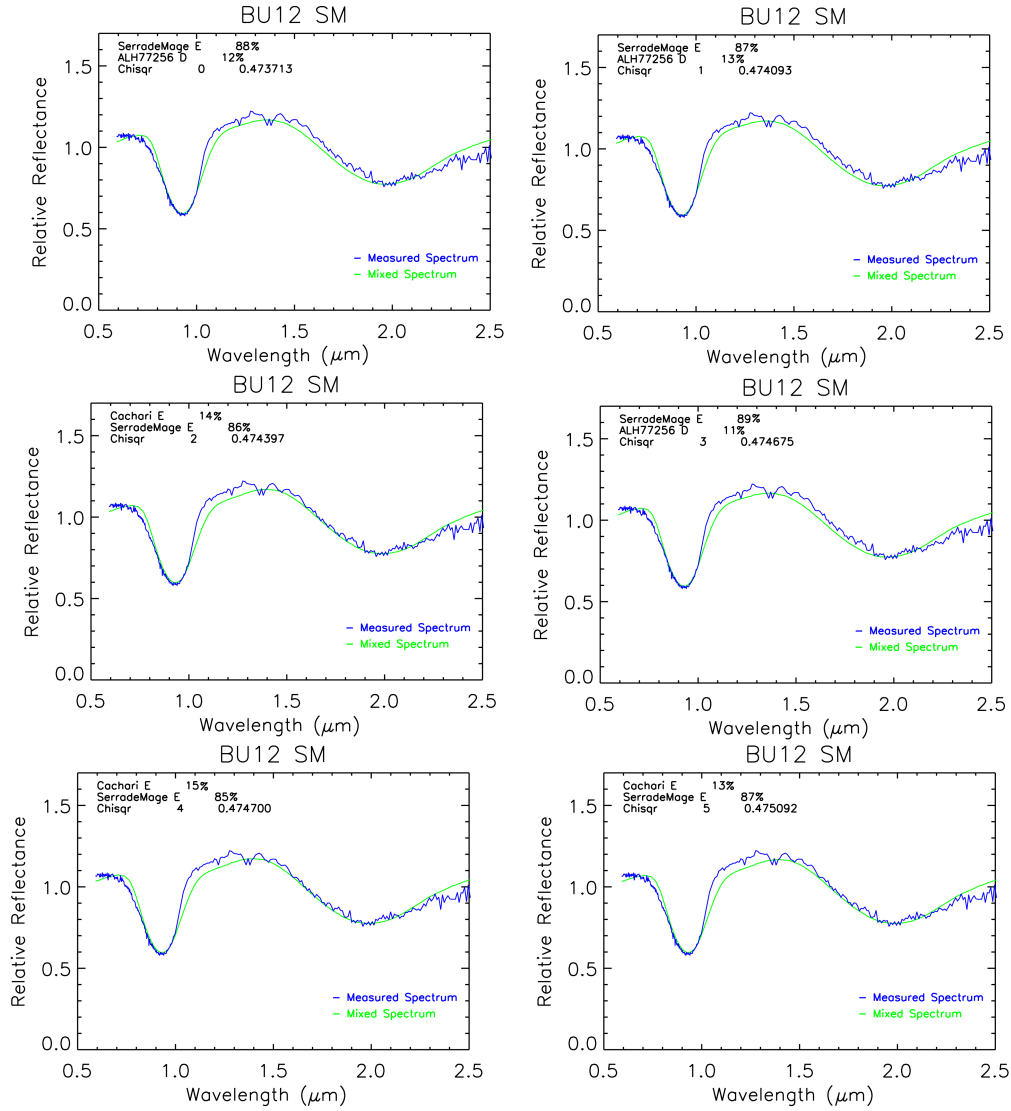


Figure 7.20: Abundances estimated for the ten lowest χ^2 values for BU12-SM. In this case the fit is not optimal and for small χ^2 variations, different endmembers may be found.

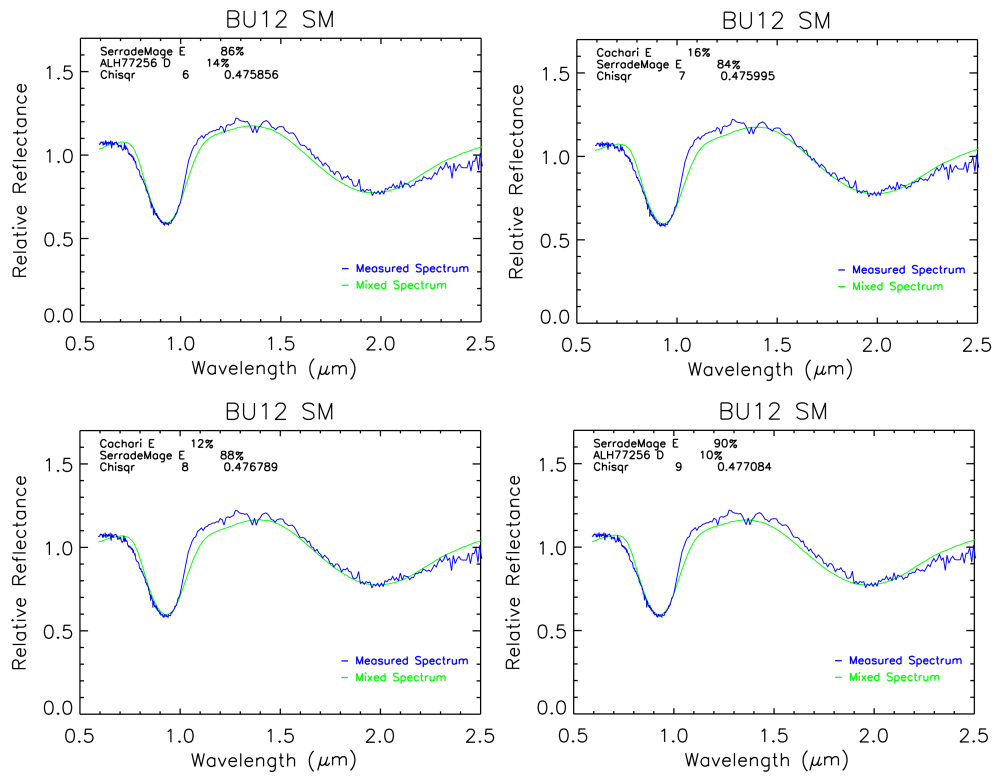


Figure 7.21: Abundances estimated for the ten lowest χ^2 values for BU12-SM. In this case the fit is not optimal and for small χ^2 variations, different endmembers may be found.

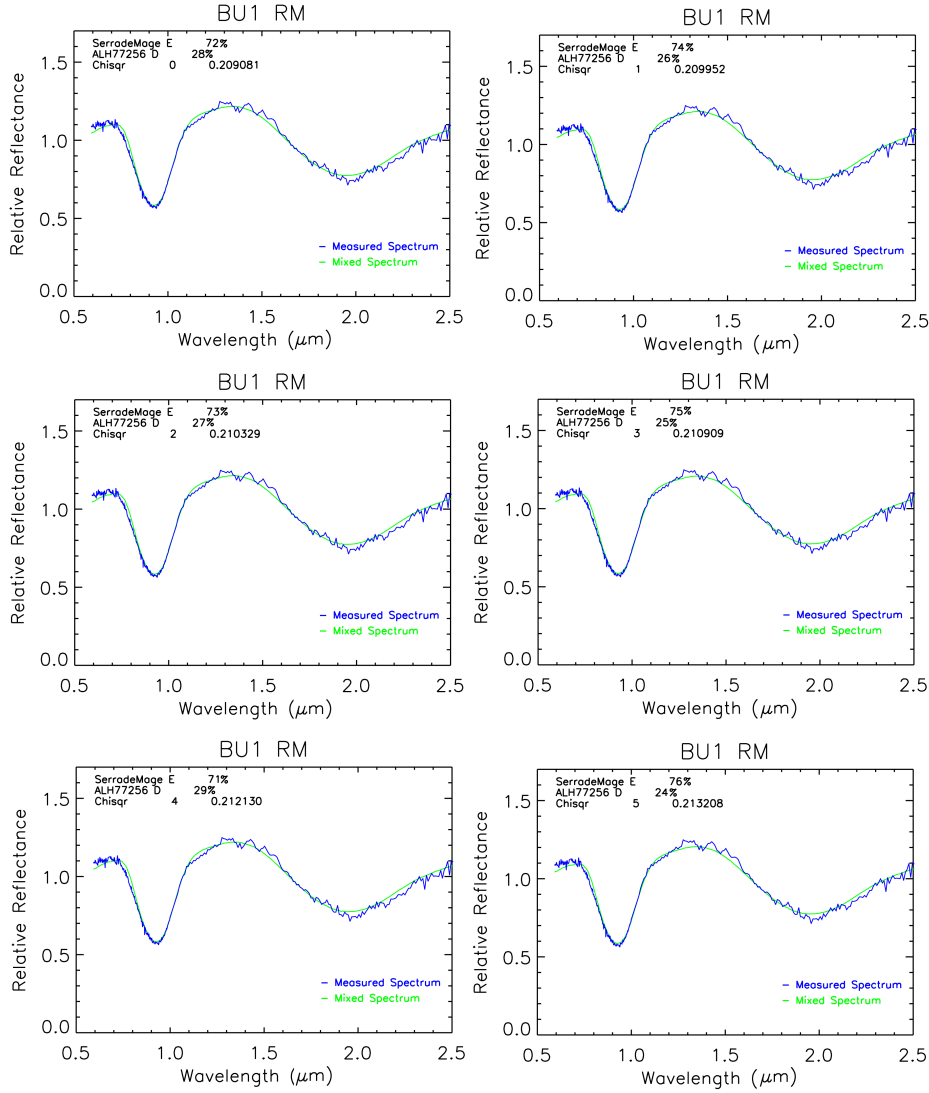


Figure 7.22: Abundances estimated for the ten lowest χ^2 values for the BU1-RM. In this case χ^2 is low, and the fit is good. For small χ^2 variations, the endmembers remain the same.

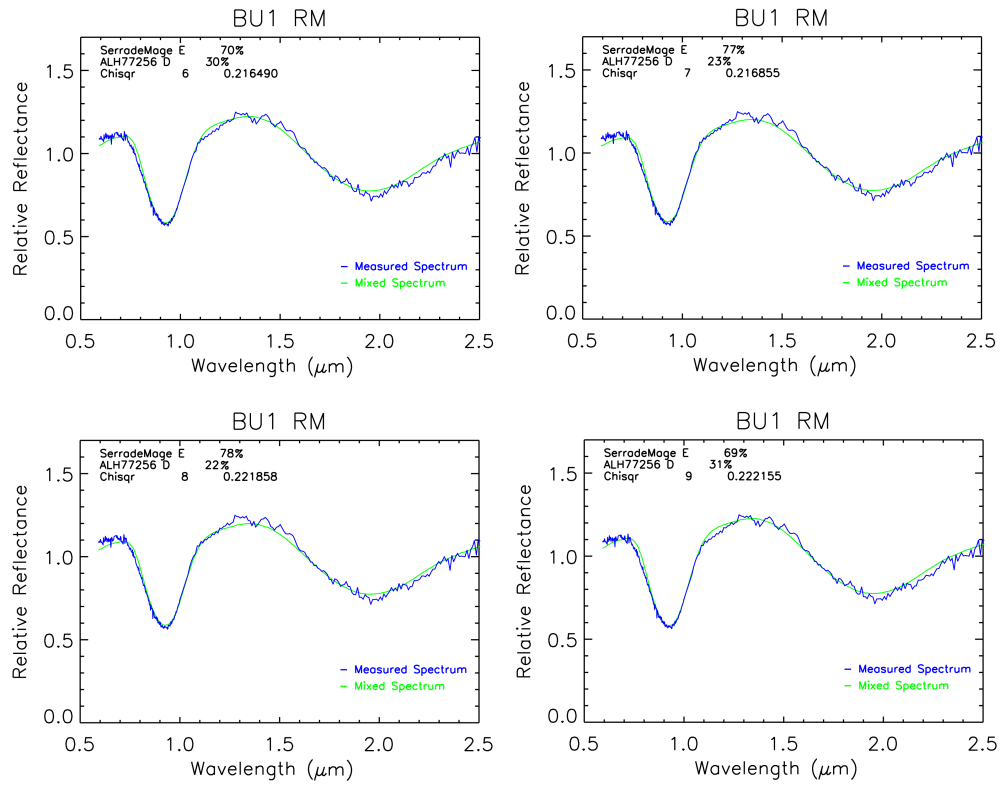


Figure 7.23: Abundances estimated for the ten lowest χ^2 values for the BU1-RM. In this case χ^2 is low, and the fit is good. For small χ^2 variations, the endmembers remain the same.

Conclusioni

In questa tesi abbiamo utilizzato diverse tecniche per ridurre e analizzare dati iperspettrali e multispettrali di superfici planetarie. Abbiamo illustrato come georeferenziare e proiettare immagini iperspettrali e multispettrali, e abbiamo prodotto molte mappe locali e globali di dati misurati e derivati (Appendice A). Le immagini proiettate e le mappe prodotte durante questa tesi sono state utilizzate per interpretare i dati delle missioni Dawn e Messenger. In particolare, i dati di VIR a bordo di Dawn, qui elaborati sono stati presentati in molti articoli (De Sanctis et al., 2012a,b, 2013; Ammannito et al., 2013a,b; Tosi et al., 2014a,b) (vedi Appendice). Abbiamo utilizzato diverse tecniche di analisi in base alla tipologia di dati trattata. Abbiamo applicato i metodi di classificazione sui dati di MASCS e MDIS (Capitoli 2, 5), abbiamo derivato e analizzato parametri spettrali, come centri e profondità di banda e band area ratio per i dati di VIR, e abbiamo infine applicato il linear spectral unmixing per derivare la composizione delle unità chiare di Vesta.

L'applicazione dei metodi di classificazione ai dati di VIRS e MDIS ci ha permesso di discriminare diverse tipologie di terreni sulla superficie di Mercurio. In particolare abbiamo considerato i dati relativi alla regione di Rudaki del secondo flyby di Messenger. Il classificatore ISODATA applicato ai dati di VIRS, ha identificato sei classi, permettendo di distinguere diversi livelli di riflettanza, e quindi diversi terreni. La proiezione dei footprint delle classi sul corrispondente mosaico della camera ha rivelato una buona corrispondenza tra l'informazione spettrale e morfologica. Abbiamo trovato che classi relative a regioni chiare hanno una minore pendenza spettrale indicativa dei terreni più giovani, mentre pendenze più elevate sono associate a regioni a minore riflettanza. La classificazione ISODATA sui dati di MDIS non è in grado di distinguere le regioni realmente chiare dai bordi illuminati dei crateri, e quelle a bassa riflettanza da quelle in ombra. Per risolvere questo problema abbiamo applicato la classificazione ISODATA alle regioni a basse e alta riflettanza separatamente. In questo modo il classificatore è in grado di distinguere le regioni chiare dai bordi illuminati dai crateri e le regioni a

basse riflettanza da quelle in ombra. Quindi abbiamo scelto gli endmember da utilizzare con il metodo delle DISTANZA MINIMA. Questo classificatore supervised ci ha permesso di determinare le classi associate ai differenti tipi di terreni in questa regione, e di scartare le due classi affette da condizioni di illuminazione sfavorevoli. Il metodo della DISTANZA MINIMA ci ha permesso di distinguere smooth plains, regioni chiare e regioni rugose. Confrontando i risultati ottenuti dai dati VIRS e MDIS-WAC, abbiamo notato una buona corrispondenza tra le classi. Gli smooth plains sono stati identificati con la stessa classe, e allo stesso modo le regioni rugose. La copertura dei dati di VIRS in questa regione è limitata, non abbiamo quindi potuto analizzare regioni estese. In ogni caso il buon accordo tra le classificazioni dei diversi dati rafforza i risultati ottenuti.

Vesta ha un albedo medio elevato ed è caratterizzata da molte regioni con grande contrasto di albedo, bright (BM) and dark (DM) material units. In questo lavoro riportiamo la prima analisi dettagliata di un grande campione di unità chiare di Vesta, fatta utilizzando i dati di VIR con la migliore risoluzione spaziale disponibile, al fine di poterne studiare la natura e l'origine. Abbiamo cercato di determinare se le BM units sono tutte composte dallo stesso materiale o se sono caratterizzate da diverse mineralogie. Inoltre, abbiamo classificato queste unità come eucritiche, diogenitiche ed howarditiche per determinare tra queste la litologia dominante. Abbiamo confrontato le BM units con i terreni intermedi abbiamo ricercato la presenza di materiali diversi dai pirosseni (Zambon et al., 2014b).

In generale, abbiamo trovato che le BM units hanno la stessa mineralogia delle regioni circostanti ma spesso mostrano maggiori profondità di banda. La profondità delle bande è legata a fattori come l'abbondanza dei minerali assorbiti, la dimensione dei grani, la presenza di materiali opachi e lo space weathering (Clark, 1983; Pieters et al., 2012; Reddy et al., 2012a).

L'analisi delle profondità di banda per le BM units indica che la grain size non è responsabile di questo aumento (vedi Capitolo 6). Anche i processi di space-weathering possono influenzare le bande. Gli ejecta freschi dei crateri di Vesta, mostrano profondità di banda relativamente forte, indicando che i processi di mixing sulla superficie di Vesta sono sufficientemente robusti da alterare la proprietà ottiche, riducendo sia l'albedo che le profondità di banda (Pieters et al., 2012). Quindi, bande più profonde e il maggiore livello di albedo delle regioni chiare è indicativo di materiale più puro e meno miscelato.

Usando il diagramma della BI/BII possiamo associare gli spettri dei BM a quelli di specifiche HED ed è possibile calcolare la percentuale di BM units che mostrano una specifica litologia. Tutte le litologie relative alle HED, dalla diogenite all'eucrite, sono rappresentate nelle BM units, e la maggior

parte di loro sono identificate come howardite ricca in eucrite (Zambon et al., 2014b).

I risultati ottenuti da questa analisi indicano che le BM units hanno origine endogena e che sono rappresentative dei materiali più freschi e meno contaminati sottostanti la superficie.

Dopo aver derivato le proprietà spettrali delle unità chiare di Vesta, siamo stati in grado di selezionare un buon campione di endmember per poter applicare il linear spectral unmixing (Zambon et al. 2014 in preparation), con l'obiettivo di stimare la composizione di queste unità. L'analisi spettrale ha rivelato la presenza di eucrite, diogenite, howardite e olivina. Abbiamo scelto un campione di 26 eucriti, 10 diogeniti e 2 olivine con una grain size compatibile con quella delle unità chiare Vesta. Abbiamo considerato tutte le possibili combinazioni lineari di due endmember tra il campione di spettri selezionato, e abbiamo selezionato lo spettro risultante con il minor χ^2 . In questo modo l'algoritmo è stato in grado di scegliere automaticamente gli endmember corretti, derivando la composizione delle BM units. Test eseguiti su miscele di laboratorio hanno permesso di identificare i limiti di questo metodo; inoltre a regioni maggiormente eucritiche corrispondono centri banda spostati a lunghezze d'onda maggiori, come ci aspettavamo e vice versa. I risultati ottenuti sulle BM units rivelano che le regioni chiare sono dominate da eucrite, con una componente variabile di diogenite. Questo metodo ha inoltre permesso di rilevare la presenza di olivina. Tutte le unità identificate come ricche in olivina sono state confermate e ne abbiamo inoltre calcolato l'ammontare (vedi Capitolo 7).

Il lavoro svolto durante la tesi ha permesso di acquisire competenze specifiche nel campo dell'analisi di dati iperspettrali provenienti da missioni spaziali. Le analisi svolte sono state utilizzate per interpretare i dati e sono state incluse in diversi articoli.

Conclusions

In this thesis we use different techniques to reduce and analyze hyperspectral and multispectral data. We illustrate how to georeference and project hyperspectral and multispectral images. Many global and local maps have been produced of measured data and derived products (Appendix A). The projected images and the maps produced during this thesis have been used to interpret the data of Dawn and Messenger missions. In particular, the data from VIR on Dawn here elaborated has been presented in many articles (De Sanctis et al., 2012a,b, 2013; Ammannito et al., 2013a,b; Tosi et al., 2014a,b) (see Appendix). We use different techniques of analysis based on the typology of the data treated. We apply classification method on MASCS and MDIS data (Chapters 2, 5), we derive and analyze spectral parameters, such as band centers, band depths and band area ratio, for the VIR data, and finally we apply linear spectral unmixing to derive the composition of the bright material units on Vesta.

Application of classification methods on VIRS and MDIS data allows us to discriminate different types of terrains on Mercury's surface. In particular we consider VIRS and MDIS data of the second Messenger flybys of Mercury relative to the Rudaki areas.

The ISODATA classifier identifies six classes on VIRS spectra, allowing to distinguish different reflectance levels, and thus different terrains. The projection of the footprints of the classes on the correspondent camera mosaics reveals a good correspondence between spectral information and morphology. We find that classes relative to bright areas have shallower spectral slope indicative of younger terrains, while steeper spectral slope are associated with low reflectance regions match with rough and more mature areas. ISODATA classification of the MDIS data is not able to distinguish the real bright areas from the illuminated edge of the craters and the shadow to the low reflectance regions. To solve this problem we apply the ISODATA classification method to the regions detected by the low reflectance and high reflectance classes separately. In this way the classifier distinguishes the high reflectance from the illuminated edges of the craters, and the shadow regions from the low

reflectance areas. Thus we select the endmembers for the MINIMUM DISTANCE classifier. This supervised classifier allows us to determine the classes associated to the different terrain present on this area, and to discard the two classes affected by the illumination condition. The MINIMUM DISTANCE classification method allows us to distinguish smooth plains, bright areas, and rough regions. Comparing the results obtained by VIRS and MDIS-WAC data, we notice a good correspondence between the classes. Smooth planes are identified with the same class, as well as rough regions. The coverage of VIRS in this area is limited, thus we cannot check extended regions. In any case the good agreement of the classification results strengthens the results obtained.

Vesta has a high average albedo and a very large albedo contrasts with many bright (BM) and dark (DM) material units. In this work we report the first detailed analysis of a large sample of Vesta BM units, using VIR data with the best spatial resolution available in order to understand the origin and the nature of these units. We sought to determine whether BM units are all composed of the same material or whether they have different mineralogies. Further, we classify the units as eucritic, diogenitic or howarditic in order to determine if there is a dominant lithology among them. We also compare the BM regions to their immediate surroundings and search for the presence of other non-pyroxene minerals (Zambon et al., 2014b).

In general, BM have the same mineralogy as the surrounding terrain, but they often show greater band depths. Band depth is linked to factors such as the abundances of the absorbing minerals, the grain size, the presence of opaque material, and the extent of space weathering (Clark, 1983; Pieters et al., 2012; Reddy et al., 2012a).

Band depth analysis for the BM units indicates that grain-size effects are not responsible for the enhanced band depths (see Chapter 6). Space-weathering processes could also affect the bands. Fresh ejecta from Vesta craters shows relatively strong band depths, indicating that the physical mixing processes on Vesta is sufficiently robust to alter optical properties, reducing both the albedo and the band depths (Pieters et al., 2012). Thus, the deep bands and the high albedo of the bright regions are indicative of pure, less mixed, material.

Using the BI/BII diagram we can associate BM spectra with specific HED lithologies. It is also possible to compute the percentage of BM that shows a specific lithology. All the HED lithologies, from diogenite to eucrite, are represented in the BM units, and the majority are eucrite-rich howardite (Zambon et al., 2014b).

The results obtained from this spectral analysis of the BM units indicate that the bright regions have an endogenous origin. The BM represent fresh,

less contaminated material derived from below the surface of Vesta.

After deriving the spectral properties of the BM units, we have been able to select a good sample of endmembers to apply linear spectral mixing (Zambon et al. 2014 in preparation), with the aim of estimating the composition of the BM units on Vesta. The spectral analysis revealed the presence of eucrite, diogenite, howardite and olivine on Vesta BM. We choose a sample of 26 eucrite, 10 diogenite and 2 olivine with a grain size compatible with those of the BM. We mix linearly all the possible combinations of two endmembers among the samples elements, and we select the mixed spectrum with the minor χ^2 . In this way the algorithm chooses automatically the right endmembers, deriving the composition of the BM units. Tests performed on laboratory mixtures identify the limits of this method; moreover regions in which high amounts of eucrite have been found correspond with long band centers as expected, and vice versa. The results obtained on the BM reveals that bright areas are dominated by eucrite, with a variable component of diogenite. This method is also able to detect the presence of olivine. All bright units identified as rich in olivine have been confirmed and the olivine amount has been calculated (see Chapter 7).

The work done during the thesis permits the acquisition of specific expertise in the field of the analysis of hyperspectral data from the space missions. The analyses performed are used to interpret the data and are included in several articles.

Appendix A

Maps obtained by the VIR data

Here are shown the mosaics and projections of single frame produced during my PhD. These mosaics are obtained directly by the VIR calibrated data. Many of these maps have been presented in several international conferences. Fig. B.1 has been published in De Sanctis et al. (2012a), while Figs A.9, A.10 have been published in Ammannito et al. (2013b). Fig A.3 has been selected for the "Dawn Events Calendar" (<http://dawn.jpl.nasa.gov/multimedia/calendar.asp>) and for NASA's Dawn mission T-Shirt (<http://www.vesta.direct2garments.com/>).

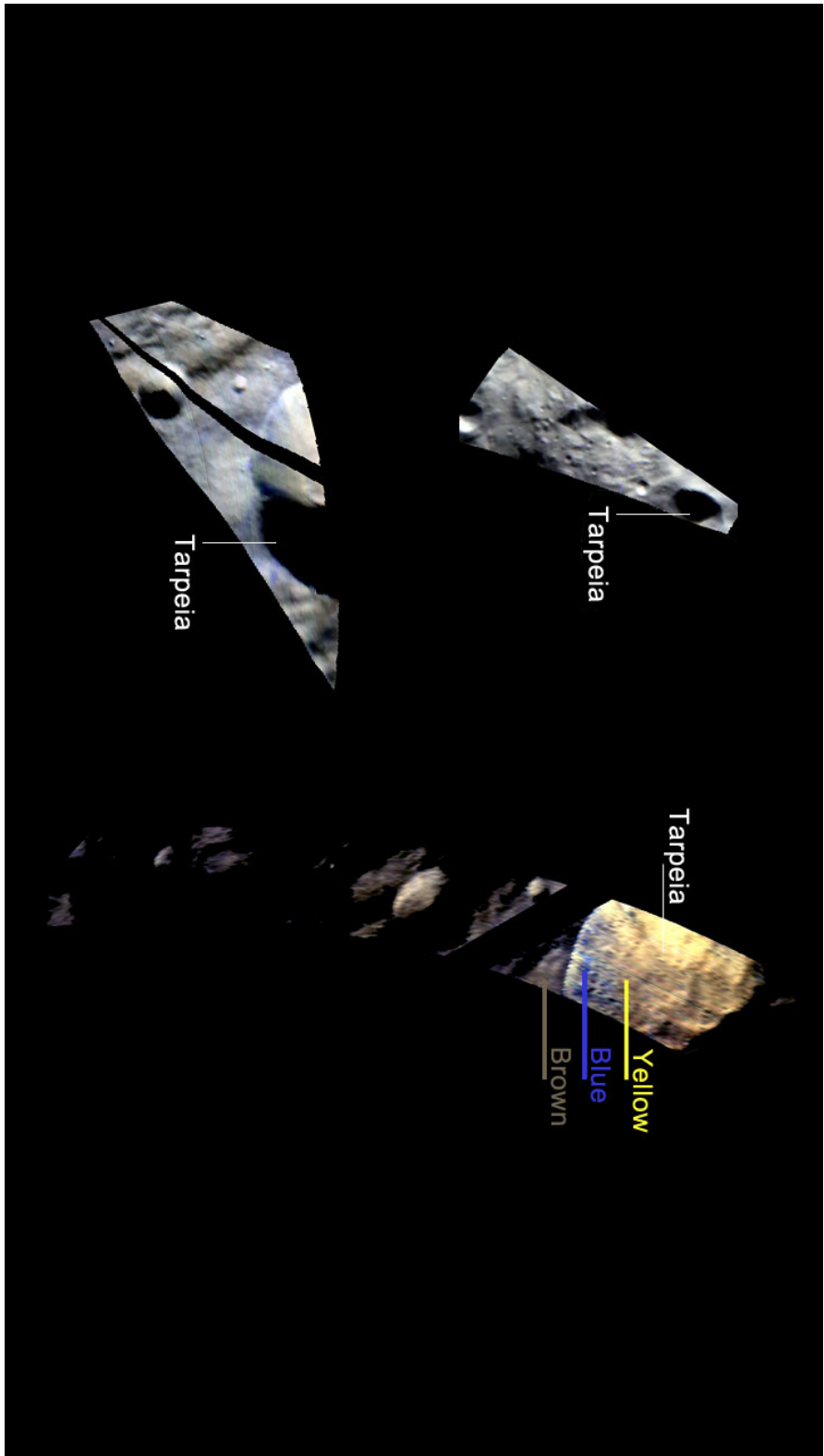


Figure A.1: RGB (red: reflectance at $1.9\mu\text{m}$, green: reflectance at $1.5\mu\text{m}$, blue: reflectance at $1.2\mu\text{m}$) images of Tarpeia crater mosaics in Vesta south pole derived by the VIR data relative to the LAMO phase mission in polar stereographic projection ([http://dawn.jpl.nasa.gov/multimedia/tarpeia\\$\\$_crater.asp](http://dawn.jpl.nasa.gov/multimedia/tarpeia$$_crater.asp)).

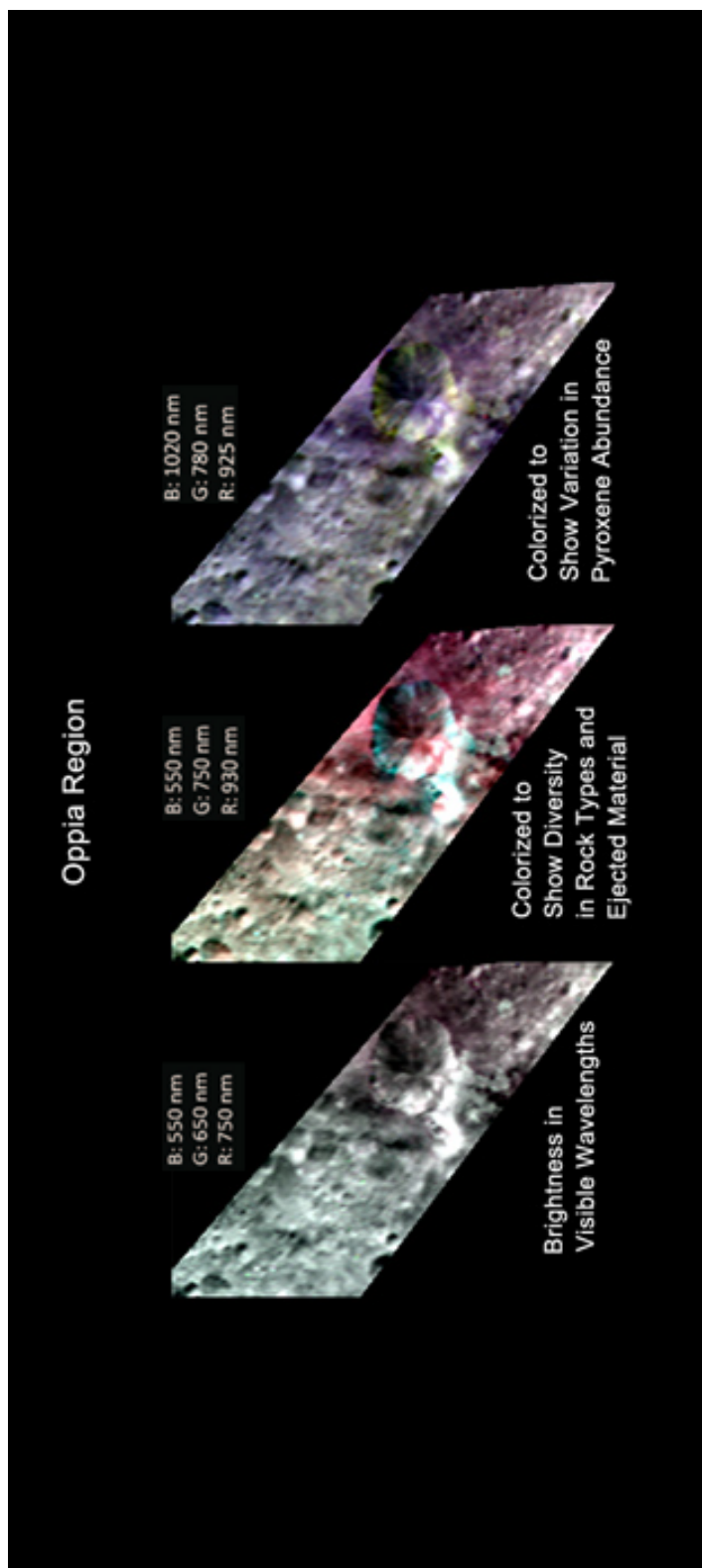


Figure A.2: RGB image of the Oppia region derived by the VIR data relative to the Survey phase mission in simple cylindrical projection (De Sanctis et al., 2012a) (http://dawn.jpl.nasa.gov/multimedia/tarpeia_temperature.asp).



Figure A.3: Vesta global mosaic derived by the VIR data relative to the HAMO phase mission at $0.55\mu\text{m}$ in orthographic projection (<http://dawn.jpl.nasa.gov/multimedia/imageoftheday/image.asp?date=20120208>). The image has been selected for the Dawn Events Calendar (<http://dawn.jpl.nasa.gov/multimedia/calendar.asp>).



Figure A.4: Vesta global mosaic derived by the VIR data relative to the HAMO2 phase mission at $0.55\mu\text{m}$ in simple cylindrical projection.



Figure A.5: Vesta mosaic of the north pole derived by the VIR data of the HAMO2 phase mission at $0.55\mu\text{m}$ in polar stereographic projection.

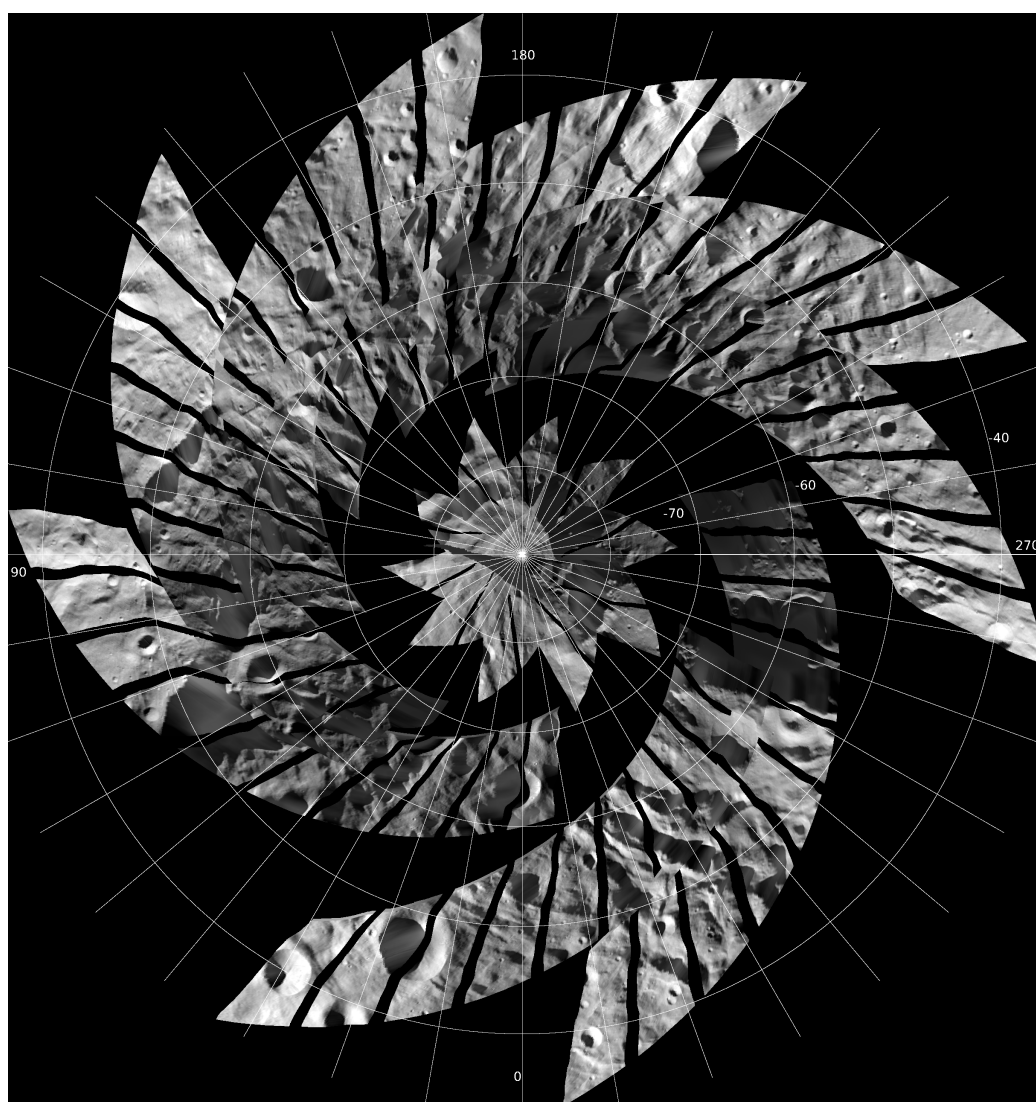


Figure A.6: Vesta mosaic of the south pole derived by the VIR data relative to the HAMO2 phase mission at $0.55\mu\text{m}$ in polar stereographic projection.

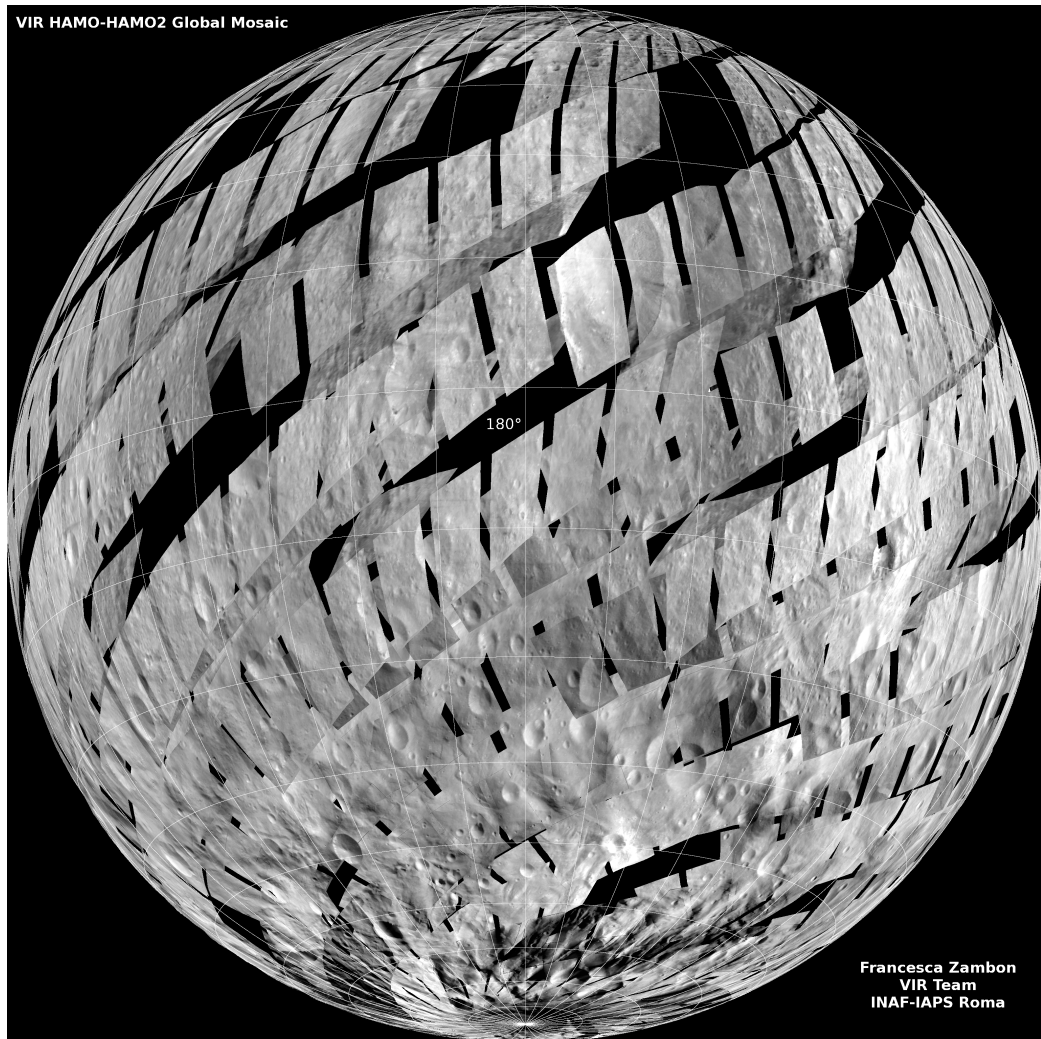


Figure A.7: Vesta global mosaic derived by the VIR data relative to the HAMO and HAMO2 phase mission at $0.55\mu\text{m}$ in orthographic projection.

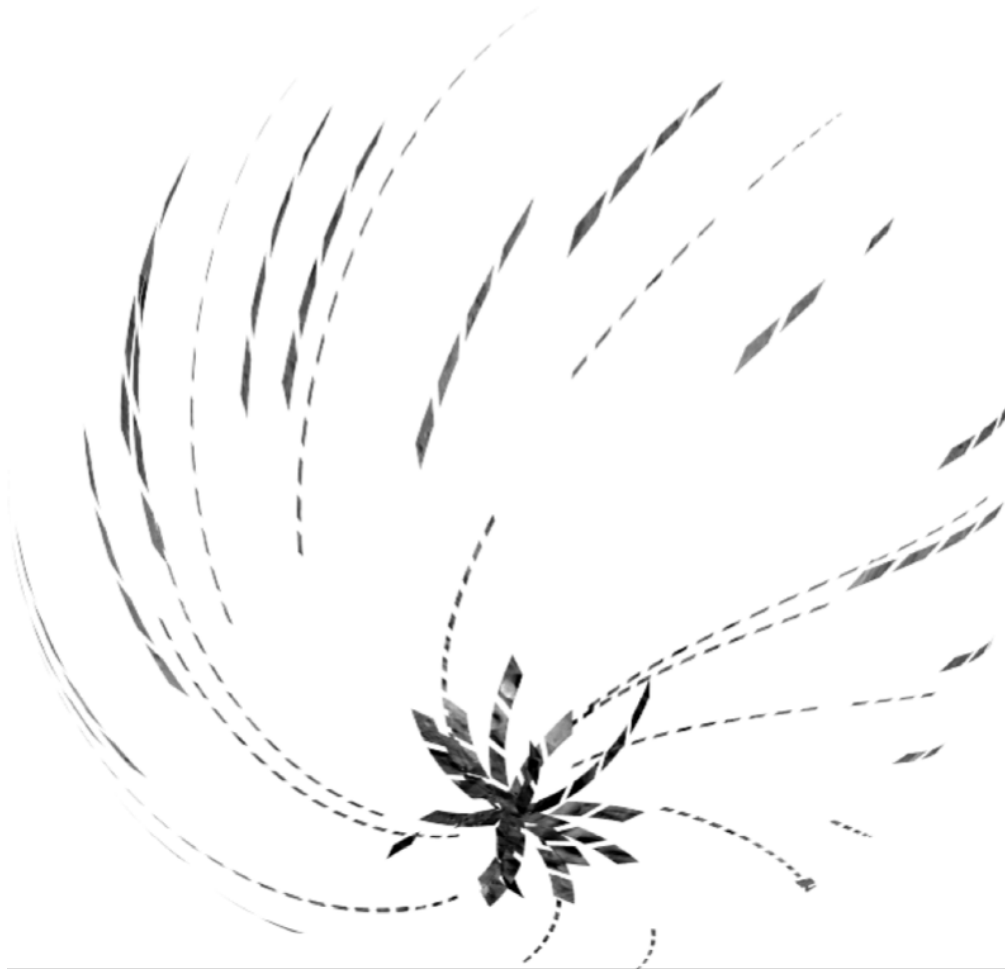


Figure A.8: Vesta global mosaic derived by the VIR data relative to the LAMO phase mission at $0.55\mu\text{m}$ in orthographic projection.

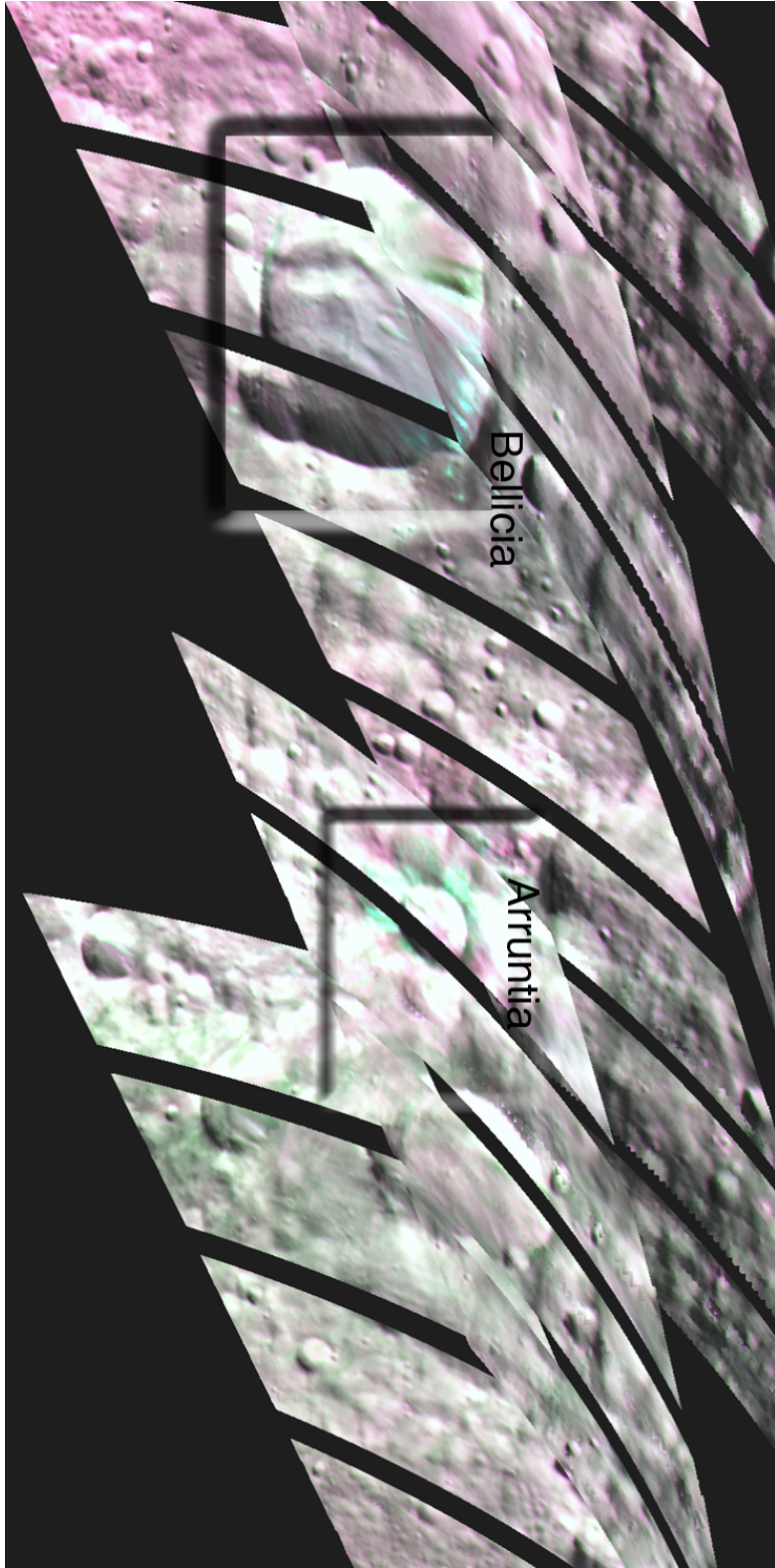


Figure A.9: Mosaic of Bellicia and Arruntia region relative to the HAMO2 phase mission in simple cylindrical projection (Ammannito et al., 2013b) ([http://dawn.jpl.nasa.gov/multimedia/Two\\$Craters\\$01ivine.asp](http://dawn.jpl.nasa.gov/multimedia/Two$Craters$01ivine.asp)).

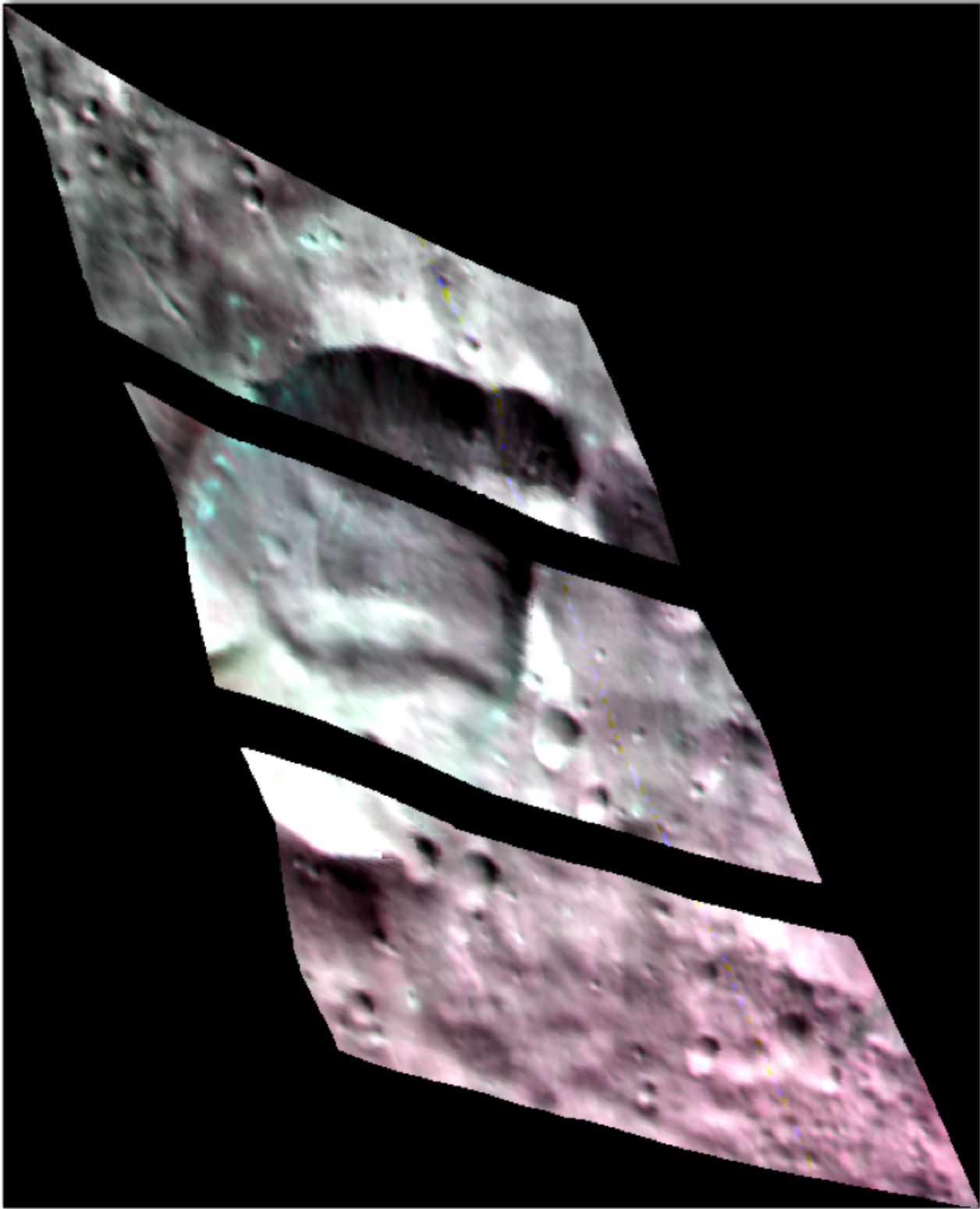


Figure A.10: Mosaic of Bellicia region relative to the HAMO2 phase mission in simple cylindrical projection (Amman-nito et al., 2013b) ([http://dawn.jpl.nasa.gov/multimedia/Contrast\\$_\\$enhanced\\$_\\$Bellicia\\$_\\$_Crater_.asp](http://dawn.jpl.nasa.gov/multimedia/Contrast$_$enhanced$_$Bellicia$_$_Crater_.asp)).

Appendix B

Maps and projection of retrieved data

In this section are shown the maps and projections of retrieved products derived by the VIR data produced during my PhD. Temperature global maps of the and temperature global maps at different Local Solar Time (LST) intervals has been reported (Tosi et al., 2014b). This mosaics are presented at the "Vesta in the Light of Dawn". Moreover projections of incidence angle and photometrically corrected data have been produced for specific VIR cubes, and published in Tosi et al. (2014a).

B.1 Single cube projections

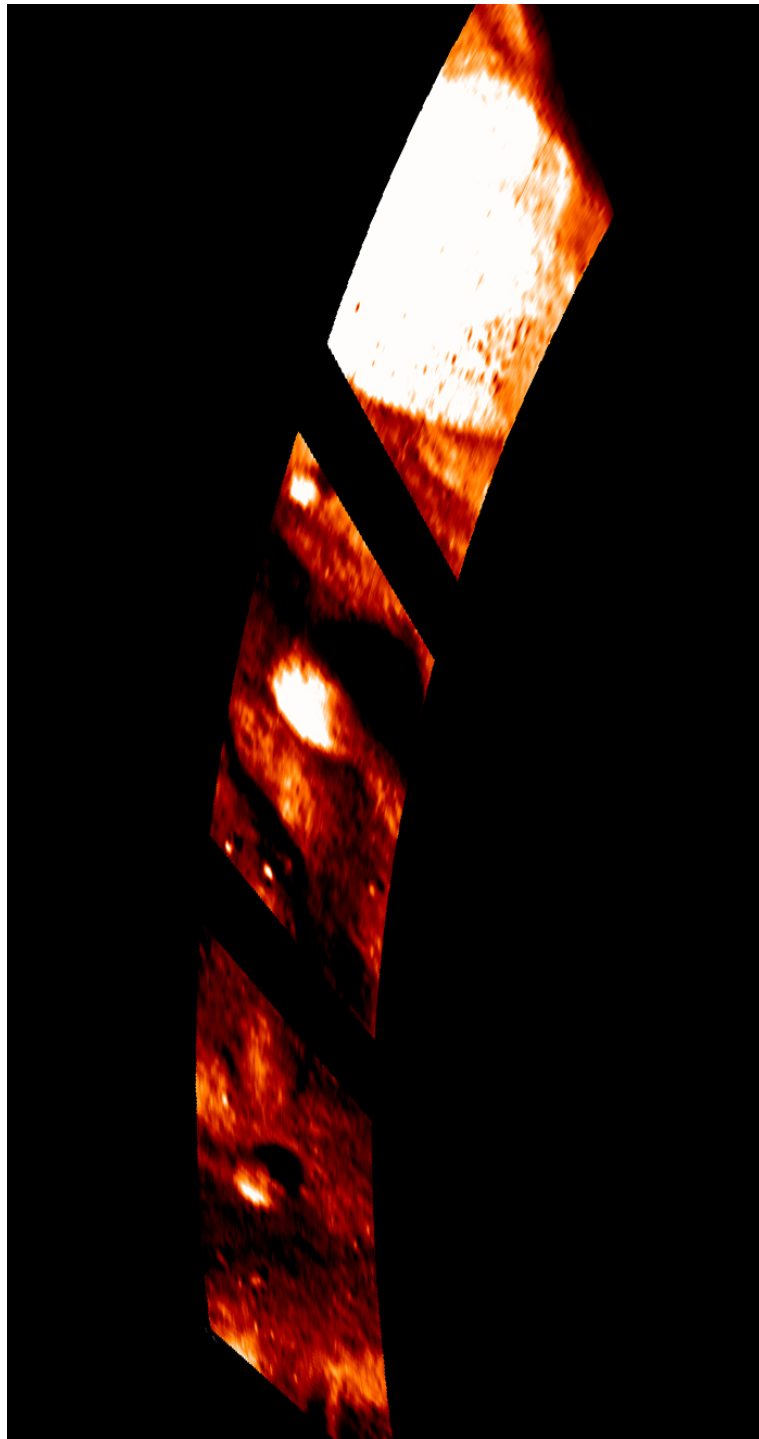


Figure B.1: Temperature mosaic of the Tarpeia region in Vesta south pole derived by the VIR data relative to the LAMO phase mission in polar stereographic projection ([http://dawn.jpl.nasa.gov/multimedia/tarpeia\\$_\\$temperature.asp](http://dawn.jpl.nasa.gov/multimedia/tarpeia$_$temperature.asp)).

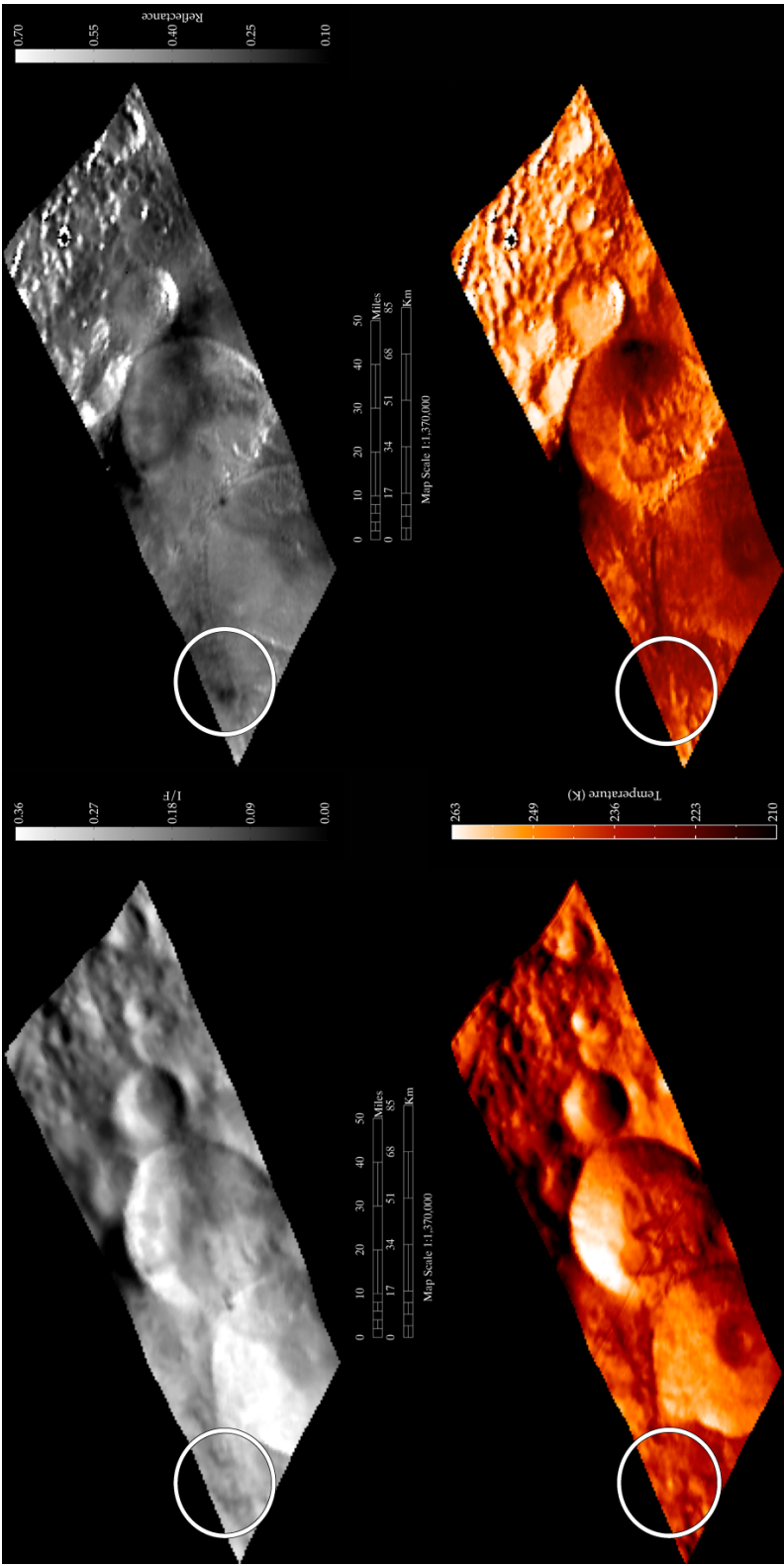


Figure B.2: Marcia images relative to the Survey phase mission in equirectangular projection. In this figure are represented temperature, reflectance at $1.4\mu\text{m}$ no photometrically corrected and photometrically corrected by Akimov and incidence angle (Tosi et al., 2014a).

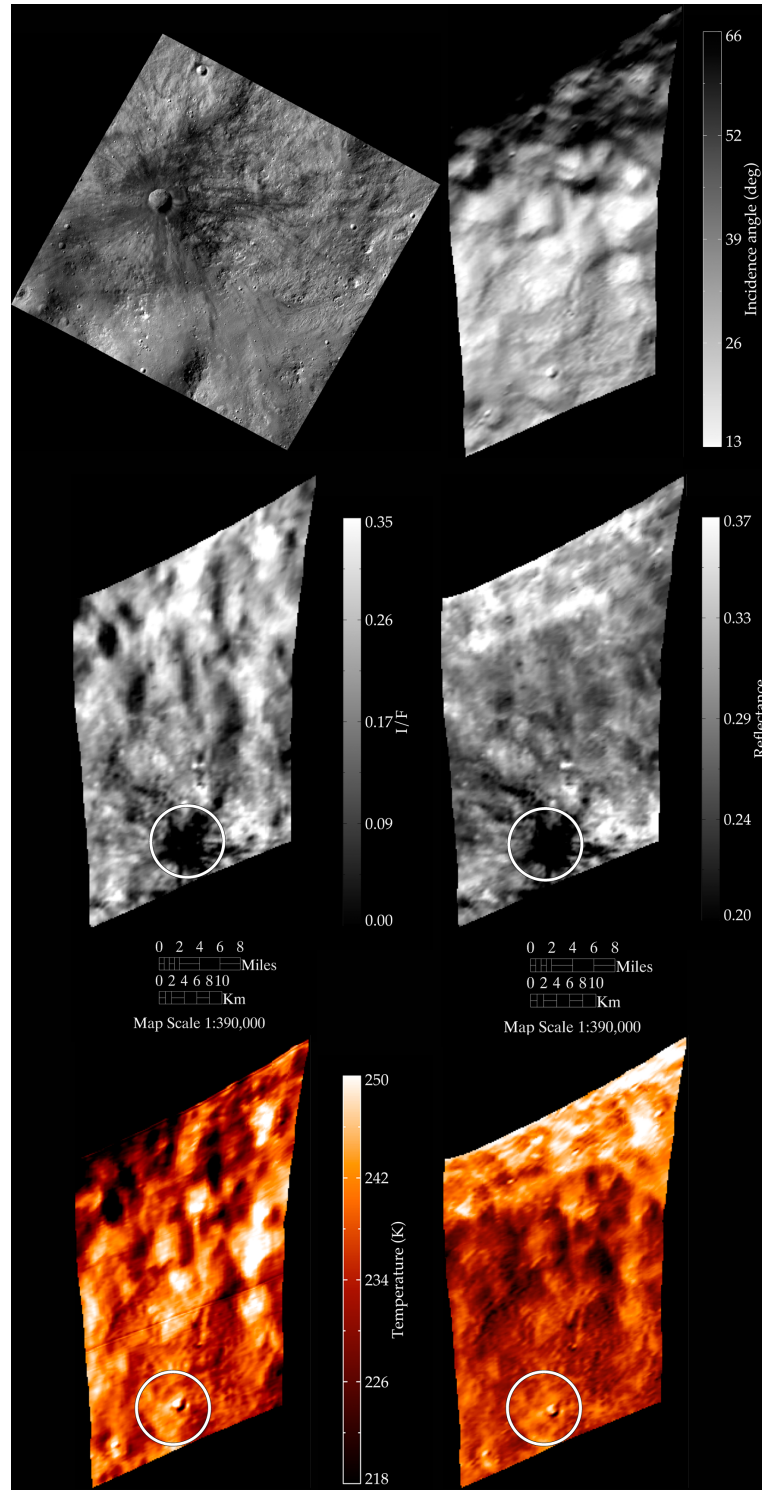


Figure B.3: Very dark material near Marcia Crater relative to the HAMO2 phase mission in equirectangular projection. In the after left panel is represented a LAMO camera clear filter image of the same region in equirectangular projection. In this figure are the reflectance at $1.4\mu\text{m}$ no photometrically corrected and photometrically corrected by Akimov with the relative temperature (Tosi et al., 2014a).

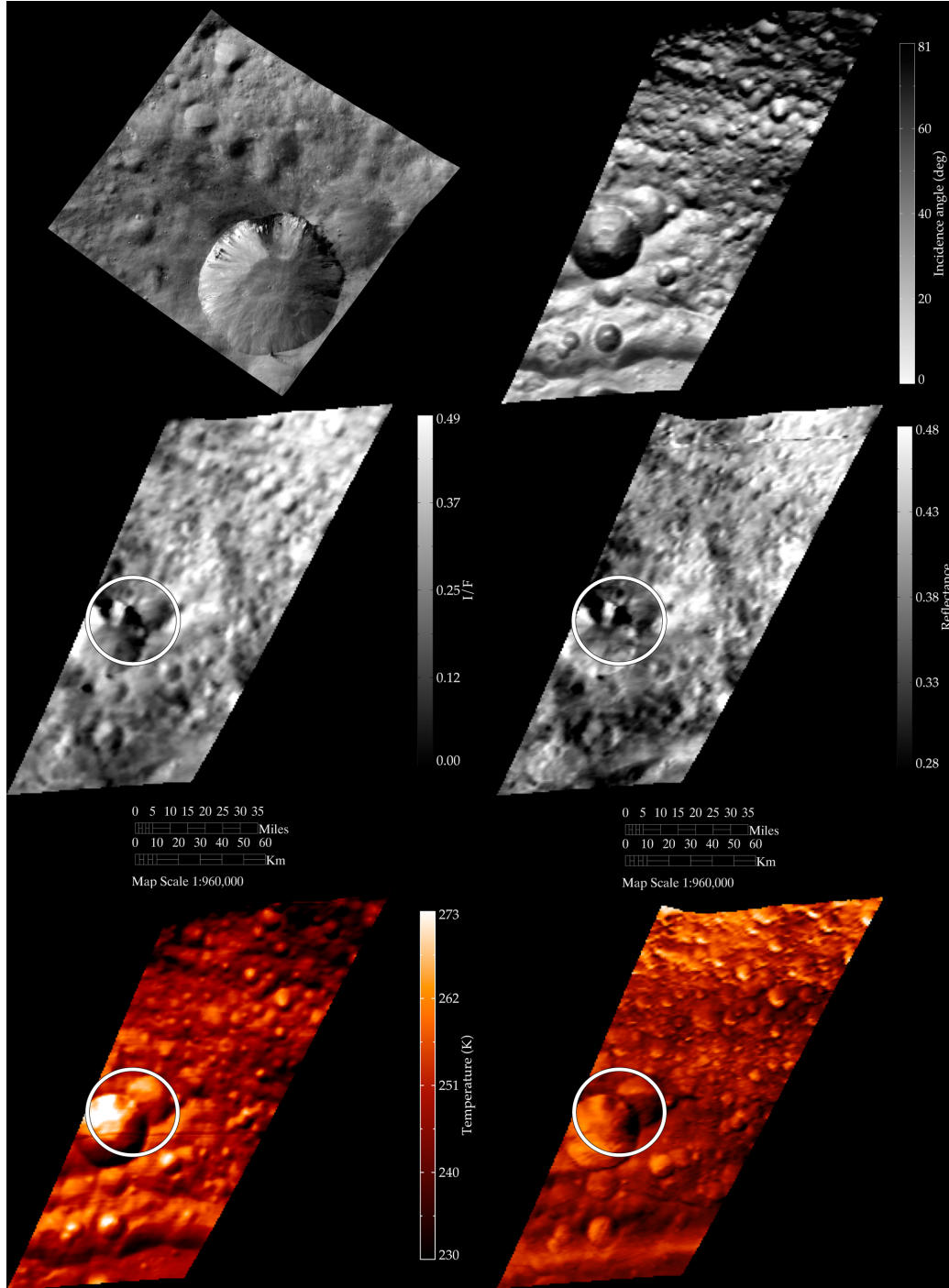


Figure B.4: Very dark unit in the Numisia crater region relative to the Survey phase mission in equirectangular projection. In the after left panel is represented a HAMO camera clear filter image of the same region in equirectangular projection. In this figure are the reflectance at $1.4\mu\text{m}$ not photometrically corrected and photometrically corrected by Akimov with the relative temperature (Tosi et al., 2014a).

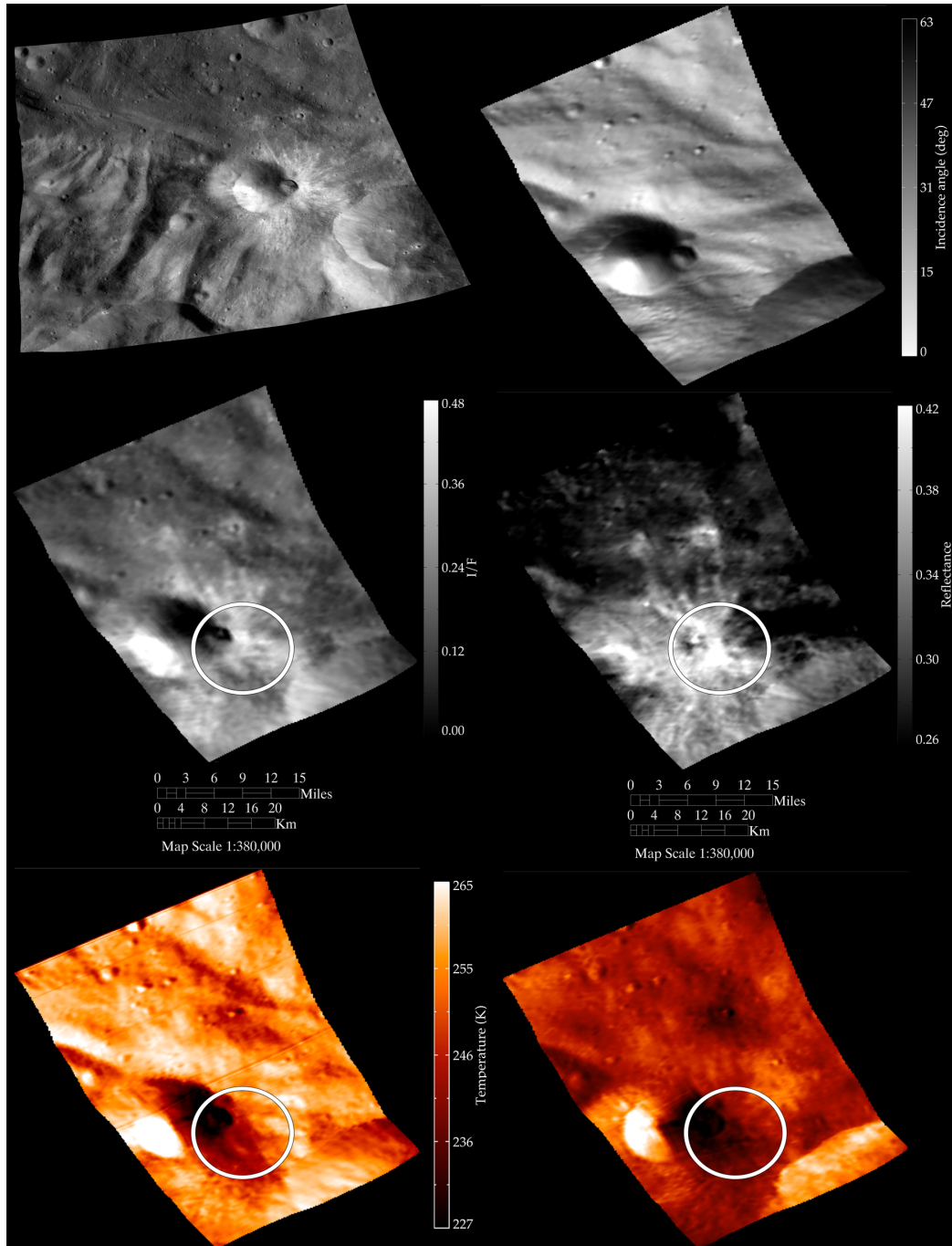


Figure B.5: Very bright unit Tuccia images relative to the HAMO phase mission in equirectangular projection. In the after left panel is represented a HAMO camera clear filter image of the same region in equirectangular projection. In this figure are the reflectance at $1.4\mu\text{m}$ no photometrically corrected and photometrically corrected by Akimov with the relative temperature (Tosi et al., 2014a).

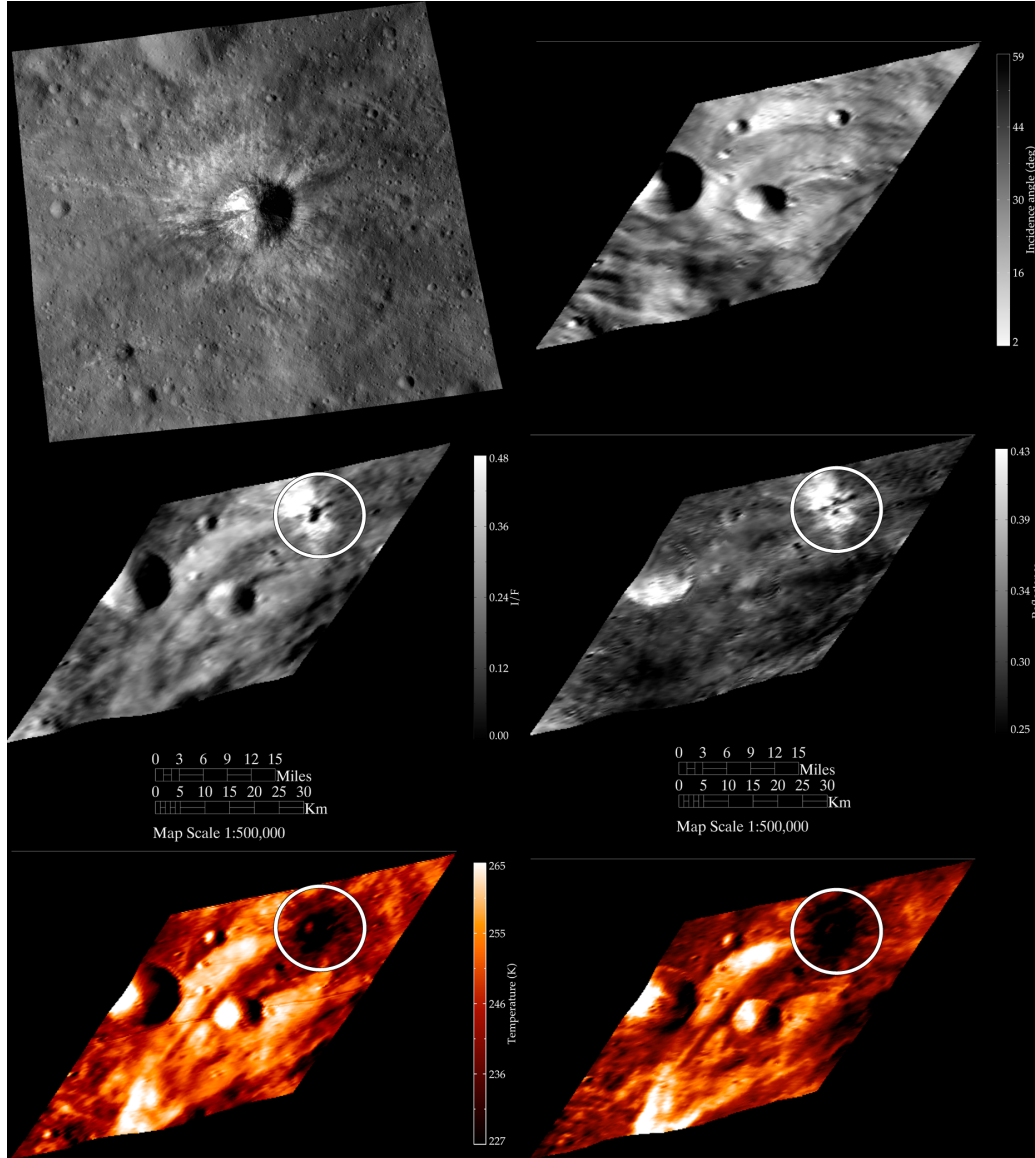


Figure B.6: Very bright Unit 3 (BU3) images relative to the HAMO phase mission in equirectangular projection. In the after left panel is represented a LAMO camera clear filter image of the same region in equirectangular projection. In this figure are the reflectance at $1.4\mu\text{m}$ no photometrically corrected and photometrically corrected by Akimov with the relative temperature (Tosi et al., 2014a).

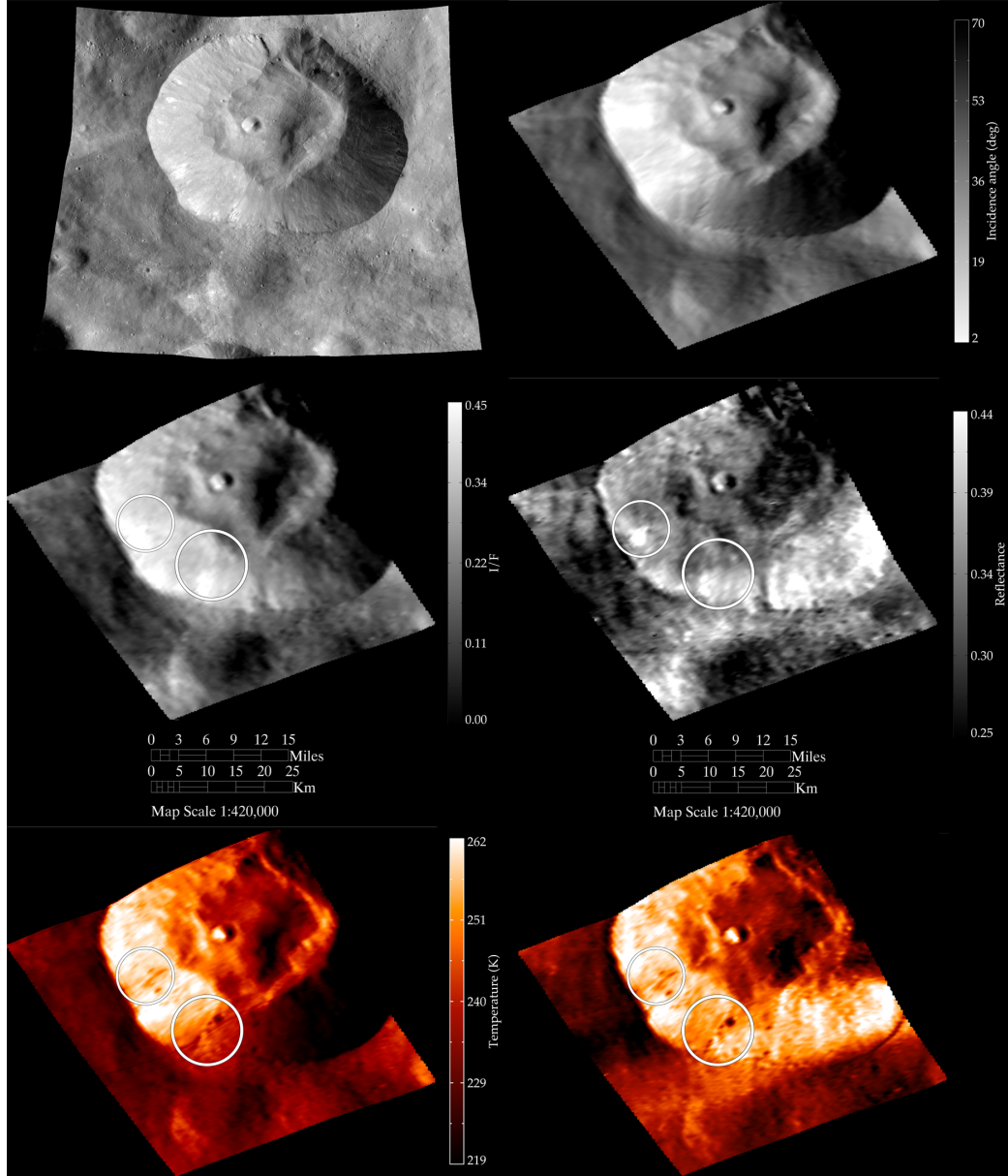
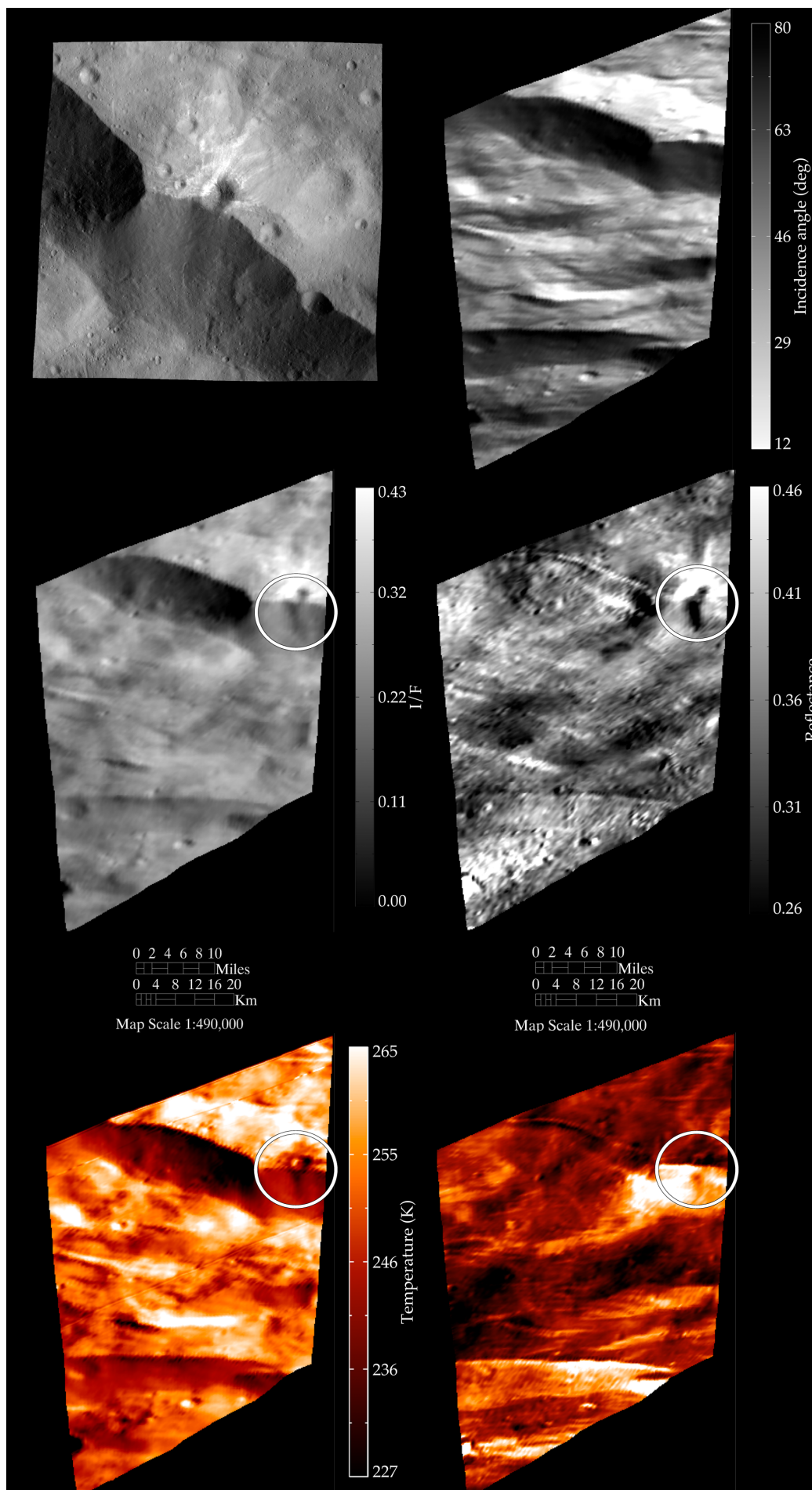


Figure B.7: Bright material in Pinaría crater images relative to the HAMO phase mission in equirectangular projection. In the after left panel is represented a HAMO camera clear filter image of the same region in equirectangular projection. In this figure are the reflectance at $1.4\mu\text{m}$ no photometrically corrected and photometrically corrected by Akimov with the relative temperature (Tosi et al., 2014a).



B.2 Global temperature maps

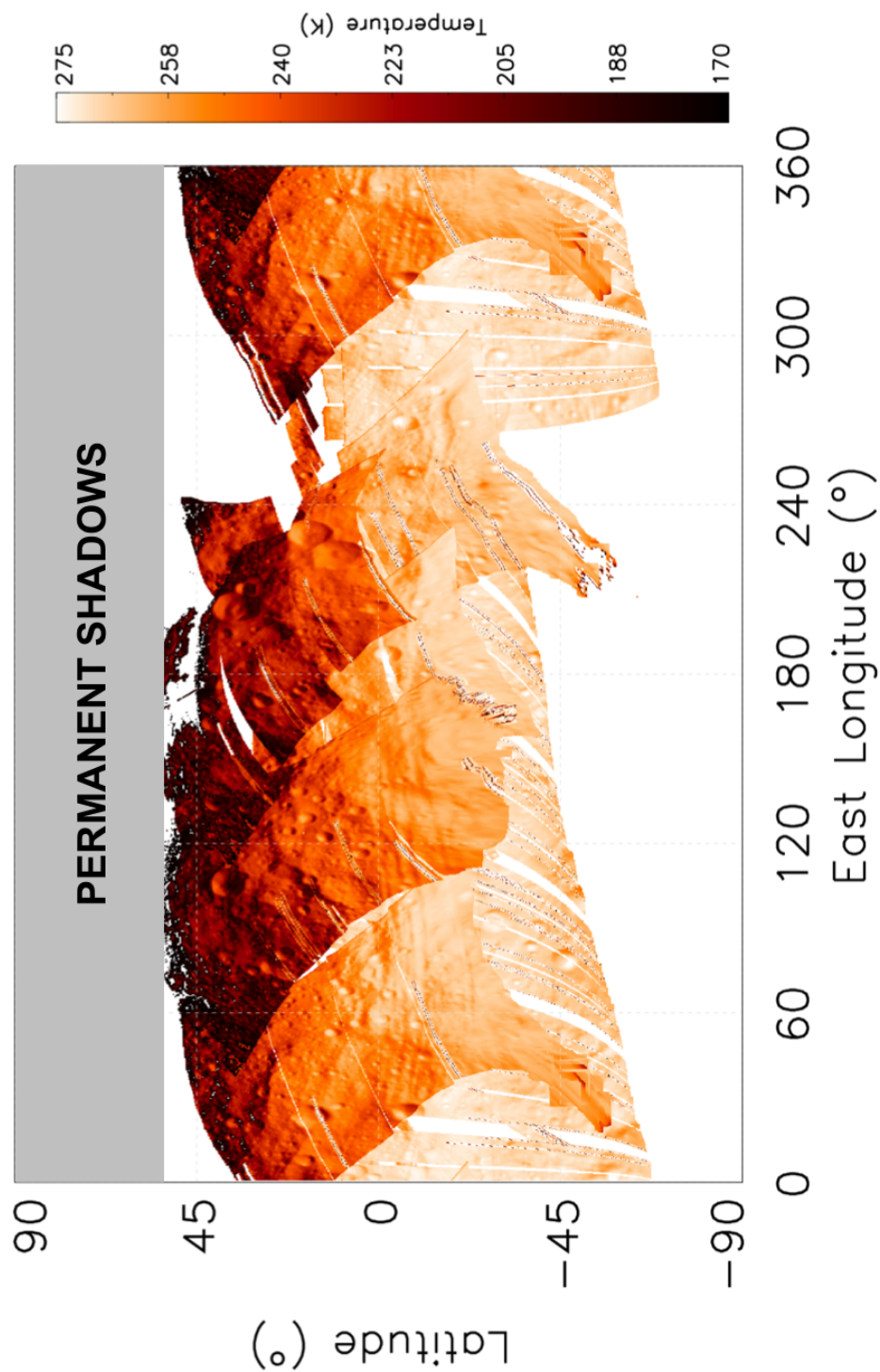


Figure B.9: Temperature global mosaic of Vesta derived by the VIR data relative to the Survey phase mission in equirectangular projection (Tosi et al., 2014b).

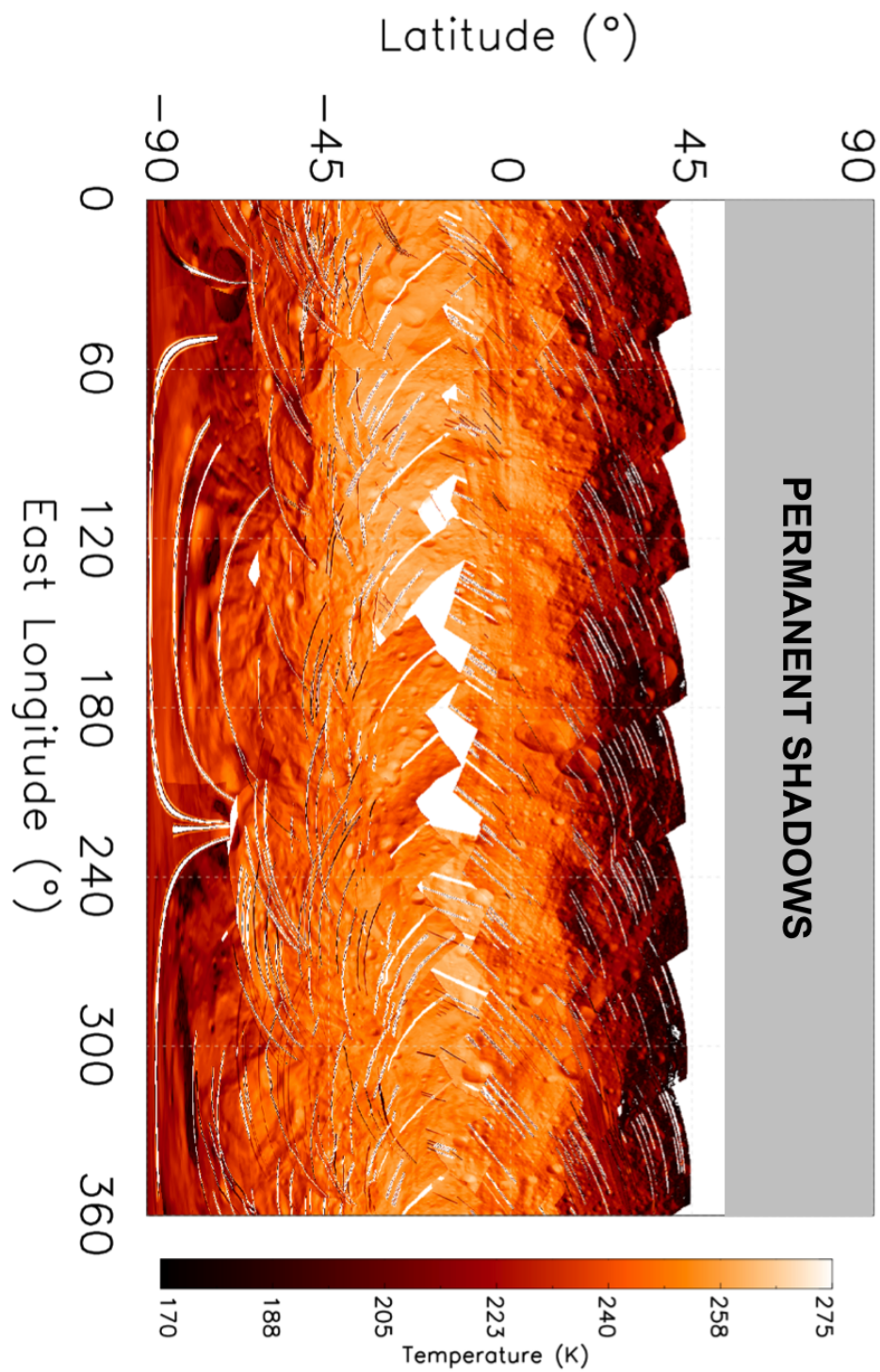


Figure B.10: Temperature global mosaic of Vesta derived by the VIR data relative to the Survey phase mission in equirectangular projection (Tosi et al., 2014b).

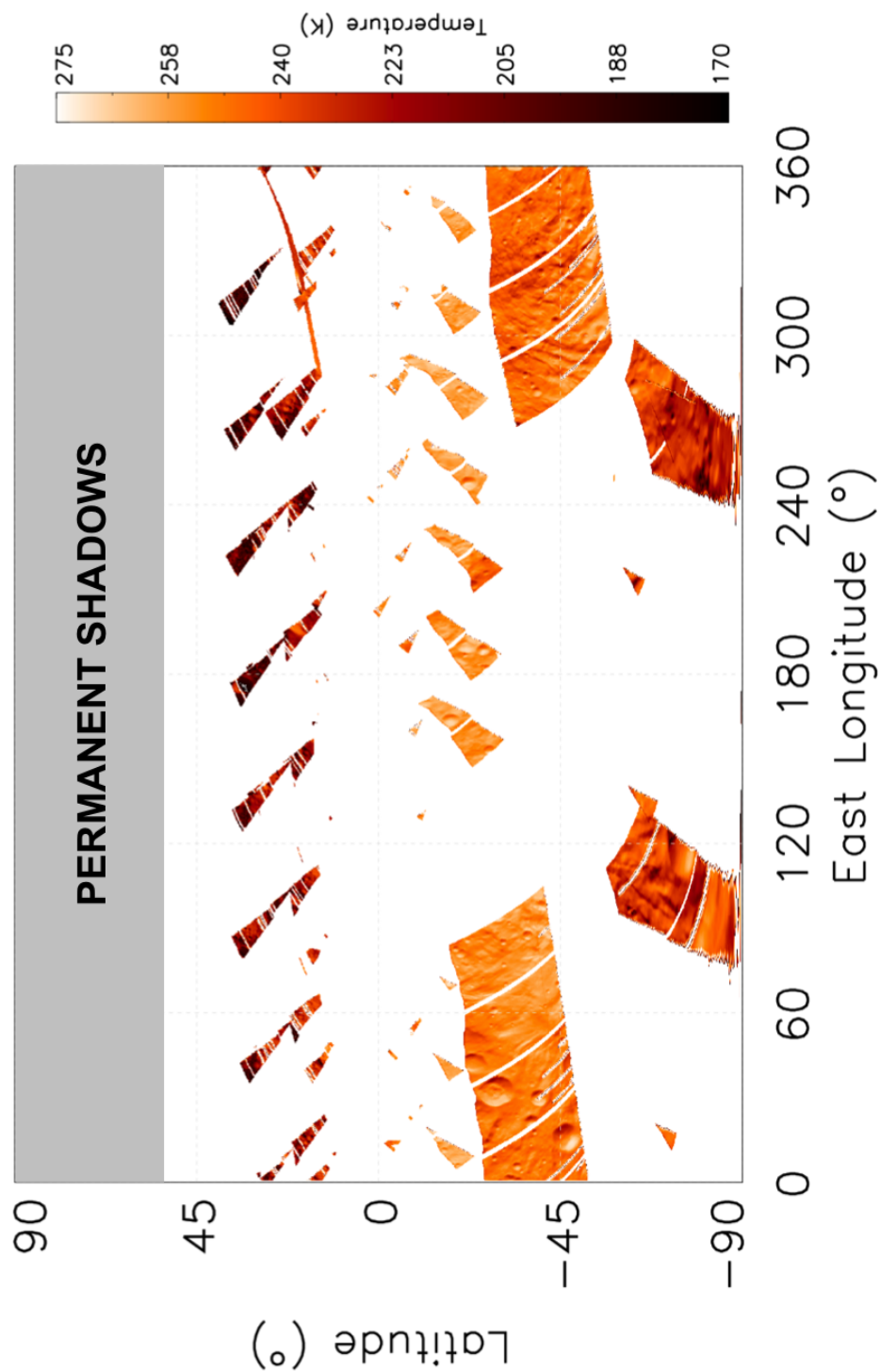


Figure B.11: Temperature global mosaic of Vesta derived by the VIR data relative to the Survey phase mission filtered by local solar time between 8 and 10 h in equirectangular projection (Tosi et al., 2014b).

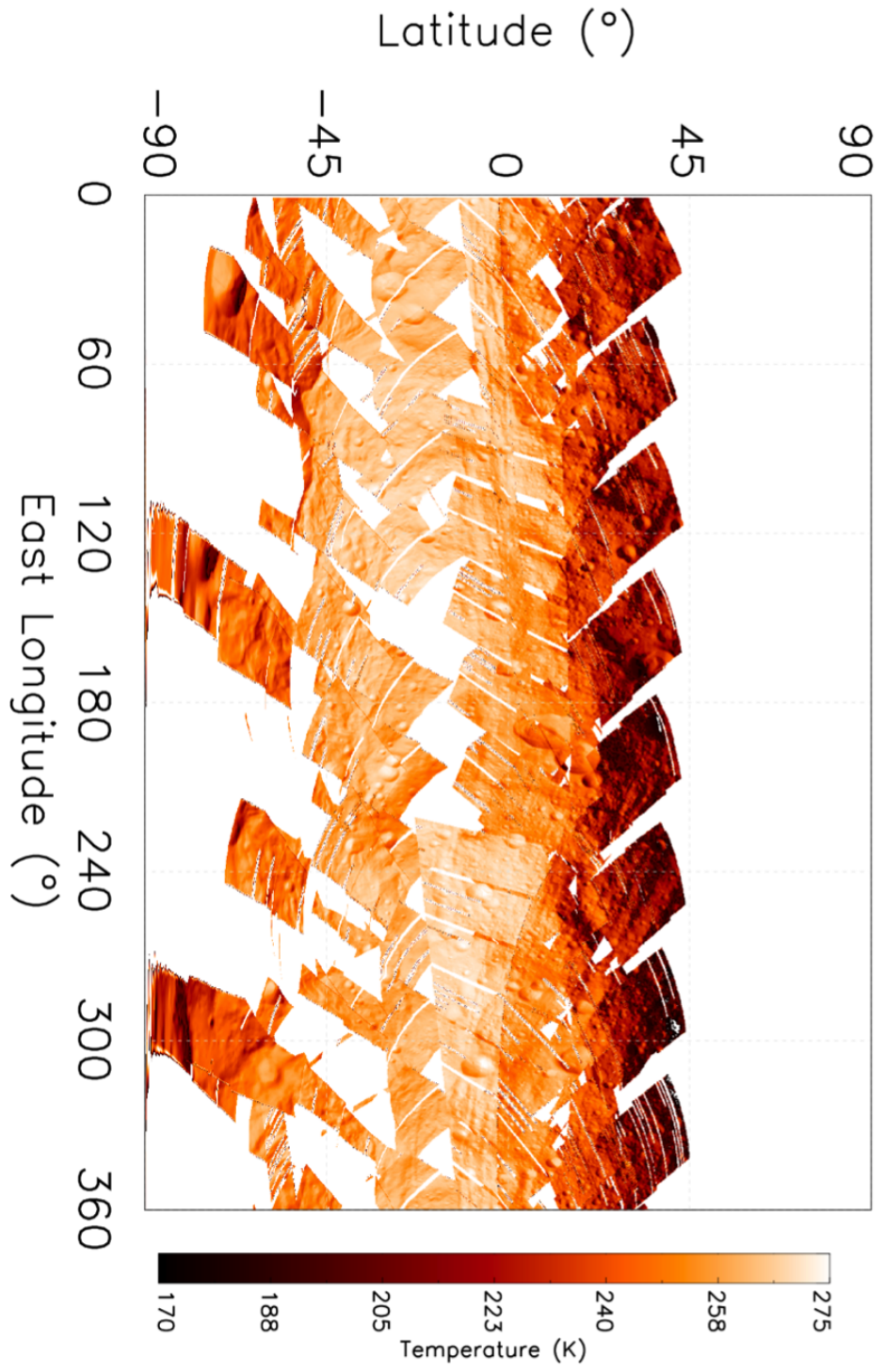


Figure B.12: Temperature global mosaic of Vesta derived by the VIR data relative to the Survey phase mission filtered by local solar time between 10 and 12 h in equiarectangular projection (Tosi et al., 2014b).

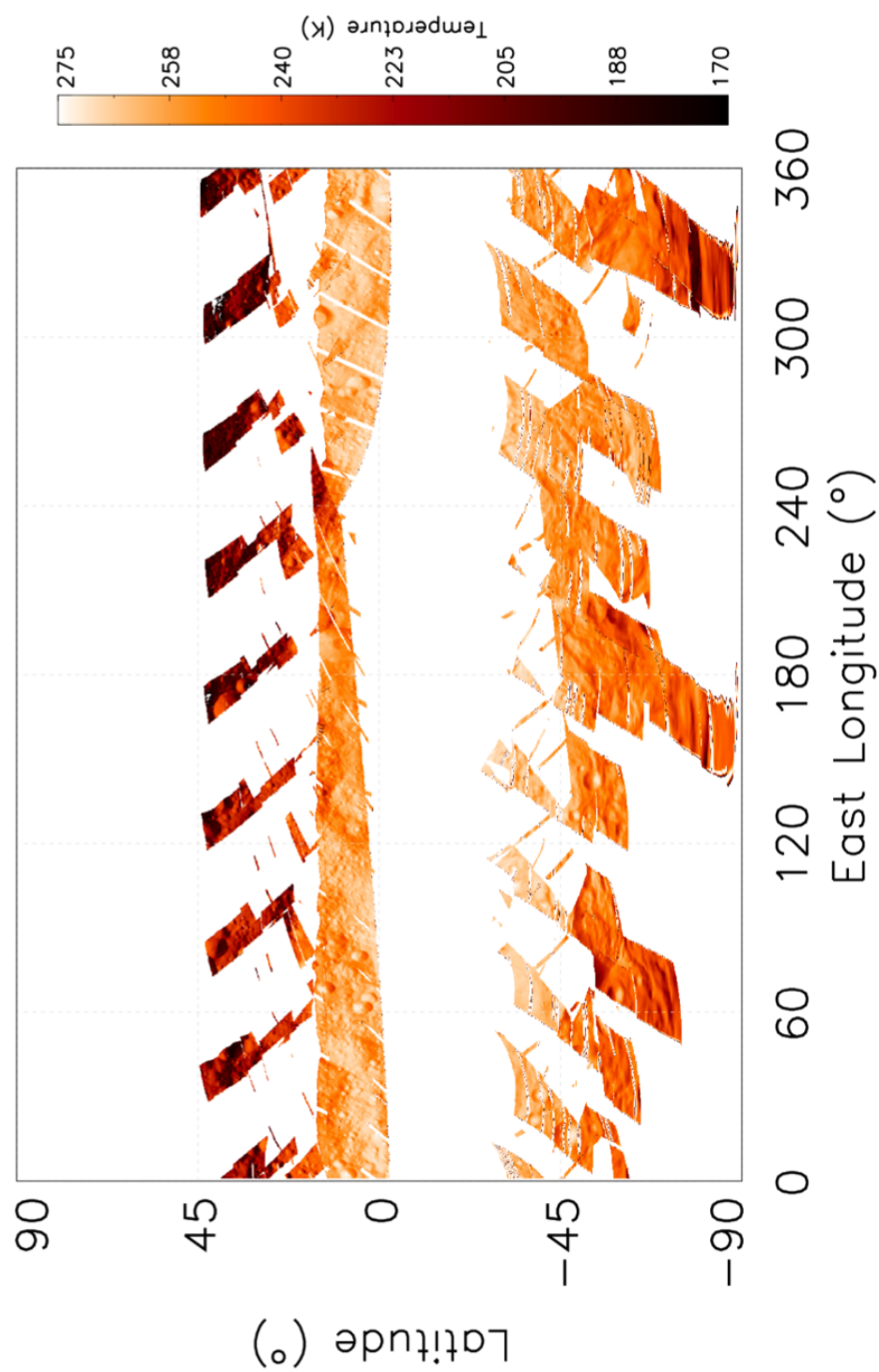


Figure B.13: Temperature global mosaic of Vesta derived by the VIR data relative to the Survey phase mission filtered by local solar time between 12 and 14 h in equirectangular projection (Tosi et al., 2014b).

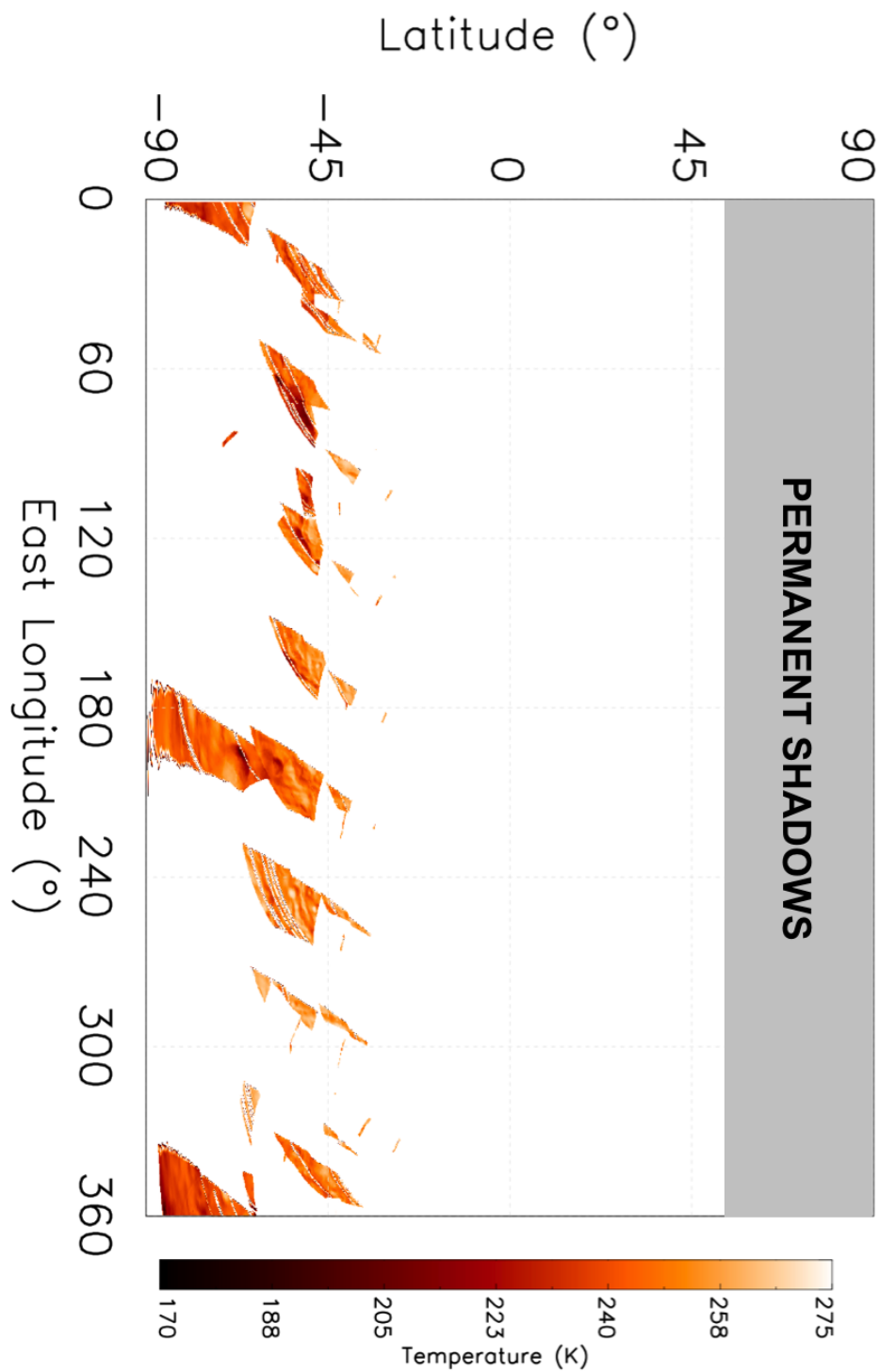


Figure B.14: Temperature global mosaic of Vesta derived by the VIR data relative to the Survey phase mission filtered by local solar time between 14 and 16 h in equirectangular projection (Tosi et al., 2014b).

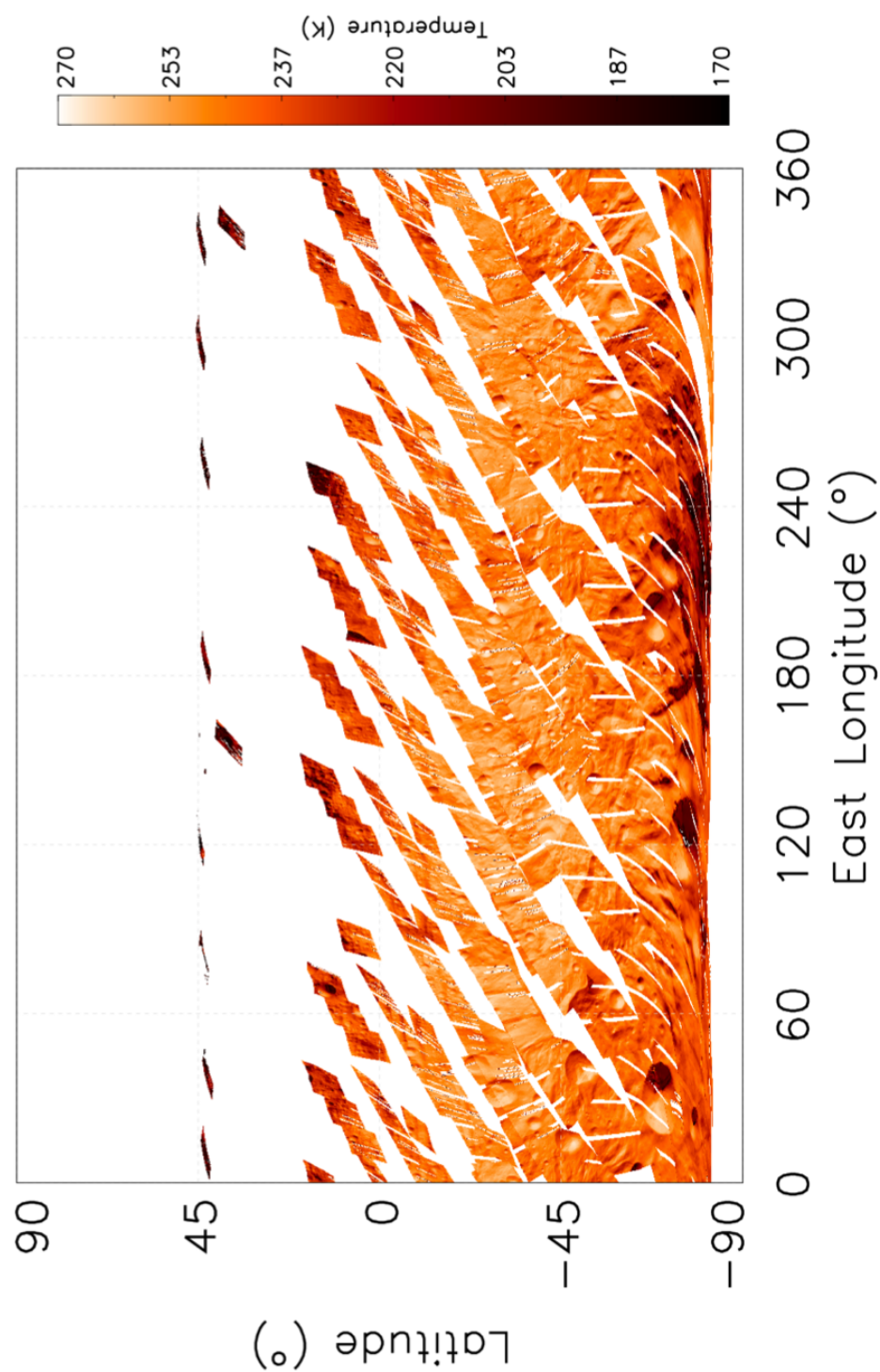


Figure B.15: Temperature global mosaic of Vesta derived by the VIR data relative to the HAMO phase mission in equirectangular projection (Tosi et al., 2014b).

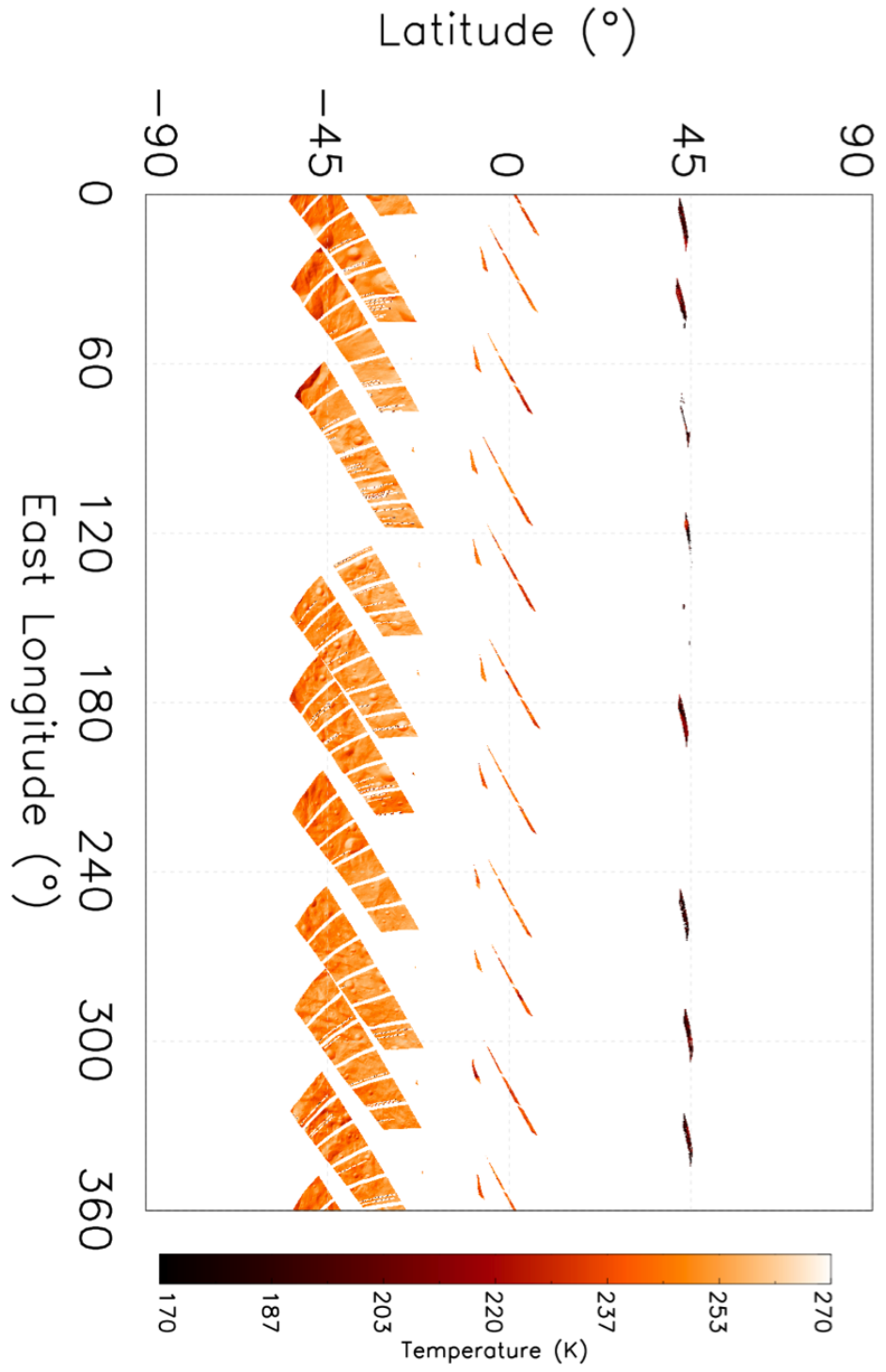


Figure B.16: Temperature global mosaic of Vesta derived by the VIR data relative to the HAMO phase mission filtered by local solar time between 10 and 12 h in equirectangular projection (Tosi et al., 2014b).

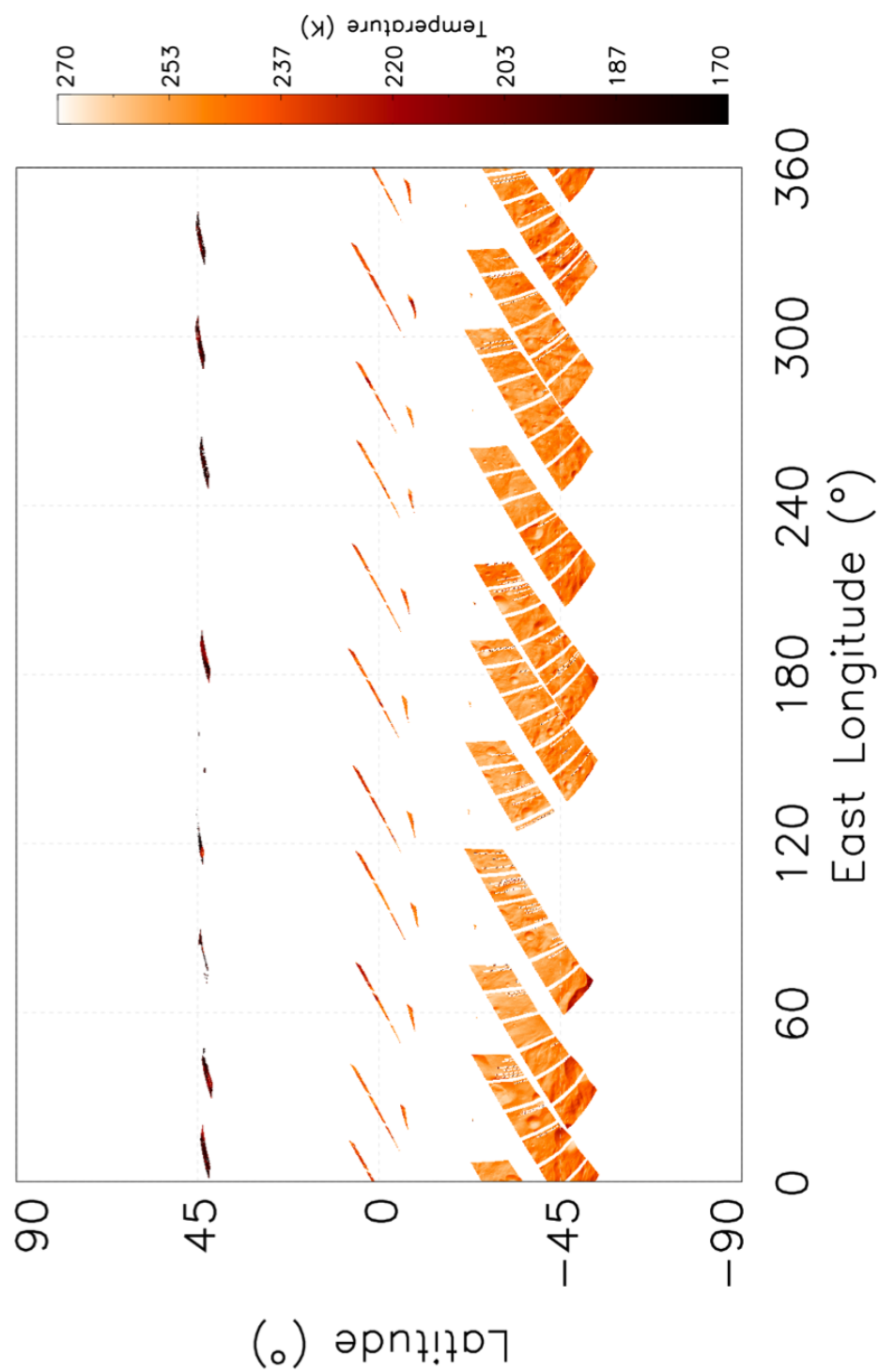


Figure B.17: Temperature global mosaic of Vesta derived by the VIR data relative to the HAMO phase mission filtered by local solar time between 10 and 12 h in equirectangular projection (Tosi et al., 2014b).



Figure B.18: Temperature global mosaic of Vesta derived by the VIR data relative to the LAMO phase mission in orthographic projection (Tosi et al., 2014b).

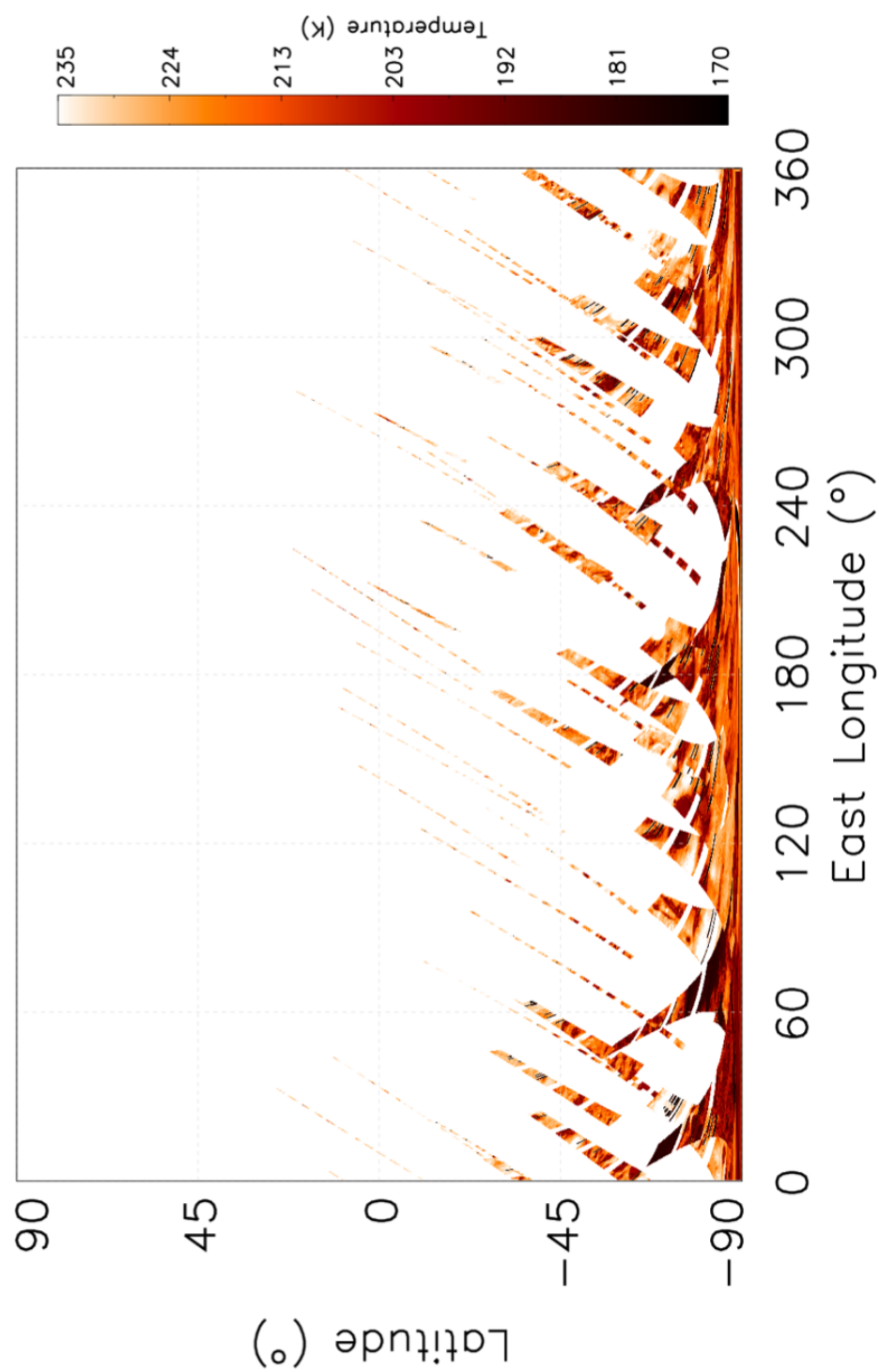


Figure B.19: Temperature global mosaic of Vesta derived by the VIR data relative to the LAMO phase mission in equirectangular projection (Tosi et al., 2014b).

Appendix C

Tables

Here we report the tables that summarize the results obtained on the bright material units analysis described in Chapter 6 and published in (Zambon et al., 2014b).

Crater Wall Material		
Name	BI Center(μm)	BII Center(μm)
Bellicia	0.944 \pm 0.009	1.964 \pm 0.009
Arruntia	0.934 \pm 0.006	1.970 \pm 0.012
BU14	0.930 \pm 0.002	1.956 \pm 0.005
Licina	0.928 \pm 0.001	1.943 \pm 0.007
Calpurnia	0.932 \pm 0.002	1.969 \pm 0.005
BU12	0.932 \pm 0.003	1.970 \pm 0.006
Marcia-1	0.932 \pm 0.002	1.980 \pm 0.022
Marcia-2	0.930 \pm 0.003	1.976 \pm 0.008
Eumachia	0.936 \pm 0.002	1.996 \pm 0.006
Oppia	0.930 \pm 0.002	1.964 \pm 0.008
Cornelia-1	0.929 \pm 0.001	1.956 \pm 0.002
Cornelia-2	0.929 \pm 0.002	1.949 \pm 0.015
Cornelia-3	0.929 \pm 0.001	1.957 \pm 0.002
Aelia	0.929 \pm 0.002	1.960 \pm 0.004
Drusilla	0.931 \pm 0.002	1.967 \pm 0.005
BU2-1	0.933 \pm 0.002	1.979 \pm 0.001
BU2-2	0.928 \pm 0.002	1.972 \pm 0.003
BU9	0.932 \pm 0.002	1.979 \pm 0.003
Pinaria	0.928 \pm 0.001	1.961 \pm 0.005
BU10-1	0.929 \pm 0.002	1.976 \pm 0.006
BU10-2	0.931 \pm 0.002	1.979 \pm 0.006
Canuleia	0.925 \pm 0.003	1.963 \pm 0.005
Justina-1	0.930 \pm 0.001	1.985 \pm 0.005
Justina-2	0.930 \pm 0.002	1.984 \pm 0.006
BU5	0.924 \pm 0.001	1.943 \pm 0.006
Sextilia	0.929 \pm 0.003	1.982 \pm 0.016
BU8	0.924 \pm 0.001	1.934 \pm 0.004
BU4	0.930 \pm 0.003	1.975 \pm 0.011
BU15	0.930 \pm 0.002	1.961 \pm 0.006

Table C.1: Band center positions for Crater Wall Material.

Slope Material		
Name	BI Center(μm)	BII Center(μm)
Arruntia	0.931 \pm 0.002	1.967 \pm 0.006
BU14	0.931 \pm 0.002	1.961 \pm 0.004
Licina	0.927 \pm 0.001	1.945 \pm 0.004
Lepida	0.929 \pm 0.001	1.946 \pm 0.022
BU12	0.931 \pm 0.004	1.962 \pm 0.009
BU13	0.932 \pm 0.001	1.973 \pm 0.005
Marcia-1	0.930 \pm 0.003	1.973 \pm 0.010
Marcia-2	0.930 \pm 0.002	1.977 \pm 0.004
Eumachia	0.936 \pm 0.001	1.997 \pm 0.005
Oppia	0.931 \pm 0.002	1.976 \pm 0.006
Cornelia-1	0.930 \pm 0.002	1.960 \pm 0.002
Cornelia-2	0.927 \pm 0.001	1.956 \pm 0.008
Cornelia-3	0.929 \pm 0.001	1.958 \pm 0.003
Aelia	0.924 \pm 0.004	1.942 \pm 0.022
Drusilla	0.932 \pm 0.002	1.973 \pm 0.010
BU2-1	0.933 \pm 0.002	1.983 \pm 0.002
BU2-2	0.931 \pm 0.002	1.983 \pm 0.003
BU9	0.932 \pm 0.002	1.982 \pm 0.002
Pinaria	0.928 \pm 0.002	1.968 \pm 0.010
BU10-1	0.930 \pm 0.002	1.987 \pm 0.003
BU10-2	0.931 \pm 0.002	1.986 \pm 0.006
BU11-1	0.932 \pm 0.001	1.983 \pm 0.002
BU11-2	0.932 \pm 0.002	1.989 \pm 0.005
BU11-3	0.930 \pm 0.002	1.986 \pm 0.006
Canuleia	0.929 \pm 0.002	1.968 \pm 0.005
Justina-1	0.930 \pm 0.001	1.987 \pm 0.003
Justina-2	0.930 \pm 0.002	1.984 \pm 0.004
BU5	0.927 \pm 0.002	1.956 \pm 0.005
Sextilia	0.930 \pm 0.002	1.987 \pm 0.025
BU8	0.927 \pm 0.001	1.950 \pm 0.005
BU6	0.930 \pm 0.001	1.978 \pm 0.002
BU15	0.929 \pm 0.002	1.959 \pm 0.004

Table C.2: Band center positions for Slope Material.

Radial Material		
Name	BI Center(μm)	BII Center(μm)
Arruntia	0.930 ± 0.003	1.961 ± 0.005
BU7	0.930 ± 0.002	1.977 ± 0.010
Aelia	0.932 ± 0.001	1.984 ± 0.007
BU3	0.931 ± 0.004	1.970 ± 0.005
Canuleia-1	0.928 ± 0.002	1.962 ± 0.010
Canuleia-1	0.933 ± 0.002	1.981 ± 0.002
Justina-1	0.931 ± 0.002	1.972 ± 0.008
Justina-2	0.930 ± 0.002	1.972 ± 0.008
BU5	0.923 ± 0.002	1.929 ± 0.014
BU1	0.928 ± 0.001	1.959 ± 0.004
Tuccia	0.932 ± 0.002	1.993 ± 0.006
BU6	0.930 ± 0.002	1.969 ± 0.005
Myia	0.928 ± 0.002	1.977 ± 0.010

Table C.3: Band center positions for Radial Material.

Crater Wall Material		
Name	Wo (%)	Fs (%)
Bellicia	15.6±2.1	49.4±3.1
Arruntia	9.5±2.3	41.7±4.0
BU14	8.0±0.7	38.4±0.9
Licina	6.9±0.6	35.6±1.2
Calpurnia	8.5±0.9	40.3±1.5
BU12	8.5±1.1	40.5±1.6
Marcia-1	8.6±0.9	41.6±3.0
Marcia-2	7.9±1.0	40.3±1.76
Eumachia	10.1±0.6	45.1±1.3
Oppia	7.7±0.6	38.8 ±1.3
Cornelia-1	7.5±0.6	37.6±0.8
Cornelia-2	7.4±0.6	36.9±1.3
Cornelia-3	7.3±0.5	37.6±0.8
Aelia	7.3±0.8	37.9±1.5
Drusilla	8.4±0.8	39.9±1.3
BU2-1	9.1±0.9	42.2±1.1
BU2-2	6.9±0.7	38.7±0.9
BU9	8.5±0.8	41.4±1.1
Pinaria	7.0±0.5	37.5±1.1
BU10-1	7.5±0.8	39.7±1.4
BU10-2	8.0±0.9	40.9±1.3
Canuleia	5.8±1.2	36.2±1.4
Justina-1	7.8±0.5	41.1±0.8
Justina-2	7.8±0.7	41.0±1.5
BU5	5.3±0.7	34.0±1.2
Sextilia	7.4±1.1	40.9±3.7
BU8	5.5±0.3	32.9±0.5
BU4	7.8±1.0	40.1±1.9
BU15	7.7±0.8	38.5±1.2

Table C.4: Molar content of wollastonite and ferrosilite for Crater Wall Material.

Slope Material		
Name	Wo (%)	Fs (%)
Arruntia	8.1±1.0	39.6±1.5
BU14	8.4±0.8	39.3±1.2
Licina	6.7±0.4	35.5±0.8
Lepida	7.3±0.3	36.4±2.0
BU12	8.3±1.4	39.3±2.2
BU13	8.5±0.5	40.7±1.0
Marcia-1	8.0±1.1	40.1±2.1
Marcia-2	7.9±0.8	40.3±1.1
Eumachia	10.1±0.5	45.3±1.0
Oppia	8.3±0.7	40.9 ±1.2
Cornelia-1	7.9±0.9	38.7±1.2
Cornelia-2	6.8±0.5	36.8±0.9
Cornelia-3	7.3±0.5	37.7±0.8
Aelia	5.4±1.3	33.8±4.0
Drusilla	8.5±0.8	40.7±1.3
BU2-1	9.1±1.0	42.5±1.4
BU2-2	8.3±0.6	41.5±0.9
BU9	8.8±0.8	42.1±1.0
Pinaria	7.1±0.7	38.4±1.5
BU10-1	7.8±0.8	41.2±1.2
BU10-2	8.4±0.7	41.9±1.3
BU11-1	8.7±0.6	42.0±0.8
BU11-2	8.5±0.6	42.5±0.9
BU11-3	7.9±0.8	41.3±1.5
Canuleia	7.6±0.9	39.0±1.3
Justina-1	7.9±0.5	41.4±0.9
Justina-2	8.0±0.8	41.2±1.0
BU5	6.5±0.7	36.5±0.8
Sextilia	7.7±0.7	41.1±3.0
BU8	6.6±0.5	36.0±1.1
BU8	7.9±0.5	40.5±0.5
BU15	7.3±0.8	37.7±1.2

Table C.5: Molar content of wollastonite and ferrosilite for Slope Material.

Radial Material		
Name	Wo (%)	Fs (%)
Arruntia	7.7±1.1	38.5±1.5
BU7	8.0±0.6	40.5±1.4
Aelia	8.5±0.5	41.9±0.9
BU3	8.1±1.4	39.9±2.1
Canuleia-1	8.9 ±0.9	42.1±1.2
Canuleia-2	7.2 ±0.9	38.0±2.0
Justina-1	7.9±0.9	39.9±1.8
Justina-2	8.3±0.8	40.4±1.5
BU5	5.0±0.9	31.6±2.2
BU1	7.1±0.6	37.5±0.7
Tuccia	8.8±0.8	43.1±1.3
BU6	7.6±0.7	39.3±1.1
Myia	7.2±0.8	39.6±1.8

Table C.6: Molar content of wollastonite and ferrosilite for Radial Material.

Crater Wall Material										
Name	Lat (°)	Lon (°)	Norm. Vis. Alb.	%	BI Depth	BII Depth	BAR	Ph. (°)	Inc. (°)	Em. (°)
Bellicia	41.1	50.5	not av.	not av.	0.388±0.019	0.146±0.015	0.677±0.077	38	54	26
Arruntia	39.5	71.1	not av.	not av.	0.364±0.042	0.152±0.036	0.896±0.189	40	45	66
BU14	28.1	73.3	0.377±0.025	-0.8	0.369±0.009	0.164±0.015	0.976±0.120	37	32	39
Licina	24.9	16.3	0.411±0.047	8.2	0.502±0.012	0.276±0.011	1.315±0.053	33	29	37
Calpurnia	21.2	196.4	0.320±0.044	-15.8	0.411±0.020	0.214±0.007	1.316±0.040	34	13	21
BU12	15.7	357.7	0.407±0.007	7.1	0.462±0.008	0.225±0.005	1.154±0.059	34	40	16
Marcia-1	12.0	195.2	0.407±0.019	7.1	0.446±0.019	0.259±0.020	1.438±0.073	37	56	33
Marcia-2	6.9	184.1	0.386±0.026	1.6	0.476 ±0.018	0.279±0.011	1.430±0.073	39	21	56
Eumachia	-1.2	165.1	0.350±0.022	-7.9	0.421±0.011	0.223±0.007	1.275±0.030	35	19	42
Oppia	-6.7	306.0	0.368±0.016	-3.2	0.465±0.014	0.258±0.017	1.381±0.072	38	19	28
Cornelia-1	-9.5	224.0	0.469±0.018	23.4	0.506±0.006	0.271±0.008	1.261±0.039	29	20	31
Cornelia-2	-9.7	224.1	0.488±0.003	28.4	0.507±0.011	0.284±0.016	1.377±0.081	34	20	28
Cornelia-3	-9.4	224.1	not av.	not av.	0.506±0.007	0.294±0.005	1.414±0.040	38	7	32
Aelia	-14.1	140.4	not av.	not av.	0.470±0.019	0.281±0.003	1.375±0.040	41	24	25
Drusilla	-15.2	259.3	0.438±0.014	16.6	0.498±0.013	0.262±0.015	1.296±0.058	38	16	31
BU2-1	-28.3	140.6	not av.	not av.	0.445±0.012	0.234±0.005	1.247±0.015	35	5	39
BU2-2	-28.5	140.7	0.407±0.014	7.1	0.394±0.012	0.248±0.008	1.440±0.070	36	32	34
BU9	-28.7	198.3	0.399±0.004	5.0	0.419±0.007	0.223±0.005	1.335±0.047	36	4	35
Pinaria	-31.9	28.0	0.429±0.010	12.9	0.501±0.022	0.286±0.016	1.422±0.055	37	11	39
BU10-1	-33.4	101.8	0.405±0.023	6.6	0.441±0.008	0.250±0.006	1.362±0.045	38	12	31
BU10-2	-33.5	101.8	0.401±0.026	5.5	0.439±0.009	0.243±0.009	1.324±0.050	35	11	44
Canuleia	-33.8	293.7	0.446±0.016	17.4	0.492±0.037	0.327±0.013	1.477±0.097	48	41	27
Justina-1	-33.9	317.2	0.449±0.014	18.2	0.484±0.008	0.320±0.008	1.561±0.023	38	43	10
Justina-2	-33.9	317.2	0.443±0.013	16.6	0.475±0.010	0.312±0.008	1.547±0.015	35	40	40
BU5	-37.7	92.0	not av.	not av.	0.561±0.018	0.296±0.008	1.240±0.108	40	25	38
Sextilia	-38.1	143.9	0.410±0.021	7.9	0.497±0.046	0.294±0.041	1.385±0.071	44	30	22
BU8	-39.5	26.8	0.397±0.010	4.5	0.554±0.015	0.332±0.017	1.394±0.067	52	41	30
BU4	-56.5	299.2	0.443±0.009	20.7	0.507±0.020	0.311±0.013	1.439±0.055	32	23	10
BU15	-65.6	357.7	0.419±0.023	10.3	0.532±0.049	0.342±0.031	1.469±0.081	59	35	28

Table C.7: Overview of CWM characteristics. In the table are reported the values of the latitude and longitude of the crater wall material (second and third columns). The fourth column contains the normal visual albedo and the fifth one the how the crater wall material albedo exceed the mean albedo of Vesta. Band I and II depth, while Band area ratio (BAR) are reported in sixth, seventh and eighth columns. In the three columns there are the phase, incidence and emission angles. All the values reported are the average of bright areas. Values of latitude and longitude refer to the Claudia coordinates system.

Name	Lat (°)	Lon (°)	Norm. Vis.	Alb.	%	Slope Material					Ph. (°)	Inc. (°)	Em. (°)
						BI Depth	BII Depth	BAR					
Arunnita	40.2	71.9	not av		not av	0.396±0.029	0.180±0.020	0.968±0.111	40	24	36		
BU14	28.1	73.5	0.383±0.013		0.8	0.347±0.015	0.153±0.010	0.938±0.060	37	22	28		
Lucia	24.6	16.4	0.416±0.025		9.5	0.512±0.017	0.293±0.017	1.389±0.064	33	29	36		
Lepida	15.6	303.1	0.396±0.010		4.2	0.454±0.009	0.250±0.010	1.386±0.042	37	26	60		
BU12	15.7	358.0	0.405±0.012		6.6	0.471±0.006	0.239±0.004	1.234±0.043	35	31	8		
BU13	12.8	219.2	0.432±0.003		13.7	0.489±0.009	0.268 ±0.006	1.341±0.014	35	25	15		
Marcia-1	11.3	192.9	0.398±0.018		4.7	0.462±0.020	0.273±0.013	1.444±0.053	37	43	23		
Marcia-2	9.7	186.0	0.409±0.009		7.6	0.466 ±0.007	0.266±0.003	1.426±0.019	38	18	48		
Eumachia	-1.4	165.6	0.336±0.014		-11.6	0.421±0.008	0.221±0.010	1.272±0.039	34	21	45		
Oppia	-5.9	306.9	0.355±0.011		-6.6	0.441±0.012	0.242±0.008	1.363±0.041	38	10	28		
Cornelia-1	-9.4	224.5	0.412±0.051		8.4	0.492±0.016	0.274±0.012	1.362±0.038	29	20	36		
Cornelia-2	-6.6	224.4	0.429±0.027		12.9	0.503±0.012	0.283±0.010	1.391±0.036	34	22	34		
Cornelia-3	-9.4	224.5	0.429±0.018		12.9	0.492±0.019	0.285±0.015	1.428±0.049	38	8	32		
Aelia	-14.3	140.6	0.337±0.040		-11.3	0.486±0.062	0.290±0.042	1.402±0.045	41	28	27		
Drusilla	-15.7	260.3	0.404±0.018		3.4	0.479±0.023	0.252±0.011	1.341±0.057	38	22	31		
BU2-1	-28.2	140.9	0.434±0.006		14.2	0.435±0.008	0.238±0.007	1.330±0.039	35	9	37		
BU2-2	-28.3	140.9	0.414±0.004		14.1	0.425±0.010	0.251±0.007	1.433±0.039	36	17	30		
BU9	-28.5	198.8	0.387±0.010		1.8	0.411±0.006	0.222±0.004	1.352±0.034	36	5	39		
Pinaria	-31.4	28.6	0.434±0.009		14.2	0.485±0.013	0.274±0.009	1.437±0.026	37	15	42		
BU10-1	-33.1	102.1	0.428±0.005		12.6	0.433±0.005	0.250±0.006	1.419±0.024	38	5	37		
BU10-2	-33.2	102.0	0.428±0.009		12.6	0.433±0.005	0.252±0.004	1.433±0.020	35	16	51		
BU11-1	-33.9	176.7	0.399±0.009		5.0	0.415±0.006	0.235±0.006	1.409±0.030	37	8	29		
BU11-2	-33.9	176.6	0.403±0.004		6.1	0.418±0.004	0.231±0.007	1.339±0.051	36	14	44		
BU11-3	-34.1	176.9	0.402±0.004		5.8	0.424±0.023	0.234±0.008	1.318±0.049	49	25	25		
Cameleia	-33.8	293.9	0.441±0.011		16.1	0.514±0.028	0.332±0.027	1.531±0.065	48	42	22		
Justina-1	-34.2	317.2	0.439±0.017		15.1	0.475±0.006	0.313 ±0.005	1.548±0.021	38	30	15		
Justina-2	-34.3	317.3	0.431±0.016		13.4	0.459±0.018	0.288±0.017	1.497±0.032	35	26	44		
BU5	-37.5	92.0	0.406±0.002		6.8	0.474±0.022	0.267±0.009	1.398±0.061	40	22	38		
Sextilia	-38.1	144.2	0.414±0.018		8.9	0.494±0.044	0.303±0.047	1.472±0.061	44	30	25		
BU8	-41.1	27.5	0.409±0.014		7.6	0.499±0.008	0.301±0.006	1.468±0.030	52	23	30		
BU6	-44.9	300.3	0.446±0.002		17.4	0.513±0.023	0.323±0.014	1.485±0.027	31	27	42		
BU15	-65.6	358.6	0.532±0.018		40.0	0.463±0.034	0.238±0.020	1.433±0.041	59	29	31		

Table C.8: Overview of SM characteristics. In the table are reported the values of the latitude and longitude of the slope material (second and third columns). The fourth column contains the normal visual albedo and the fifth one the how the slope material albedo exceed the mean albedo of Vesta. Band I and II depth and (Band Area Ratio) BAR are reported in sixth, seventh and eighth columns. In the three columns there are the phase, incidence and emission angles. All the values reported are the average of bright areas. Values of latitude and longitude refer to the Claudia coordinates system.

Radial Material										
Name	Lat (°)	Lon (°)	Norm. Vis. Alb.	%	BI Depth	BII Depth	BAR	Ph. (°)	Inc. (°)	Em. (°)
Arruntia	37.4	73.4	not av.	not av.	0.364±0.021	0.164±0.015	1.006±0.086	40	39	55
BU7	-8.9	179.9	0.432±0.015	13.7	0.498±0.014	0.298±0.006	1.454±0.046	40	39	36
Aelia	-13.8	142.0	0.341±0.012	-10.3	0.404±0.008	0.225±0.012	1.354±0.055	41	25	21
BU3	-25.1	309.2	0.456±0.012	20.0	0.474±0.014	0.293±0.011	1.480±0.047	36	24	37
Canuleia-1	-35.2	294.8	0.446±0.017	17.4	0.513±0.009	0.322±0.006	1.481±0.031	43	35	13
Canuleia-2	-33.2	295.8	0.439±0.032	15.5	0.521±0.026	0.346±0.018	1.551±0.054	47	46	16
Justina-1	-34.7	318.8	0.427±0.033	12.4	0.499±0.016	0.330±0.014	1.570±0.035	38	38	11
Justina-2	-34.7	319.7	0.448±0.010	17.9	0.485±0.015	0.320±0.012	1.551±0.026	35	26	32
BU5	-37.1	92.8	0.401±0.012	5.5	0.492±0.020	0.274±0.020	1.300±0.119	40	32	31
BU1	-39.1	312.0	0.433±0.022	13.9	0.495±0.018	0.307±0.015	1.482±0.074	36	33	37
Tuccia	-40.3	199.2	0.511±0.031	34.5	0.485±0.012	0.319±0.014	1.540±0.029	36	29	29
BU6	-45.7	300.9	0.433±0.021	13.9	0.494±0.012	0.317±0.009	1.538±0.052	31	38	40
Myia	-50.0	106.2	0.456±0.020	20.0	0.471±0.017	0.292±0.012	1.475±0.049	30	23	25

Table C.9: Overview of RM characteristics. In the table are reported the values of the latitude and longitude of the radial material (second and third columns). The fourth column contains the normal visual albedo and the fifth one the how the radial material albedo exceed the mean albedo of Vesta. Band depth I, II and (Band Area Ratio) BAR are reported in sixth, seventh and eighth columns. In the three columns there are the phase, incidence and emission angles. All the values reported are the average of bright areas. Values of latitude and longitude refer to the Claudia coordinates system.

BU15 SM - Very Bright Area			
BI Center (μm)	BII Center (μm)	BI Depth	BII Depth
0.929	1.955	0.354	0.286
0.929	1.962	0.467	0.235
0.935	1.957	0.442	0.217
0.935	1.957	0.391	0.208
0.929	1.955	0.356	0.227
0.926	1.953	0.373	0.248
0.928	1.957	0.457	0.252
0.931	1.957	0.436	0.249
0.933	1.955	0.412	0.256
0.931	1.960	0.426	0.269
0.931	1.962	0.474	0.269
0.929	1.962	0.461	0.267
BU15 SR			
0.933	1.965	0.478	0.289
0.930	1.972	0.479	0.276
0.933	1.967	0.468	0.277

Table C.10: Band centers and band depths values of the very bright steak in BU15-SM (black circle in Fig. 6.11) and of its surroundings.

HEDs band depths at different grain size		
Grain Size	BI Depth	BII Depth
EET87503		
0-25 μm	0.373	0.207
25-45 μm	0.447	0.288
45-75 μm	0.487	0.371
75-125 μm	0.477	0.369
ALHA76005		
0-25 μm	0.372	0.237
25-45 μm	0.476	0.372
45-75 μm	0.535	0.453
75-125 μm	0.511	0.469
Juvinas		
0-25 μm	0.460	0.292
25-45 μm	0.579	0.447
45-75 μm	0.601	0.504
75-125 μm	0.586	0.517
Millbillillie		
0-25 μm	0.443	0.268
25-45 μm	0.574	0.413
45-75 μm	0.577	0.445
75-125 μm	0.556	0.456
ALH78132		
0-25 μm	0.416	0.267
25-45 μm	0.573	0.428
45-75 μm	0.607	0.496
Y74450		
0-25 μm	0.365	0.205
25-45 μm	0.514	0.354
45-75 μm	0.551	0.416
75-125 μm	0.531	0.435
EETA79002		
0-25 μm	0.507	0.280
25-45 μm	0.642	0.417
45-75 μm	0.638	0.442
75-125 μm	0.613	0.443
Ellemeet		
0-25 μm	0.610	0.457
25-45 μm	0.596	0.375
Johnstown		
0-25 μm	0.665	0.514
25-45 μm	0.696	0.537
Y75032		
0-25 μm	0.510	0.299
25-45 μm	0.654	0.461

Table C.11: Band depths values of RELAB samples of HEDs with different grain size.

BI Center and BAR of HED with grain size 0-25 μm			
Sample Name	Type	BI Center (μm)	BAR
Binda	Howardite	0.928	1.662
Bununu	Howardite	0.930	1.537
EET83376	Howardite	0.935	1.786
EET87503	Howardite	0.930	1.432
EET87513	Howardite	0.933	1.483
Frankfort	Howardite	0.929	1.689
GRO95535	Howardite	0.931	1.675
Kapoeta	Howardite	0.930	1.370
LeTeilleul	Howardite	0.929	1.761
Petersburg	Howardite	0.936	1.939
QUE94200	Howardite	0.924	1.740
Y7308	Howardite	0.927	1.675
Y790727	Howardite	0.932	1.859
Y791573	Howardite	0.928	1.799
A87272	Eucrite	0.940	1.569
A881819	Eucrite	0.931	1.634
ALH78132	Eucrite	0.932	1.934
ALH85001	Eucrite	0.927	1.635
ALHA76005	Eucrite	0.936	1.936
Bereba	Eucrite	0.940	1.766
Bouvante	Eucrite	0.944	2.408
Cachari	Eucrite	0.939	1.746
EET87542	Eucrite	0.942	1.470
EET90020	Eucrite	0.940	1.312
EETA79005	Eucrite	0.934	1.880
GRO95533	Eucrite	0.940	1.818
Ibitira	Eucrite	0.939	1.413
Jonzac	Eucrite	0.939	2.011
Juvinas	Eucrite	0.936	1.730
LEW87004	Eucrite	0.935	1.726
Millbillillie	Eucrite	0.937	1.584
MooreCounty	Eucrite	0.938	1.521
PCA82502	Eucrite	0.941	2.214
Padvarninkai	Eucrite	0.949	1.330
Pasamonte	Eucrite	0.940	1.904
SerradeMage	Eucrite	0.931	1.566
Stannern	Eucrite	0.938	1.920
Y74450	Eucrite	0.935	1.579
Y792510	Eucrite	0.941	1.646
Y792769	Eucrite	0.941	1.796
A881526	Diogenite	0.920	1.470
ALH77256	Diogenite	0.922	1.646
AiounelAtrouss	Diogenite	0.924	1.563
EETA79002	Diogenite	0.920	1.441
GRO95555	Diogenite	0.923	1.591
Johnstown	Diogenite	0.918	1.307
LAP91900	Diogenite	0.922	1.566
Tatahouine	Diogenite	0.920	1.554
Y74013	Diogenite	0.923	1.685
Y75032	Diogenite	0.927	1.597

Table C.12: Band center I and BAR values of RELAB samples of HEDs with grain size between 0 and 25 μm .

Bibliography

- Adams, J. B., 1974. Visible and near-infrared diffuse reflectance spectra of pyroxenes as applied to remote sensing of solid objects in the solar system. *Journal of Geophysical Research* 79, 4829–4836. DOI: 10.1029/JB079i032p04829.
- Adams, J. B., Gillespie, A. R., 2006. Remote Sensing of Landscapes with Spectral Images: A Physical Modeling Approach.
- Adams, J. B., Smith, D. E., Johnson, T. V., 1986. Spectral mixture modeling: A new analysis of rock and soil types at the Viking Lander 1 site. *Journal of Geophysical Research* 91, 8098–8112. DOI: 10.1029/JB091iB08p08098.
- Akamatsu, Y., Arai, K., Inoue, K., Iwashita, A., Ueshi, T., Uchida, O., Endo, S., Ohyama, Y., al., 1996. Remote sensing notes.
- Ammannito, E., De Sanctis, M., Fonte, S., Magni, G., Capaccioni, F., Carraro, F., Capria, M., Farina, M., Frigeri, A., Marchi, S., Palomba, E., Tosi, F., Zambon, F., Blewett, D., Combe, J., McCord, T. B., Mittlefehldt, D., McSween, H. Y., Pieters, C., Sunshine, J., Titus, T., Toplis, M., Joy, S., Polanskey, C., Raymond, C., Russell, C., 2012. Vesta and the HED meteorites: comparison of spectral properties. *ACM*.
- Ammannito, E., De Sanctis, M. C., Capaccioni, F., Capria, M., Carraro, F., Combe, P., J., Fonte, S., Frigeri, A., Joy, S., Longobardo, A., Magni, G., McCord, T. B., McFadden, L. A., McSween, H., Palomba, E., Pieters, C., P., C., Raymond, C. A., Sunshine, J., Tosi, F., Zambon, F., Russell, C. T., 2013a. Vestan lithologies mapped by VIR. *Maps*.
- Ammannito, E., De Sanctis, M. C., Palomba, E., Longobardo, A., Mittlefehldt, D. W., McSween, H. Y., Marchi, S., Capria, M. T., Capaccioni, F., Frigeri, A., Pieters, C. M., Ruesch, O., Tosi, F., F., Z., Carraro, F., Fonte, S., Hiesinger, H., Magni, G., McFadden, L. A., Raymond, C. A.,

- C.T., R., Sunshine, J. M., 2013b. Olivine from vesta's mantle exposed on the surface. *Nature* 504, 122–125. DOI: 10.1038/nature12665.
- Anderson, B. J., Johnson, C. L., Korth, H., Purucker, M. E., Winslow, R. M., Slavin, J. A., Solomon, S. C., McNutt, R. L., Raines, J. M., Zurbuchen, T. H., 2011. The Global Magnetic Field of Mercury from MESSENGER Orbital Observations. *Science* 333, 1859. DOI: 10.1126/science.1211001.
- Archinal, B. A., A'Hearn, M. F., Bowell, E., Conrad, A., Consolmagno, G. J., Courtin, R., Fukushima, T., Hestroffer, D., Hilton, J. L., K. G. A., Neumann, G., Oberst, J., Seidelmann, P. K., Stooke, P., Tholen, D. J., Thomas, P. C., Williams, I. P., 2009. Report of the IAU working group on cartographic coordinates and rotational elements: 2009. *Cel. Mech. Dyn. Astron.* 109 (2), 101–135. DOI: 10.1007/s10569-010-9320-4.
- Ball, G. H., Hall, D. J., 1965. ISODATA a novel method of data analysis and pattern classification.
- Barrat, J.-A., Yamaguchi, A., Zanda, B., Bollinger, C., Bohn, M., 2010. Relative chronology of crust formation on asteroid Vesta: Insights from the geochemistry of diogenites. *Geochimica et Cosmochimica Acta* 74 (21), 6218–6231. DOI: 10.1016/j.gca.2010.07.028.
- Beck, A. W., McSween, H. Y., 2010. Diogenites as polymict breccias composed of orthopyroxenite and harzburgite. *Meteoritics & Planetary Science* 45, 850–872. DOI: 10.1111/j.1945-5100.2010.01061.x.
- Beck, A. W., Welten, K. C., McSween, H. Y., Viviano, C. E., Caffee, M. W., 2012. Petrologic and textural diversity among the PCA 02 howardite group, one of the largest pieces of the Vestan surface. *Meteoritics & Planetary Science* 47(6) (947-969. DOI: 10.1111/j.1945-5100.2012.01360.x.).
- Berman, M., Kiiveri, H., Lagerstrom, R., Ernst, A., Dunne, R., Huntington, J. F., 2004. ICE: A Statistical Approach to Identifying Endmembers in Hyperspectral Images. *IEEE TRANSACTIONS ON GEOSCIENCE AND REMOTE SENSING* 42 (10), 2085–2095. DOI: 10.1109/TGRS.2004.835299.
- Bin Luo, J., Doute, S., Liangpei, Z., 2013. Empirical Automatic Estimation of the Number of Endmembers in Hyperspectral Images. *IEEE TRANSACTIONS ON GEOSCIENCE AND REMOTE SENSING* 10 (1), 24–28. DOI: 10.1109/LGRS.2012.2189934.

- Bioucas-Dias, J. M., Nascimento, J. M. P., 2008. Hyperspectral Subspace Identification. *IEEE TRANSACTIONS ON GEOSCIENCE AND REMOTE SENSING* 46 (8), 2435–2445. DOI: 10.1109/TGRS.2008.918089.
- Bioucas-Dias, J. M., Plaza, A., Dobigeon, N., Parente, M., Du, Q., Gader, P., Chanussot, J., 2012. Hyperspectral Unmixing Overview: Geometrical, Statistical, and Sparse Regression-Based Approaches. *IEEE JOURNAL OF SELECTED TOPICS IN APPLIED EARTH OBSERVATIONS AND REMOTE SENSING* 5, 354–379. DOI: 10.1109/JSTARS.2012.2194696.
- Blatt, H., Tracy, R., 1996. *Petrology: Igneous, Sedimentary, and Metamorphic*. Third Edition Text Art Download.
- Blewett, D. T., Chabot, N. L., Denevi, B. W., Ernst, C. M., Head, J. W., Izenberg, N. R., Murchie, S. L., Solomon, S. C., Nittler, L. R., McCoy, T. J., Xiao, Z., Baker, D. M. H., Fassett, C. I., Braden, S. E., Oberst, J., Scholten, F., Scholten, F., Preusker, F., Hurwitz, D. M., 2011. Hollows on Mercury: MESSENGER Evidence for Geologically Recent Volatile-Related Activity. *Science* 333 (6051), 1856. DOI: 10.1126/science.1211681.
- Blewett, D. T., Vaughan, W. M., Xiao, Z., Chabot, N. L., Denevi, B. W., Ernst, C. M., Helbert, J., D’Amore, M., Maturilli, A., Head, J. W., Solomon, S. C., 2013. Mercury’s hollows: Constraints on formation and composition from analysis of geological setting and spectral reflectance. *Journal of Geophysical Research* 118 (5), 1013–1032. DOI: 10.1029/2012JE004174.
- Boardman, J. W., Kruse, F. A., Green, R. O., 1995. MAPPING TARGET SIGNATURES VIA PARTIAL UNMIXING OF AVIRIS DATA. Fifth Annual JPL Airborne Earth Science Workshop 1, AVIRIS Workshop, 23–26.
- Bottke, W. F., Nolan, M. C., Greenberg, R., Kolvoord, R. A., 1994. Velocity distributions among colliding asteroids. *Icarus* 107, 255–268. DOI: 10.1006/icar.1994.1021.
- Bowman, L. E., Spilde, M. N., Papike, J. J., 1997. Automated eds modal analysis applied to the diogenites. *Meteoritics & Planetary Science* 32 (869–875). DOI: 10.1111/j.1945-5100.1997.tb01577.x).
- Breuer, D., Hauck, S. A., Buske, M., Pauer, M., Spohn, T., 2007. Interior Evolution of Mercury. *Space Science Reviews* 132 (2–4), 229–260. DOI: 10.1007/s11214-007-9228-9.

- Burbine, T. H., Buchanan, P. C., Binzel, R. P., 2007. Deriving formulas from HED spectra for determining the pyroxenes mineralogy of Vesta and asteroids. 38th LPSC.
- Burbine, T. H., Buchanan, P. C., Dolgar, T., Binzel, R. P., 2009. Pyroxene mineralogies of near-Earth vestoids. *Meteoritics & Planetary Science* 44, 1331–1341. DOI: 10.1111/j.1945–5100.2009.tb01225.x.
- Burns, R., 1993. *Mineralogical Applications of Crystal Field Theory*. Second Edition. Cambridge University Press.
- Chandrasekhar, S., 1960. *Radiative transfer*.
- Chang, C., 2009. Virtual dimensionality for hyperspectral imagery. SPIE, DOI: 10.1117/2.1200909.1749.
- Chang, C., Du, Q., 2004. Estimation of Number of Spectrally Distinct Signal Sources in Hyperspectral Imagery. *IEEE TRANSACTIONS ON GEOSCIENCE AND REMOTE SENSING* 42 (3), 608–619. DOI: 10.1109/TGRS.2003.819189.
- Clark, R. N., 1983. Spectral properties of mixtures of montmorillonite and dark grains - implications for remote sensing minerals containing chemically and physically adsorbed water. *Journal of Geophysical Research* 88, 10635–10644. DOI: 10.1029/JB088iB12p10635.
- Clark, R. N., 1999. *Remote Sensing for the Earth Sciences - Manual of Remote Sensing*. Vol. 3. John Wiley and Sons, New York.
- Clark, R. N., Roush, T. L., 1984. Reflectance spectroscopy: Quantitative analysis techniques for remote sensing applications. *Journal of Geophysical Research* 89, 6329–6340. DOI: 10.1029/JB089iB07p06329.
- Cloutis, E. A., Gaffey, M. J., Jackowski, T. L., Reed, K. L., 1986. Calibrations of phase abundance, composition, and particle size distribution for olivine-orthopyroxene mixtures from reflectance spectra. *Journal of Geophysical Research* 91, 641–653. DOI: 10.1029/JB091iB11p11641.
- Cloutis, E. A., Izawa, M. R. M., Pompilio, L., Reddy, V., Hiesinger, H., Nathues, A., Mann, P. J., Le Corre, L., Palomba, E., Bell, J. F., 2013. Spectral reflectance properties of HED meteorites + CM2 carbonaceous chondrites: Comparison to HED grain size and compositional variations and implications for the nature of low-albedo features on Asteroid 4 Vesta. *Icarus* 223, 850–877. DOI: 10.1016/j.icarus.2013.02.003.

- Coradini, A., Turrini, D., Federico, C., Magni, G., 2011. Vesta and Ceres: Crossing the History of the Solar System. *Space Science Reviews* 163, 25–40. DOI: 10.1007/s11214-011-9792-x.
- Craig, M. A., Cloutis, E. A., Bailey, D. T., 2007. The effects of grain size, 45–1000 μm , on the reflectance spectrum of planetary analogs from 0.35–2.5 μm . 38th Lunar and Planetary Science Conference.
- Craig, M. A., Cloutis, E. A., Reddy, V., Bailey, D. T., Gaffey, M. J., 2008. The effects of grain size, 10 μm – 4.75 mm, on the reflectance spectrum of planetary analogs from 0.35–2.5 μm . 39th Lunar and Planetary Science Conference.
- Crown, D. A., Pieters, C. M., 1987. Spectral properties of plagioclase and pyroxene mixtures and the interpretation of lunar soil spectra. *Icarus* 72, 492–506. DOI: 10.1016/0019-1035(87)90047-9.
- De Sanctis, M., Ammannito, E., Capria, M., Tosi, F., Z., Carraro, F., Fonte, S., Frigeri, A., Jaumann, R., Magni, G., Marchi, S., McCord, T. B., McFadden, L., McSween, H. Y., Mittlefehldt, D. W., Nathues, A., Palomba, E. P., C.M., Raymond, C., Russell C.T. and Toplis, M. J., Turrini, D., 2012a. Spectroscopic Characterization of Mineralogy and Its Diversity Across Vesta. *Science* 336, 697–700. DOI: 10.1126/science.1219270.
- De Sanctis, M., Coradini, A., Ammannito, E., Filacchione, G., Capria, M., Fonte, S., Magni, G., Barbis, A., Bini, A., Dami, M., Fici-Valtroni, I., Preti, G., the VIR Team, 2011. The VIR Spectrometer. *Space Science Reviews* 163, 329–369. DOI: 10.1007/s11214-010-9668-5.
- De Sanctis, M. C., Ammannito, E., Capria, M. T., Capaccioni, F., Combe, J.-P., Frigeri, A., Longobardo, A., Magni, G., Marchi, S., McCord, T. B., Palomba, E., Tosi, F., Zambon, F., Carraro, F., Fonte, S., Li, J.-Y., McFadden, L. A., Mittlefehldt, D. W., Pieters, C. M., Jaumann, R., Stephan, K., Raymond, C. A., Russell, C. T., 2013. Vesta’s mineralogical composition as revealed by the visible and infrared spectrometer on Dawn. *Meteoritics & Planetary Science*, DOI: 10.1111/maps.12138.
- De Sanctis, M. C., Combe, J.-P., Ammannito, E., Palomba, E., Longobardo, A., McCord, T. B., Marchi, S., Capaccioni, F., Capria, M. T., Mittlefehldt, D. W., Pieters, C. M., Sunshine, J., Tosi, F., Zambon, F., Carraro, F., Fonte, S., Frigeri, A., Magni, G., Raymond, C. A., Russell, C. T., Turrini, D., 2012b. Detection of widespread hydrated materials on Vesta by the VIR

- imaging spectrometer on board the DAWN mission. *The Astrophysical Journal Letters* 758, L36. DOI:10.1088/2041-8205/758/2/L36.
- Deer, W. A., Howie, R. A., Zussman, J., 1992. *An Introduction to the Rock-Forming Minerals*. Longman Scientific & Technical.
- Denevi, B. W., Ernst, A., Meyer, H. M., Robinson, M. S., Murchie, S., Whitten, J. L., Head, J. W., Watters, T. R., Solomon, S. C., Ostrach, L. R., Chapman, C. R., Byrne, P. K., Klimczak, C., Peplowski, P. N., 2013. The distribution and origin of smooth plains on Mercury. *Journal of Geophysical Research* 118, 891–907. DOI: 10.1002/jgre.20075, 2013.
- Dexter, D. L., 1956. Absorption of light by atoms in solids. *Physical Review* 101, 48–55.
- Dor, E. B., Malthus, T., Plaza, A., Schläpfer, D., 2012. *Airborne Measurements for Environmental Research*. Manfred Wendisch & Jean-Louis Brenguier.
- Eches, O., Dobigeon, N., Tourneret, J.-Y., 2010. Estimating the Number of Endmembers in Hyperspectral Images Using the Normal Compositional Model and a Hierarchical Bayesian Algorithm. *IEEE JOURNAL OF SELECTED TOPICS IN SIGNAL PROCESSING* 4 (3), 582–591. DOI: 10.1109/JSTSP.2009.2038212.
- Espiritu, R., Malaret, E., 2012. Experiment Data Record Software Interface Specification for the MESSENGER Mercury Atmospheric and Surface Composition Spectrometer/ Visible and Infrared Spectrograph (MASCS/VIRS) SIE-06-045 D. MASCS/VIRS EDR SIS Version 2.2, http://pds--geosciences.wustl.edu/messenger/mess--e_v_h--mascs--2--virs--edr--v1/messmas_1001/document/virsedrsis.pdf.
- Feierberg, M. A., Drake, M. J., 1980. The meteorite-asteroid connection - The infrared spectra of eucrites, shergottites, and Vesta. *Science* 209, 805–807. DOI: 10.1126/science.209.4458.805.
- Gaffey, M. J., 1976. Spectral reflectance characteristics of the meteorite classes. *Journal of Geophysical Research* 81, 905–920. DOI: 10.1029/JB081i005p00905.
- Gaffey, M. J., 1997. Surface Lithologic Heterogeneity of Asteroid 4 Vesta. *Icarus* 127, 130–157. DOI: dx.doi.org/10.1006/icar.1997.5680.

- Gaffey, M. J., Burbine, T. H., Piatek, J. L., Reed, K. L., Chaky, D. A., Bell, J. F., Brown, R. H., 106. Mineralogical variations within the S-type asteroid class. *Icarus*, 573. DOI: 10.1006/icar.1993.1194.
- Gaffey, M. J., Cloutis, E. A., Kelley, M. S., Reed, K. L., 2002. *Mineralogy of Asteroids. Asteroids III*-University of Arizona Press, Tucson.
- Goetz, A. F. H., Vene, G., Solomon, J. E., Barrett, N. R., 1985. Imaging Spectrometry for Earth Remote Sensing. *Science* 228, 1147–1153. DOI: 10.1126/science.228.4704.1147.
- Goguen, J. D., 1981. A theoretical and experimental investigation of the photometric functions of particulate surfaces. Ph.D. Thesis Cornell Univ., Ithaca, NY.
- Gounelle, M., Zolensky, M. E., Liou, J.-C., Bland, P. A., Alard, O., 2003. Mineralogy of carbonaceous chondritic microclasts in howardites: identification of C2 fossil micrometeorites. *Geochimica et Cosmochimica Acta* 67 (3), 507–527. DOI: 10.1016/S0016-7037(02)00985-7.
- Grace, J. N., Disney, M. L. P., Qquaife, T., Bowyer, P., 2007. Can we measure terrestrial photosynthesis from space directly, using spectral reflectance and fluorescence? *Global Change Biology* 11, 1484–1497.
- Guanter, L., Richter, R., Moreno, J., 2006. Spectral calibration of hyperspectral imagery using atmospheric absorption features. *Applied Optics* 45, 2360–2370. DOI: 10.1364/AO.45.002360.
- Hapke, B., 1981. Bidirectional reflectance spectroscopy. I - Theory. *Journal of Geophysical Research* 86, 3039–3054. DOI: 10.1029/JB086iB04p03039.
- Hapke, B., 1993. *Theory of Reflectance and Emittance Spectroscopy*.
- Harder, H., Schubert, G., 2001. Sulfur in Mercury's Core? *Icarus* 151 (1), 118–122. DOI: 10.1006/icar.2001.6586.
- Harloff, J., Arnold, G., 2001. Near-infrared reflectance spectroscopy of bulk analog materials for planetary crust. *Planetary and Space Science* 49, 191–211. DOI: 10.1016/S0032-0633(00)00132-X.
- Hasegawa, S., Murakawa, K., Ishiguro, M., Nonaka, H., Takato, N., Davis, C. J., Ueno, M., Hiroi, T., 2003. Evidence of hydrated and/or hydroxylated minerals on the surface of asteroid 4 Vesta. *Geophysical Research Letters* 30 (21), PLA 2–1, CiteID 2123. DOI: 10.1029/2003GL018627.

- Hendrix, M. T., Garcia, I., Plaza, J., Martin, G., Plaza, A., 2012. A New Minimum-Volume Enclosing Algorithm for Endmember Identification and Abundance Estimation in Hyperspectral Data. *IEEE TRANSACTIONS ON GEOSCIENCE AND REMOTE SENSING* 50 (7), 2744–2757. DOI: 10.1109/TGRS.2011.2174443.
- Hewins, R. H., Newsom, H. E., 1988. Igneous activity in the early solar system. University of Arizona Press.
- Hinrichs, J. L., Lucey, P. G., 2002. Temperature-Dependent Near-Infrared Spectral Properties of Minerals, Meteorites, and Lunar Soil. *Icarus* 155, 169–180. DOI:10.1006/icar.2001.6754.
- Hinrichs, J. L., Lucey, P. G., Robinson, M. S., Meibom, A., Krot, A. N., 1999. Implications of temperature-dependent near-IR spectral properties of common minerals and meteorites for remote sensing of asteroids. *Geophysical Research Letters* 26, 1661–1664. DOI: 10.1029/1999GL900334.
- Hiroi, T., Pieters, C. M., Takeda, H., 1994. Grain size of the surface regolith of asteroid 4 Vesta estimated from its reflectance spectrum in comparison with HED meteorites. *Meteoritics* 29 (394-26).
- Holsclaw, G. M., McClintock, W. E., Domingue, D. L., Izenberg, N. R., Blewett, D. T., Sprague, A. L., 2010. A comparison of the ultraviolet to near-infrared spectral properties of Mercury and the Moon as observed by MESSENGER. *Icarus* 209 (1), 179–194. DOI: 10.1016/j.icarus.2010.05.001.
- Izenberg, N. R., Klima, R., Murchie, S. L., Blewett, D. T., Holsclaw, G. M., McClintock, W. E., Malaret, E., Mauceri, C., Vilas, F., Sprague, A. L., Helbert, J., Domingue, D. L., Head, J. W., Goudge, T. A., Solomon, S. C., Hibbitts, C., Dyar, M. D., 2014. The low-iron, reduced surface of Mercury as seen in spectral reflectance by MESSENGER. *Icarus* 228, 365–374. DOI: dx.doi.org/10.1016/j.icarus.2013.10.023.
- Jaumann, R., Williams, D. A., Buczkowski, D., Yingst, R., Preusker, F., Hiesinger, H., Schmedemann, N., Kneissl, T., Vincent, J. B., Blewett, D. T., Buratti, B. J., Carsenty, U., Denevi, B. W., De Sanctis, M. C., Garry, W., Keller, H. U., Kersten, E., Krohn, K., Li, J.-Y., Marchi, S., Matz, K.-D., McCord, T. B., McSween, H. Y., Mest, S., Mittlefehldt, D. W., Mottola, S., Nathues, A., Neukum, G., O'Brien, D. P., Pieters, C. M., Prettyman, T. H., Raymond, C. A., Roatsch, T., C.T., R., Schenk, P., Schmidt, B. E., Scholten, F., Stephan, K., Sykes, M. V., Tricarico, P.,

- Wagner, R., Zuber, M. T., Sierks, H., 2012. Vesta's Shape and Morphology. *Science* 336, 687. DOI: 10.1126/science.1219122.
- JPL, 2008. Planetary Science Data Dictionary Document. Jet Propulsion Laboratory and California Institute of Technology.
- JPL, 2009. Planetary Data System Standards Reference. Jet Propulsion Laboratory and California Institute of Technology.
- Keshava, N., Mustard, J., 2002. Spectral unmixing. *IEEE Signal Processing Magazine* 19 (1), 44–57. DOI: 10.1109/79.974727.
- Klima, R. L., Dyar, M. D., Pieters, C. M., 2011. Near-infrared spectra of clinopyroxenes: Effects of calcium content and crystal structure. *Meteoritics & Planetary Science* 46, 379–395. DOI: 10.1111/j.1945-5100.2010.01158.x.
- Klima, R. L., Pieters, C. M., Dyar, M. D., 2007. Spectroscopy of synthetic Mg-Fe pyroxenes I: Spin-allowed and spin-forbidden crystal field bands in the visible and near-infrared. *Meteoritics & Planetary Science* 42, 235–253.
- Lawrence, D. J., Feldman, W. C., Goldsten, J. O., Sylvestre, M., Peplowski, P. N., Anderson, B. J., Bazell, D., McNutt, R. L., Nittler, L. R., Prettyman, T. H., Rodgers, D. J., Solomon, S. C., Weider, S. Z., 2013. Evidence for Water Ice Near Mercury's North Pole from MESSENGER Neutron Spectrometer Measurements. *Science* 339 (6117), 292. DOI: 10.1126/science.1229953.
- Lax, M., 1954. The influence of lattice vibration on electronic transition in solids. Photoconductivity Conference. New York: Wiley, 111–45.
- Le Corre, L., Reddy, V., Nathues, A., Cloutis, E. A., 2011. How to characterize terrains on 4 Vesta using Dawn Framing Camera color bands? *Icarus* 216, 376–386. DOI: 10.1016/j.icarus.2011.09.014.
- Li, J. Y., 2013. Body-fixed coordinate systems for asteroid (4) Vesta. Available at: http://sbn.psi.edu/archive/dawn/fc/DWNVFC2_1A/DOCUMENT/VESTA_COORDINATES/VESTA_COORDINATES_131018.PDF.
- Li, J. Y., McFadden, L. A., Thomas, P. C., Mutchler, M. J., Parker, J. W., Young, E. F., Russell, C., Sykes, M. V., Schmidt, B. E., 2010. Photometric mapping of asteroid (4) Vesta's southern hemisphere with Hubble Space Telescope. *Icarus* 208, 238–251. DOI: 10.1016/j.icarus.2010.02.008.

- Li, J.-Y., Mittlefehldt, D. W., Pieters, C. M., De Sanctis, M. C., Schröder, S. E., Hiesinger, H., Blewett, D. T., C.T., R., Raymond, C. A., Keller, H. U., 2012. INVESTIGATING THE ORIGIN OF BRIGHT MATERIALS ON VESTA: SYNTHESIS, CONCLUSIONS, AND IMPLICATIONS. LPSC.
- Li, J. Y., Mittlefehldt, D., W., Pieters, C. M., De Sanctis, M. C., S. E., Hiesinger, H., Williams, D. A., Beck, A. W., Ammannito, E., Capaccioni, F., Capria, M. T., Palomba, E., Carsenty, U., Kelleri, H. U., Russell, C. T., Raymond, C. A., Jaumann, R., McSween, H., Y., McCord, T. B., Denevi, B. W., Sunshine, J. M., 2013. Vesta's Bright, Primordial Material. *Icarus* this issue.
- Liangrocapart, S., Petrou, M., 1998. Mixed pixels classification. *Proc. SPIE Image and Signal Process. Remote Sensing IV* 3500 (72-83).
- Longobardo, A., Palomba, E., Capaccioni, F., De Sanctis, M. C., Tosi, F., Ammannito, E., Schröder, S. E., Zambon, F., Raymond, C., A., Russell, C., 2014. Photometric behavior of spectral parameters in Vesta dark and bright region as inferred by the Dawn VIR spectrometer. *Icarus*, DOI: 10.1016/j.icarus.2014.02.014.
- Lumme, K., Bowell, E., 1981. Radiative transfer in the surfaces of atmosphereless bodies. I - Theory. II - Interpretation of phase curves. *Astronomical Journal* 86, 1694–1721. DOI: 10.1086/113054.
- Marchi, S., O'Brien, D. P., Schenk, P., De Sanctis, M. C., Gaskell, R., Jaumann, R., Mottola, S., Preusker, F., Raymond, C. A., Russell, C. T., 2012. The Violent Collisional History of Asteroid 4 Vesta. *Science* 336, 690. DOI: 10.1126/science.1218757.
- Martinez, P., Plaza, A., 2012. Spatial-Spectral Preprocessing Prior to End-member Identification and Unmixing of Remotely Sensed Hyperspectral Data. *IEEE JOURNAL OF SELECTED TOPICS IN APPLIED EARTH OBSERVATIONS AND REMOTE SENSING* 5 (2), 380–395. DOI: 10.1109/JSTARS.2012.2192472.
- Martonchik, J. V., Bruegge, C. J., Strahler, A. H., 2000. A Review of Reflectance Nomenclature Used in Remote Sensing. *Remote Sensing Reviews* 19, 9–20. DOI: 10.1080/02757250009532407.
- Mayne, R. G., Sunshine, J. M., McSween, H. Y., McCoy, T. J., Corrigan, C. M., Gale, A., 2010. Petrologic insights from the spectra of the unbrec-

- ciated eucrites: Implications for Vesta and basaltic asteroids. *Meteoritics & Planetary Science* 45, 1074–1092. DOI: 10.1111/j.1945–5100.2010.01090.x.
- McCord, T. B., Adams, J. B., Johnson, T. V., 1970. Asteroid Vesta: Spectral Reflectivity and Compositional Implications. *Science* 168, 1445–1447. DOI: 10.1126/science.168.3938.1445.
- McCord, T. B., Castillo-Rogez, J., Rivkin, A., 2011a. Ceres: Its Origin, Evolution and Structure and Dawn’s Potential Contribution. *Space Science Reviews* 163 (1-4), 63–76. DOI: 10.1007/s11214–010–9729–9.
- McCord, T. B., Li, J.-Y., Combe, J.-P., McSween, H. Y., Jaumann, R., Reddy, V., Tosi, F., Williams, D. A., Blewett, D. T., Turrini, D., Palomba, E., Pieters, C. M., De Sanctis, M. C., Ammannito, E., Capria, M. T., Le Corre, L., Longobardo, A., Nathues, A., Mittlefehldt, D. W., Schroder, S. E., Hiesinger, H., Beck, A. W., Capaccioni, F., Carsenty, U., Keller, H. U., Denevi, B. W., Sunshine, J. M., Raymond, C. A., Russell, C. T., 2012. Dark material on Vesta from the infall of carbonaceous volatile-rich material. *Nature* 461, 83–86. DOI:10.1038/nature11561.
- McCord, T. B., Sotin, C., 2005. Ceres: evolution and current state. *Journal of Geophysical Research* 110 (E5), E05009. DOI: 10.1029/2004JE002244.
- McCord, T. B., Taylor, L. A., Combe, J.-P., Kramer, G., Pieters, C. M., Sunshine, J. M., Clark, R. N., 2011b. Sources and physical processes responsible for OH/H₂O in the lunar soil as revealed by the Moon Mineralogy Mapper (M³). *Journal of Geophysical Research* 116, CiteID E00G05. DOI: 10.1029/2010JE003711.
- McSween, H. Y., Ammannito, E., Reddy, V., Prettyman, T. H., Beck, A. W., De Sanctis, M. C., Nathues, A., Le Corre, L., O’Brien, D. P., Yamashita, N., McCoy, T. J., Mittlefehldt, D. W., Toplis, M. J., Schenk, P., Palomba, E., Turrini, D., Tosi, F., Zambon, F., Longobardo, A., Capaccioni, F., Raymond, C., A., Russell, C. T., 2013a. Composition of the Rheasilvia basin, a window into Vesta’s interior. *Journal of Geophysical Research* 118, 335–346. DOI: 10.1002/jgre.20057.
- McSween, H. Y., Binzel, R. P., De Sanctis, M. C., Ammannito, E., Prettyman, T. H., Beck, A. W., Reddy, V., Le Corre, L., Gaffey, M. J., McCord, T. B., Raymond, C. A., Russell, C. T., 2013b. Dawn; the Vesta–HED connection; and the geologic context for eucrites, diogenites, and howardites. *Meteoritics & Planetary Science*, 1–15. DOI: 10.1111/maps.12108.

- McSween, H. Y., Mittlefehldt, D. W., Beck, A. W., Mayne, R. G., McCoy, T. J., 2011. Meteorites and Their Relationship to the Geology of Vesta and the Dawn Mission. *Space Science Reviews* 163 (141-174. DOI: 10.1007/s11214-010-9637-z).
- Memarsadeghi, N., Mount, D. M., Netanyahu, N. S., Le Moigne, J., 2007. A FAST IMPLEMENTATION OF THE ISODATA CLUSTERING ALGORITHM. *International Journal of Computational Geometry & Applications*, 71–103.
- Miao, L., Qi, H., 2007. Endmember Extraction From Highly Mixed Data Using Minimum Volume Constrained Nonnegative Matrix Factorization. *IEEE TRANSACTIONS ON GEOSCIENCE AND REMOTE SENSING* 45 (3), 765–777. DOI: 10.1109/TGRS.2006.888466.
- Mick, A., Murchie, S., Procter, L., Rivkin, A., Guinness, E., Ward, J., 2013. MDIS CDR/RDR SOFTWARE INTERFACE SPECIFICATION Version 1.2.13, (http://pdsimage.wr.usgs.gov/Missions/MESSENGER/MSGRMDS_5001/DOCUMENT/MDIS_CDR_RDRSIS.PDF).
- Mittlefehldt, D. W., 2000. Petrology and geochemistry of the Elephant Moraine A79002 diogenite: A genomict breccia containing a magnesian harzburgite component. *M&PS* 35 (5), 901–912. DOI: 10.1111/j.1945–5100.2000.tb01479.x.
- Mittlefehldt, D. W., Li, J.-Y., Pieters, C. M., De Sanctis, M. C., Schröder, S. E., Hiesinger, H., Blewett, D. T., Russell, C. T., Raymond, C. A., Yingst, R., 2012. Types and Distribution of Bright Materials on 4 Vesta. *LPSC*.
- Mittlefehldt, D. W., McCoy, T. J., Goodrich, C. A., Kracher, A., 1998. Non-Chondritic Meteorites from Asteroids bodies. Vol. 36. *Planetary Materials* chapter 4.
- Morimoto, N., Fabries, J., Ferguson, A. K., Ginzburg, I. V., Ross, M., Seifert, F. A., Zussman, J., Aoki, K., Gottardi, G., 1988. Nomenclature of pyroxenes. *American Mineralogist* 73, 1123–1133.
- Moroz, L., Schade, U., Wasch, R., 2000. Reflectance spectra of olivine-orthopyroxene-bearing assemblages at decreased temperatures: Implications for remote sensing of asteroids. *Icarus* 147, 79–93.

- Moskovitz, N. A., Willman, M., Burbine, T. H., Binzel, R. P., Bus, S. J., 2010. A spectroscopic comparison of HED meteorites and V-type asteroids in the inner Main Belt. *Icarus* 208, 773–788. DOI: 10.1016/j.icarus.2010.03.002.
- Nascimento, J. M. P., Bioucas-Dias, J. M., 2005. Vertex Component Analysis: A Fast Algorithm to Unmix Hyperspectral Data. *IEEE TRANSACTIONS ON GEOSCIENCE AND REMOTE SENSING* 43 (4), 898–910. DOI: 10.1109/TGRS.2005.844293.
- Nicodemus, F. E., 1965. Directional reflectance and emissivity of an opaque surface. *Applied Optics* 4, DOI: 10.1364/AO.4.000767.
- Nicodemus, F. E., Richmond, J. C., Hsia, J. J., Ginsberg, I. W., W., L. I., 1977. Geometric considerations and nomenclature for reflectance.
- Painter, T. H., Dozier, J., 2004. Measurements of the hemispherical-directional reflectance of snow at fine spectral and angular resolution. *Journal of Geophysical Research* 109, DOI: 10.1029/2003JD004458.
- Palomba, E., Longobardo, A., De Sanctis, M. C., Zambon, F., Tosi, F., Ammannito, E., Capaccioni, F., Frigeri, A., Capria, M. T., Cloutis, E. A., Jaumann, R., Combe, J.-P., Raymond, C., A., Russell, C. T., 2014. Composition and mineralogy of dark material deposits on Vesta. *Icarus* this issue.
- Papike, J. J., Shearer, C. K., Splide, M. N., Karner, J. M., 2000. METAMORPHIC DIOGENITE GRO 95555: MINERAL CHEMISTRY OF ORTHOPYROXENE AND COMPARISONS TO THE DIOGENITE SUITE. LPSC.
- Peplowski, P. N., Evans, L. G., Hauck, S. A., McCoy, T. J., Boynton, W. V., Gillis-Davis, J. J., Ebel, D. S., Goldsten, J. O., Hamara, D. K., Lawrence, D. J., McNutt, R. L., Nittler, L. R., Solomon, S. C., Rhodes, E. A., Sprague, A. L., Starr, R. D., Stockstill-Cahill, K. R., 2011. Radioactive Elements on Mercury’s Surface from MESSENGER: Implications for the Planet’s Formation and Evolution. *Science* 333, 1850. DOI: 10.1126/science.1211576.
- Pieters, C. M., Ammannito, E., Blewett, D. T., Denevi, B. W., De Sanctis, M. C., Gaffey, M. J., Le Corre, L., Li, J.-Y., Marchi, S., McCord, T. B., McFadden, L. A., Mittlefehldt, D. W., Nathues, A., Palmer, E., Reddy, V., Raymond, C. A., Russell, C. T., 2012. Distinctive space weathering on

- vesta from regolith mixing processes. *Nature* 491, 79–82. DOI: 10.1038/nature11534.
- Pieters, C. M., Goswami, J. N., Clark, R. N., Annadurai, M., Boardman, J. W., Buratti, B. J., Combe, J.-P., Dyar, M. D., Green, R. O., Head, J. W., Hibbitts, C., Hicks, M., Isaacson, P., Klima, R., Kramer, G., Kumar, S., Livo, E., Lundeen, S., Malaret, E., McCord, T. B., Mustard, J., Nettles, J., Petro, N., Runyon, C., Staid, M., Sunshine, J., Taylor, L. A., Tompkins, S., Varanesi, P., 2009. Character and Spatial Distribution of OH/H₂O on the Surface of the Moon Seen by M³ on Chandrayaan-1. *Science* 326 (5952), 568. DOI: 10.1126/science.1178658.
- Pieters, C. M., McFadden, L. A., Prettyman, T., De Sanctis, M. C., McCord, T. B., Hiroi, T., Klima, R., Li, J.-Y., Jaumann, R., 2011. Surface Composition of Vesta: Issues and Integrated Approach. *Space Science Reviews* 163, 117–139. DOI: 10.1007/s11214-011-9809-5.
- Plaza, A., 2013. Spectral Unmixing of Hyperspectral Data. WHISPERS tutorial.
- Plaza, A., Martinez, P., Perez, R., Plaza, J., 2002. Spatial/Spectral End-member Extraction by Multidimensional Morphological Operations. *IEEE TRANSACTIONS ON GEOSCIENCE AND REMOTE SENSING* 40 (9), 2025–2041. DOI: 10.1109/TGRS.2002.802494.
- Pompilio, L., Pedrazzi, G., Sgavetti, M., Cloutis, E. A., Craig, M. A., Roush, T. L., 2009. Exponential Gaussian approach for spectral modeling: The EGO algorithm I. Band saturation. *Icarus* 201, 781–794. DOI: 10.1016/j.icarus.2009.01.022.
- Potter, A. E., Killen, R. M., Sarantos, M., 2006. Spatial distribution of sodium on Mercury. *Icarus* 181 (1), 1–12. DOI: 10.1016/j.icarus.2005.10.026.
- Prettyman, T. H., Feldman, W. C., McSween, H. Y., Dingler, R. D., Enemark, D. C., Patrick, D. E., Storms, S. A., Hendricks, J. S., Morgenthaler, J. P., Pitman, K. M., Reedy, R. C., 2011. Dawn’s Gamma Ray and Neutron Detector. *Space Science Reviews* 163, 371–459. DOI: 10.1007/s11214-011-9862-0.
- Prettyman, T. H., Mittlefehldt, D. W., Yamashita, N., Lawrence, D. J., Beck, A. W., Feldman, W. C., McCoy, T. J., McSween, H. Y., Toplis, M. J., Titus, T. N., Tricarico, P., Reedy, R. C., Hendricks, J. S., Forni, O.,

- Le Corre, L., Li, J.-Y., Mizzon, H., Reddy, V., Raymond, C. A., Raymond, C. A., Russell, C., 2012. Elemental Mapping by Dawn Reveals Exogenic H in Vesta's Regolith. *Science* 338 (6104), 242. DOI: 10.1126/science.1225354.
- Reddy, V., Le Corre, L., O'Brien, D. P. and Nathues, a., Cloutis, E. A., Durda, D., Bottke, W. F., B. M. U., Nervorny, D., Buczkowski, D., Scully, J. E. C., Palmer, E. M., Sierks, H., Mann, P. J., Becker, K. J., Beck, A. W., Mittlefehldt, D. W., Li, J.-Y., Gaskell, R., Russell, C. T., Gaffey, M. J., McSween, H. Y., McCord, T. B., Combe, J.-P., Blewett, D. T., 2012a. Delivery of dark material to Vesta via carbonaceous chondritic impacts. *Icarus* 223, 544–559. DOI: 10.1016/j.icarus.2012.10.006.
- Reddy, V., Li, J.-Y., Le Corre, L., Scully, J. E. C., Gaskell, R., Russell, C. T., Park, R. S., Nathues, A., Gaffey, M. J., Sierks, H., Becker, K. J., McFadden, L. A., 2013. Comparing Dawn, Hubble Space Telescope, and ground-based interpretations of (4) Vesta. *Icarus* 226, 1103–1114. DOI: 10.1016/j.icarus.2013.07.019.
- Reddy, V., Nathues, A., Le Corre, L., Sierks, H., Li, J.-Y., Gaskell, R., McCoy, T. J., Beck, A. W., Schröder, S. E., Pieters, C. M., Becker, K. J., Buratti, B. J., Denevi, B. W., Blewett, D. T., Christensen, U., Gaffey, M. J., Gutierrez-Marques, P., , Hicks, M., Keller, H. U., Maue, T., Mottola, S., McFadden, L. A., McSween, H. Y., Mittlefehldt, D. W., O'Brien, D. P., Raymond, C. A., Russell, C. T., 2012b. Color and Albedo Heterogeneity of Vesta from Dawn. *Science* 336, 700–704. DOI: 10.1126/science.1219088.
- Research System, i., 2004. ENVI User Guide.
- Richards, J. A., 2013. Remote Sensing Digital Image Analysis. Springer. DOI: 10.1007/978-3-642-30062-2.
- Righter, K., Drake, M. J., 1997. A magma ocean on Vesta: Core formation and petrogenesis of eucrites and diogenites. *Meteoritics & Planetary Science* 32, 929–944. DOI: 10.1111/j.1945-5100.1997.tb01582.x.
- Riner, M. A., Lucey, P. G., 2012. Spectral effects of space weathering on Mercury: The role of composition and environment. *Geophysical Research Letters* 39 (12), CiteID L12201. DOI: 10.1029/2012GL052065.
- Rivkin, A. S., Howell, E. S., Vilas, F., Lebofsky, L. A., 2002. Hydrated Minerals on Asteroids: The Astronomical Record. Asteroids III-University of Arizona Press, Tucson.

- Rivkin, A. S., McFadden, L. A., Binzel, R. P., Sykes, M., 2006. Rotationally-resolved spectroscopy of Vesta I: 2–4 μm region. *Icarus* 180 (2), 464–472. DOI: 10.1016/j.icarus.2005.09.012.
- Roatsch, T., Kersten, E., Matz, K.-D., Preusker, F., Scholten, F., Jaumann, R., Raymond, C. A., Russell, C. T., 2012. High resolution Vesta High Altitude Mapping Orbit (HAMO) Atlas derived from Dawn framing camera images. *Planetary and Space Science* 73, 283–286. DOI: 10.1016/j.pss.2012.08.021.
- Rogge, D., Rivard, B., Zhang, J., Sanchez, J. H., Freng, J., 2007. Integration of spatial-spectral information for the improved extraction of endmembers. *Remote Sensing of Environment* 110 (3), 287–303. DOI: 10.1016/j.rse.2007.02.019.
- Roush, T. L., Singer, R. B., 1986. Gaussian analysis of temperature effects on the reflectance spectra of mafic minerals in the 1- μm region. *Journal of Geophysical Research* 91, 10301–10308. DOI: 10.1029/JB091iB10p10301.
- Russell, C., Raymond, C., McSween, H., Jaumann, R., Nathues, A., DeSanctis, M., Prettyman, T., Marchi, S., Schmedemann, N., Turrini, D., Scully, J., Hoffman, M., Otto, K., Buczkowski, D., 2013. Vesta in the light of Dawn. 44th LPSC.
- Russell, C. T., Capaccioni, F., Coradini, A., De Sanctis, M. C., Feldman, W. C., Jaumann, R., Keller, H. U., McCord, T. B., McFadden, L. A., Mottola, S., Pieters, C. M., Prettyman, T. H., Raymond, C. A., Sykes, M. V., Smith, D. E., Zuber, M. T., 2007. Dawn Mission to Vesta and Ceres. *Symbiosis between Terrestrial Observations and Robotic Exploration. Earth, Moon, and Planets* 101, 65–91. DOI: 10.1007/s11038-007-9151-9.
- Russell, C. T., Raymond, C. A., 2011. The Dawn Mission to Vesta and Ceres. *Space Science Reviews* 163, 3–23. DOI: 10.1007/s11214-011-9836-2.
- Russell, C. T., Raymond, C. A., Coradini, A., McSween, H. Y., Zuber, M. T., Nathues, A., De Sanctis, M. C., Jaumann, R., Konopliv, A. S., Preusker, F., Asmar, S. W., Park, R. S., Gaskell, R., Keller, H. U., Mottola, S., Roatsch, T., Scully, J. E. C., Smith, D. E., Tricarico, P., Toplis, M. J., Christensen, U. R., Feldman, W. C., Lawrence, D. J., McCoy, T. J., Prettyman, T. H., Reedy, R. C., Sykes, M. E., Titus, T. N., 2012. Dawn at Vesta: Testing the protoplanetary paradigm. *Science* 336, 684–686. DOI:10.1126/science.1219381.

- Ruzicka, A., Snyder, G. A., Taylor, L. A., 1997. Vesta as the HED Parent Body: Implications for the Size of a Core and for Large-Scale Differentiation. *Meteoritics & Planetary Science* 32, 825–840: DOI: 10.1111/j.1945–5100.1997.tb01573.x.
- Schaepman-Strub, G., Schaepman, M. E., Painter, T. H., Dangel, S., Martonchik, J. V., 2006. Reflectance quantities in optical remote sensing—definitions and case studies. *Remote Sensing of Environment* 103, 27–42. DOI: 10.1016/j.rse.2006.03.002.
- Schröder, S. E., Mottola, S., Keller, H., 2013. Resolved Photometry of Vesta Reveals Physical Properties of Crater Regolith. *Planetary and Space Science*, DOI: dx.doi.org/10.1016/j.pss.2013.06.009.
- Serventi, G., Carli, C., Sgavetti, M., Ciarniello, M., Capaccioni, F., Pedrazzi, G., 2013. Spectral variability of plagioclase–mafic mixtures (1): Effects of chemistry and modal abundance in reflectance spectra of rocks and mineral mixtures. *Icarus* 226, 282–298. DOI: dx.doi.org/10.1016/j.icarus.2013.05.041.
- Sierks, H., Keller, H. U., Jaumann, R., Michalik, H., Behnke, T., Buben-
hagen, F., Buttner, I., Carsenty, U., Christensen, U., Enge, R., Fiethe,
B., Gutierrez Marques, P., Hartwig, H., Kruger, H., Kuhne, W., Maue,
T., Mottola, S., Nathues, A., Reiche, K.-U., Richards, M. L., Roatsch, T.,
Schroder, S. E., Szemerey, I., Tschentscher, M., 2011. The dawn framing
camera. *Space Science Reviews* 163, 263–327.
- Smith, D. E., Zuber, M. T., Phillips, R. J., Solomon, S. C., Hauck, S. A.,
Lemoine, F. G., Mazarico, E., Neumann, G., Peale, S. J., Margot, J.-L.,
Johnson, C. L., Torrence, M. H., Perry, M. E., Rowlands, D. D., Goossen,
S., Head, J. W., Taylor, A. H., 2012. Gravity Field and Internal Structure
of Mercury from MESSENGER. *Science* 336 (6078), 214. DOI: 10.1126/sci-
ence.1218809.
- Snyder, J. P., 1982. Map Projections Used by the U.S. Geological Survey.
GEOLOGICAL SURVEY BULLETIN 1532. Second edition.
- Snyder, J. P., 1987. Map projection - A working manual. U.S.G.S. profes-
sional paper; 1395.
- Solomon, S. C., McNutt, R. L., Gold, R. E., Domingue, D. L., 2007. MES-
SENGER Mission Overview. *Space Science Reviews* 131 (1-4), 3–39. DOI:
10.1007/s11214-007-9247-6.

- Somers, B., Zortea, M., Plaza, A., 2012. Automated extraction of image-based endmember Bundles for Improved Spectral Unmixing. *EEE JOURNAL OF SELECTED TOPICS IN APPLIED EARTH OBSERVATIONS AND REMOTE SENSING* 5 (2), 396–408. DOI: 10.1109/JS-TARS.2011.2181340.
- Spudis, P. D., Guest, J. E., 1988. *Stratigraphy and geologic history of Mercury*. University of Arizona Press, Tucson.
- Stephan, K., Jaumann, R., De Sanctis, M. C., Ammannito, E., Tosi, F., Krohn, K., Marchi, S., Ruesch, O., Zambon, F., Matz, K.-D., Preusker, F., Roatsch, T., Raymond, C. A., Russell, C. T., 2014. A compositional and geological view of fresh ejecta of small impact craters on asteroid 4 Vesta. *Journal of Geophysical Research* in review.
- Stimpfl, M., Ganguly, J., 2002. THERMAL HISTORY OF THE UNBREC-CIATED DIOGENITE GRO (GROSVENOR MOUNTAINS) 95555: CONSTRAINTS FROM INTER- AND INTRA CRYSTALLINE FE-MG EXCHANGE REACTION. LPSC.
- Sunshine, J. M., Farnham, T. L., Feaga, L. M., Groussin, O., Merlin, F., Milliken, R. E., A'Hearn, M. F., 2009. Temporal and Spatial Variability of Lunar Hydration As Observed by the Deep Impact Spacecraft. *Science* 326 (5952), 565. DOI: 10.1126/science.1179788.
- Tedesco, E. F., Williams, J. G., Matson, D. L., Weeder, G. J., Gradie, J. C., Lebofsky, L. A., 1989. A three-parameter asteroid taxonomy. *Astronomical Journal* 97, 580–606.
- Thomas, P. C., Binzel, R. P., Gaffey, M. J., Storrs, A. D., Wells, E. N., Zellner, B. H., 1997a. Impact Excavation on Asteroid 4 Vesta: Hubble Space Telescope Results. *Science* 227, 1492–1495. DOI: 10.1126/science.277.5331.1492.
- Thomas, P. C., Binzel, R. P., Gaffey, M. J., Zellner, B. H., Storrs, A. D., Wells, E. N., 1997b. Vesta: Spin pole, size, and shape from HST images. *Icarus* 128 (1), 88–94. DOI: 10.1006/icar.1997.5736.
- Tosi, F., Capria, M. T., De Sanctis, M. C., Combe, J.-P., Zambon, F., Nathues, A., Schröder, S. E., Li, J.-Y., Palomba, E., Longobardo, A., Blewett, D. T., Denevi, B. W., Palmer, E., Capaccioni, F., Sunshine, J. M., Ammannito, E., Titus, T., Mittlefehldt, D. W., Blewett, D. T., Russell, C. T., Raymond, C. A., the Dawn/VIR Team, 2014a. Thermal behavior

- of dark and bright surface features on Vesta as derived from Dawn/VIR. *Icarus*, DOI: 10.1016/j.icarus.2014.03.017.
- Tosi, F., F., Z., Capria, M. T., De Sanctis, M. C., Capaccioni, F., Ammannito, E., Titus, T. N., Palomba, E., C.T., R., Raymond, C. A., 3-4 February, 2014 2014b. Global Resolved Temperature Maps of Vesta. In: *Vesta in the Light of Dawn: First Exploration of a Protoplanet in the Asteroid Belt*. No. 1773. LPI, p. 2026.
- Wacker, A. G., Landgrebe, D. A., 1972. Minimum Distance Classification in Remote Sensing.
- Warell, J., Valegard, P.-G., 2006. Albedo-color distribution on Mercury. A photometric study of the poorly known hemisphere. *Astronomy and Astrophysics* 460 (2), 625–633. DOI: 10.1051/0004-6361:20065850.
- Warren, P. H., 1997. MgO-FeO mass balance constraints and a more detailed model for the relationship between eucrites and diogenites. *Meteoritics & Planetary Science* 32, 945–963. DOI: 10.1111/j.1945-5100.1997.tb01583.x.
- Watters, T. R., Robinson, M. S., Cook, A. C., 1998. Topography of lobate scarps on Mercury: New constraints on the planet’s contraction. *Geology* 26 (11), 991. DOI: 10.1130/0091-7613(1998)026;0991:TOLSOM;2.3.CO;2.
- Winter, M. E., 1999. N-FINDR: an algorithm for fast autonomous spectral end-member determination in hyperspectral data. *SPIE Conference on Imaging Spectrometry* 3753.
- Zambon, F., Tosi, F., De Sanctis, M. C., Blewett, D. T., Ammannito, E., Russell, C., Raymond, C. A., 2014a. TESTING LINEAR SPECTRAL UNMIXING ON LABORATORY MIXTURES: APPLICATION TO VIR DATA FOR ASTEROID VESTA. WHISPERS.
- Zambon, F. F., De Sanctis, M. C., Schröder, S. E., Tosi, F., Longobardo, A., Ammannito, E., Blewett, D. T., Mittlefehldt, D. W., Li, J.-Y., Palomba, E., Capaccioni, F., Frigeri, A., Capria, M. T., Fonte, S., Nathues, A., Pieters, C. M., Russell, C. T., Raymond, C., A., 2014b. Spectral Analysis of the Bright Materials on the Asteroid Vesta. *Icarus*.
- Zare, A., Gader, P., 2007. Sparsity Promoting Iterated Constrained Endmember Detection in Hyperspectral Imagery. *IEEE GEOSCIENCE AND REMOTE SENSING LETTERS* 4 (3), 446–450. DOI: 10.1109/LGRS.2007.895727.

- Zolensky, M. E., Weisberg, M. K., Buchanan, P. C., Mittlefehldt, D. W., 1996. Mineralogy of carbonaceous chondrite clasts in HED achondrites and the Moon. *Meteoritics & Planetary Science* 31 (4), 518–537. DOI: 10.1111/j.1945–5100.1996.tb02093.x.
- Zortea, M., Plaza, A., 2009. Spatial Preprocessing for Endmember Extraction. *IEEE TRANSACTIONS ON GEOSCIENCE AND REMOTE SENSING* 47 (8), 2679–2693. DOI: 10.1109/TGRS.2009.2014945.
- Zuber, M. T., McSween, H. Y., Binzel, R. P., Elkins-Tanton, L. T., Konopliv, A. S., Pieters, C. M., Smith, D. E., 2011. Origin, Internal Structure and Evolution of 4 Vesta. *Space Science Reviews* 163, 77–93. DOI:10.1007/s11214–011–9806–8.